# GALAXY FLOWS IN AND AROUND THE LOCAL SUPERCLUSTER

A Dissertation

Presented to the Faculty of the Graduate School

of Cornell University

in Partial Fulfillment of the Requirements for the Degree of

Doctor of Philosophy

by

Karen L. Masters

August 2005

# GALAXY FLOWS IN AND AROUND THE LOCAL SUPERCLUSTER

Karen L. Masters, Ph.D.
Cornell University 2005

We present a new look at the peculiar velocity field in and around the Local Supercluster, using a much larger sample of velocity field tracers than has previously been available. This sample is a combination of galaxies, groups and clusters with primary distances taken from the literature or secondary distances from the luminosity-line width (Tully-Fisher) relation of spiral galaxies. The SFI++ Tully-Fisher sample presented here represents a significant increase in the number of available tracers in the local universe. A new template Tully-Fisher relation is fit to a subset of 911 galaxies in the vicinity of 36 nearby clusters and applied to derive peculiar velocities for $\sim 2000$ galaxies within $H_0 d = 6000$ km s$^{-1}$. Parametric models allowing for bulk motion of the sample, a quadrupolar component to the velocity field and describing infall onto spherical attractors are fit to the velocity field. Our preferred model includes infall onto attractors we identify with the Virgo Cluster and Hydra-Centaurus supercluster, a quadrupole describing extra expansion out of the Supergalactic plane, and a dipole we suggest is largely due to the gravitational attraction of Shapley supercluster. We see the benefit of combining the Tully-Fisher and primary distances in localizing the attractors and in defining the direction and magnitude of the residual dipole and quadrupole. The entire motion of the Local Group is accounted for by this model.

This parametric velocity field model is fit with the aim of providing an empirical correction to distances derived from redshifts in the local universe. We show that in the absence of redshift independent distances, the use of such a model is necessary to remove systematic bias from distance dependent quantities in local galaxy surveys (for example in deriving mass or luminosity functions). We fit a similar model to mock distance data from a constrained simulation of the real universe and use it to provide a practical guide to estimating realistic distances and their errors from flow models.

## TABLE OF CONTENTS


**1 Introduction** **1**
1.1 Peculiar velocities . . . 1
1.1.1 Gravitational Instability Theory . . . 1
1.2 Peculiar Velocities in and around the Local Supercluster . . . 3
1.2.1 Multiattractor Models . . . 4
1.2.2 Non-parametric modeling . . . 6
1.2.3 Recent studies of the local velocity field . . . 6
1.3 Overview of Thesis . . . 7

**2 The Impact of Distance Uncertainties on Local Luminostity and Mass Functions** **9**
2.1 Introduction . . . 9
2.2 Survey Simulations . . . 11
2.3 Results and Discussion . . . 12
2.3.1 Simulated HIPASS BGC . . . 12
2.3.2 Simulated Virgo cluster survey . . . 13
2.4 Conclusions . . . 15

**3 Testing Multiattractor Models on a Constrained Simulation of the Local Universe** **17**
3.1 Introduction . . . 17
3.2 The Multiattractor Model . . . 18
3.3 Goodness of fit estimators . . . 20
3.4 Information Criteria - which model is best? . . . 23
3.5 Mock Distance Catalogs . . . 23
3.6 Results of Fits . . . 24
3.6.1 Dipole Only Model . . . 26
3.6.2 Single Attractor Model . . . 26
3.6.3 Two Attractors . . . 27
3.6.4 Three Attractors - no constraints on location . . . 29
3.6.5 Multiple attractors at density peaks . . . 29
3.6.6 Two Attractors and a Quadrupole . . . 30
3.6.7 Thermal Velocity Dispersion . . . 31
3.7 Predicting Distances from the Multiattrator Model . . . 33
3.7.1 A Guide to Applying Flow Model Distances . . . 35
3.7.2 Illustrative Example Galaxies . . . 41
3.8 Conclusions . . . 46

**4 The SFI++ and a Tully-Fisher Template** **48**
4.1 Introduction . . . 48
4.2 Tully-Fisher Observables . . . 50
4.2.1 Optical Imaging Data . . . 50
4.2.2 Rotation Widths . . . 51
4.3 Deriving a Tully-Fisher Template . . . 53
4.3.1 Sample Selection . . . 53
4.3.2 Bias Corrections . . . 53
4.3.3 Fitting the TF Relation . . . 64
4.3.4 Individual Cluster TF Relations . . . 66
4.3.5 A TF Template Relation . . . 66
4.3.6 Comparison with SCI TF Relation . . . 71
4.4 The Scatter in the TF Relation . . . 78
4.5 Conclusions . . . 79

**5 Internal Extinction in Spirial Galaxies in the Near Infra-red** **82**
5.1 Introduction . . . 82
5.2 Description of the Samples . . . 83
5.3 Description of data . . . 84
5.3.1 I-band photometry . . . 84
5.3.2 Photometric quantities from the 2MASS XSC . . . 84
5.3.3 Corrections . . . 86
5.4 Reddening . . . 88
5.5 Effect of inclination on isophotal radius . . . 91
5.5.1 Formal corrections for inclination . . . 91
5.5.2 Are disks transparent at $r_{21}$? . . . 93
5.5.3 A statistical test for the inclination dependence of isophotal radius . . . 95
5.6 Effect of inclination on magnitude . . . 97
5.6.1 Formal corrections for inclination . . . 97
5.6.2 A statistical test for the inclination dependence of total magnitude . . . 97
5.6.3 The Modified Holmberg Test . . . 98
5.7 Photometric Model . . . 101
5.8 Luminosity dependence . . . 104
5.8.1 Isophotal radius . . . 104
5.8.2 Magnitude . . . 105
5.9 Conclusions . . . 108

**6 A Local Field TF sample from the SFI++** **112**
6.1 Introduction . . . 112
6.2 Sample Selection . . . 112
6.2.1 Grouping . . . 113
6.3 Peculiar Velocities from Tully-Fisher . . . 115

6.4 The Local Peculiar Velocity Field from the SFI++ . . . 115
6.5 Conclusions . . . 116

**7 Primary Distance Sample** **119**
7.1 Introduction . . . 119
7.2 Primary Distance Methods . . . 120
7.2.1 Cepheid Variable Stars . . . 120
7.2.2 Surface Brightness Fluctuations . . . 121
7.2.3 Tip of the Red Giant Branch . . . 122
7.2.4 Extragalactic Geometric Distances . . . 122
7.2.5 Brightest Stars . . . 122
7.2.6 Planetary Nebulae . . . 123
7.2.7 Other methods . . . 123
7.3 Data Presentation . . . 125
7.3.1 Galaxies with multiple distances . . . 125
7.3.2 Galaxies with Tully-Fisher distances . . . 127
7.4 The Peculiar Velocity Field . . . 128
7.5 Conclusions . . . 129

**8 The Velocity Field in the Local Supercluster** **132**
8.1 Introduction . . . 132
8.2 Dipole Only Model . . . 133
8.3 Infall onto a Single Attractor . . . 135
8.4 Infall onto Virgo and a Second Attractor . . . 140
8.5 Two Attractors and a Quadrupole . . . 144
8.6 Just dipole and quadrupole model . . . 145
8.7 Three Attractors . . . 146
8.8 Multiple Attractors from Cluster Catalog . . . 147
8.9 Velocity Dispersion . . . 149
8.10 Summary of Velocity Field Models . . . 151
8.10.1 Model fit to SFI++ data alone . . . 151
8.10.2 Model fit to primary distances alone . . . 151
8.10.3 Model fit to the Full Sample . . . 151
8.11 Discussion . . . 153
8.11.1 Infall onto Virgo . . . 153
8.11.2 The “Great Attractor” . . . 155
8.11.3 The Dipole . . . 157
8.11.4 The Quadrupole . . . 157
8.11.5 Net Motion of the Local Group . . . 158
8.12 Conclusions . . . 159

**9 Conclusions** **161**
9.1 Summary of Conclusions . . . . . 161
9.2 Suggestions for Future Work . . . . . 163
9.2.1 The Tully-Fisher Relation . . . . . 164
9.2.2 The Velocity Field in the Local Universe . . . . . 166

## LIST OF TABLES


1.1 Recent Fits to Multiattactor models . . . . . 7

2.1 Parameters in published HIMFs . . . . . 10

3.1 NFW Profile Fits to Clusters . . . . . 21
3.2 Likelihoods and Information Criteria for Multiattractor model fits. 25
3.3 Parameters of best fit Multiattractor Models to the mock distance catalogs . . . . . 31
3.4 Mock galaxies at $d < 3$ Mpc in the constrained simulation . . . . . 43
3.5 Mock galaxies with $v_{\rm CMB} \sim 900$ km s$^{-1}$ ($d_{\rm Hubble} \sim 12.9$ Mpc) in the constrained simulation . . . . . 45

4.1 RC3 Morphological Types for Spiral Galaxies . . . . . 51
4.2 Incompleteness Function Co-efficients (see Equation 4.10) and cluster size bias . . . . . 65

4.3 Tully-Fisher relation fits for individual cluster samples . . . . . 67
4.4 Fit offsets for individual cluster samples . . . . . 73
4.5 Linear TF parameters for global samples. . . . . 75
4.6 Quadratic TF parameters for global samples. . . . . 78

5.1 Samples for the study of $r_{\rm iso}$ and $m_{\rm ext}$ vs. $\log(a/b)$. . . . . 95
5.2 Measured and estimated values of $\delta$. . . . . 96
5.3 Measured values of $\gamma$. . . . . 98
5.4 Summary of results for $\delta$ in $r_{21}/r_{21}^{\circ} = 1 + \delta \log(a/b)$. . . . . 109
5.5 Summary of results for $\gamma$ in $\Delta M = \gamma \log(a/b)$ . . . . . 110

7.1 Typical errors and useful ranges of various redshift independent distance measures. . . . . 120

8.1 Nearby Concentrations of Mass . . . . . 138
8.2 Likelihoods and information criteria for multiattractor model fits. 141
8.3 Parameters of the best fit multiattractor model. . . . . 155
8.4 Measurements of the dipole. . . . . 158

## LIST OF FIGURES


2.1 Difference between input and reconstructed HIMFs for a mock HIPASS BGC survey . . . 13
2.2 Difference between input and reconstructed HIMFs from simulated ALFA drift scans of Virgo. . . . 14
2.3 Difference between input and reconstructed HIMFs from simulated ALFA drift scans of the Anti-Virgo region . . . 14

3.1 Distribution of observed distances for the SBF sample of TB00 and our mock distance catalog . . . 25
3.2 Hubble diagram for the mock distance catalog . . . 26
3.3 Error contours for the location and size of the best fit attractor in a single attractor model . . . 28
3.4 Error contours for the location and size of the "Virgo attractor" in a two attractor model . . . 28
3.5 Error contours for the location and size of the "great attractor" in a two attractor model . . . 29
3.6 Contours of constant CMB velocity for the best fit model. . . . 32
3.7 Estimated vs. actual distance for mock galaxies . . . 33
3.8 Histogram of errors on estimated distance . . . 34
3.9 Relative error on predicted distance as a function of distance . . . 36
3.10 As in Figure 3.9, except showing absolute error, and dividing the sky into quadrants. . . . 37
3.11 Mean distance bias and scatter in twelve regions of the sky as a function of distance. . . . 38
3.12 Mean distance bias and scatter in twelve regions of the sky as a function of redshift. . . . 39

4.1 TF relation for the **in+** sample divided by source of rotational velocity. . . . 54
4.2 TF relation for the **in+** sample divided by morphological type . . . 56
4.3 Bias corrections for the Antlia cluster . . . 57
4.4 Completeness histograms for each of the **in+** cluster sample. . . . 58
4.5 Incompleteness correction for each cluster. . . . 60
4.6 Dependence of the incompleteness correction on assumptions. . . . 61
4.7 Impact of luminosity function assumption on incompleteness corrections . . . 62
4.8 Cluster size – sample incompleteness for the Antlia cluster. . . . 64
4.9 TF relations for individual cluster samples. . . . 70
4.10 Line of sight peculiar velocities for clusters . . . 72
4.11 Global TF relation. . . . 77
4.12 Comparison of absolute magnitude distributions for the SFI++ template sample and the SCI . . . 79

4.13 Total observed scatter in the TF relation of the **in+** sample . . . . 80

5.1 Seeing correction for axial ratios . . . . . 86
5.2 NIR color trends with inclination for galaxies with I-band data . . 89
5.3 I-band NIR color trends with inclination . . . . . 90
5.4 NIR color trends with inclination for full sample of 15224 galaxies . 92
5.5 Radius at which galaxies become optically thick with an exponential dust disk . . . . . 94
5.6 Averaged values of the isophotal radius, $r_{21}$ in $K_s$-band in bins of $\log(a/b)$ . . . . . 96
5.7 Holmberg test in $K_s$-band . . . . . 100
5.8 Modified Holmberg test in J and H-bands . . . . . 101
5.9 Extinction in the "triple exponential" model for dust in disk galaxies 102
5.10 Comparison of model extinction with Holmberg test . . . . . 103
5.11 Distribution of total magnitude in $K_s$-band of galaxies in the AGC$z$ sample. . . . . 104
5.12 Change of $2.302 r_d/r_{21}$ with luminosity for galaxies in SFI2 sample . 106
5.13 Values of $\gamma$ as a function of luminosity . . . . . 107

6.1 Tully-Fisher relation of field galaxies within 86 Mpc/$h_{70}$ . . . . . 113
6.2 SFI++ peculiar velocities and errors as a function of CMB velocity. 114
6.3 SFI++ peculiar velocity field in the Supergalactic plane . . . . . 117
6.4 SFI++ peculiar velocity field perpendicular to the Supergalactic plane . . . . . 118

7.1 Spatial distribution of galaxies with published primary distances . 124
7.2 Cepheid and TRGB distances compared with other methods . . . . 126
7.3 Brightest star distances compared with other methods . . . . . 126
7.4 Galaxies with TF and primary distances . . . . . 127
7.5 TF relation for galaxies with Cepheid distances . . . . . 128
7.6 Peculiar velocity field from primary distances in the supergalactic plane. . . . . 130
7.7 Peculiar velocity field from primary distances perpendicular to the supergalactic plane . . . . . 131

8.1 Peculiar velocity field from the combined SFI++ and primary distance sample . . . . . 134
8.2 Direction of dipole in dipole only model . . . . . 136
8.3 Residual peculiar velocity field after removal of best fit dipole. . . . 137
8.4 Error contours for location and mass of the Virgo attractor in a two attractor model. . . . . 142
8.5 Error contours for location and mass of the second attractor in a two attractor model. . . . . 143
8.6 Error contours for the dipole in a two attractor model . . . . . 144
8.7 Covariance between the quadrupole components $Q_{xx}$ and $Q_{zz}$ . . . 146

8.8 Covariance between the mass of a Shapley supercluster attractor and the magnitude of the dipole . . . . . 147
8.9 Distribution of HIFLUGCS clusters used as attractors . . . . . 148
8.10 Contours of constant CMB velocity for the model using HIFLUGCS clusters as attractors . . . . . 150
8.11 Residual peculiar velocities from best fit multiattractor model . . . 152
8.12 Contours of constant CMB velocity for the best fit multiattractor model . . . . . 154

9.1 Tully-Fisher relation and sky distribution of galaxies in the Ursa Major cluster. . . . . 165

# Chapter 1

# Introduction

## 1.1 Peculiar velocities

The deviations of the motions of galaxies from smooth Hubble flow are know as "peculiar velocities". These deviations arise as a direct result of gravity acting on the initial quantum density fluctuations at the end of inflation. The fluctuations and resulting inhomogeneous gravitational potential field cause the motion of mass towards overdensities, which grow as they collect this matter and eventually form the large scale structures we see so clearly in the distribution of galaxies today. This gradual build up of overdensities under the influence of gravity is know as "gravitational instability" and forms the basis of all peculiar velocity studies.

The peculiar velocities of galaxies are measured observationally by taking the difference between the observed recessional velocity and the expected smooth expansion velocity at the distance, $d$, of the galaxy ($v_{\rm pec} = v_{\rm obs} - H_0 d$, where $H_0$ is Hubble's constant). Such measurements can only be made for galaxies in the nearby universe. With the methods available today, distance errors typically range from 10-20%, and the peculiar velocities of galaxies typically have amplitudes of a few hundred km s$^{-1}$. Beyond redshifts of a few thousand km s$^{-1}$ (or $z \sim 0.02$) the error on a measured peculiar velocity will therefore be equal to or larger than the peculiar velocity itself. A promising techinique to extend measurements of peculiar velocities to much larger distances is the kinetic SZ effect. The SZ effect (Sunyaev & Zeldovich 1972) refers to the distortion of cosmic microwave background (CMB) photons as they pass through the hot gas in a cluster of galaxies. The signature of motion of a cluster is present in the shape of the distortion, and the error on the inferred peculiar velocity is independent of redshift, although at present too large for anything but limits to be measured (Benson *et al.* 2003).

### 1.1.1 Gravitational Instability Theory

In an expanding universe filled with gravitating matter there is an eternal battle between the expansion, which pulls everything apart and gravity pulling masses back together. Small density perturbations in the early universe, creating tiny regions where gravity begins to win out over the expansion, are able to grow and eventually collapse to form the structures we see in the universe today. All models for infall in the expanding universe are therefore based on gravitational instability theory, or the theory of density perturbations. If it is assumed that the density perturbations in the early universe have a mean overdensity relative to the background, $\bar{\rho}$, of $\delta = \Delta\rho/\bar{\rho} << 1$ and that the velocities produced are much less than the speed of light, $\mathbf{v} << c$ (*i.e.* we are in the linear regime) then mass

conservation in an expanding universe, with scale factor $a(t)$, gives the equation

$$\frac{\partial \delta}{\partial t} + \frac{\nabla.\mathbf{v}}{a(t)} = 0, \tag{1.1}$$

where $\delta(\mathbf{x},t) = (\rho(\mathbf{x},t) - \bar{\rho}(t))/\bar{\rho}(t)$, the overdensity relative to the background, and $\mathbf{v}$ is the velocity with respect to the expanding or co-moving frame (the peculiar velocity). This equation has the standard solution

$$\mathbf{v}(\mathbf{x},t) = -\frac{a}{4\pi}\int \frac{(\mathbf{x}-\mathbf{x}')}{|\mathbf{x}-\mathbf{x}'|^3}\frac{\partial \delta(\mathbf{x}',t)}{\partial t} d^3x'. \tag{1.2}$$

It is common to assume that $\delta(\mathbf{x},t)$ is separable into growing and shrinking modes and that the shrinking mode can be neglected at late times. If we further separate the growing mode into a spatially and temporally varying parts as $\delta(\mathbf{x},t) = \delta_+(\mathbf{x})D_+(t)$, then

$$\mathbf{v}(\mathbf{x}, t = t_{\rm now}) = -\frac{H_0}{4\pi}\left(\frac{dD_+}{da}\right)_0 \int \frac{(\mathbf{x}-\mathbf{x}')}{|\mathbf{x}-\mathbf{x}'|^3}\delta_+(\mathbf{x}')d^3x', \tag{1.3}$$

(recall Hubble's parameter, $H(t) = a/\dot{a}$, and $a(0) \equiv 1$).

From Poisson's equation we also have

$$\frac{\nabla.\mathbf{g}}{a} = -4\pi G\bar{\rho}\delta(\mathbf{x},t) \tag{1.4}$$

which has a similar solution:

$$\mathbf{g}(\mathbf{x}) = -G\bar{\rho}aD_+ \int \frac{(\mathbf{x}-\mathbf{x}')}{|\mathbf{x}-\mathbf{x}'|^3}\delta_+(\mathbf{x})d^3x', \tag{1.5}$$

again using only growing part of $\delta(\mathbf{x},t)$. Combining this with Equation 1.3 gives the result

$$\mathbf{v}(\mathbf{x}) = \frac{2}{3H_0\Omega_0} f\mathbf{g}(\mathbf{x}) \tag{1.6}$$

where we use $\bar{\rho} = 3H_0^2\Omega_0/8\pi G$, ($\Omega_0$ being the present day matter density relative to the critical density) and follow convention by defining $f = \frac{a}{D_+}\frac{dD_+}{da}$. A useful empirical relation from numerical simulations is $f \sim \Omega_0^{0.6}$. The function, $f$, which describes the rate of growth of structure in the universe, is relatively insensitive to the presence of a cosmological constant (Lahav *et al.* 1991). This derivation was first presented by Peebles (1976).

Gravitational instability theory therefore says that the peculiar velocity field, at least in the linear regime, is directly proportional to the underlying gravitational potential field, the proportionality constant only having to do with cosmological parameters (Eqn. 1.6). Peculiar velocities therefore provide an extremely powerful tool for probing the underlying mass distribution in our universe, independent of where the light is. In the "post-WMAP" era of cosmology (Bennett *et al.* 2003), in which the general consensus is that the basic cosmological parameters are well known, peculiar velocity studies can provide independent checks of these parameters, or take them as a given to study the mass distributions.

## 1.2 Peculiar Velocities in and around the Local Supercluster

The presence of an overdensity of galaxies in the local universe (within $cz \sim 3000$ km s$^{-1}$) was first noted by de Vaucouleurs (1958) who described it as a local supercluster of galaxies or a local "supergalaxy", and defined the supergalactic plane (SGP) in which most of the galaxies were found as well as the supergalactic longitude and latitude; $L$ and $B$ (for a recent review of the supergalactic plane see Lahav *et al.* 2000). The potential for this overdensity to perturb the local expansion rate was also noted by de Vaucouleurs (1958), at the time without the benefit of any observational evidence for such an effect. Rubin *et al.* (1976) reported the first attempt to look for observational evidence of the motion of the Local Group, but the study of peculiar velocities did not make any significant progress until the early 1980s, when the discovery of new methods for estimating redshift independent distances to external galaxies such as the Tully-Fisher relation for spiral galaxies (Tully & Fisher 1977; also see Chapter 4), and later the $D_n - \sigma$ relation for elliptical galaxies (Dressler *et al.* 1987) made it possible to measure peculiar velocities for much larger numbers of galaxies.

The first models for the velocity field in the local universe considered infall onto the nearest large cluster, and what de Vaucouleurs (1958) considered the center of the Local Supercluster – the Virgo cluster. The simplest models for infall onto a region of space make the assumption that the overdensity is spherically symmetric. This assumption goes back to the original Peebles (1976) discussion, which looked at infall onto the Virgo cluster under the assumption that it was a spherical overdensity with $\rho(r) \propto r^{-\gamma}$ ($r$ being the distance from the center of the cluster). Numerical simulations of the growth of structure in a $\Lambda$CDM universe have shown that motion along filaments towards the elliptical dark matter halos of clusters form the dominant pattern of infall in the universe. Even observations support the idea that clusters (which contain most of the mass) are far from spherical for the most part: for example there are hints that the Virgo cluster is elongated along our line of sight and that the Local Group's motion toward it is along a filament stretching from our location, through Virgo and onto towards Coma/A1367 in the background. In light of this, the spherical approximation seems like an unjustified simplification, and certainly breaks down close to Virgo. A common argument for the use of the assumption is that it is really the potential distribution (and not the mass distribution) that it of interest for peculiar velocity studies. Potentials are significantly rounded with respect to their generating mass. Furthermore, the potential which a galaxy feels as it falls into a cluster will vary over time (as cluster galaxies move), and the time average will smooth out to be more spherical than the instantaneous potential.

Assuming spherical symmetry also has several strong advantages over more complicated distributions of mass. The linear infall model (along with the partially non-linear approximation of Yahil 1985 which we describe later) assumes

a spherical distribution for the over-density. Under the assumption of spherical symmetry then, the gravitational potential $\mathbf{g} \sim GM/r^2$ (in the direction towards the attractor), and $M \sim 4\pi r^3 \bar{\rho}\delta$, so that Eqn. 1.6 becomes

$$u_{\rm infall} = \frac{1}{3} H_0 r \Omega_0^{0.6} \delta. \tag{1.7}$$

It is also possible to extend this model into the partially non-linear regimes. Yahil's "$\rho^{1/4}$" approximation (Yahil 1985), has been shown to hold reasonably until $\delta \sim 30$ for spherical distributions of mass (Giavalisco *et al.* 1993), and is

$$u_{\rm infall} \simeq \frac{1}{3} H_0 r \Omega_0^{0.6} \delta (1+\delta)^{-1/4}. \tag{1.8}$$

Under this model, all that is needed is the mean overdensity interior to the galaxy's position $\mathbf{r}$, giving an infall velocity $u_{\rm infall}$, onto an attractor at $\mathbf{r}_A$. The peculiar velocity of the galaxy is then given by

$$\mathbf{v}_{\rm pec}(\mathbf{r}) = u_{\rm infall} \frac{(\mathbf{r}_A - \mathbf{r})}{|\mathbf{r}_A - \mathbf{r}|}, \tag{1.9}$$

pointing directly towards the attractor. The first estimate of the Local Group's infall velocity onto Virgo, suggested an amplitude of $\sim 250$ km s$^{-1}$ (Peebles 1976). Estimates since then have ranged between a favored value of $\sim 220$ km s$^{-1}$ (see *e.g.* Federspiel, Tammann & Sandage 1998), similar to what is derived from a estimate using the $M \sim 10^{15}\ M_\odot$ virial mass of Virgo, to higher values of $\sim 400$ km s$^{-1}$ (see *e.g.* Lu, Salpeter & Hoffman 1994), the significant variation presumably coming from fitting a complicated velocity field with infall onto only a single attractor.

### 1.2.1 Multiattractor Models

The best known peculiar velocity in the universe is the motion of the Sun with respect to the CMB which was measured first to a high accuracy by the COBE satellite to be $369 \pm 2.5$ km s$^{-1}$ towards $(l, b) = (264.31^\circ, 48.05^\circ) \pm 0.15^\circ$ (Lineweaver *et al.* 1996) and recently confirmed by WMAP at $368 \pm 1.9$ km s$^{-1}$ towards $(l, b) = (263.85^\circ, 48.25^\circ) \pm 0.1^\circ$ (Bennett *et al.* 2003). Removing the Sun's motion with respect to the center of our Galaxy, and the Galaxy's motion with respect to the center of mass of the Local Group (LG), which give a net solar motion with respect to the LG of $306 \pm 18$ km s$^{-1}$ towards $l = 99 \pm 5^\circ$, $b = -4 \pm 4^\circ$; (Courteau & van den Bergh 1999), we find that the LG motion in the CMB frame is $621 \pm 24$ km s$^{-1}$ in the direction $(l, b) = (272 \pm 3^\circ,\ 28 \pm 1^\circ)$, or $(\alpha, \delta) = (10.8 \pm 0.2\text{h},\ -27 \pm 1^\circ)$. Early in the study of the local peculiar velocity field, it was noted that Virgo could not account for most of this motion, which is in a direction $\sim 40^\circ$ from the line of sight to Virgo at $(\alpha, \delta) \sim (12\text{h}, 12^\circ)$ and much too large (*e.g.* . Tammann & Sandage 1985). This mismatch can be explained if the

whole of the Local Supercluster (including the Virgo cluster) is moving towards a direction $(\alpha, \delta) \sim$ (10.0h, -48.0°) at a speed of $\sim$ 500 km s$^{-1}$ (here we assume an infall velocity towards Virgo of $\sim$ 220 km s$^{-1}$). This direction points towards the large mass overdensities of the Hydra-Centaurus supercluster, at a distance of about 45 Mpc, and the (then unknown) Shapley supercluster behind it at $D \sim 200$ Mpc, suggesting immediately that either (or both) of these concentrations of mass may also be responsible for a significant fraction of the motion of the Local Group.

Lynden-Bell *et al.* (1988) studied the velocity field of the local universe using a sample of 400 elliptical galaxies with distances from the $D_n - \sigma$ relation (errors $\sim 20\%$) and concluded that the field was in fact best fit by a "great" attractor of mass $M \sim 5 \times 10^{16}\ M_\odot$ or about 50 times more massive than Virgo, at a distance of about 60 Mpc and centred at $(\alpha, \delta) \sim$ (13.3h, -53.7°), only 9° from the plane of our Galaxy and therefore predominantly hidden from our view (although it should be noted here that the angular position they derive is simply the direction they find for bulk flow for all the galaxies in their sample with $cz < 8000$ km s$^{-1}$ and has errors $\sim \pm 10°$). They concluded that it could not be the Hydra-Centaurus supercluster which was responsible for the motions, because it in fact partakes in the flow and argued that this "great attractor" (GA) must be behind the Hydra-Centaurus supercluster and should in fact be considered the new center of the Local Supercluster having a larger impact on the velocity of the Local Group than Virgo itself in their model.

Han & Mould (1990) were the first to consider a model including infall onto both Virgo and a second attractor in the Hydra-Centaurus direction. Such multi-attractor models illustrate another nice feature of the simple spherical infall models in the linear regime – that the influence of multiple attractors can simply be added as vectors. In Han & Mould (1990) the model was fit to a sample of $\sim$ 300 galaxies with Tully-Fisher distances (the sample of Aaronson *et al.* 1982), and since the sample did not extend out to the distance of the GA of Lynden-Bell *et al.* (1988), they use the location derived in that study for their second attractor, and found a good fit for the two attractors, both of which had less impact than if considered alone.

The suggestion of a concentration of mass perhaps hidden from our view by the Milky Way led to a string of attempts to locate it. Scaramella *et al.* (1989) noted a large concentration of clusters in the general direction of the GA and roughly behind the Hydra-Centaurus superclusters (the Shapley Supercluster) suggesting that this might in fact be responsible for the motion of the local volume in that direction. Backside infall onto the GA (thus constraining its maximum distance) was reported by Dressler & Faber (1990), but Mathewson, Ford & Buchorn (1992b) disagreed with this finding, seeing no such evidence in their independent data set. The issue has not yet been settled. In their "Streaming Motions of Abell Clusters" sample (SMAC), Hudson *et al.* (2004) claim the bulk motions seen are inconsistent with the GA as suggested by Lynden-Bell *et al.* (1988), and report marginal evidence for infall onto Shapley, while Tonry *et al.* (2000) independently fit for the location of a "great attractor" in their sample of $\sim$ 300 galaxies with distances

from the method of surface brightness fluctuations (SBF; as described in Chapter 7), and find an attractor in a similar direction to the original GA, but at $D \sim 48$ Mpc/$h_{70}$. Mieske *et al.* (2005) in a study of the Hydra-Centaurus region suggest that this attractor, if shifted to lie behind the Hydra cluster could account for the motions they see. Observations are ongoing to search for large structures hidden by the Zone of Avoidance, and in 2004 an entire conference was devoted to the subject (see Fairall & Lahav 2004 for a summary). The solution seems likely to lie in a combination of both answers. It is well understood that infall models vastly oversimplify the complicated matter distribution in the real universe, and that the motions of galaxies may well be dominated by infall along filaments. The best fit attractor found in any sample gives only an idea of the center of mass of the distribution traced by the sample, somehow weighted by the relative distances, and perhaps leading to seemingly conflicting results. Drinkwater *et al.* (2004) find evidence for a filamentary link between the Hydra-Centaurus and Shapley superclusters, so the conflict may well result from departures from spherical infall due to the complicated mass distribution in this area, and the likely solution will include infall of some magnitude onto both Hydra-Centaurus and Shapley.

### 1.2.2 Non-parametric modeling

Non-parametric modeling of the local velocity field has great potential to reveal the underlying matter distribution, and remove conflicts about the most significant single attractors by allowing for much more complicated mass distributions. Such methods suffer however from the effects sparse and noisy peculiar velocity data, so require significant smoothing and filtering of the data to be successful. The POTENT method (Dekel, Bertschinger & Faber 1990) relies on the result that the velocity field is proportional to the gravitational potential field as discussed above (Eqn 1.6), and therefore the full three dimensional velocity and density fields can in theory be reconstructed from the radial peculiar velocities alone. This method has been used extensively to reconstruct local density fields, but smoothing on scales of several megaparsecs must first be applied, so only the very largest peaks in the density field are recovered.

### 1.2.3 Recent studies of the local velocity field

The most recent attempts at fitting multiattractor models to the velocity field in the local universe have used samples of elliptical galaxies with distances from the SBF method (see Chapter 7). Tonry *et al.* (2000) fit such a model to a sample of roughly 300 galaxies with SBF distances. They include two spherical attractors which they associate with Virgo and the "great attractor" (GA), a non-attracting cluster at the position of Fornax and a quadrupole centered on the origin. In Willick & Batra (2001) the same model is fit to the same galaxies, however they remove the Hubble constant from the fit (by using distances in km s$^{-1}$) and use the VELMOD formalism to fit the calibration of the SBF distances at the same time as

Table 1.1: Recent Fits to Multiattactor models

| Parameter | TB00 Fit | WB01 Fit |
|---|---|---|
| **Virgo** | | |
| Position (Mpc/$h_{70}$) | (-3.5, 18.6, -1.8) | (-3.6, 18.6, -2.0) |
| Enclosed overdensity | 0.974 | 1.076 |
| Cutoff radius (Mpc/$h_{70}$) | 13.1 | 13.8 |
| **GA** | | |
| Position (Mpc/$h_{70}$) | (-41.1, 16.4, -19.2) | (-42.1, 16.7, -19.6) |
| Enclosed overdensity | 0.781 | 0.448 |
| Cutoff radius (Mpc/$h_{70}$) | 55.4 | 57.3 |
| **Fornax** | | |
| Position (Mpc/$h_{70}$) | (-2.1, -16.8, -15.0) | (-2.1, -16.9, -15.0) |
| **Dipole** (km s$^{-1}$) | (-55, 143, -8) | (-70, 230, -40) |
| **Quadrupole** | 16.4: (-0.8, 0.0, -0.6) | 15.2: (-0.9, 0.0, -0.5) |
| ($h_{70}$ km s$^{-1}$ Mpc$^{-1}$) | 13.2: ( 0.6, 0.2, -0.8) | 12.7: ( 0.5, 0.2, -0.8) |
| | 3.2: (-0.1, 1.0, 0.2) | 2.5: (-0.1, 1.0, 0.2) |

the velocity field. In both analyses, some of the parameters are held fixed at values discussed in Tonry *et al.* (2000). These include the thermal velocity dispersion (187 km s$^{-1}$), virial velocities of Virgo (650 km s$^{-1}$) the GA (500 km s$^{-1}$) and Fornax (235 km s$^{-1}$), and parameters describing the shape of the attractor density profiles. Tonry *et al.* (2000) find $H_0 = 78.4$ km s$^{-1}$Mpc$^{-1}$. In Table 1.1 we report the values of the fits found, correcting for a sign error in Table 6 of Willick & Batra (2001). $h_{70} = H_0/70$ km s$^{-1}$Mpc$^{-1}$. Components are listed in supergalactic co-ordinates. These values can be compared with the fits to a mock data set of $N \sim 500$ in Chapter 3, and our final sample of $\sim 1700$ velocity field tracers (from both Tully-Fisher and primary distances) in Chapter 8.

## 1.3 Overview of Thesis

In this thesis we take a new look at the motions of galaxies in around the Local supercluster using a much larger sample of velocity field tracers than has been available before. This sample is a combination of galaxies, groups and clusters with peculiar velocities measured from both the luminosity-line width (or Tully-Fisher) relation in spiral galaxies and primary distance indicators.

In Chapters 2 and 3 we provide motivations for the need for a better understanding of the local peculiar velocity field. Chapter 2 studies the impact that neglecting peculiar velocities can have on the derivation of physical properties of local galaxies, namely in the estimation of unbiased local mass and luminosity functions. This Chapter is published in Masters, Haynes & Giovanelli (2004). In Chapter 3 we fit a multiattractor model to a mock sample of galaxies taken from a constrained simulation of the local universe. There we provide a practical guide

for the best method to estimate distances to galaxies from their redshifts. In this Chapter we also discuss the methods used to fit multiattractor models and how we choose the preferred model.

In Chapter 4 we introduce the SFI++ sample of galaxies, which includes 5653 galaxies with measurements suitable for use in the Tully-Fisher relation. A subset of 911 of these galaxies, which lie in the vicinities of 36 nearby clusters are used to derive a template Tully-Fisher relation. In this Chapter we introduce the Tully-Fisher relation and the observables needed to derive distances (or peculiar velocities) of spiral galaxies from it. In Chapter 5 we explore one of the largest sources of error in the Tully-Fisher relation: the correction of the observed magnitudes of galaxies for internal extinction. Chapter 5 is published in Masters, Giovanelli & Haynes (2003).

In Chapters 6 and 7 we describe respectively a local "field" spiral sample extracted from the SFI++, and a sample of galaxies with primary distance measurements taken from the literature. These samples are combined in Chapter 8 where we use them to fit simple multiattractor models for the velocity field in and around the Local Supercluster.

We provide an overview of the main results from each Chapter and suggestions for future work in the Conclusion.

# Chapter 2

# The Impact of Distance Uncertainties on Local Luminostity and Mass Functions *

## 2.1 Introduction

One of the perplexing discrepancies between observations and CDM theory revolves around the "missing satellite" problem. Numerical simulations in $\lambda$CDM predict a value for the logarithmic slope of the faint end of the halo mass function, $\alpha$, which is close to the value of $-1.8$ that arises analytically from the Press-Schechter formalism (Press & Schechter 1974), but most recent determinations of the optical luminosity function (LF) in the local volume yield values of $\alpha$ that are significantly flatter. Complementary to the results on the optical LF, several determinations of the local HI mass function (HIMF) have likewise yielded relatively flat faint-end slopes. The over-prediction of the number of low mass objects relative to those actually observed is considered one of the last remaining stumbling blocks for $\lambda$CDM, and points towards a new understanding of the baryon physics of galaxy formation. It is obviously desirable that all of the uncertainties in the observed luminosity and mass functions be well understood.

To derive a luminosity (or mass) function from observational data, the sample selection effects must be considered carefully. In most surveys, the lowest luminosity (or mass) objects are only visible nearby, and their contribution must be weighted accordingly. Fractional distance errors can be large for relatively nearby objects, and can thus have a very strong impact on determinations of the faint end characteristics of luminosity (or mass) functions. When those functions are evaluated using data obtained in clusters, the principal source of uncertainty lies in the assessment of membership; assuming that uncertainty is to first order independent on luminosity (or mass), it can have a small impact on the estimate of LF slopes. Determinations of the HIMF, however, have to rely on relatively shallow, wide area surveys to detect low HI mass objects over a sufficient volume, and are thus most susceptible to uncertainties associated with distance errors in the nearby population.

Primary distances (eg. cepheids, the tip of the red giant branch or surface brightness fluctuations, the best of which give distances to $\pm$ 10%) are available for $\sim$ 600 galaxies, most within $\sim$ 30 Mpc. Secondary distances (which rely on the above methods for calibration) carry larger errors ($\sim$ 15–30%) but do account for peculiar velocities for some 5000 objects. For all other galaxies, the only indication of distance is their redshift. Outside of $cz = 6000$ km s$^{-1}$, pure Hubble flow works

*This Chapter is published in Masters, Haynes & Giovanelli (2004)

Table 2.1: Parameters in published HIMFs

| Reference | Z97 | RS02 | Z03 |
|---|---|---|---|
| Survey | AHISS | ADBS | HIPASS |
| $\phi_\star[h_{70}^3\mathrm{Mpc}^{-3}]$ | 0.0048 | 0.0047 | 0.0070 |
| $\log(M_\star/M_\odot) + 2\log h_{70}$ | 9.86 | 9.94 | 9.85 |
| $\alpha$ | -1.20 | -1.53 | -1.30 |
| Survey area | 65 deg$^2$ | 430 deg$^2$ | 20,600 deg$^2$ |
| $D_{\rm lim}$ for $10^8 M_\odot$ | 100 Mpc | 13 Mpc | 7 Mpc |
| # galaxies | 61 | 265 | 1000 |

well, since a typical peculiar velocity of a few hundred km s$^{-1}$ creates an uncertainty on the redshift distance of $< 10\%$. For closer galaxies, however, the relative error is much larger, and, for the nearest objects, whose recessional velocities are dominated by peculiar motions, the error can be a factor of two or more. Furthermore, peculiar velocities are not random but exhibit coherent flows towards local over-densities. In some directions, the redshift-distances of all (nearby) galaxies will be systematically under- or over- estimated if peculiar velocities are ignored.

The effects of peculiar velocities on distance determinations can be mitigated by the use of parametric models of the local velocity field. While clearly oversimplifications of the real flows, such models give a direction-dependent redshift-distance prescription. A recent example of such a model is the multi-attractor model of Tonry *et al.* (2000; hereafter TB00: also see Willick & Batra 2001).

In order to investigate the effects of distance uncertainties on local luminosity or mass functions, we consider here the derivation of the HIMF. Recent determinations of the local HIMF have yielded discrepant results on the abundance of low HI mass objects, namely: Zwaan *et al.* (1997; Z97), Rosenberg & Schneider (2002; RS02) and Zwaan *et al.* (2003; Z03). The Z03 HIMF is based on the HI Parkes All Sky Survey (HIPASS) Bright Galaxy Catalogue (BGC), while the Z97 and RS02 HIMFs are both based on drift scan surveys conducted at Arecibo during the period of its recent upgrade (respectively called AHISS, the Arecibo HI Strip Survey, and ADBS, the Arecibo Dual Beam Survey). A summary of the results of those surveys is provided in Table 1, parameterized as Schechter functions,

$$\phi(x) = \frac{dn}{d\log M} = \ln 10\ \phi_\star\ x^{(\alpha+1)}\ e^{-x}, \tag{2.1}$$

where $x = M/M_\star$, $M$ is the HI mass, and $n$ is the total number density of galaxies. The faint end slopes of the HIMF derived by the three surveys vary between $-1.20$ and $-1.53$, yielding extrapolations below $M_{HI} = 10^7\ M_\odot$ that disagree by an order of magnitude, the RS02 HIMF having the steeper slope.

Previous studies of the impact of distance errors (from ignoring peculiar velocities) on HIMFs have modeled the effect, often called the 'Eddington effect', by adding random Gaussian noise to the distances. Using this model, RS02 conclude

that the effect is negligible in their survey volume until velocity dispersions of 600 km s$^{-1}$ are reached, while Z03 find that for an assumed velocity dispersion of 50-100 km s$^{-1}$ in the local universe ($cz < 3000$ km s$^{-1}$) the slope of the low mass end of the HIMF probably steepens by $\Delta\alpha < 0.05$. Since the peculiar velocity field in the local universe is not random but rather dominated by in-fall onto the Virgo cluster, these models could easily hide the main bias. In this paper, we investigate whether all or part of the discrepancy among the three HIMF determinations can be accounted for by the effects of distance uncertainties introduced by the different methods used by Z97, RS02 and Z03 to assign distances.

Here, we construct mock catalogs designed to mimic the HI surveys conducted by Z97, RS02 and Z03 and then derive mock HIMFs under different distance assumptions. $H_\circ = 70$ km s$^{-1}$Mpc$^{-1}$ is assumed throughout, and the dependence on $H_\circ$ is explicitly listed using $h_{70} = H_\circ/(70$ km s$^{-1}$Mpc$^{-1})$.

## 2.2 Survey Simulations

We first construct a mock catalog of HI rich objects in the local universe, which is then "observed". In order to account for the known local variations in the 3D distribution of galaxies, a version of the density and velocity fields derived from the IRAS Point Source Catalog Redshift Survey (PSC$z$) with a value $\beta = \Omega_{mass}^{0.6}/b = 0.5$ is used (kindly provided by E. Branchini, see Branchini *et al.* 1999 for details). This map extends to a distance of 120 $h^{-1}$ Mpc with a grid spacing is 0.9375 $h^{-1}$ Mpc in the inner 60 $h^{-1}$ Mpc, and twice that in the outer shell. The map has been smoothed with a Gaussian filter of radius 3.2 $h^{-1}$ Mpc.

The volume is seeded with HI rich galaxies according to the density field, and masses are assigned from a given HIMF. The HI sizes of the galaxies and velocity widths are calculated according to empirical scaling relations derived from our own HI survey data and from Broeils (1992). Inclinations are randomized, realistic scatter is added to the scaling relations (as measured from the empirical fit) and a turbulent velocity of 10 km s$^{-1}$ is added to construct the observed velocity width.

The HI mass of a galaxy at a distance $D$ (in Mpc), and with observed HI line flux can be approximated as $M_{HI}/M_\odot \simeq 2.356 \times 10^5 D^2 S_{\rm peak} W_{\rm HI}$, where $S_{\rm peak}$ is the peak flux in the HI line in Jy and $W_{\rm HI}$ is its width in km s$^{-1}$. The detectability of a HI rich galaxy depends on both the peak flux and the width of the HI line. If we assume that smoothing of the spectrum is applied to match the width of the lines, up to a maximum of $W_{\rm smo} = 100$ km s$^{-1}$, the signal-to-noise ratio can be derived from the standard radiometer equation such that

$$S/N = \frac{6.06 \left(\frac{M_{HI}}{10^6 M_\odot}\right) \left(\frac{W_{\rm HI}}{100}\right)^\gamma f_\beta t_{\rm int}^{1/2} \sqrt{(\rm CBW/25kHz)}}{(D^2 T_{\rm sys}/G)}, \qquad (2.2)$$

where $\gamma = -3/4$ for $W_{\rm HI} \leq 100$ km s$^{-1}$, and $\gamma = -1$ for $W_{\rm HI} > 100$ km s$^{-1}$, accounting for the effects of smoothing; $f_\beta$ is the fraction of the source covered by the telescope beam; $t_{\rm int}$ is the integration time; CBW is the channel bandwidth

and $T_{\rm sys}/G$ describes the gain of the telescope. Specific details of the simulated observations are given in Section 3 below.

The observed HI mass of a galaxy is $M_{\rm obs} = M_{\rm true}(D_{\rm obs}/D_{\rm true})^2$, where $D_{\rm obs}$ is the distance assigned to the galaxy and $D_{\rm true}$ is its true distance. From the set of "detections" we construct HIMFs by summing $1/V_{\rm lim}$ (the total volume within which a galaxy can be seen) weighted by the average density in that volume (from the PSC$z$ density field) in bins of $\log(M_{HI}/M_{\odot})$. This method prevents over- or under- dense regions from giving an over- or under-estimate of number counts in certain bins. If $D_{\rm obs} = D_{\rm true}$, we recover the input HIMF. We investigate below the effect that $D_{\rm obs} \neq D_{\rm true}$ has on the recovered HIMF for various survey geometries and depths.

## 2.3 Results and Discussion

### 2.3.1 Simulated HIPASS BGC

First, we consider a mock catalog constructed to mimic the HIPASS BGC which contains the 1000 galaxies in the southern sky with the largest peak HI flux (see Z03). To remove the effects of cosmic variance an average obtained from 10 simulations is used.

Most of the galaxies in the real BGC have their distances estimated using Hubble's Law, and yet are within $cz = 3000$ km s$^{-1}$. We investigate what effect this assumption has (if any) on the derived HIMF. As noted in Table 1, the HIMF derived from the HIPASS BGC has a shallower low mass end slope than that derived from the ADBS in RS02. We will see if any part of this discrepancy can be accounted for by the use of Hubble's Law to assign distances by Z03.

Figure 2.1 shows the difference between the input and reconstructed HIMFs for the input (or "true") distances, distances derived by assuming Hubble flow, and distances from the multi-attractor model of TB00. Clearly, significant variations arise among the HIMFs constructed from the mock HIPASS BGC when different distance estimators are used. The HIPASS survey volume does not contain the Virgo Cluster and therefore has a fairly quiet local velocity field; however, as can be seen from the figure, the low mass slope of the HIMF will be **underestimated** if pure Hubble flow is assumed. In Figure 2.1, the input HIMF is the same as Z03 (see Table 1), except that the low mass slope has been steepened to $\alpha = -1.4$. The HIMF recovered from this mock HIPASS BGC is close to that reported by Z03 when Hubble flow is assumed.

We suggest that an adjustment of $\Delta\alpha \simeq -0.1$ should be applied to the Z03 low mass slope, making it $\alpha = -1.4 \pm 0.1$. This correction makes the result **consistent** with the RS02 result of $\alpha = -1.53 \pm 0.2$ (where here the error on the RS02 result is estimated by scaling that reported for Z03 by $\sqrt{N_{\rm gal}}$). This change in low mass slope, while interesting in the light of comparisons with $\lambda$CDM, has little effect in the total HI mass density implied by the surveys. The total mass density, dominated by $M_\star$ galaxies, is already in agreement between the two surveys.

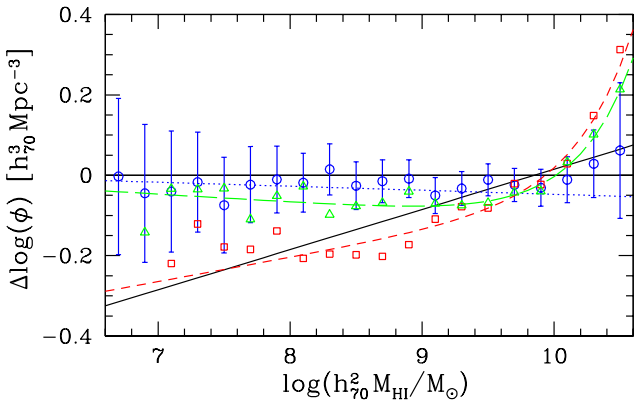



Figure 2.1: Difference between input and reconstructed HIMFs for a mock HIPASS BGC survey (shown are the average of 10 simulations). The HIMF derived when "true" distances are used (circular points and dotted line), along with the HIMF constructed when multi-attractor model distances are used (triangular points and long-dashed line) reconstructs the input HIMF within the errors (here typical Poisson counting errors are shown only on the "true" distance points). When pure Hubble flow is assumed (square points and short dashed line), the low mass end of the HIMF is underestimated. The solid line shows the Z03 HIMF, which differs from the input by $\Delta\alpha = 0.1$.

### 2.3.2 Simulated Virgo cluster survey

As the nearest rich cluster to us, Virgo represents the highest density region in the local Universe, and thus constitutes the obvious choice for the study of the HIMF in a high density environment. The northern hemisphere sky accessible to the Arecibo telescope covers both the Virgo cluster and comparably-far regions of lowest cosmic density located roughly in the anti–Virgo direction. The arrival in 2004 of the Arecibo L-Band Feed Array (ALFA) will revolutionize mapping capability at the Arecibo telescope and will allow study of possible variations in the HIMF in different density environments, already suggested by RS02 but with low statistical significance. Here, we investigate the potential of a proposed ALFA survey of an area $30^\circ \times 30^\circ$ centered on the Virgo cluster (RA=$11 - 13^h$, DEC=$0 - 27^\circ$), assuming $T_{\rm sys}/G = 3$ Jy, and with $t_{\rm int} = 12$s (drift scan) and CBW=25 kHz. The mean noise in such a survey would be $\sim 4$ mJy/beam (at our assumed maximum resolution of 5 km s$^{-1}$). This can be compared to 20 mJy/beam for HIPASS and $\sim 8.6$ mJy/beam for the ADBS, see Barnes *et al.* (2001) and RS02; here both values have been scaled to a resolution of 5 km s$^{-1}$. We also consider an equal area in the anti-Virgo region. (RA=$23 - 1^h$, DEC=$-27 - 0^\circ$). This region of the sky is not accessible to Arecibo, but for the purposes of illustrating the effects of distance uncertainties on the construction of HIMFs, the combination of such a Virgo-anti-Virgo survey provides a good comparison between the nearest regions of high and low cosmic density.

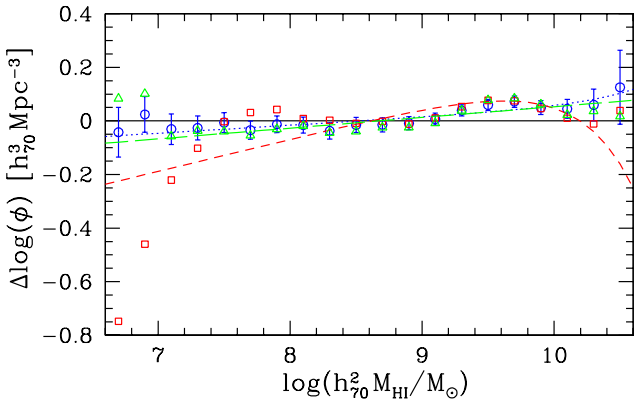



Figure 2.2: Difference between input and reconstructed HIMFs from simulated ALFA drift scans of Virgo (shown is the average of 10 simulations; roughly 4000 galaxies are seen in each survey). As in Figure 2.1, the input HIMF (that of Z03, but with $\alpha$ steepened to -1.4) has been subtracted, but note that here the y-scale has been extended down to accommodate the huge deviation when Hubble flow distances are used. Line and point types are the same as in Figure 2.1. When the "true" distances are used the fit to the low mass slope of the HIMF is $\alpha = -1.37$; the multi-attractor model distances give $\alpha = -1.36$, while the Hubble flow distances give $\alpha = -1.28$.

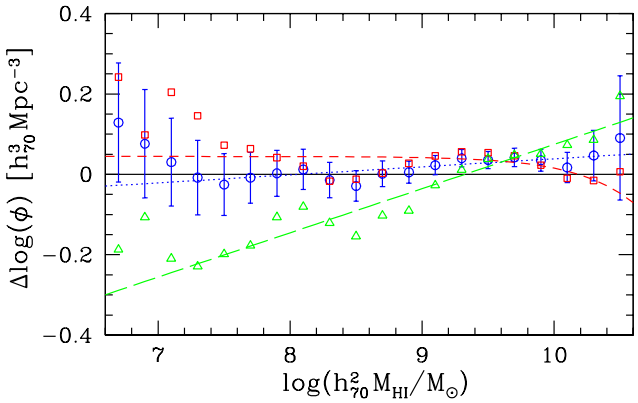



Figure 2.3: Difference between input and reconstructed HIMFs from simulated ALFA drift scans of the Anti-Virgo region (shown is the average of 10 simulations; roughly 3000 galaxies are seen in each survey). Line and point types are the same as in Figures 2.1 & 2.2. Note that this region will not be accessible to ALFA, but is included here to illustrate the difference between comparable surveys of the nearest regions of high and low cosmic density.

In the Virgo region, we are able to reconstruct the input HIMF well when the "true" distances are used, and reasonably well with distances taken from the multi-attractor model of TB00. However, if pure Hubble flow is assumed, the number of galaxies at the low mass end of the HIMF is seriously underestimated (see Figure 2.2). The lowest mass galaxies in our mock survey are seen only in the foreground of Virgo (the mass limit at 17 Mpc, the approximate distance of the Virgo cluster, is $\sim 10^8$ $M_\odot$ from Eqn 2 assuming $W_{HI}$=100 km $s^{-1}$ and CBW=25 kHz). If pure Hubble flow is assumed the vast majority of these foreground galaxies will have their distances (and hence masses for a given HI flux) overestimated, since they are in-falling towards Virgo.

The two recent Arecibo–based derivations of the HIMF (Z97 and RS02) include part of the Virgo cluster within the overall survey area. The low mass end slopes derived from these surveys differ by $\Delta\alpha = 0.3$ (with Z97 having the shallower slope). In RS02, the multi-attractor model of TB00 is used to assign distances, while in Z97 pure Hubble flow is assumed. However, the difference between the two HIMFs cannot be explained by their use of different distance estimators. The Z97 survey was designed to be extremely sensitive but covers a very small area. In deeper surveys, we expect the effect described above diminishes. We have constructed a Z97-like survey (of similar depth and area), and, as expected, the HIMF can be reconstructed equally well in such a deep survey with all three distance estimates. We therefore must resort to the usual arguments of small-number statistics (noting that there were only 65 galaxies in the Z97 HIMF) and differing treatments of completeness to explain the discrepancy between the HIMFS of Z97 and RS02.

In the Anti-Virgo region, the input HIMF can be reconstructed well using either "true" distances or by assuming Hubble flow. Here the use of the multi-attractor model of TB00 causes the largest bias; acting to create an underestimate of the number of low mass HI galaxies (see Figure 2.3). The multi-attractor model of TB00 is based on distances to $\sim$ 300 elliptical galaxies. There are approximately 30 of these galaxies in the Virgo region discussed here, but fewer than 5 in the anti-Virgo region. At the depth of these HI surveys, the anti-Virgo region is relatively under-dense, making it unavoidable that there will be few tracer galaxies in that direction. This undersampling has the effect of forcing the model for the velocity field to fit better towards Virgo at the expense of the fit in the anti-Virgo direction. The multi-attractor model of TB00 consistently over-estimates the distance for a given velocity in the anti-Virgo direction leading to the observed underestimate of the number of low mass galaxies (as discussed above).

## 2.4 Conclusions

We have used mock HI survey data to demonstrate that distance uncertainties can create serious biases in the low mass end of the HIMF; similar arguments could be applied to studies of the field galaxy optical LF. When the effects of the local

peculiar velocity field are ignored, incorrect estimates of the HIMF will be derived. The exact nature and size of the bias will depend both on the survey geometry and its depth.

In a survey constructed to simulate the HIPASS BGC, the low mass HIMF slope is **underestimated** if peculiar velocities are neglected. We suggest that the HIMF reported by Z03 suffers from this problem, which when corrected, would bring the Z03 and RS02 HIMFs into agreement within their errors. The adjusted value of the Z03 low mass slope is $\alpha = -1.4 \pm 0.1$, which is to be compared with the RS02 value of $\alpha = -1.5 \pm 0.2$. This change does not affect the implied HI mass density since it is dominated by $M_\star$ galaxies.

For a survey where low mass galaxies are seen only in the foreground of Virgo, the distances (and therefore masses) of the nearby low mass galaxies will be overestimated and the low mass end of the HIMF **seriously underestimated** if in-fall onto Virgo is neglected. In deeper surveys, the effect becomes negligible, so that differences in the adopted distances alone cannot explain the discrepancy between the Z97 and RS02 HIMFs.

A simulated survey in the anti-Virgo region points to the limitations of currently available models for the local velocity field. In such a survey, use of distances taken from a multi-attractor model for the local velocity field leads to an underestimate of the low mass HIMF slope. Currently available flow models are not well constrained in the anti-Virgo direction because of a lack of galaxies with primary distances in the region. Velocity field models based on larger numbers of tracer galaxies will be required to solve this problem.

The use of a good model for the local peculiar velocity field is found to be essential to provide distances for nearby galaxies for which no redshift-independent distances are available. Without such a model, it is difficult to derive an unbiased HIMF, and in particular, the low mass end may be in error. Disentangling the effects of environment and evolution of the HIMF will not be possible unless the local flow model is well understood. Other applications where distances to galaxies are needed will also benefit from a better understanding of local flows.

# Chapter 3

# Testing Multiattractor Models on a Constrained Simulation of the Local Universe

## 3.1 Introduction

Our views of the universe are unavoidably influenced by our location in it. In today's era of "precision cosmology" and highly accurate observations of galaxies, the removal of this effect (or foreground subtraction) is becoming more and more important. We observe from telescopes based on (in orbit around, or sometimes trailing) a planet which orbits the Sun once a year. Dust in the plane of our solar system, tiny particles knocked off comets and asteroids, shows up in observations as the Zodiacal light. Our location inside the Milky Way galaxy has a huge impact on extragalactic astronomy and cosmology. We see its imprint on even the most recent all sky maps of the cosmic microwave background (CMB), and we cannot see optically the galaxies which lie behind its obscuring dust. Even outside of the Galaxy, we are not yet into the textbook homogeneous universe. The large scale structure of galaxies has inhomogeneities up to a scale of a few hundred million parsecs (Mpc). The Galaxy is a member of a small group, known as the Local Group, which sits on the edge of a modest supercluster, the Local Supercluster (or sometimes Virgo supercluster). While the effect of the Galaxy is usually considered on cosmological observations, often our location in the Local Supercluster is ignored.

The Local Supercluster shows up in all sky surveys of galaxies as an overabundance of galaxies along the supergalactic plane (see Lahav *et al.* 2000 for a recent review). This anisotropy has a definite impact on observations of the extragalactic sky. For example, it was recently shown that it would dominate the power spectrum of SZ observations of the sky (Dolag *et al.* 2005). The local supercluster also has an impact due to the distortions it causes in the expansion of the local universe. Nearby galaxies have observed recessional velocities which can differ from Hubble's Law by more than a factor of two. There are $\sim 8000$ galaxies with measured redshifts $cz < 3000$ km s$^{-1}$, but only $\sim 600$ galaxies (or less than 10%) have published primary distances. To study the physical properties of the nearest (and therefore most accessible) galaxies, we must have accurate distances, which currently requires an understanding of the local velocity field.

Numerical simulations in the $\Lambda$CDM paradigm and redshift surveys have given

us a consistent picture of the filamentary large scale structure of the universe in which the dominant motions of galaxies are that of infall onto clusters along filaments. In light of this picture the traditional infall models used to study the velocity field of the Local Supercluster going back to Peebles (1976), and most recently used by Tonry *et al.* (2000) and Willick & Batra (2001) are at best over simplifications and at worst simply wrong. The assumption of spherical symmetry for attractors is clearly an over simplification, even for a single cluster like Virgo which is made up of many sub-groups, let alone for a filamentary or pancake like supercluster.

However, multiattractor models have many nice features which leads to their continuing use. They are simple to apply, and the non-linear approximation of Yahil (1985), which is only valid for spherical masses, has been shown to work reasonably well to overdensites of $\delta \sim 30$ (Giavalisco *et al.* 1993). For a galaxy which has only a position on the sky and a redshift, a multiattractor model will provide a unique distance over much (but not all) of its volume. A multiattractor model can in principle have any number of spherical attractors which could be combined to give more complicated mass distributions, and other components, such as quadrupole moments in the velocity field (perhaps from the tidal influence of distant masses) are also easy to add. A multiattractor model can also give you an idea of the dominant sources of attraction in the local volume.

In this Chapter we test the validity of a simple multiattractor model, and its usefulness for estimating distances to nearby galaxies. We fit the model to a mock sample of galaxies with primary distances generated from the Virgo Consortium's publicly available constrained simulations of the local universe (Mathis *et al.* 2002), and then test how well it does at predicting distances for the rest of the particles in the simulation. The model is described in Section 3.2, we discuss goodness of fit estimators in Section 3.3 and the mock catalog in Section 3.4. The results of fitting are shown in Section 3.5. In Sections 3.6 and 3.7 we discuss the validity of distances estimated for all particles in the constrained simulation from the velocity field model, and provide illustrative example galaxies from the real universe. We assume $H_0 = 70$ km s$^{-1}$Mpc$^{-1}$ throughout.

A similar model to the one described in this Chapter is fit to the peculiar velocity data described in Chapters 4, 6 & 7 in Chapter 8 of this thesis.

## 3.2 The Multiattractor Model

The model discussed here has a similar functional form to the one described in Tonry *et al.* (2000; hereafter TB00). The mean velocity at a given point in the model has several components. The first is a contribution from Hubble flow and a dipole velocity $\mathbf{w}$ which give a velocity at a position $\mathbf{r}$ of $H_0\mathbf{r} + \mathbf{w}$. In contrast to TB00, but following Willick & Batra (2001) we do not fit for the Hubble constant, but instead assume $H_0 = 70$ km s$^{-1}$Mpc$^{-1}$ throughout. The dipole component means that the velocities we fit are not forced into any one frame which might

artificially inflate the impact of certain attractors. We also allow for a quadrupole component $\mathbf{Q}$ which might account either for the influence of outside masses or non-spherical infalls. The quadrupole results in a velocity

$$u_{\mathbf{Q}} = e^{-r^2/2r^2_{\rm quad}}\mathbf{Q}.(\mathbf{r}-\mathbf{r_Q}), \tag{3.1}$$

where $\mathbf{r_Q}$ is the position of the center of the quadrupole, and an exponential cut-off is applied. The quadrupole is forced to have zero trace by insisting that $Q_{yy} = -Q_{xx} - Q_{zz}$, which means that the net Hubble expansion is always carried by $H_0$ and the quadrupole merely describes any deviation from spherically symmetric expansion. Following TB00 we set $r_{\rm quad} = 50$ Mpc, so that the Hubble flow becomes isotropic at large distances. The only component of the model which does not vanish at large distances is the dipole.

The model allows for any number of spherical attractors which have some enclosed overdensity $\delta(r) = (\rho - \bar{\rho})/\bar{\rho})$, where $\bar{\rho}$ is the mean density of the universe. In TB00 the attractors are modeled as having a density profile

$$\rho(r) = \frac{\rho_0}{(1 + r^3/r_c^3)^{\gamma/3}}. \tag{3.2}$$

This profile is a slight modification of the $\rho(r) \sim r^{-\gamma}$ profiles which were commonly used in early infall models. The mean overdensity enclosed at a radius $r$ from a given attractor for this profile is

$$\delta(r) = \frac{\delta_0 e^{-r/r_{cut}}}{1-\gamma/3}\left(\frac{r}{r_{cut}}\right)^{-3}\left[\left(1+\frac{r^3}{r_c^3}\right)-1\right], \tag{3.3}$$

when an exponential cut-off $e^{-r_A/r_{cut}}$ is applied to prevent the total mass from diverging. Note that $\delta_0 = \delta(0)$.

We choose to do something slightly different here and use the NFW profile (Navarro *et al.* 1997),

$$\rho(r)/\rho_{\rm crit} = \frac{\delta_c}{cx(1+cx)^2}, \tag{3.4}$$

where $x = r/r_{200}$ (recall $\rho_{\rm crit} = 3H_0^2/8\pi G$). The profile can be completely parameterized by $c$, the concentration parameter which is a function of the characteristic density, $\delta_c$,

$$\delta_c = \frac{200}{3}\frac{c^3}{\ln(1+c) - c/(1+c)} \tag{3.5}$$

and the virial radius, $r_{200}$ (note that $hr_{200} = 1.63 \times 10^{-2}(Mh/M_\odot)^{1/3}$ kpc) . The concentration parameter $c$ is weakly dependent on the halo mass, and $c \sim 6$ is a reasonable estimate for cluster sized halos, as shown in Figure 6 of Navarro *et al.* (1997). The NFW profile has been shown to fit well to cluster mass profiles (see *e.g.* Buote & Lewis 2004 or Collister & Lahav 2005; a compilation of fits to clusters is show in Table 3.1). We do not fit for the concentration parameter in our multiattractor model, but use $c = 5$ for all attractors. This value is chosen as a

compromise between the predicted value of $c \sim 6$ from simulations and a weighted mean of the fits shown in Table 3.1 (neglecting the major outlier Hydra A) which gives $c = 4.4$ with a variance in the nine values of $\sigma_c = 1.8$.

There has been some debate recently over the application of this profile to the cores of halos. Since we are interested in the linear to mildly non-linear regime here, we are well away from the cores of attractors (where we expect the velocity model to break down in any case), so that is of no concern. The mean overdensity enclosed at a radius $r$ for the NFW profile is

$$\delta(r) = \frac{\delta_c}{\Omega_\circ (cx)^3} \left[ \ln(1+cx) - \frac{cx}{1+cx} \right] \tag{3.6}$$

($x = r/r_{200}$). At large radii this has a similar profile to Equation 3.3, which has an artificial exponential cut-off applied.

In gravitational instability theory, spherical overdensities cause a deviation from the smooth velocity field of the form

$$u_{\rm infall} = \frac{1}{3} H_0 r \Omega_M^{0.6} \delta (1+\delta)^{-1/4}, \tag{3.7}$$

where $u_{\rm infall}$ is the infall velocity of a galaxy (ie. toward the center of the overdensity) at a distance $r$. The factor of $(1+\delta)^{1/4}$ is Yahil's $\rho^{1/4}$ non-linear approximation (Yahil 1985) which works to $\delta \sim 30$ for spherical attractors (Giavalisco *et al.* 1993). The dependence on $\Omega_M^{0.6}$ is an empirical fit to numerical simulations for the rate of growth of structure.

The final component of the model is the velocity dispersion at a given point. This is given by the quadrature sum of a thermal velocity dispersion (which is the same at all points) and viral velocity dispersions centered on clusters which fall off spatially as a Gaussian with a sigma $r_c$. We use the values suggested by TB00 for these velocity dispersions, namely a thermal velocity dispersion of 187 km s$^{-1}$; a velocity dispersion of 650 km s$^{-1}$ for Virgo and 500 km s$^{-1}$ for the other attractors.

## 3.3 Goodness of fit estimators

Here we discuss various goodness of fit estimators which we later use to fit the multiattractor model to a catalog of velocity field tracers (galaxies with redshift independent distances and redshifts). We consider three such estimators of increasing sophistication. In all cases a downhill simplex method (AMOEBA in *Numerical Recipes*, Press *et al.* 2001) is used to find the minima. Care is taken that the minima is not local, and multiple starting locations are considered. The first goodness of fit estimator considered is the simple $\chi^2$ minimization,

$$\chi^2 = \frac{(v_{\rm obs} - v_{\rm model}(d))^2}{2\sigma_v(d)^2}, \tag{3.8}$$

Table 3.1: NFW Profile Fits to Clusters

| Cluster | $r_{200}$ (Mpc/$h_7$0) | c | Radius range ($/r_{200}$) | Reference |
|---|---|---|---|---|
| Abell 2589 | 1.03 ± 0.51 | 4.9 ± 2.4 | 0.02-0.07 | Buote & Lewis (2004) |
| Abell 478 | 2.08 ± 0.11 | 4.2 ± 0.4 | 0.01-0.5 | Pointecouteau *et al.* (2004) |
| Abell 2029 | 2.39 ± 0.62 | 4.4 ± 0.9 | 0.001-0.1 | Lewis, Buote & Stocke (2003) |
| PKS0745-191 | 2.45 ± 0.47 | 3.8 ± 0.4 | 0.1-0.5 | Allen *et al.* (2001) |
| Abell 2390 | 2.43 ± 3.31 | 3.2±1.7 | 0.1-0.5 | Allen *et al.* (2001) |
| Abell 1835 | 2.32 ± 0.66 | 4.2±0.6 | 0.1-0.5 | Allen *et al.* (2001) |
| MS2137-2353 | 1.39 ± 0.31 | 8.7±1.1 | 0.1-0.5 | Allen *et al.* (2001) |
| RXJ1347-1145 | 2.35 ± 1.96 | 6.3±1.5 | 0.1-0.5 | Allen *et al.* (2001) |
| 3C295 | 1.26 ± 1.00 | 7.9±1.7 | 0.1-0.5 | Allen *et al.* (2001) |
| Hydra A | 0.95 ± 0.12 | 12.3 ± 0.18 | 0.01-0.2 | David *et al.* (2001) |
| Weighted mean and variance (neglecting Hydra A) | | 4.4 ± 1.8 | | |

where $\sigma_v(r)^2 = (H_0\sigma_d)^2 + \sigma_{\rm model}(d)^2$. The minimum of this only finds the best fit model in the case of Gaussian errors in the difference between the measured and predicted velocities. Given that the error in the predicted velocity depends on the error in the measured distance in a complicated way this assumption is not valid here, but we are interested to know how much this affects the best fit model found. The other two estimators consist of maximizing the likelihood of the model as measured by various conditional probabilities. In both cases we minimize,

$$\mathcal{L} = -2\sum \ln P, \tag{3.9}$$

deviations of this value about the minima can be used to evaluate confidence intervals (ie. $\Delta\mathcal{L} = n^2$ gives $n\sigma$ errors, where $n$ is an integer). In the first example

$$P_\mu = \int P(v_{\rm obs}|r)P(d|r)dr, \tag{3.10}$$

where, since we assume Gaussian errors in the distance modulus,

$$P(d|r) = \frac{1}{\sqrt{2\pi}\sigma_\mu}\exp\left[-\frac{[\ln(d/r)]^2}{2\sigma_\mu^2}\right], \tag{3.11}$$

and the fit of the velocity field model is described by

$$P(v_{\rm obs}|r) = \frac{1}{\sqrt{2\pi}\sigma_v(r)}\exp\left[-\frac{(v_{\rm obs} - v_{\rm model}(r))^2}{2\sigma_v(r)^2}\right]. \tag{3.12}$$

In the second example we also take into account the probability of finding a galaxy at a given distance, which means that we are taking into account the effects of Malmquist bias in the sample. This gives

$$P_{\rm VELMOD}(d|v_{\rm obs}) = \frac{\int P(r)P(d|r)P(v_{\rm obs}|r)dr}{\int P(r)P(v_{\rm obs}|r)dr}, \tag{3.13}$$

where

$$P(r) \propto n(r)r^2 \tag{3.14}$$

where $n(r)$ is the density field.

These are both improvements over simple $\chi^2$ minimization. The first takes into account the effect of non Gaussian errors in measured vs. predicted velocity by assuming Gaussian errors in the distance modulus, $\mu$, and integrating the probability of the model fitting the data over the range of possible distances to the galaxy. This method is basically the same as that used in TB00, except that they take only 11 points of the integration between $\mu - 2d\mu$ and $\mu + 2d\mu$. We integrate from $\pm 10d\mu$ in 100 steps. Finally, the last goodness of fit estimator we consider, shown in Eqn. 9, also assumes the presence of Gaussian errors in the distance modulus, and in addition takes into account the effects of Malmquist bias in the distance catalog. Malmquist bias causes the measured distance of a galaxy to be

systematically different from the real value, either because the volume considered increases along the line of sight so the galaxy is more likely to be further away than closer (homogeneous Malmquist bias), or because of actual variations in the density of galaxies due to large scale structure in the universe (inhomogeneous Malmquist bias). This last goodness of fit estimator is the basis of the VELMOD method described in Willick *et al.* (1997) and used to fit a multiattractor model in Willick & Batra (2001). We note that no Malmquist like bias is added to the mock catalog considered in this paper, so we will not use this method until we consider real data in Chapter 8.

## 3.4 Information Criteria - which model is best?

As discussed in Liddle (2004) the selection of the preferred model given a range of parameter choices is a problem which arises in many areas of science and which is deeply rooted in the theory of statistical inference. Fortunately however, this theory results in relatively simple equations for the "Information Criteria" which is minimized for the preferred model. Here we will consider the Akaike information criteria,

$$\mathrm{AIC} = -2 \ln P_{\max} + 2k, \tag{3.15}$$

and the Bayesian information criteria.

$$\mathrm{BIC} = -2 \ln P_{\max} + k \ln N, \tag{3.16}$$

where $-2 \ln P_{\max}$ is the quantity we minimize to find the best fit, $k$ is the number of parameters, and $N$ is the number of data points. The model with the lowest AIC and BIC is the best description of the data. Any addition of new parameters should of course improve the goodness of fit measure, but will be penalized by the second term in the information criteria. If the parameters do not improve the fit sufficiently to warrant inclusion the information criteria will be larger than for the simpler model. Since $N > e^2$ in all data sets considered here, the BIC is always harder on the introduction of new parameters. There is ongoing debate over which information criteria should be preferred (see Liddle 2004 for a discussion of this). The AIC at least provides a limit on the most parameters which should be considered. An improvement of 6 or more in the BIC should be considered strong evidence that the model is preferred.

## 3.5 Mock Distance Catalogs

The mock catalogs described here are based on the constrained simulation of Mathis *et al.* (2002). These simulations are started from initial conditions constructed from the IRAS 1.2 Jy Survey (see Kolatt *et al.* 1996 for more details) and are designed to mimic the large scale features in the local density field. The simulations consist of a volume which is a box of side 160 Mpc/$h$. Galaxy formation is

grafted onto the N-body simulation after merger trees are constructed and using a phenomenological model based on that of Kauffmann *et al.* (1999). The galaxy catalogs thus produced are publicly available from the Virgo Consortium website (`http://www.mpa-garching.mpg.de/Virgo/`).

We generate a mock sample of distance indicators from the galaxy catalog by taking only those galaxies which are brightest in the simulated apparent I-band magnitude. We choose a cut-off at an I-band magnitude of 12 mag, and keep a random fraction of those to give a catalog with $\sim$ 500 galaxies. This sample is also limited in volume to $v_{LG} < 4000$ km s$^{-1}$. We create observed distances for the galaxies by adding Gaussian scatter in the distance modulus of width 0.2 mag to the real space distances. This provides a sample of distances with errors $\sim$10%, similar in magnitude to that found in SBF or TRGB samples . We generate two samples, one which is uniform over the whole sky and one which has no galaxies within $\pm 10^\circ$ of the Galactic plane. These two samples will give an indication of the effect that the zone of avoidance has on velocity field models fit to real samples with an absence of tracers in the plane of our Galaxy. We note here that at present we have no added any Malmquist like bias to the distance errors, and as such will only consider the $\chi^2$ and $P_\mu$ goodness of fit estimators (Eqns. 3.8 and 3.10).

Figure 3.1 shows the distance distribution of the mock sample which has no galaxies in the Zone of Avoidance (ZoA) compared to the sample of $\sim$ 300 galaxies with SBF distances discussed in TB00. As you can see this mock sample mimics the SBF sample at small distances, but at large distances has extra galaxies. The mocks in this paper are designed to roughly mimic a combination of the the SFI++ Tully-Fisher sample discussed in Chapters 4 & 6 and a sample of galaxies with primary distances collected from the literature (which is dominated by the SBF sample discussed in TB00; see Chapter 7), although it should be noted that they were constructed before the SFI++ sample was finalized. A multiattractor model fit to the real data will be presented in Chapter 8.

## 3.6 Results of Fits

In the previous sections we have introduced a multiattractor model which theoretically could have any number of spherical attractors distorting the local velocity field from that of pure Hubble expansion. This model also allows for a net motion of the entire volume in question (a bulk flow) and the addition of a quadrupolar component in the distortion of the velocity field.

In what follows we will discuss the fitting on this model primarily to the mock distance sample which lacks tracers in the zone of avoidance. The more uniform sample was also fit using the same procedure and we will use that to illustrate the impact of the zone of avoidance on local velocity field models.

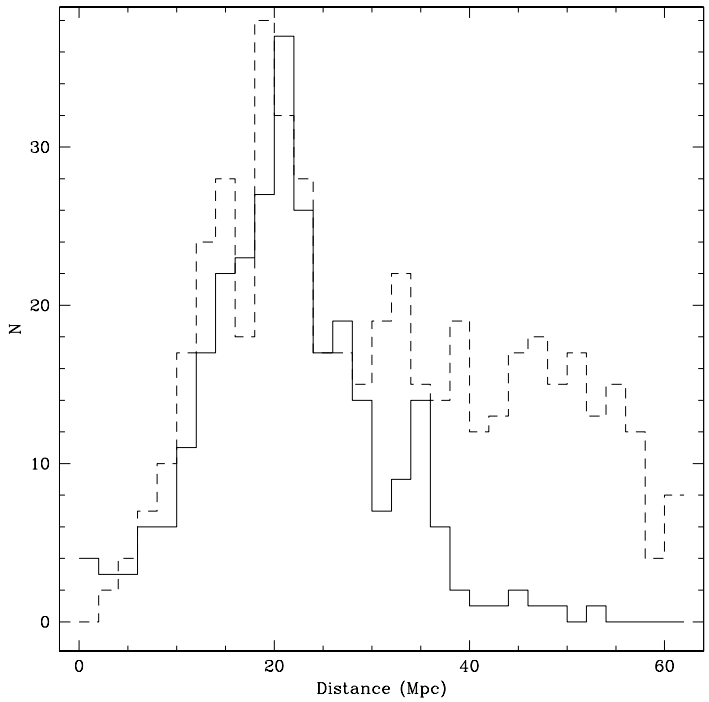



Figure 3.1: Distribution of observed distances for the SBF sample of TB00 (solid line) and the mock distance catalog described above (dotted line).

Table 3.2: Likelihoods and Information Criteria for Multiattractor model fits.

| Model | Likelihood | Degrees of Freedom | $N_{\rm parm}$ | AIC | BIC |
|---|---|---|---|---|---|
| Mock sample without ZoA tracers | | | | | |
| Dipole only | 10.88 | 487 | 3 | 16.88 | 29.46 |
| Virgo attractor | -117.82 | 483 | 7 | -103.82 | -74.46 |
| Virgo + GA | -189.70 | 479 | 11 | -167.70 | -121.56 |
| Two fixed attractors + quadrupole | **-222.00** | 480 | 10 | **-202.00** | **-160.06** |
| Three attractors | -209.40 | 475 | 15 | -179.40 | -116.48 |
| Mock sample with ZoA tracers | | | | | |
| Dipole only | -34.3 | 489 | 3 | -28.3 | -15.70 |
| Virgo attractor | -123.7 | 485 | 7 | -109.70 | -80.31 |
| Virgo + GA | -195.2 | 481 | 11 | -173.20 | -127.02 |
| Two fixed attractors + quadrupole | **-218.4** | 482 | 10 | **-198.40** | **-156.42** |

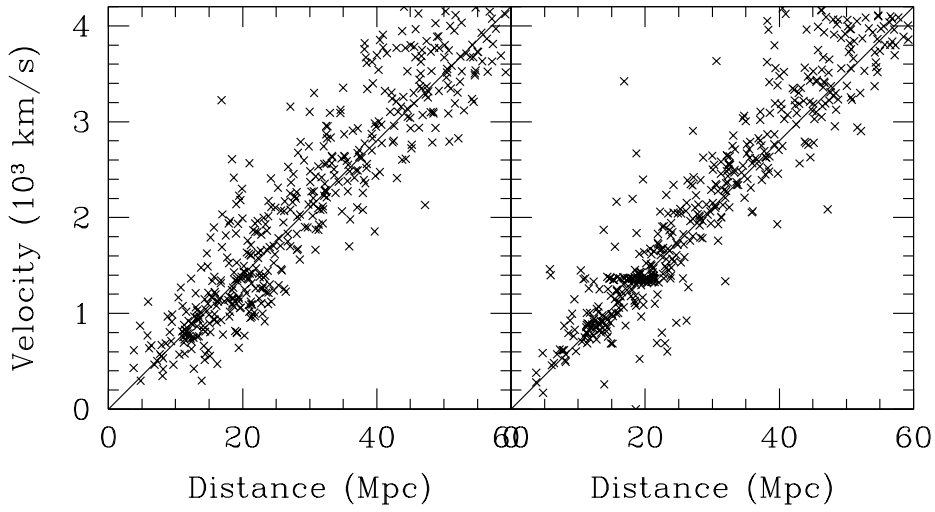



Figure 3.2: Hubble diagram for the mock catalog of velocity field tracers (this is the same with no tracers in the zone of avoidance). On the left is shown the dipole only model (in which a constant dipole of $(-47\pm33, 259\pm24, -153\pm37)$ km s$^{-1}$ has been subtracted). On the right is shown the full Virgo, GA and quadrupole model. The line shows a Hubble constant of 70 km s$^{-1}$ Mpc$^{-1}$ as used in the constrained simulation.

### 3.6.1 Dipole Only Model

Here we fit for a net vector velocity of the entire sample volume only. We set $H_0 = 70$ km s$^{-1}$Mpc$^{-1}$, the value used in the constrained simulations, thus making the assumption that we are considering a large enough volume of the universe that using the mean value of Hubble's Constant is valid (*i.e.* the volume on average is not overdense or underdense with respect to the average density of the universe). The left-hand panel of Figure 3.2, shows a Hubble diagram for the mock distance catalog with this dipole removed. This model fits with a likelihood (as defined in Section 3) of $-2\Sigma P_\mu = 10.8$. There are no serious covariances between the parameters which are found to be $(-47 \pm 33, 259 \pm 24, -153 \pm 37)$ km s$^{-1}$, where $1\sigma$ errors are quoted. When there are tracers present in the ZoA the likelihood improves to -34.3, and the dipole changes to (-99, 210, -165) km s$^{-1}$, less than $\sim 2\sigma$ away from the value found with no ZoA tracers.

### 3.6.2 Single Attractor Model

The next model we consider is a simple single attractor infall model. In both mock samples (with and without the ZoA) the addition of a single attractor increases the goodness of fit of the model. A summary of the likelihoods of various models is provided in Table 3.2. The removal of tracers from the zone of avoidance again

causes the model to have a slightly worse fit as measured by all three estimators, but changes the best fit parameters relatively little.

When the $\chi^2$ minimization is used, a "great attractor" (GA) at (SGX, SGY, SGZ) $\sim (-60, 10, -8)$ Mpc (13h30, -54°, $D \sim 60$ Mpc) with $M_{200} \sim 10^{16}\ M_\odot$ fits which a slightly lower $\chi^2$ than an attractor close to Virgo. This GA is very similar to the one found in Lynden-Bell *et al.* (1988) in which something similar to $\chi^2$ minimization is used to fit an infall model to a sample of $\sim 300$ elliptical galaxies (after their $D_n - \sigma$ distances are corrected for Malmquist bias). Using simple $\chi^2$ minimization with this mock sample we might come to the same conclusions as in Lynden-Bell *et al.* (1988), but we again comment that $\chi^2$ minimization is not appropriate here as we cannot consider the main error to be Gaussian in the measured/predicted velocity.

The appropriate goodness of fit estimator prefers a Virgo like attractor at $(\alpha, \delta)$ $\sim$ 12h, +05°. A density peak in the constrained simulation places the mock Virgo cluster at (-7.1, 17.9, -3.6) Mpc, somewhat difference from its location in the real universe. The best fit single attractors are within $\sim$ 2 Mpc of this location, at (-5.2, 18.4, -4.4) Mpc and (-5.5, 17.1, -4.8) Mpc for the mock sample without ZoA tracers and with respectively, with the biggest deviation being in the direction towards the attractor, which may be being influenced by the signature of infall towards the GA region. (The formal $1\sigma$ errors are $\sim 0.1$ Mpc on all co-ordinates.)

We expect there to be covariances between the best fit distance and mass of an attractor, since the impact it has on the velocity field will depend on a combination of the two. This small effect is illustrated in Figure 3.3 which also shows the 1, 2 and $3\sigma$ error contours for the position on the sky of the attractor found using the mock sample without ZoA tracers.

### 3.6.3 Two Attractors

The addition of a second attractor improves the goodness of fit in all cases. Both the $\chi^2$ minimization and using $P_\mu$, find the best fit with an attractor close to the position of Virgo in the mock universe and a GA at $D \sim 60$ Mpc, $\alpha =$ 13h30, $\delta = -45°$ (roughly where the Hydra-Centaurus supercluster is located). Contour plots of the 1, 2 and $3\sigma$ error ellipses for the location and size of the two attractors (found using the mock sample without ZoA tracers) are shown in Figures 3.4 and 3.5. For the second attractor the covariance between the distance and the size of the attractor is stronger, suggesting that its radial position is not well constrained. It's location on the sky is also less well constrained that the Virgo attractor, and there are covariances between the co-ordinates. There is a small covariance between the size of the second attractor and the dipole $x$ component.

The positions of the best fit attractors are (-4.9, 18.6, -3.5) Mpc and (-57.1, 17.0, -3.0) Mpc for the mock with no ZoA tracers. Density peaks are found in the constrained simulation at (-7.1, 17.9, -3.6) Mpc and (-50.0, 17.9, -3.6) Mpc, which in the real universe might correspond to the Virgo cluster, and the center of mass of the Hydra-Centaurus supercluster.

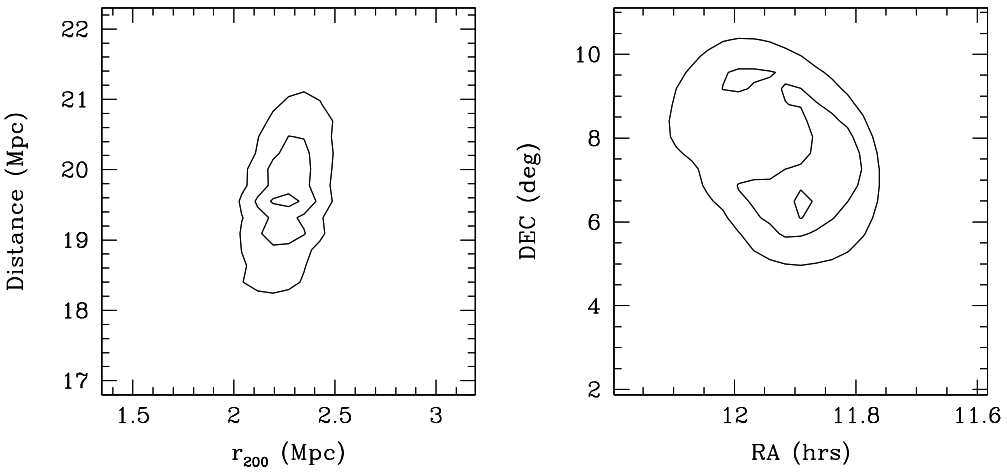



Figure 3.3: Contours of 1, 2 and $3\sigma$ errors for the location and size of the best fit attractor in a single attractor model. On the left is shown the covariance between the distance to the attractor and its mass, expressed in terms of the virial radius ($r_{200} = 2$ Mpc corresponds to $\sim 10^{15} M_{\odot}$). On the right are shown the contours describing the location of the best fit attractor on the sky.

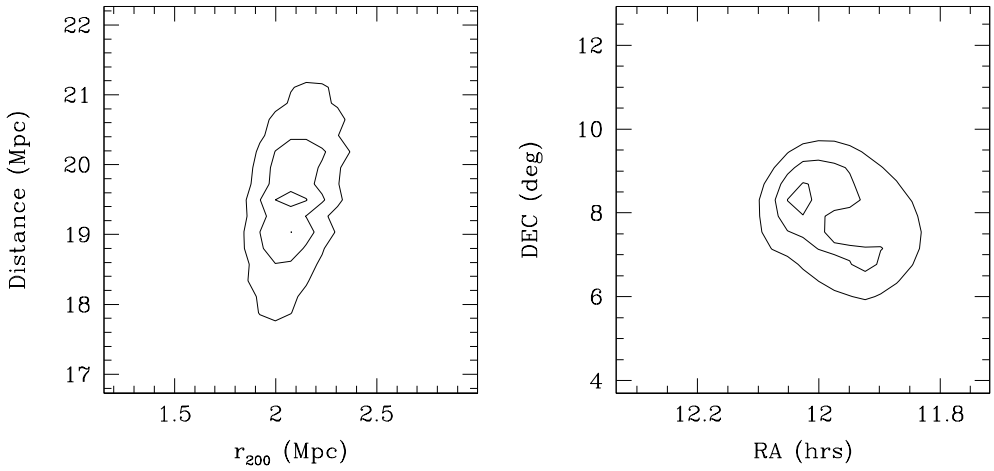



Figure 3.4: Contours of 1, 2 and $3\sigma$ errors for the location and size of the attractor at roughly the position of Virgo in a two attractor model. On the left is shown the covariance between the distance to the attractor and its mass, expressed in terms of the virial radius ($r_{200} = 2$ Mpc corresponds to $\sim 10^{15} M_{\odot}$). On the right are shown the contours describing the location of the best fit attractor on the sky. Note that Virgo in the mock universe is slightly offset from its "real" location, being at $D = 19.5$ Mpc, $(\alpha, \delta) = (12.2\text{h}, 1.7^{\circ})$.

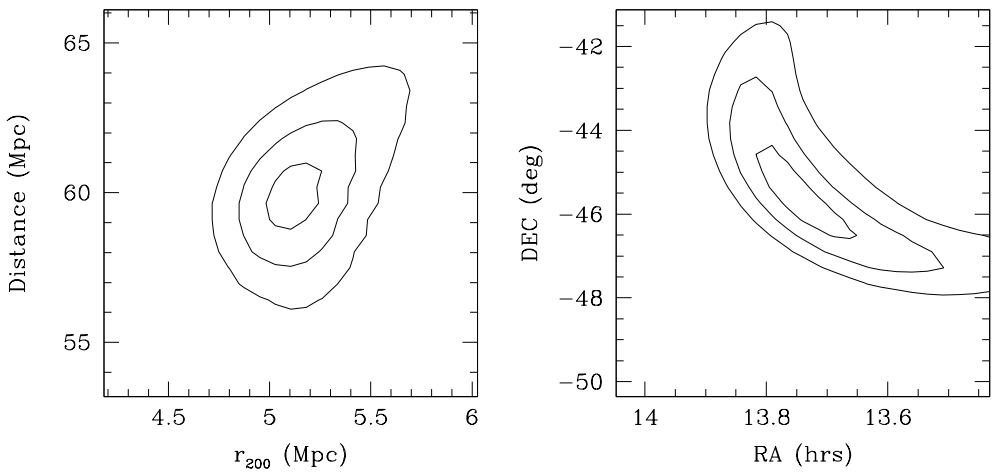



Figure 3.5: Contours of 1, 2 and $3\sigma$ errors for the location and size of the second attractor in a two attractor model. On the left is shown the covariance between the distance to the attractor and its mass, expressed in terms of the virial radius ($r_{200} = 5$ Mpc corresponds to $\sim 10^{16} M_{\odot}$). On the right are shown the contours describing the location of the best fit attractor on the sky. This attractor is close to the position of the Hydra-Centaurus cluster in the mock universe.

### 3.6.4 Three Attractors - no constraints on location

The addition of a third attractor also improves the goodness of fit, but not significantly enough to improve the information criteria. The third attractor ends up at roughly the same SGX as the Hydra-Centaurus region (GA region), but at somewhat larger SGY and SGZ. This might be a way to account for the non-spherical nature of the masses in that region, but the location is also near another peak in the density field at (-60.7, 21.4, -42.9) Mpc.

### 3.6.5 Multiple attractors at density peaks

We now explore the use of peaks in the density distribution of the constrained simulation to constrain the location of attractors. Peaks are found in the the density distribution after it has been smoothed with a Gaussian of width 10 Mpc. In order of decreasing overdensity we find peaks at (SGX, SGY, SGZ) = (71.4, -7.1, -17.9) Mpc; (-50.0, 17.9, -3.6) Mpc (the GA or Hydra-Centaurus), (32.1, -21.4, -50.0) Mpc, (-60.7, 21.4, -42.9) Mpc, (0.0, 103.6, 10.7) Mpc (the Coma cluster), (57.1, -46.4, 53.6) Mpc and (-7.1, 17.9, -3.6) Mpc (Virgo). We stop when we find Virgo.

Fitting a two attractor model using these locations for Virgo and Hydra-Centaurus, we find attractor sizes of $r_{200} = 2.29$ Mpc$/h_{70}$ and $r_{200} = 3.72$ Mpc$/h_{70}$ respectively. This model fits significantly less well than when the locations of the

two attractors are allowed to vary freely. We now proceed to search through the remaining 5 density peaks for the 3rd attractor with the best model likelihood. It is found that the peak at (57.1, -46.4, 53.6) Mpc provides the best fit; with a size of $r_{200} = 6.48$ Mpc/$h_{70}$ ($\mathcal{L} = -134$). The size of the Virgo and Hydra-Centaurus attractors appears to be relatively insensitive to the location or size of this third attractor. We now repeat the procedure to find the 4th attractor and find the peak at (71.4, -7.1, -17.9) Mpc with a size $r_{200} = 4.93$ Mpc/$h_{70}$ as the best fit ($\mathcal{L} = -142$). The addition of this attractor decreases the size of the 3rd attractor to $r_{200} = 5.93$ Mpc/$h_{70}$, but does not significantly affect the size of either Virgo or Hydra-Centaurus. The addition of a 5th attractor at any of the density peaks shown above does not improve the goodness of fit further. The goodness of fit for this model always remains worse than the models in which the location of the attractors is allowed to vary, although with the advantage of removing three free parameters for each attractor location.

### 3.6.6 Two Attractors and a Quadrupole

This model includes both attractors, now fixed at the best fit position of the two attractor model, and also a quadrupole component centered on the origin. The addition of this component again improves the fit with both goodness of fit estimators. The quadrupolar component is small in all cases. This, and the dipole are the components most affected by the presence of the ZoA. It is largely the orientation of the dipole and quadrupole which changes. When there are no tracers in the ZoA the quadrupole is an expansion of 12.58 km s$^{-1}$ along (0.3, 0.5, 0.8) and compressions of 7.2 and 5.3 km s$^{-1}$ along (0.7, -0.7, 0.1) and (-0.6, -0.6, 0.6) respectively, but this changes to an expansion of 10.3 km s$^{-1}$ along (0.4, 0.6, 0.7) and compressions of 7.2 and 3.1 km s$^{-1}$ along (0.9, -0.3, -0.3) and (-0.1, -0.8, 0.6) when there are tracers in the ZoA (directions are given as unit vectors in supergalactic Cartesian co-ordinates). The dipole changes from a flow of $329 \pm 50$ km s$^{-1}$ along $l = 185 \pm 20°$, $b = 16 \pm 20°$ to $281 \pm 50$ km s$^{-1}$ along $(l, b) = (180°, 17°)$. This should be compared with previous determinations of the dipole (now from the real universe of course), such as $\sim 150$ km s$^{-1}$ towards $(l, b) = (294°, 67°) \pm 43°$ from TB00, $151 \pm 120$ km s$^{-1}$ towards $(l, b) = (295°, 28°) \pm 45°$ from Giovanelli *et al.*(1999) or $372 \pm 127$ km s$^{-1}$ towards $(l, b) = (273°, 6°)$ from Hudson *et al.* (2004). In Chapter 8 we derive a dipole in the equivalent model fit to our real peculiar velocity sample of $368 \pm 60$ km s$^{-1}$ towards $(l, b) = (264°, 21°) \pm 14°$. Note that all of these samples cover a region of space small enough that the convergence depth ($cz \sim 10000$ km s$^{-1}$) has not yet been reached.

This model has the best overall likelihood of any of those considered here, as well as the best information criteria (AIC and BIC, see Section 3.4), and is similar to both the best fit model found in TB00, and found by us in Chapter 8. This will therefore be taken as the default model for studying the impact of using a flow model on estimating distances. Figure 3.6 shows contours of constant CMB velocity for this model in a plane which intersects both attractors. Overlayed are

Table 3.3: Parameters of best fit Multiattractor Models to the mock distance catalogs

| Parameter | Tracers in ZoA | No tracers in ZoA |
|---|---|---|
| **"Virgo"** | | |
| Position (Mpc/$h_{70}$) | (-4.9, 18.6, -3.5) | (-5.7, 17.7, -4.7) |
| Mass ($10^{15}$ $M_\odot/{h_{70}}^3$) | 1.0 | 1.1 |
| Enclosed overdensity | 0.80 | 0.94 |
| **"GA"** | | |
| Position (Mpc/$h_{70}$) | (-57.1, 17.0, -3.0) | (-57.6, 18.8, -9.0) |
| Mass ($10^{15}$ $M_\odot/{h_{70}}^3$) | 14.9 | 20.5 |
| Enclosed overdensity | 0.45 | 0.56 |
| **Dipole** (km s$^{-1}$) | (196, 104, -173) | (213, 117, -222) |
| **Quadrupole** | 10.3: ( 0.4, 0.6, 0.7) | 12.5: ( 0.3, 0.5, 0.8) |
| ($h_{70}$ km s$^{-1}$ Mpc$^{-1}$) | 7.2: ( 0.9, -0.3, -0.3) | 7.2: ( 0.7, -0.7, 0.1) |
| | 3.1: (-0.1, -0.8, 0.6) | 5.3: (-0.6, -0.6, 0.6) |

the locations of the mock velocity field tracers used to fit the model. The fit parameters for both the sample with and without tracers in the ZoA are shown in Table 3.3. Recall that the Virgo cluster in the constrained simulation is at somewhat larger distances than the Virgo cluster in the real universe.

### 3.6.7 Thermal Velocity Dispersion

The cosmic thermal velocity dispersion measures velocities on small scales. It is a measure of the dispersion of galaxy velocities about the mean flow. Tonry *et al.* (2000) fit a velocity dispersion of 187±14 km s$^{-1}$ to their sample of $\sim$ 300 galaxies with SBF distances. From the mock sample described above, we derive a somewhat higher thermal velocity dispersion, but note that as no attempt is made to remove cluster galaxies from the sample the thermal velocity dispersion will include components due to virial motions in clusters and therefore is not reliable. We choose instead to assume the value estimated by Tonry *et al.* (2000), and also note that this value is on the small side of numbers found from peculiar velocity studies, which is often assumed to be about $\sigma_{\rm cosmic} = 250$ km s$^{-1}$. Strauss, Cen & Ostriker (1993) calculated the thermal velocity dispersion from several peculiar velocity surveys (both using TF and the $D_n - \sigma$ relation for elliptical galaxies and found $\sigma_{\rm cosmic} = 250-420$ km s$^{-1}$; Giovanelli *et al.* (1998b) found $\sigma_{\rm cosmic} = 300\pm80$ km s$^{-1}$ for a sample of 24 clusters. In Chapter 8 we find a velocity dispersion of 163±21 km s$^{-1}$ from the peculiar velocity sample presented in this thesis. We return to the issue of cosmic velocity dispersion in the next section.

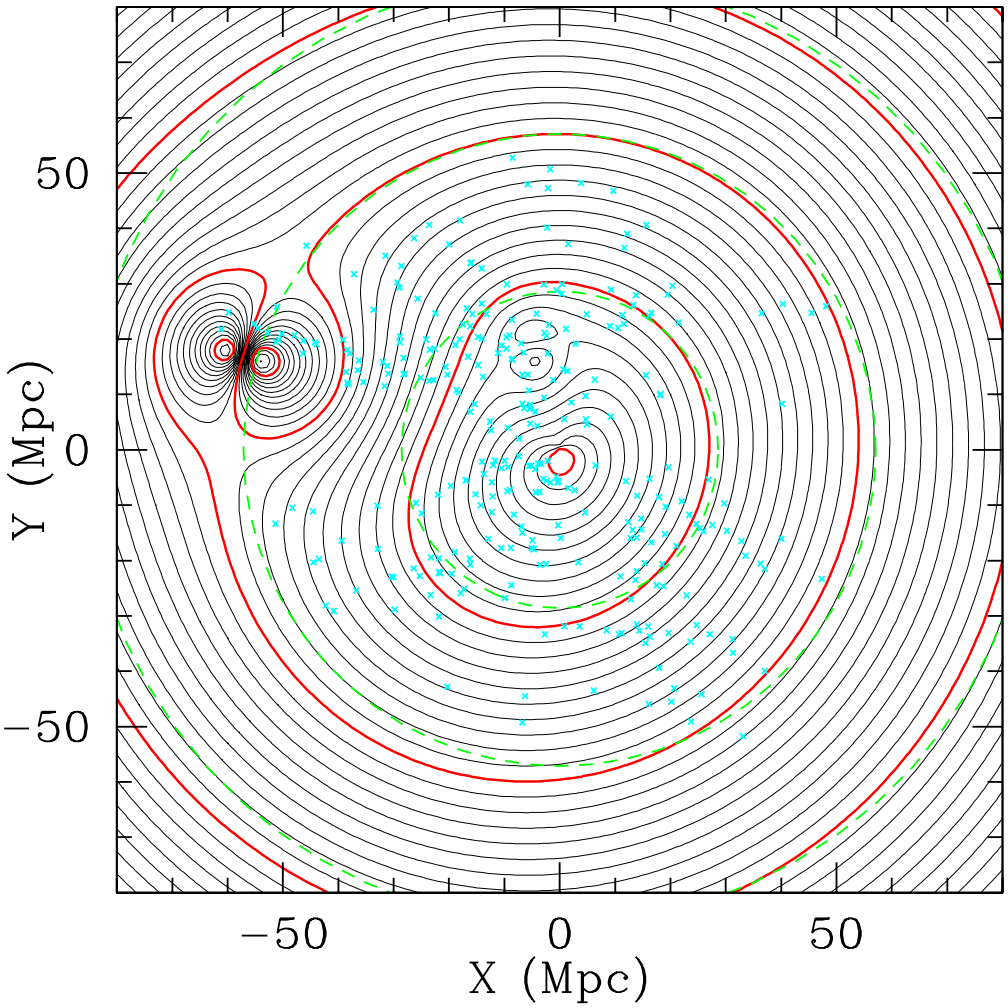



Figure 3.6: Contours of constant CMB velocity in a plane intersecting both attractors in the Virgo, GA plus quadrupole model fit to the mock sample with no tracers in the ZoA. The locations of the tracers are also shown. Contours are placed at 200km $s^{-1}$intervals, with heavy contours every 2000 km $s^{-1}$. The concentric dashed lines show pure Hubble flow with a Hubble's constant of 70 km $s^{-1}Mpc^{-1}$.

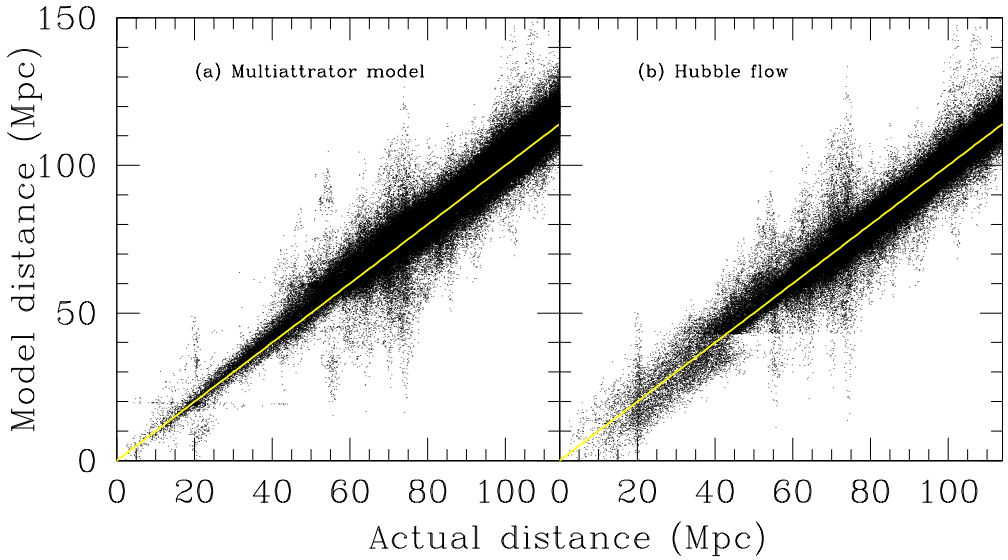



Figure 3.7: Model distances (left panel is the best fit multiattractor model, right is Hubble's Law) plotted versus actual distance for the 189123 galaxies in the constrained simulation. A subset of 500 galaxies was used to fit the velocity field model, as described in Section 5. The scatter in this plot is shown in Figure 3.9.

## 3.7 Predicting Distances from the Multiattrator Model

A flow model gives you the observed radial velocity of a galaxy at a given position on the sky and distance. The problem here is to invert the model to give a distance for a galaxy which has a known position and redshift. Complications arise because models with infall can have multi-valued regions where a single velocity can correspond to two or three distances. Some choices have to be made to pick a single distance for a galaxy. In finding a flow model distance for a galaxy, the first thing we do is to assign galaxies close to the cores of the attractors to those positions. In triple valued regions we pick the middle distance and inflate the error on the distance to include the nearer and further one. These galaxies are also flagged.

Panel (a) of Figure 3.7 shows distances predicted by the multiattractor model for all the constrained simulation galaxies vs. their actual distance, while panel (b) shows the distance from Hubble's Law, where we have used the CMB velocity for $cz > 3000$ km s$^{-1}$, and the velocity with respect to the center of the Local Group (LG) within 3000 km s$^{-1}$, as is common practice; the discontinuity due to this transition is observed in the figure. The vertical lines in both panels are due to the presence of galaxies in clusters with large viral motions. A multiattractor model obviously should not be used for such galaxies, and also would not be used for galaxies with distances larger than $\sim$ 60 Mpc, where the peculiar velocity (expect for galaxies in clusters) will be much smaller than the radial velocity due to the expansion of the universe. The horizontal lines in Panel (a) are due to the

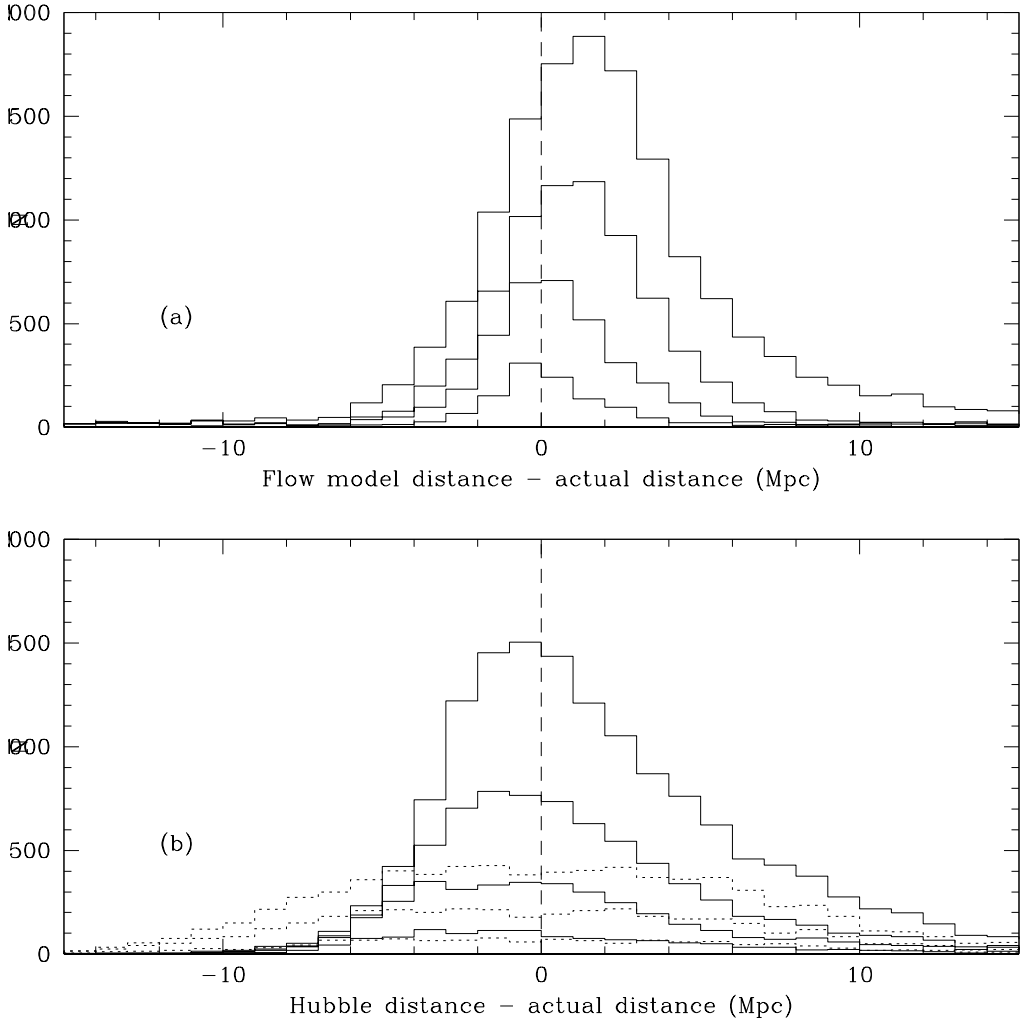



Figure 3.8: Error on predicted distance for galaxies within $D = 20$, 30, 40 and 50 Mpc (a) when Flow model is used or (b) when Hubble's law is used (dotted histograms use LG velocity, solid histograms use CMB velocity). The distribution of residuals is obviously far from Gaussian in either case, partly because negative distances are not possible. The width ($\sigma$) of the histograms are 4.7 and 6.1 (7.0) Mpc, for the flow model and Hubble's law (CMB or LG velocity respectively) within 20 Mpc; 4.6 and 5.6 (6.8) Mpc within 30 Mpc; 4.0 and 4.9 (6.6) Mpc within 40 Mpc; and 4.9 and 5.1 Mpc within 50 Mpc.

erroneous assignment of galaxies along the line of sight towards the Virgo cluster and the GA in the model to the cores of those attractors. The multiattractor model should be treated with caution in these directions.

For galaxies with actual distances $D < 50$ Mpc, the difference between the actual and predicted distances are also shown as a histograms in Figure 3.8 which compares them with the error found if Hubble's law is assumed to estimate distances. Histograms are shown for galaxies within 20, 30, 40 and 50 Mpc respectively. In all cases the width of the histogram is smaller for the flow model than when Hubble's Law is assumed, although obviously the distribution is far from Gaussian in most cases. The widths are 4.7 and 6.1 (7.0) Mpc within 20 Mpc; 4.6 and 5.6 (6.8) Mpc within 30 Mpc; 4.0 and 4.9 (6.6) Mpc within 40 Mpc; and 4.9 and 5.1 Mpc within 50 Mpc (for the flow model and Hubble's Law respectively; the values in brackets show the width when LG velocities are used in Hubble's Law). These widths give a measure of the cosmic thermal velocity dispersion, or velocities on scales not accounted for by the flow model, in the constrained simulation. The value is larger than the value of 2.7 Mpc derived by Tonry *et al.* (2000) and 2.3 Mpc derived later in Chapter 8, but is comparable to other measures, for example the velocity dispersion for clusters measured by Giovanelli *et al.* (1998b). It is interesting that the use of LG velocity in Hubble's Law for the most nearby galaxies appears to increase the scatter, and indicates that this common practice may be in error outside of the immediate vicinity of the Local Group. We proceed in the rest of this Chapter to use the CMB velocity of all galaxies (even nearby ones) in the derivation of Hubble flow distances, but with the caveat that LG velocities are commonly used in the literature for galaxies within the Local Supercluster ($D \sim 40$ Mpc).

The velocity dispersion is illustrated again in Figures 3.9 and 3.10, where the scatter in Figure 3.7 is shown as a function of distance for the whole sky, and for the sky divided into 4 quadrants. The locations of Virgo, at about 20 Mpc in panel (a), and the Hydra-Centaurus (GA) region at about 50 Mpc in panel (c) show up as areas where the velocity dispersion from the model increases. There is also an increase in the velocity dispersion at about 70 Mpc in the Northern fall sky. In the Southern hemisphere the Fall sky shows a relatively calm velocity field.

### 3.7.1 A Guide to Applying Flow Model Distances

We now ask how well on average the velocity field model does at estimating the distances to galaxies in various regions of the sky. We consider the sky divided into 12 regions, as indicated in the top left corner of Figures 3.11 and 3.12. This division is intended to provide roughly equal volumes, and place the Virgo cluster in the center of one of the regions (Fig3.11d). What is immediately obvious from Figures 3.11 and 3.12 is that the answer to how well the velocity field model does at estimating distances varies widely over the sky. In some regions there is little difference between the velocity field model and Hubble's law and they do equally well (or badly). In some regions (for example DEC=-45-0°, RA=9-15hrs)

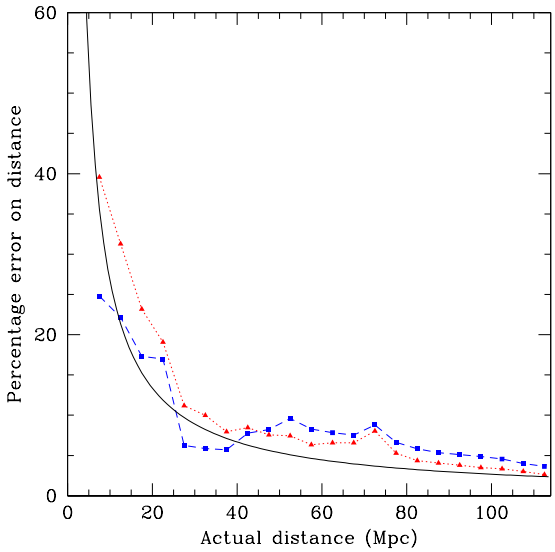



Figure 3.9: Percent error on predicted distance as a function of actual distance when the best fit flow model is used (squares and dashed line) and when Hubble's Law is used (triangles and dotted line). The solid line shows the error expected from a thermal velocity dispersion of 187 km $s^{-1}$. Only galaxies in the single valued region of the model, have been used.

the velocity field model does much better than the use of Hubble's Law at most distances, while in other regions, and at certain distances, the velocity field model does worse. Also shown in this figure is the scatter about the mean distance, which illustrates the variation of the cosmic thermal velocity dispersion. We show this result binned in real space distances (Figure 3.11) and in redshift space distances (Figure 3.12). The former being more useful for illustrating how well the model fits, the latter being more useful as a practical guide to redshift ranges where the velocity field model provides reliable distances. Note that where Hubble's Law underestimates distances, that implies a negative peculiar velocity so galaxies are moved to the left in Figure 3.12 relative to their position in Figure 3.11, while where Hubble's Law overestimates distances the galaxies move to the right.

Here we will summarize and discuss the information shown in Figures 3.11 and 3.12.

**Region a: QHF.** 9-21hrs, 45-90°. Both the velocity model and Hubble's Law do reasonably well at all distances in this region near the North celestial pole, where the flow model differs little from Hubble's Law. This area is similar to the quiet Hubble Flow (QHF) region identified by Courteau *et al.* (1993), at $\delta > 0$, SGY $> 0$.

**Regions b and e: Galactic anti-center.** 21-9hrs, 45-90°, 3-9hrs, 0-45°. These region contains the Galactic anti-center and other parts of the Galactic plane, and therefore have few velocity field tracers in our mock sample. Both the velocity

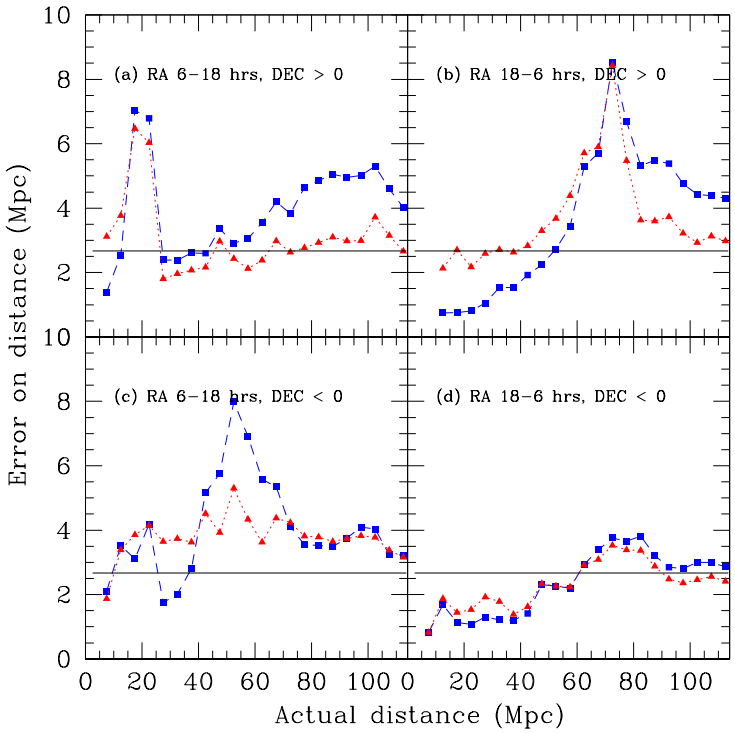



Figure 3.10: As in Figure 3.9, except showing absolute error, and dividing the sky into quadrants.

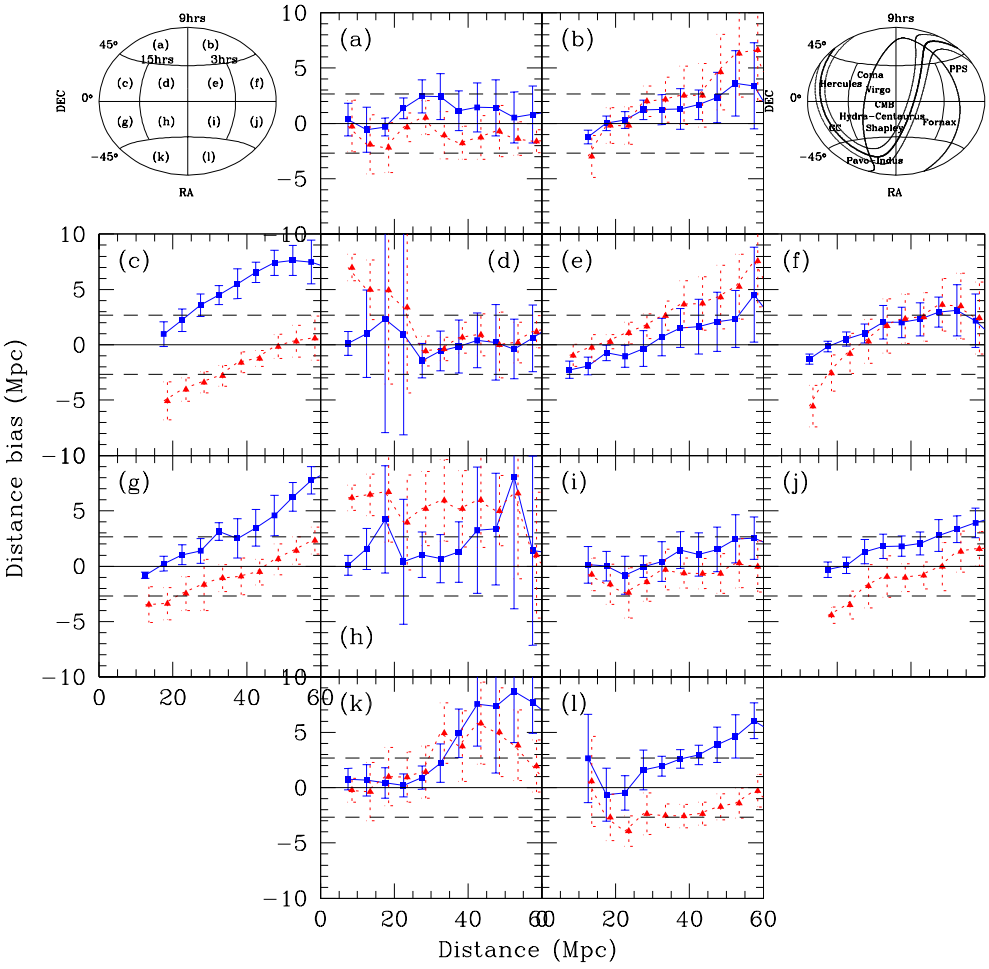



Figure 3.11: The mean distance bias and scatter divided into 12 regions of the sky as shown in the key at top left. The squares and solid line show the result when the best fit flow model is used, while the triangles and dotted line show the result using Hubble's Law. The distance bias and scatter is shown as a function of the actual distance to the particles in the constrained simulation. Only galaxies in the single valued region of the velocity field model have been used. The solid line shows a zero bias, while the dashed lines indicate a cosmic velocity dispersion of 187 km $s^{-1}$. The key at top right indicates nearby clusters and superclusters; the direction of the CMB dipole motion; and the location of the Galactic plane, or ZoA, $b \pm 10°$, and supergalactic plane.

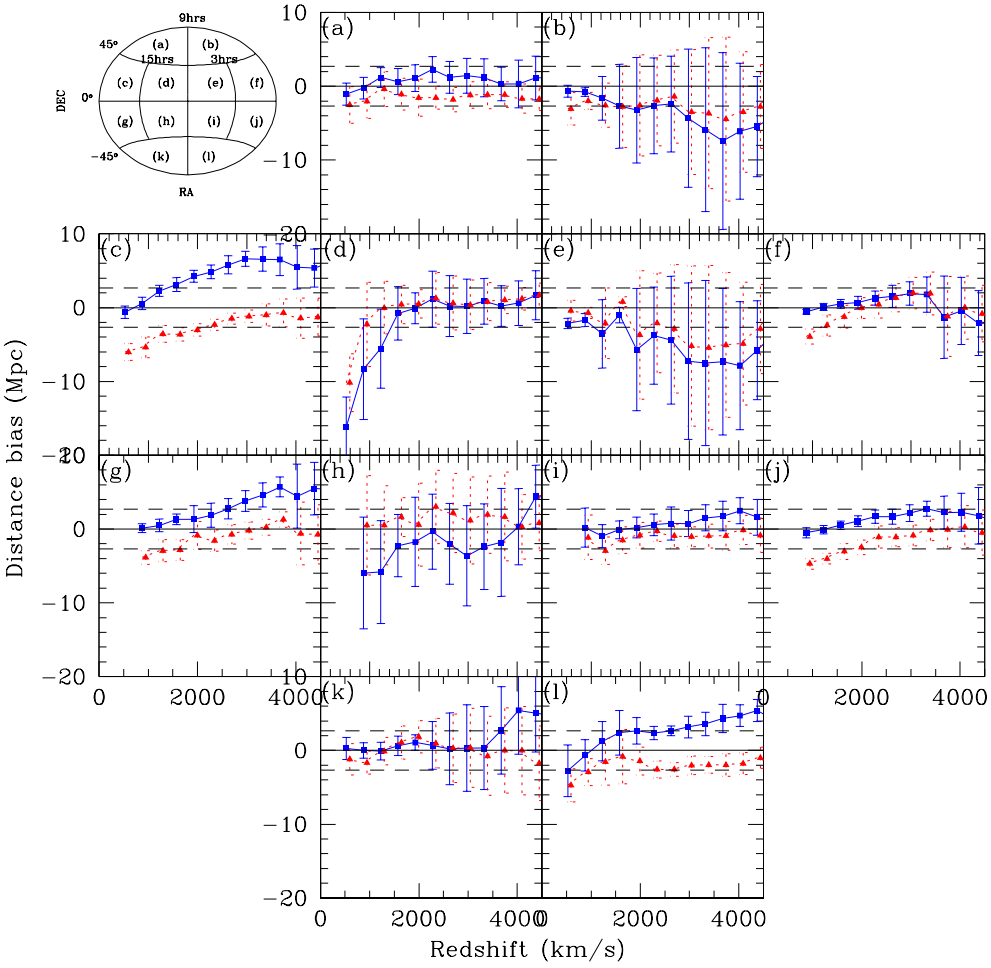



Figure 3.12: As in Figure 3.11 except that now galaxies are binned in redshift space, so galaxies with positive peculiar velocities are moved to the right here (relative to Fig 3.11), and those with negative peculiar velocities are moved to the left.

model and Hubble's Law are similar in both regions, but as you go out in distance both overestimate the distance to objects by progressively larger amounts. In redshift space, this amounts to an underestimate of the distance at a given redshift, getting progressively larger as the redshift increases, because the positive peculiar velocity of the galaxies moves them into larger redshift bins than their distance would imply.

**Regions c and g: Galactic center.** 15-21hrs, 0-45° and -45-0°. Both these regions contain large areas of the Galactic plane, including the Galactic center in Region g, so the velocity field model should be expected to be badly constrained here, as it appears to be. The shape of the distance bias is similar for the velocity model and Hubble's law, but the offset changes such that Hubble's law underestimates distances in both regions at small distances while it does reasonably at large distances. The velocity model does reasonably at low distances but then becomes an increasingly larger overestimate with distance. In redshift space the story is similar, except that because the small distance objects have negative peculiar velocities and the large distance objects have positive peculiar velocities the trend is stretched out and therefore looks less severe.

**Region d: Virgo Cluster.** 9-15hrs, 0-45°. This is the region containing Virgo (at 19 Mpc in the constrained simulation), which causes significant deviations from pure Hubble flow, and also drastically increases the velocity dispersion. Infall onto Virgo from the near side, causes Hubble's Law to overestimate distances for all objects in the foreground of Virgo, although on the backside of Virgo, on average Hubble's Law does well. The velocity model corrects the distortions from smooth expansion well in this region, but velocity model distances also have a large scatter about the correct value at around the distance of Virgo. In redshift space one can see the impact of backside infall onto Virgo, in that galaxies at smaller redshifts than the cluster itself systematically have their distances underestimated, because some of them are at very large distances with large negative peculiar velocities. The velocity dispersion is again very large. Except at relatively large distances/redshifts (beyond 30 Mpc or about 2000 km $s^{-1}$) any distance estimated from a velocity in this region (either from Hubble's Law or an infall model) should be treated with extreme caution.

**Region f: Pisces-Perseus foreground.** 21-3hrs, 0-45°. This region, containing the void in the foreground of the large Pisces-Perseus supercluster appears well constrained by the velocity field model, which is not much different from pure expansion except between 10-20 Mpc. In this near part, Hubble's Law underestimates the distances. Both estimates have a small positive bias at large distances. The same applies to redshift space.

**Region h: Hydra-Centaurus.** 9-15hrs, -45-0°. This is the direction towards the "great attractor" in the velocity field model, at roughly the location of the Hydra-Centaurus cluster. The Shapley supercluster lies in the background, and there appears to be a net motion of the local volume in this direction. This is the

reason for the systematic overestimate of distances when Hubble's Law is used. The velocity field model fits well between about 10-40 Mpc, except for a region of overestimated distances at about 20 Mpc (maybe due to infall onto the Virgo cluster which is close enough to this direction to have some influence). Beyond 50 Mpc the velocity field model becomes similar to Hubble's Law, and both tend to overestimate distances slightly. The velocity dispersion is large except between 25-40 Mpc. Because of the net positive peculiar velocity in this region, in redshift space all galaxies are moved to larger redshift bins, leaving only galaxies with little, or negative peculiar velocities in the lower velocity bins, and therefore reducing the overestimates of distances, however because of the large velocity dispersion in this region neither method for estimating distances should be trusted.

**Region i: Fornax/Galactic plane.** 3-9hrs, -45-0°. Both the velocity field model and Hubble's Law are similar and do reasonably well at predicting distances, with the velocity field model distances on average a little larger than Hubble's Law which is an underestimate nearby.

**Region j: Anti-Virgo region.** 21-3hrs, -45-0°. This region is roughly opposite Virgo and in the supergalactic plane. The velocity model starts off predicting distances well, while Hubble's Law is an underestimate because all nearby galaxies have negative peculiar velocities as they infall towards Virgo. At larger distances both are slight overestimates, with the velocity field having the larger overestimate.

**Region k: Galactic plane.** 9-21hrs, -90, -45°. Both estimates do reasonably well within 30 Mpc, then there is a large area where both the velocity model and Hubble's Law overestimate distances. In redshift space these galaxies are moved to the right of the plot, past then edge of the plot.

**Region l: SCP.** 21-9hrs, -90, -45°. Over much of the distance range Hubble's Law on average underestimates distances, while the velocity model overestimates them. At around 20 Mpc the velocity model fits well.

### 3.7.2 Illustrative Example Galaxies

We now consider several example galaxies, for which primary distances have been measured. We choose these galaxies to illustrate the application of flow models in various regions of the sky, because they also have primary distance measurements as an independent check. As a caveat it should be repeated that the velocity field model above was fit to a sample of mock galaxies taken from a *constrained simulation* of the local universe. This simulation was run with the aim of reproducing the large scale structure in the local universe, but on smaller scales is unconstrained. Major features in the nearby universe, like the Virgo cluster, are slightly shifted from their equivalent location in the real universe. The findings in the above section therefore, in broad terms can be applied to the real universe, but may not exactly reproduce it. In deriving flow model distances for these real galaxies we use the velocity field model of Tonry *et al.* (2000) and the best fit model in Chapter

8, which are similar to the model fit above to mock galaxies from the constrained simulation, but is not exactly the same.

**HIZSS3 - a possible Local Group dI**

HIZSS3 was discovered during a blind HI (21cm) survey of the ZoA (Henning *et al.* 2000) at a Galactic latitude of $b = 0.09°$. Its location so close to the plane of the Milky Way make optical identifications of the object tricky. Recently Begum *et al.* (2005) have presented GMRT observations of the source, splitting it into a galaxy pair. At their assumed distance, the smaller of these two galaxies has a HI mass of $2.6 \times 10^6 M_\odot$, making it one of the lowest mass HI galaxies known. The distance they use of $1.69 \pm 0.07$ Mpc is based on the location of the tip of the red giant branch, as measured by Silva *et al.* (2005) in the K-band; however given the low Galactic latitude the large amount of extinction, will make such a measurement unreliable (see Chapter 7 for a review of TRGB distances). At its location the DIRBE extinction maps (Schlegel *et al.* 1998) derived a visual extinction of 4.5 mags; however Schlegel *et al.* (1998) note that at Galactic latitude $b < |5|°$, the maps are uncertain and untrustworthy, and that the nominal error of 10% on the value should be taken as a lower limit.

This galaxy pair, at (RA,DEC) = (07h 00 29.3, -04° 12 30) has heliocentric velocities of $288 \pm 2.5$ and $322.6 \pm 1.4$ km s$^{-1}$ for the larger and smaller of the pair respectively. If it is assumed that the peculiar velocity of the larger of the pair is zero, this implies a distance of 2.4 Mpc (when the YTS correction to the local group frame is used, rather than the more commonly applied RC2 correction - see Courteau & van den Bergh (1999) for a discussion of corrections to the Local Group frame and we assume $H_0 = 70$ km s$^{-1}$ Mpc$^{-1}$), if we instead use the average of the two velocities as a measure of the distance to the galaxy pair we get 2.7 Mpc. The flow model discussed above (which we note was fit to a constrained simulation of the universe, not real data itself, but is still illustrative) gives a distance of 3.6 Mpc, while the Tonry *et al.* (2000) model gives a distance of $5.0 \pm 2.7$ Mpc, more than twice that implied by the TRGB distance. The model we fit in Chapter 8 gives a distance of $4.1 \pm 2.3$ Mpc. The dispersion between all these difference estimates of the distance is less than 4 Mpc, but for a galaxy that might physically be at less than 2 Mpc this is not acceptable. If the TRGB distance is underestimated, and the flow models provide a better estimate, the association of this galaxy pair with the Local Group may be wrong, and the HI masses may be almost an order of magnitude larger.

We now attempt to identify mock galaxies from the constrained simulation with similar properties. Because of the resolution of the N-body simulation, no galaxies with magnitudes smaller than $M_B = -16.27$ are generated, creating a sparsity of dwarf galaxies in the Local Group. However, there are 7 galaxies in the simulation at distances smaller than 3 Mpc. As can be seen in Table 3.4 in the Local Group (and just beyond) when estimating distances, the use of Hubble's Law with velocities transformed to the Local Group frame, and the use of this

Table 3.4: Mock galaxies at $d < 3$ Mpc in the constrained simulation

| RA, DEC | L, B | $v_{\rm helio}$ (km s$^{-1}$) | $v_{\rm LG}/H_0$ (Mpc) | $d_{\rm flow}$ (Mpc) | $d_{\rm true}$ (Mpc) | $v_{\rm pec,LG}$ (km s$^{-1}$) |
|---|---|---|---|---|---|---|
| 16.76, 45.588 | 71.10, 40.59 | -81 | -1.3 | 0.00 | 2.29 | -249 |
| 1.33, -15.552 | 153.84,-76.70 | 26 | 1.5 | 0.30 | 2.30 | -55 |
| 15.55, -53.325 | 325.75, 2.22 | 301 | 1.0 | 5.04 | 2.54 | -110 |
| 14.58, -30.178 | 328.14, 27.57 | 342 | 1.8 | 4.93 | 2.64 | -58 |
| 16.80, 40.513 | 64.45, 40.07 | -160 | -0.1 | 0.00 | 2.75 | -198 |
| 16.46, 42.027 | 66.36, 43.93 | 236 | 5.5 | 5.73 | 2.79 | 187 |
| 15.37, -43.142 | 330.06, 11.63 | 272 | 1.0 | 4.53 | 2.90 | -149 |

flow model can do equally badly! A typical error on a distance estimated from a velocity should be the random thermal velocity of galaxies, measures of which vary from our calculation of $163 \pm 20$ km s$^{-1}$ (Chapter 8) to higher estimates of $\sim 250$ km s$^{-1}$. This translates to a theoretical distance error of at least 2-4 Mpc for any distance estimated from a recessional velocity. No distance estimated from a redshift should be trusted for galaxies within $\sim$5 Mpc.

**NGC 4395 - The nearest Seyfert Galaxy**

NGC 4395 (12 25 48.8, +33 32 47, $v_\odot = 319$ km s$^{-1}$) is the nearest Seyfert galaxy and has a Cepheid variable star distance of $4.0 \pm 0.3$ Mpc (Thim *et al.* 2004). NGC 4395 is interesting, because it has one of the lowest mass central black holes of an active galaxy, and also no bulge, creating an interesting test of the black hole mass – bulge velocity dispersion relation (Filippenko & Ho 2003). Its CMB velocity, of 583 km s$^{-1}$, would imply a distance from Hubble's Law of $\sim$8.3 Mpc (using $v_{\rm LG}$ gives a distance of 4.4 Mpc), while the flow model of TB00 gives a distance of $4.1 \pm 2.7$ Mpc and our flow model (Chapter 8) gives $4.4 \pm 2.3$ Mpc. This galaxy is in Panel (d) of Figures 3.11 & 3.12, where for nearby galaxies Hubble's Law tends to provide large overestimates (due to the impact of infall onto the Virgo cluster at $\sim$ 12hrs, 12°, while the velocity model appears to do well, as supported by this result. This galaxy serves to illustrate the wide area over which infall onto the Virgo cluster has an impact. If no Cepheid distance were know for this nearest Seyfert, and Hubble's Law (with $v_{\rm CMB}$) was used to estimate a distance blindly, the dynamical mass of its black hole $M \sim v^2 r/G$ would be overestimated by a factor of 2, providing a less tight upper limit on the mass of the black hole, perhaps even making the galaxy look like it diverges from the black hole mass – bulge velocity dispersion relation more significantly.

**IZwicky18**

IZw18 (RA = 09 34 02, DEC = +55 14 28) is the most metal poor star forming galaxy known. Recently Izotov & Thuan (2005) have observed this galaxy with

the ACS camera on HST, and from the photometry of its resolved stars estimated a distance of between 12.6-15 Mpc, with a preference for the upper part of the range. If Hubble's Law is assumed to derive a distance to this galaxy, which has a CMB radial velocity of 903 km $s^{-1}$, a distance of 12.9 Mpc would be inferred (or 12.1 Mpc using $v_{\rm LG}$). This is contrary to Izotov & Thuan (2005)'s claim that the Hubble Flow distance would be 10 Mpc, which comes from erroneously using the heliocentric radial velocity of 751 km $s^{-1}$ in Hubble's Law. The Tonry *et al.* (2000) infall model implies a distance of $13.8 \pm 2.7$ Mpc, while our flow model gives $12.2 \pm 2.3$ Mpc. In this instance both Hubble's Law and the infall model do comparably well at estimating the distance to this galaxy, as would be expected from Figure 3.11, since this galaxy falls into Panel (a), or the quiet Hubble flow (QHF) region, where Hubble's Law and the flow model tend to provide similar estimates.

If we consider mock galaxies in the constrained simulation above with CMB velocities similar to that of IZw18, but located in all directions on the sky we find galaxies with a range of distances from 4 Mpc (infalling onto Virgo from the foreground), to 20 Mpc (associated with Virgo itself). These galaxies are shown, in order of "true" distance in Table 3.5, and serve to illustrate the realistic range of error one should assume if Hubble's law is used at this observed CMB velocity. Flow model distances are shown in bold where the assumed error of $\pm 2.7$ Mpc does not bracket the actual distance to the mock galaxy, these erroneous distances include galaxies assumed to lie in the foreground infall region of the Virgo cluster, but which are actually part of the cluster region (centered on 12h, 8deg in the infall model), and galaxies at a similar declination to the Hydra-Centaurus region in the south, serving to illustrate the care that must be taken in applying infall models in the directions towards the attractors.

### A Fornax Cluster Galaxy - NGC 1425

NGC 1425 is a large spiral galaxy in the Fornax cluster (RA = 03 42 11, DEC=-29 53 36, $v_\odot = 1510$ km $s^{-1}$). It is one of the galaxies used in the Hubble Key project (Freedman *et al.* 2001) and as such has its distance of $20.89 \pm 0.48$ measured using the luminosity period relation for Cepheid variable stars. NGC 1425 has a CMB radial velocity of 1412 km $s^{-1}$, implying a distance of 20.2 Mpc from Hubble's Law (with $H_0 = 70$ km $s^{-1}$ $Mpc^{-1}$). The Tonry *et al.* (2000) model implies a distance of $23.5 \pm 3.3$ Mpc, while the model presented in Chapter 8 implies $D = 19.5 \pm 2.3$ (although because of the galaxies proximity to the Fornax cluster the error perhaps should be inflated, as it is somewhat in the TB00 model). This galaxy falls in Panel (j) of Figures 3.11 and 3.12, or the anti-Virgo region where Hubble's Law and the velocity field model both do reasonably well at predicting distances.

Table 3.5: Mock galaxies with $v_{\rm CMB} \sim 900$ km s$^{-1}$ ($d_{\rm Hubble} \sim 12.9$ Mpc) in the constrained simulation

| RA, DEC | $v_{\rm CMB}$ | Distance (Mpc) | $v_{\rm pec,CMB}$ (km s$^{-1}$) | Flow model distance (Mpc) |
|---|---|---|---|---|
| 11.811, -1.949 | 905 | 3.72 | 644 | 5.44 |
| 6.493, -33.536 | 904 | 8.87 | 282 | **14.24** |
| 8.586, -38.039 | 902 | 9.09 | 266 | 11.00 |
| 7.179, -51.932 | 908 | 10.41 | 178 | **14.14** |
| 6.281, -33.039 | 906 | 13.73 | -55 | 14.53 |
| 1.468, -76.498 | 898 | 14.31 | -103 | 15.84 |
| 18.519, -66.895 | 904 | 14.57 | -115 | 14.10 |
| 23.925, 78.152 | 893 | 15.18 | -169 | 14.64 |
| 8.493, -54.926 | 901 | 15.19 | -162 | **12.35** |
| 20.908, -43.718 | 903 | 15.68 | -194 | 16.73 |
| 8.350, -56.403 | 892 | 15.92 | -223 | **12.46** |
| 7.225, -80.033 | 901 | 16.08 | -224 | 14.17 |
| 20.238, -43.823 | 897 | 16.25 | -240 | 16.33 |
| 18.340, -12.633 | 909 | 17.02 | -282 | 17.65 |
| 20.646, 28.580 | 904 | 18.08 | -361 | 18.95 |
| 19.949, 22.659 | 909 | 18.40 | -379 | 19.72 |
| 18.662, 4.999 | 908 | 18.41 | -380 | 19.46 |
| 3.928, -47.684 | 909 | 18.53 | -388 | 17.09 |
| 23.303, -38.511 | 900 | 18.57 | -399 | 17.11 |
| 20.089, 23.162 | 904 | 18.63 | -400 | 19.53 |
| 12.004, 8.161 | 897 | 20.11 | -510 | 19.50 |
| 11.930, 2.292 | 899 | 20.27 | -519 | **5.45** |
| 12.203, -4.530 | 907 | 20.69 | -541 | **5.66** |

**NGC 3621**

NGC 3621 is a spiral (SA) galaxy located at $\alpha, \delta = 11\ 18\ 17$, -32 48 51 (Panel (h), or the Hydra-Centaurus direction in Figs 3.11 & 3.12). The galaxy, like NGC 1425 above is one used in the HST Key Project, and has a distance measured using the Cepheid period-luminosity relation of $6.6 \pm 0.2$ Mpc. NGC 3621 has a radial velocity in the CMB frame of 1067 km s$^{-1}$, implying a distance from Hubble's Law of 15.2 Mpc, which overestimates the actual distance by more than a factor of two. The Tonry *et al.* (2000) flow model distance for this galaxy is $8.1 \pm 2.7$ Mpc, while the model in Chapter 8 estimates $D = 8.9 \pm 2.3$ Mpc, both within $\sim$1 $\sigma$ of the actual distance. This finding is as implied by Fig 3.11(h), which shows that the multiattractor model predicts more accurate distances than Hubble's Law in this region of the sky, in which nearby galaxies being in the fore-ground of the Hydra-Centaurus supercluster tend to have positive peculiar velocities.

## 3.8 Conclusions

We have fit a multiattractor model for the local velocity field to a sample of mock distance indicators (with 10% distance error) taken from a constrained simulation of the local universe. This was done with the aim of comparing distances derived from the flow model for all particles in the constrained simulation with their actual distances in the simulated universe, to provide a practical guide to deriving distances and realistic errors from flow models.

Two mock samples were considered: with and without tracers in the zone of avoidance. The removal of tracers in the ZoA, causes all model discussed in Section 3.6 to have a slightly worse goodness of fit. The direction of the dipole and quadrupole are the components most affected by the removal of tracers from the ZoA, but the removal also has the effect of moving both attractors a small amount further away (and correspondingly making them slightly larger).

We discuss three related goodness of fit measure, the first being simple $\chi^2$ minimization. The other measures account for the impact of non-Gaussian peculiar velocity errors and the Malmquist bias. We note that using a $\chi^2$ minimization procedure, similar to that used by Lynden-Bell *et al.* (1988) to find the original GA, we find a similar best fit attractor. Once a goodness of fit which accounts for the non-Gaussian errors is applied, the best fit single attractor is again Virgo.

Information criteria are described, and used to select the preferred model among several choices with different numbers of parameters.

The best fit model found is one similar to that in Tonry *et al.* (2000) which includes infall onto the Virgo cluster, a second attractor roughly at the position of the Hydra-Centaurus supercluster and a quadrupole component. There is a covariance between the size and distance to the second attractor, indicating that its location is not well constrained. We also consider using peaks in the density distribution of the mock catalog to constrain the location of attractors, and the inclusion of extra attractors in the model. Neither of these improves the goodness

of fit.

We derive distances for all of the particles in the constrained simulation using the velocity field model, and compare these distances with those got from Hubble's law and the "real" distances. Figures 3.11 and 3.12 are shown to provide a practical guide to regions of the sky and distance (Fig 3.11) or redshift (Fig 3.12) ranges where the velocity field model can be reliably applied to predict distances, and region where it cannot.

The use of a multiattractor model to estimate distances for nearby galaxies from their redshifts does not provide a "miracle solution". There is no replacement for a redshift independent distance measurement, but where such a measurement does not exist the use of a multiattractor model can provide a first order correction to the simple application of Hubble's Law. Several important caveats should be noted:

- There is no getting over the thermal velocity dispersion of $\sim$ 200 km s$^{-1}$, which gives a distance error of $\sim$ 3 Mpc on all distance estimated from redshifts (either using Hubble's Law or a multiattractor model). Distances to galaxies within 5 Mpc should therefore be treated with extreme caution, and may be as much as 100 % wrong, unless a redshift independent distance exists.

- In directions towards the attractors in a multiattractor model special care must be taken, the model also does poorly in regions where there are few velocity tracers (like the zone of avoidance).

- For distances larger than about 40 Mpc, Hubble's Law and multiattractor models do equally well. If the multiattractor model has a non vanishing component (for example a dipole accounting for the net motion of the distance sample in the CMB frame) the best method for estimating distances from the redshift is simple Hubble's Law.

The aim of this Chapter is to illustrate the impact that velocity field models have on observations, and physical measurements made in extragalactic astronomy. In an ideal world, all galaxies within the region of space where distortions from pure expansion are significant would have redshift independent distances. In reality, the best that can be done often is to use the redshift, and apply a velocity field model, or Hubble's Law with caution. Hubble's Law may be simpler to apply, but velocity field models make an attempt to correct for the systematic distortions from pure expansion caused by our location on the edge of the Local Supercluster, and can remove systematic biases from surveys (as shown in the previous Chapter and Masters *et al.* 2004).

# Chapter 4

# The SFI++ and a Tully-Fisher Template

## 4.1 Introduction

In this chapter we will discuss the derivation of a template Tully-Fisher (TF) relation from a sample of galaxies in clusters. Here we introduce the TF (or luminosity-line width) relationship for spiral galaxies and discuss the observables needed to derive distances from this relation. In Chapter 6 we use the template to calibrate TF distances for a sample of field spirals, which will be used in Chapter 8 (and in future work) to study the velocity field in and around the Local Supercluster.

The Tully-Fisher relation (Tully & Fisher 1977) is an empirical relationship between the rotational velocity and absolute magnitude (or luminosity) of spiral galaxies. Since the rotational velocity (either as measured by the HI line widths or an optical rotation curve, ORC), is a quantity which is independent of distance, while the observed luminosity drops off with distance squared, the relationship provides a natural distance indicator for spiral galaxies. Tully & Fisher (1977) first calibrated the relationship using a sample of 10 nearby galaxies which had well determined distances, which at the time restricted it to the two large spirals (M31 and M33) in the Local Group, galaxies in the M81 group (at 3.25 Mpc) and M101 group (at 7.24 Mpc). Combining these data with 8 galaxies in the Virgo cluster by shifting the Virgo points by the (then) estimated distance modulus to the cluster, Tully & Fisher (1977) estimated the relationship (for photographic magnitudes) to be

$$M - 5\log h = -19.13 - 6.25(\log W - 2.5), \tag{4.1}$$

where $M$ is the absolute magnitude, $W = v_{\rm max}/2$ is the width of the Doppler broadened spectral line and $h = H_0/70$ km s$^{-1}$ Mpc$^{-1}$. This relationship is equivalent to $L \propto v_{\rm max}^{2.5}$. Tully & Fisher (1977) and estimated there was a scatter of 0.3 mag around the relation, resulting in a 15% error on the estimated distance.

The application of the Tully-Fisher relation to measure distances to spiral galaxies has had a large impact on extragalactic Astronomy since its discovery. The relationship can also be used to constrain models of galaxy formation, and by studying it's variation with environment, galaxy type and its evolution over the age of the universe many clues into how the disks of galaxies are assembled have been found. There is a simple derivation of the Tully-Fisher relation, which results in a scaling similar to that observed. Kinetic and gravitational potential energy balance for the disk of a galaxy gives

$$\frac{1}{2}v_{\rm max}^2 = \frac{GM_{\rm tot}}{r}, \tag{4.2}$$

where $v_{\rm max}$ is the maximum rotation velocity reached at a radius, $r_{\rm max}$, and $M_{\rm tot}$ is the total mass within this radius. If we assume a constant mass to light ratio $\alpha = M_{\rm tot}/L$, and a constant central surface brightness $\mu_0 = L/r_{\rm max}^2$, then

$$v_{\rm max}^2 = \frac{2G\alpha L}{\sqrt{L/\mu}}, \tag{4.3}$$

or

$$L = \left(\frac{1}{4\mu\alpha^2 G^2}\right) v_{\rm max}^4. \tag{4.4}$$

If the mass-to-light ratio or central surface brightness of disk are not constant, but vary with the luminosity of the galaxy, the exponent in this relationship will change from the simple value of 4.

Observationally the convenient quantities are the magnitude ($\propto 2.5 \log L$) and the width of the Doppler broadened spectral line (usually HI or H$\alpha$) which is twice the rotational velocity and is usually plotted as a log to show a linear relationship. The parameters are usually expressed as an intercept, $a$ and slope, $b$ in $M = a + b(\log W - 2.5)$ (where the offset of 2.5 is used to make $a$ the absolute magnitude of a typical galaxy). The slope $b/2.5$ gives the empirically measured exponent, ie $L \propto v^{b/2.5}$. The slope and intercept may depend on wavelength (perhaps getting steeper into the NIR, Verheijn (1997)), and morphological type of the galaxies. Giovanelli *et al.* (1997b) calibrated the Tully-Fisher relation in I-band using a sample of 555 spiral galaxies in the fields of 24 clusters. They found $M - 5\log h = -21.01 - 7.68(\log W - 2.5)$, or $L \propto v^{3.1}$. The scatter in the observed Tully-Fisher relation varies with the rotational velocity of the galaxy, from about 0.4 mag at the low mass end, to less than 0.3 mag at the high mass end, resulting in distance errors for individual galaxies of 15-20%.

N-body simulations in the $\Lambda$CDM paradigm are able to reproduce the slope and scatter, but not the zero point of the observed TF relation. Navarro & Steinmetz (2000) argue that the slope and scatter come about as a result of the dynamical response of the dark matter halo to the assembly of luminous matter, and are able to reproduce qualitatively the variation with wavelength. Their zero-point however, is off by more than a magnitude from the observed value, which they trace to a combination of the high concentrations of the halos (which would have to be reduced to match observations), and weaker feedback in the star formation than is observed. Mo & Mao (2000) also argue that to fit the TF relation requires less concentrated dark matter halos than are ordinarily suggested, and that the TF relation is a direct result of the gravitational interaction between the disk and halo.

In Section 4.3 we discuss the derivation of a template TF relation in the I-band. We follow a method similar to that used in Giovanelli *et al.* (1997b; hereafter G97b) and use a sample of galaxies which builds on that cluster sample, but has a significant amount of new data (including the addition of several new clusters) making a total sample of 911 galaxies in the fields of 36 clusters. In Chapter 6 this

template will be applied to a larger sample of spiral galaxies in the field, from which the peculiar velocity field (and therefore mass distribution) of the local universe will be studied.

## 4.2 Tully-Fisher Observables

The sample discussed here will be referred to as the SFI++. This sample builds on the all-sky SFI and SCI samples discussed in a series of papers in the 1990s (Giovanelli *et al.* 1994, 1995, 1997b; Haynes *et al.* 1999a,b), but also include data from the SC2 sample (Dale 1998), and the theses of Vogt (1995) and Catinella (2005). Subsets of this data have also been presented in Springob (2005) and Spekkens (2005). The bulk of the southern hemisphere data is presented in Mathewson, Ford & Buchhorn (1992a) and was made available to us in electronic form to be reprocessed using the same methods.

### 4.2.1 Optical Imaging Data

All optical data discussed here is I-band imaging data taken by members of the Cornell Extragalactic group and their collaborators at various telescopes. Data for the SFI sample of galaxies is presented in Haynes *et al.* (1999b). This was a combination of images in the Northern hemisphere taken for various projects, and the similar Mathewson, Ford & Buchhorn (1992a) survey in the Southern sky from which data was carefully recalibrated to make a homogeneous sample . For the SFI++ sample discussed here new data were taken in about 1900 fields north of $\delta = -2^\circ$ using the 0.9m KPNO telescope. The fields covered various clusters and TF candidate galaxies and were positioned in an attempt to optimize the number of TF candidate galaxies observed. These imaging data were intended to be complete to a diameter limit of about 0.5 arcmin in I, and more than double the number of TF candidate galaxies for which I-band imaging data is available.

The I-band images were reduced as described in Haynes *et al.* (1999b) to provide the observed total apparent magnitude and axial ratio of the galaxy. The observed axial ratio, $a/b$ of the galaxy comes from isophote fitting (as described in Haynes *et al.* (1999b)) and is corrected for seeing as in Giovanelli *et al.* (1997b), *i.e.*

$$e_{\rm corr} = 1 - \sqrt{\frac{(1-e)^2 - \phi^2}{1-\phi^2}}, \tag{4.5}$$

where $\phi = 0.5$ HPFW$_{\rm seeing}/a$; HPFW is the half-power full width of the seeing disk, $a$ is the radius at which the disk light drops to half its maximum value and the ellipticity, $e = 1 - b/a$. $e_{\rm corr}$ is limited to a maximum value of 1/0.12 to avoid over correction. The inclination of the galaxy is then found from

$$\cos^2 i = \frac{(1-e)^2 - q_0^2}{1-q_0^2}, \tag{4.6}$$

Table 4.1: RC3 Morphological Types for Spiral Galaxies

| T | 1 | 2 | 3 | 4 | 5 | 6 | 7 |
|---|---|---|---|---|---|---|---|
| Type | Sa | Sab | Sb | Sbc | Sc | Scd | Sd |

where $q_0$ is the intrinsic axial ratio of the galaxy, and is assumed to be $q_0 = 0.13$ for Sbc and Sc galaxies and $q_0 = 0.2$ for other types.

All magnitudes are corrected for extinction due to dust in our Galaxy using the DIRBE dust maps (Schlegel *et al.* 1998), including those from the SFI and MFB imaging data which previously used the Burstein & Heiles (1978) correction. Extinction due to dust internal to the galaxy itself is accounted for using the extinction correction derived in Giovanelli *et al.* (1994), namely $\Delta M = \gamma \log(a/b)$, where $a/b$ is the seeing corrected axial ratio of the galaxy and $\gamma$ depends on the absolute magnitude of the galaxy; $\gamma = 0.5$ for $M_I > -19$, $\gamma = 1.0$ for $-20.3 > M_I > -22$, and $\gamma$ changes linearly by -0.4 mag$^{-1}$ elsewhere. In Chapter 5 we discuss the derivation of such corrections for internal extinction (there in J, H and K-bands but following similar methods to that used in Giovanelli *et al.* (1994) for the I-band). A small type dependent k-correction as discussed in Han (1992) of $k = (0.5876 - 0.1658T)z$ is applied, where $T$ is the RC3 morphological type as listed in Table 4.1. Since the galaxies are relatively nearby this correction is negligible.

### 4.2.2 Rotation Widths

Rotation widths for the SFI++ sample come from a combination of 21cm line HI global profiles and optical rotation curves (ORCs). Where they are available and of good quality, HI global profile widths are used in preference to ORCs. The HI extent of a normal galaxy is typically about 5 times larger than its optical size, so HI global profiles are capable of tracing the rotation of galaxies to larger radii, and also have the advantage of being independent of the assumed position angle of the galaxy. The data used have been taken on a wide variety of telescopes over more than the last 15 years, but care has been taken that the rotation widths obtained from the different methods are equivalent. Approximately 60% of the galaxies in the SFI++ have their rotational velocities measured from HI global profiles the other 40% use ORCs. Just less than 20% have measurements available from both HI global profiles and ORCs.

#### HI Spectroscopy

The 21cm HI spectroscopy data used is a combination of data published in Haynes *et al.* (1999a) and Springob *et al.* (2005), reprocessed by Springob *et al.* (2005). For the purposes of the Tully-Fisher relation we are interested only in the systematic velocities and velocity widths, as discussed in Section 3.2 of Springob *et*

*al.* (2005). Raw widths are measured using an algorithm that fits low order polynomials to either side of the HI profile and then calculates the width at 50% of $f_p - rms$ (the peak flux minus the $rms$) on either side of the HI profile. These raw widths then have to be corrected for various instrumental effects, $\Delta_s$, the impact of turbulent motions $\Delta_t$, the disk inclination, $i$, and also relativistic effects from the cosmological redshift which broaden the observed profile by a factor $(1 + z)$. The corrected width is then

$$W_{\rm cor,21} = \left[\left(\frac{W_{\rm obs,21} - \Delta_s}{1+z}\right) - \Delta_t\right] \frac{1}{\sin i} \tag{4.7}$$

Where the HI widths use here differ from those in Haynes *et al.* (1999a) and earlier work of this group, is in the magnitude and trend with $S/N$ of the instrumental corrections $\Delta_s$. Springob *et al.* (2005) present the results of simulations to study the impact of spectrometer resolutions, smoothing and $S/N$ on the measured widths, and their prescribed corrections have been applied to **all** the HI widths used here (including the reprocessing of older widths by CS). This width correction $\Delta_s$ is always a small positive number, which in Springob *et al.* (2005) increases linearly with $\log(S/N)$ between $S/N$ = 4-12.5. The previous correction for instrumental broadening decreased as the $S/N$ ratio increased.

The turbulent motions correction is also done in a slightly different way from previous work. Springob *et al.* (2005) discuss the merits of this simple linear subtraction as opposed to a subtraction in quadrature. $\Delta_t = 6.5$ km s$^{-1}$ is assumed.

### Optical Spectroscopy

Optical rotation curves (ORCs) are used to fill in areas of the sky or galaxies not accessible to 21cm HI observations. For example the bulk of spectroscopy in the southern hemisphere have H$\alpha$/[NII] RCs taken at the 2.3m telescope at the Siding Springs Observatory. There are also a significant number of ORCs taken using the long slit spectrograph on the Hale 5m telescope at the Palomar Observatory. As discussed in Catinella (2005) and Catinella, Haynes & Giovanelli (2005) there are several algorithms which can be used to measure rotational velocities from ORCs. All of the widths used in the SFI++ have been derived by fitting a function to the folded ORC. The function used, the "polyex" model (Giovanelli & Haynes 2002; Catinella 2005; Catinella *et al.* 2005) has the form

$$V_{\rm PE}(r) = V_0(1 - e^{-r/r_{\rm PE}})(1 + \alpha r/r_{\rm PE}) \tag{4.8}$$

where $V_0$ gives the amplitude of the ORC, $r_{\rm PE}$ gives the exponential scale of the inner rise of the ORC, and $\alpha$ gives the slope of the outer part of the ORC. This function has no physical meaning, but provides a useful empirical fit to a wide variety of ORC shapes. Widths are derived from this fit by taking its value at the location of the optical radius of the galaxy, $R_{\rm opt}$ which is the radius within which is contained 83% of the optical light. This raw width then has to be corrected for

inclination and cosmological broadening in the same way as the HI widths, so that

$$W_{\rm cor,OPT} = \frac{W_{\rm obsOPT}}{(1+z)\sin i}. \quad (4.9)$$

As shown in Catinella (2005) there are systematic trends of the difference between polyex widths measured from ORCs and HI widths. HI widths are systematically larger than polyex widths probably because HI disks are on average twice as large as H$\alpha$ disks and ORCs in general are still rising beyond the optical radius. Catinella (2005) also shows that there is no systematic trend of this difference with width or inclination, but there is a weak dependence on the extent of the ORC. At the moment we make no correction for these trends but use the polyex widths as measured. Figure 4.1 shows the TF relation for galaxies in the **in+** sample divided into galaxies with HI widths, and galaxies with polyex (or ORC) widths. The data have been corrected for all biases discussed below. As shown in Table 4.5 there is a small difference in the TF fit to the two subsamples, with the slope fit to polyex widths being slightly steeper and the zero point slightly dimmer, however the difference is not significant.

## 4.3 Deriving a Tully-Fisher Template

### 4.3.1 Sample Selection

Clusters are chosen to be included in the TF template if they have more than ∼7 galaxies with TF data in them. Additionally considerations are made about the sky distribution of the clusters, the Virgo cluster is not included in the sample due to the complicated nature of assigning galaxies to its various subgroups, and clusters too close to the Galactic plane are not used, because of the uncertainty in Galactic extinction corrections. The final sample includes 22 of the 24 clusters used by G97b to derive the template for the SFI, and an additional 14 clusters for which we now have sufficient numbers of galaxies with data to include. The assignment of galaxies to these clusters is discussed in Springob (2005). We define two subsamples; 549 of the galaxies are considered *bona fide* cluster members, and are therefore assigned to the **in** sample. An additional 362 galaxies are considered peripheral cluster members, likely associated with the clusters. They are added in what we call the **in+** sample. In deriving absolute magnitudes, we use the cluster redshifts for galaxies in the **in** sample but the galaxy's own redshifts for those in the **in+**. Galaxies in the **in+** sample generally have recessional velocities very similar to that of the cluster.

### 4.3.2 Bias Corrections

#### Morphological Type

Figure 4.2 shows TF diagrams of galaxies in the **in+** sample divided into three groups by their morphological type. These data have been corrected for all biases

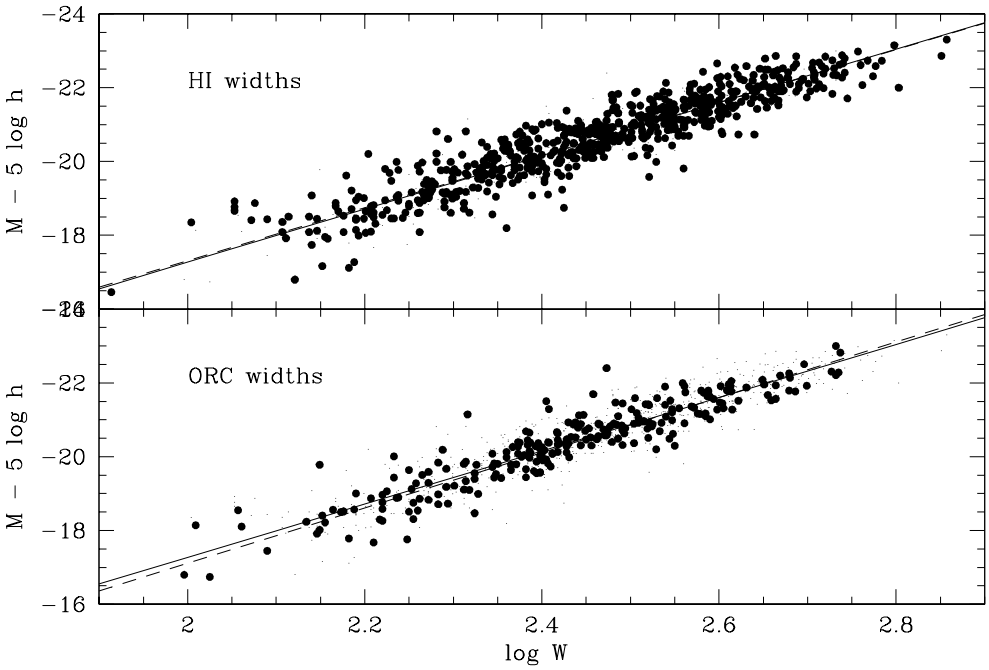



Figure 4.1: TF diagrams for galaxies in the **in+** sample. (a) galaxies with widths derived from HI spectra; (b) galaxies with widths derived from optical rotation curves (ORCs). The alternate subgroup is shown by the small points in each plot. The solid line in all three panels shows the bivariate fit to the **in+** sample, while the dashed lines show the bivariate fits to the sample divided by the source of the widths. The parameters of the fits are given in Table 4.5.

discussed below, except the morphological type bias, and galaxies in each cluster sample have been shifted by an amount $\Delta M$ to account for the cluster's peculiar velocity as discussed in Section 4.3.5. We find that earlier types have a shallower TF slope (see Table 4.5) than later types, although the change is not significant. The plain additive offset used in G97b is therefore adopted.

- Types earlier than Sb: -0.32 mag
- Type Sb: -0.10 mag
- Other types: unchanged.

**Incompleteness Bias**

Even though all the galaxies in a cluster are at roughly the same distance, this does not mean that a cluster sample constitutes a complete, volume limited sample. An implicit or explicit apparent magnitude limit in the sample means that in a given cluster we preferentially observe the brighter galaxies. Since the TF relation has an intrinsic scatter, this effect will tend to shallow the observed slope, by preferentially selecting galaxies which have brighter than expected magnitudes at the small width end of the relation. Similarly, it also brightens the zero point and decreases the observed scatter. In our treatment of this bias we follow G97b. As an example to illustrate the method for calculating the magnitude of this bias, we discuss the case of the Antlia cluster.

The top left panel of Figure 4.3 shows a histogram of the absolute magnitudes of galaxies in the **in+** sample of the Antlia cluster, which has been Hanning smoothed (convolved with a 0.25, 0.5, 0.25 function). The smooth line shows the spiral luminosity function we assume. As shown in Binggeli, Sandage & Tammann (1988), the luminosity function of just spiral galaxies has an almost Gaussian shape. We use a Schechter function with a steep faint end slope, $\alpha = -0.5$, and $M_\star = -21.6$. After smoothing the magnitude histogram is divided by the luminosity function to give the completeness histogram (shown in the bottom left panel of Fig 4.3). This histogram is then fit with a function of the form

$$c(y) = \frac{1}{e^{(y-y_F)/\eta} + 1} \tag{4.10}$$

which provides a smooth step function. The parameter $y_F$ describes the magnitude at which completeness has fallen to 50% while $\eta$ describes the steepness of the fall off. The parameters of this function fit to the completeness of the Antlia cluster (along with all the other clusters) are shown in Table 4.2, the completeness histograms for all the clusters are shown in Figure 4.4.

Once the completeness function has been derived for the cluster, we use it to generate a large number of simulated realizations of the sample. Each realization has the same distribution of widths as the real data and the same statistical completeness. Magnitudes are assigned from the widths according to a universal TF

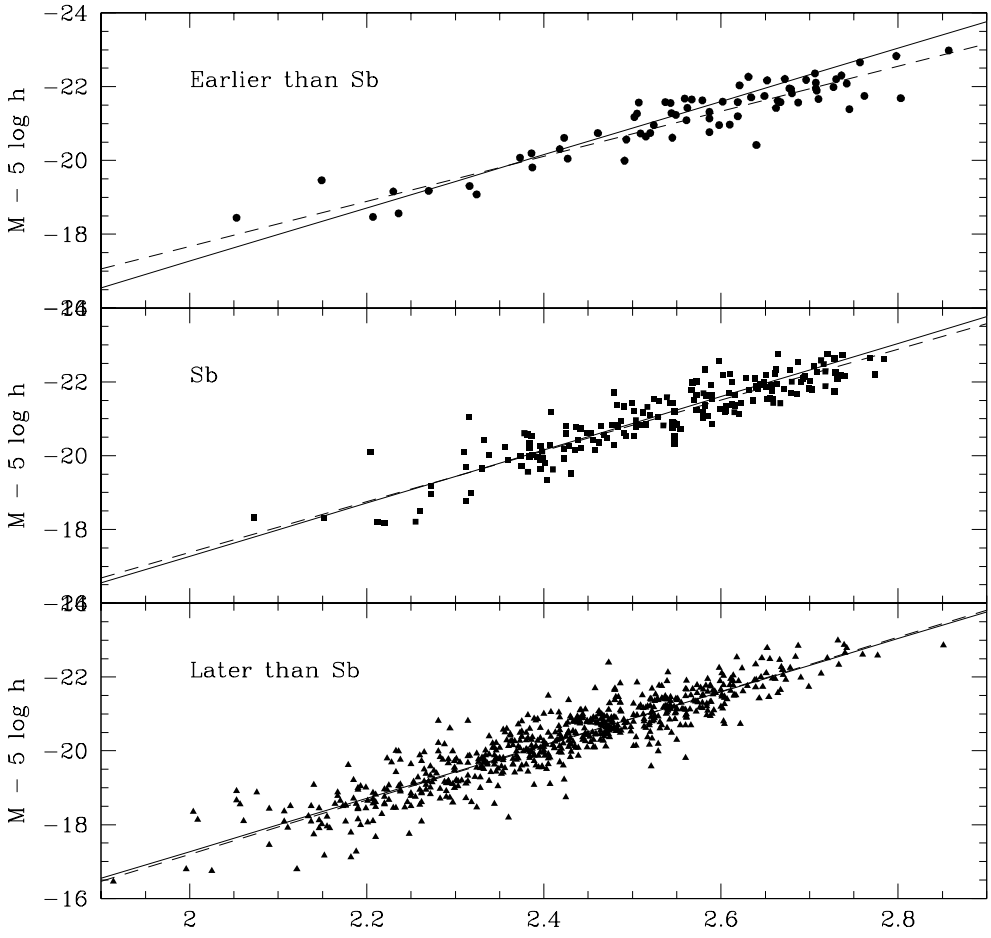



Figure 4.2: TF diagrams for galaxies in the **in+** sample. (a) galaxies with types earlier than Sb; (b) galaxies of type Sb; (c) galaxies with types later than Sb. The solid line in all three panels shows the bivariate fit to the **in+** sample, while the dashed lines show the bivariate fits to the sample divided by morphological type. The slopes vary from -6.11 for types earlier than Sb to -7.36 for types later than Sb. The parameters of the fits are given in Table 4.5.

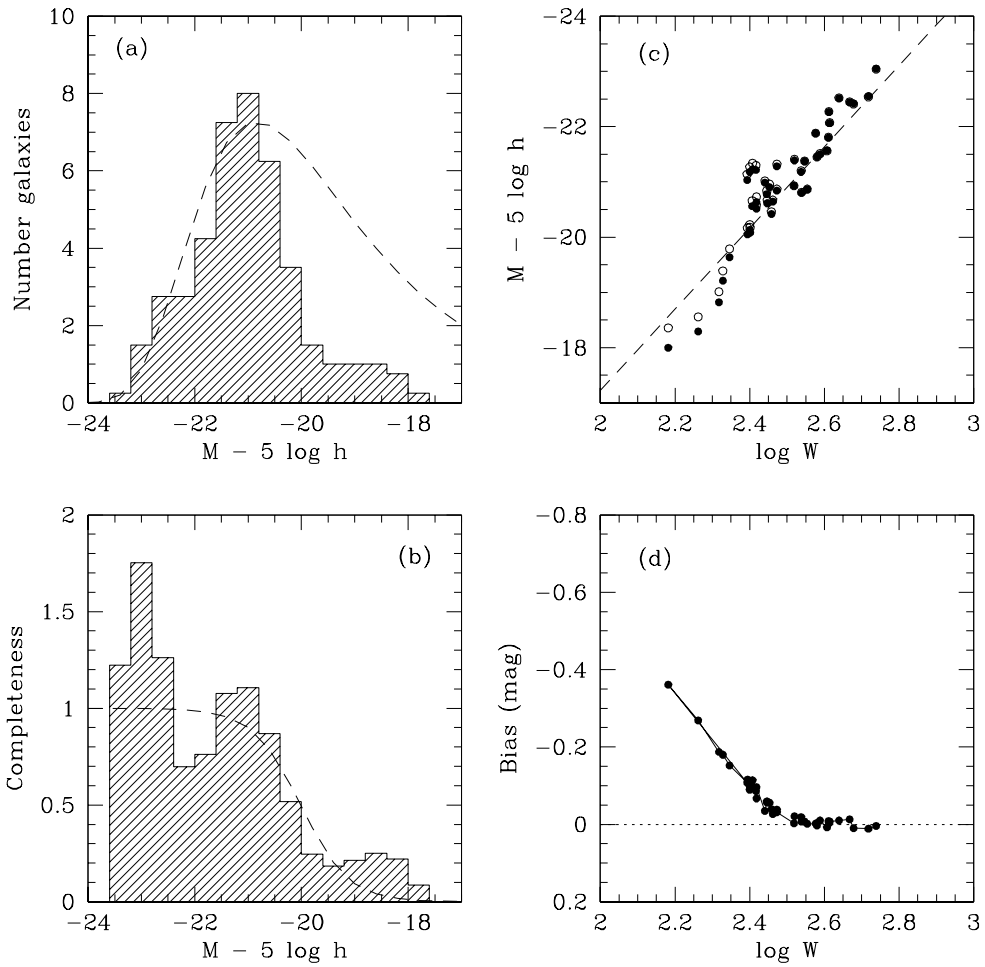



Figure 4.3: Bias correction for the Antlia cluster. Panel (a) shows the distribution of magnitude of galaxies in the **in+** sample of Antlia. The dashed line shows the luminosity function we assume this sample to be taken from. Panel (b) shows the completeness histogram, along with the completeness function fit to it. Panel (c) shows the Tully-Fisher relation for the clusters, corrected only for morphological bias (open circles) and the incompleteness bias corrected data (filled circles). The bivariate fit to the combined **in** sample plotted as the dashed line. Panel (d) shows the adopted incompleteness bias in magnitudes for this cluster.

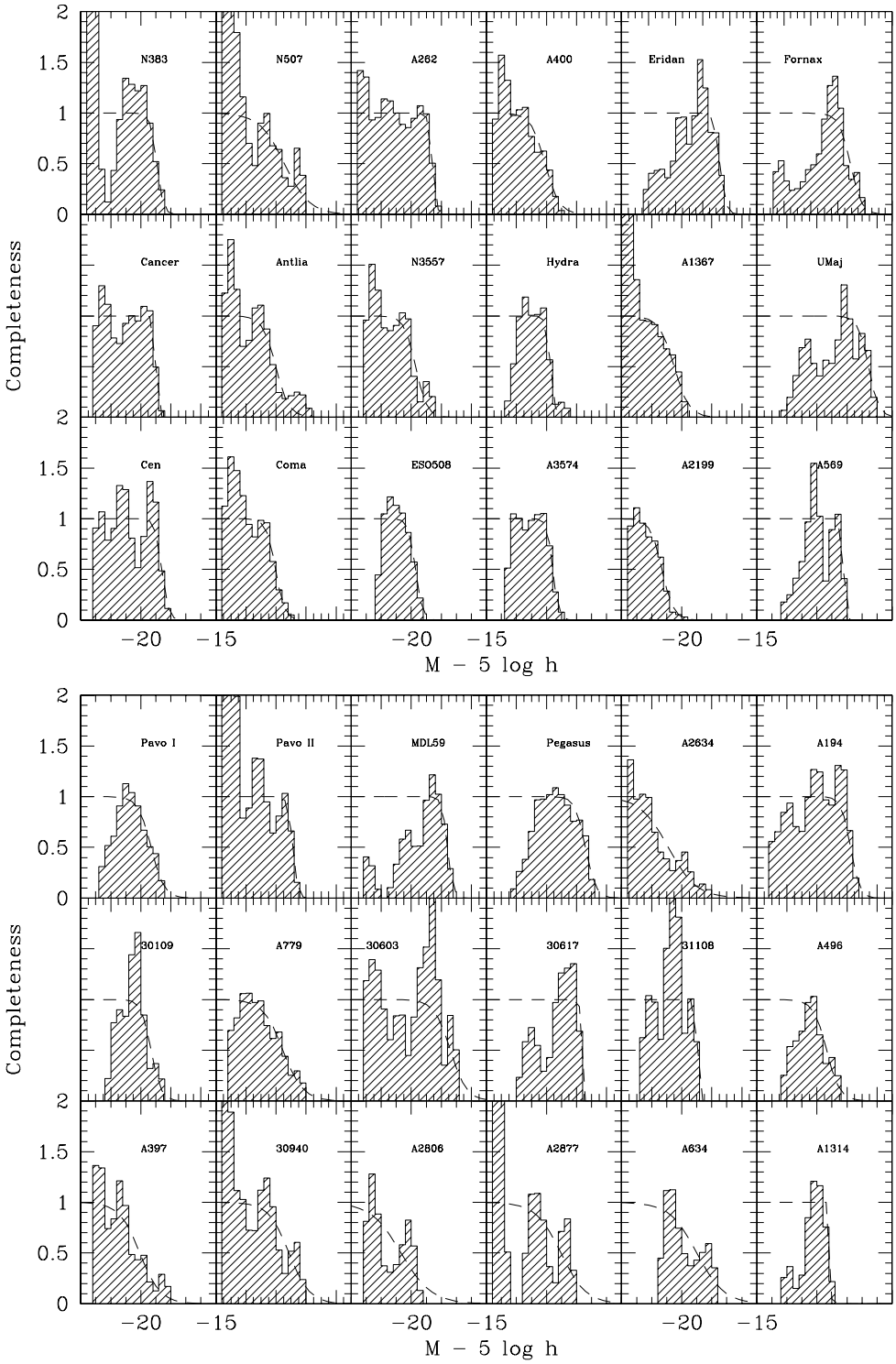



Figure 4.4: Completeness histograms for each of the **in+** cluster sample.

relation (UTF), which we for now assume to be the relation fit to the **in**+ sample of G97b (namely $M = -21.01 - 7.68(\log W - 2.5)$). To this magnitude is added a scatter which is a random Gaussian deviate with width $\epsilon = -0.325(\log W - 2.5) + 0.32$ mag, also as derived in G97b. The simulated magnitude is then passed through a completeness filter, meaning it is only kept if a uniform random number in the range 0-1 comes out smaller than the completeness function $c(y)$ for that magnitude. This procedure results in a sample with the same completeness as Antlia (or the cluster being considered). To derive the incompleteness in magnitudes for the sample we then take the average of the difference of the simulated points from the UTF. For Antlia this result is shown in the bottom right panel of Fig 4.3. The results all clusters in the sample are shown in Fig 4.5.

This correction relies on a priori knowledge of the intrinsic TF relation and scatter, and as such should proceed in an iterative manner. At present only one step of the iteration has been completed, in the future we should come back and redo this correction using the TF relation and scatter found below, especially because we do end up deriving a somewhat shallower slope and larger scatter than is found in G97b.We estimate that the second iteration will change the template TF slope by less than 0.2 $\text{mag}^{-1}$.

Figure 4.6 illustrates the impact that various assumptions make on the derived incompleteness bias for Antlia. As can be seen, by far the largest impact comes from the magnitude of the intrinsic scatter which is assumed. There is relatively little change in the derived incompleteness which the slope or intercept of the assumed UTF is changed. If the faint end slope of the assumed spiral LF is changed there is some change, because the shape of the incompleteness function assumed for the cluster changes. This effect is further illustrated in Figure 4.7. A shallower faint end slope (larger $|\alpha|$) results in a steeper fall-off in the incompleteness function and therefore a larger correction for the bias. If the LF slope we use is too steep we are therefore underestimating the bias correction, and not correcting for the full shallowing of the TF slope by incompleteness bias.

### Edge of Catalog Bias

Following G97b we make no correction for the edge of catalog bias, which they find to be negligible in the SCI sample on which this sample is based.

### Cluster size bias

In deriving the template we are explicitly assuming that all galaxies in the **in** sample are at the same distance. This assumption varies in its accuracy based on the actual line of sight depth of the cluster relative to the distance to the cluster. The finite size of the cluster introduces two separate biases into the derived TF relation, which we consider separately:

**1. The mean distance to a cluster.** In deriving the TF relation from all galaxies in a cluster assuming they are all at the same distance, we are in effect

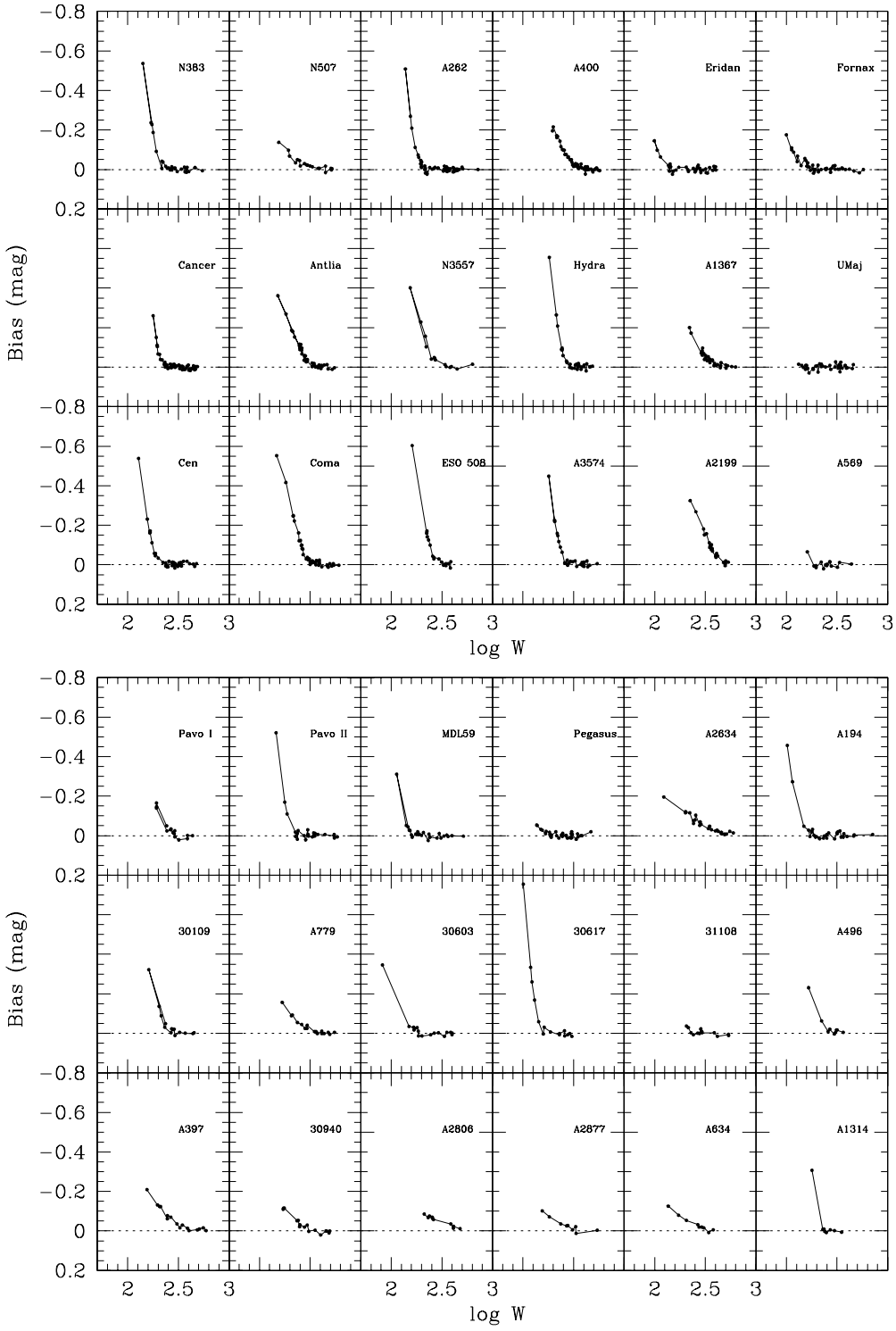



Figure 4.5: Incompleteness correction for each cluster.

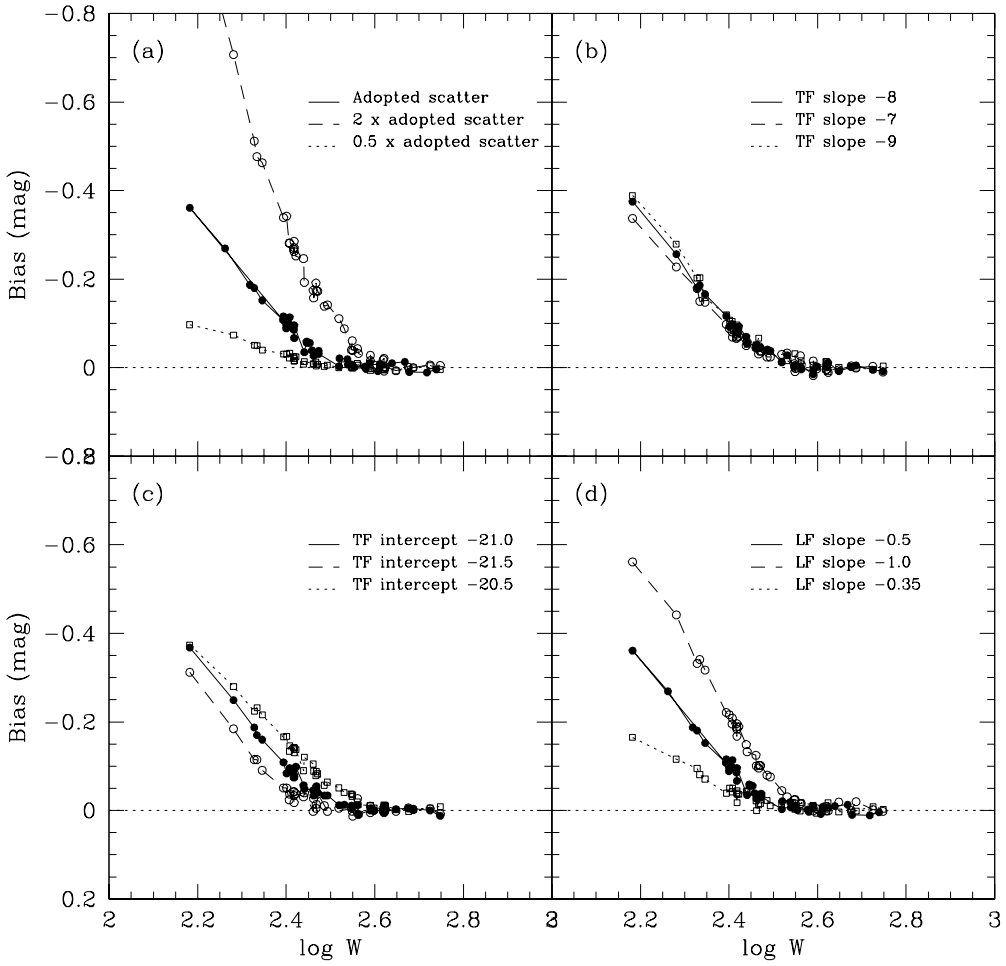



Figure 4.6: Dependence of the incompleteness bias correction (in magnitudes) on (a) the adopted scatter, (b) the assumed UTF slope and (c) intercept, and (d) the faint end slope of the adopted luminosity function.

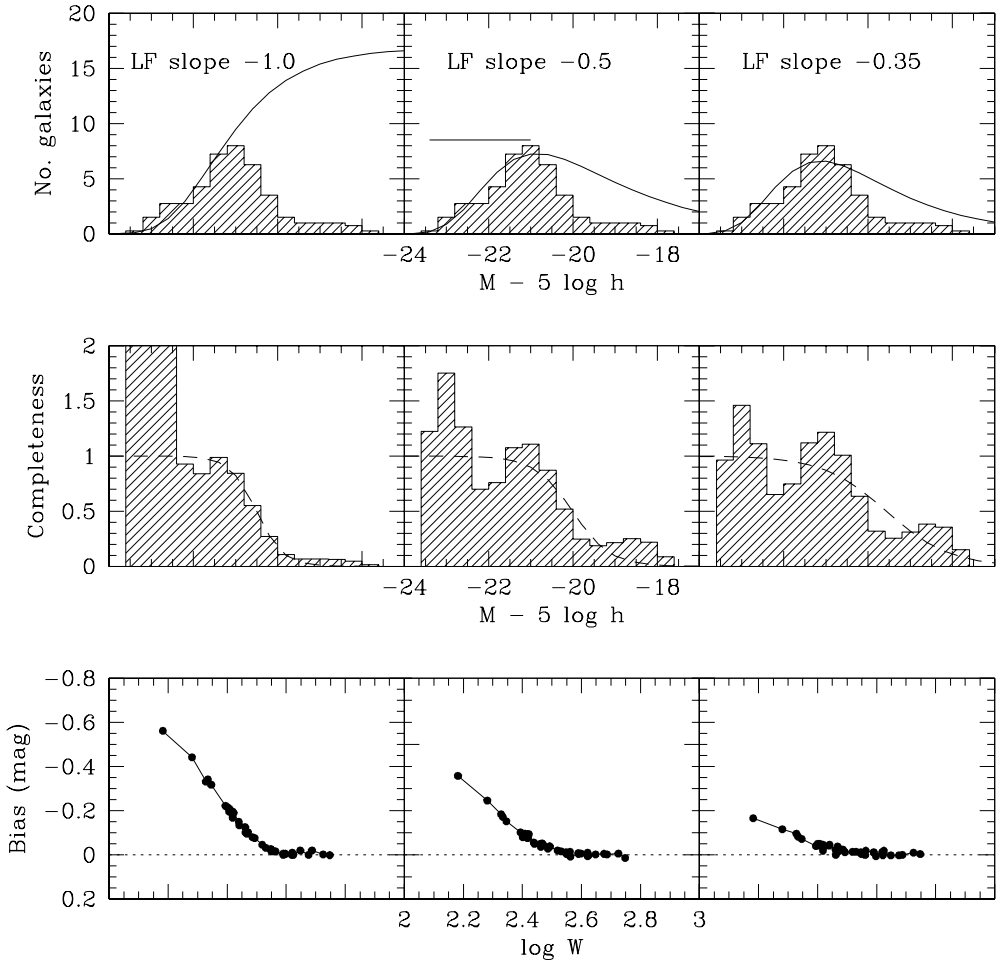



Figure 4.7: The effect that changing the slope of the faint end of the luminosity function has on the derivation of the incompleteness bias for Antlia. A steeper slope (less faint spirals) leads to a more gradual fall of in incompleteness, which gives a smaller correction for the incompleteness bias.

taking the mean of the log of the distance to the cluster (because of working with distance modulus rather than distance) when we fit for the zeropoint of the cluster TF relation. The log of the average is not the same as the average of the log, so this assumption introduces a small bias into the zeropoint. Consider a galaxy in the cluster of apparent magnitude $m$. We should derive our estimate of its absolute magnitude using the mean distance to the cluster, $\overline{d}$ (under the assumption that all galaxies are at the mean distance of the cluster), so that

$$M_{\rm true} = m - 5\log\overline{d} + 5, \tag{4.11}$$

however what is actually done implicitly in deriving the TF relation is to use

$$M_{\rm calc} = m - 5 < \log d > + 5, \tag{4.12}$$

where $< \log d >$ is the mean value of the logs of the distances to the galaxies in the cluster. The difference between these two values is the bias considered here. Let's assume that the distance to a given galaxy can be expressed as $d = \overline{d} + \epsilon_d$ where $\epsilon_d$ is a small correction due to the finite size of the cluster. We will assume that it is distributed as a Gaussian with $\sigma_d$. Then

$$< \log d >= \frac{1}{N}\sum\left(\log\overline{d} + \frac{\epsilon_d}{d} - \frac{\epsilon_d^2}{2d^2}\right) \tag{4.13}$$

Since $\epsilon_d$ is normally distributed its mean is zero, and its variance is $\sigma_d^2$, so

$$\beta_{\rm size} = M_{\rm true} - M_{\rm calc} = -\frac{5\sigma_d^2}{2d^2}. \tag{4.14}$$

Table 4.2 lists the size of this bias for the clusters in our sample, using the assumption that they all have a line of sight extent of 1 Abell radius ($R_A$, 1.5 Mpc/h or 150 km s$^{-1}$). This is a reasonable approximation for most of the in sample. For the **in+** sample, we use twice this extent, increasing the small bias by a factor of four.

**2. Cluster size – sample incompleteness.** If galaxies are close in magnitude to the completeness limit of the sample they will preferentially be seen only in the foreground parts of the cluster (*i.e.* the closest parts) and therefore their magnitudes will be biased towards brighter values. This bias is illustrated in Fig 14. of G97b, and can be estimated assuming a Gaussian extent for the cluster, and using the completeness function derive in Section 4.3.2. A galaxy with an intrinsic magnitude $M_0$, will have an observed magnitude $M = M_0 + \Delta M$, measured with a probability which we assume to be distributed as a Gaussian about $M_0$ with width $\sigma_M = 5\log(1 + \sigma_d/d)$. This assumes that a Gaussian in distance corresponds to a Gaussian in magnitude, which it does not as discussed above, but the error is second order for this bias so will be ignored. The expected value of the observed absolute magnitude for this galaxy will then be

$$\overline{M} = \frac{\int Mc(M)e^{(M-M_0)/2\sigma_M^2}dM}{\int c(M)e^{(M-M_0)/2\sigma_M^2}dM}, \tag{4.15}$$

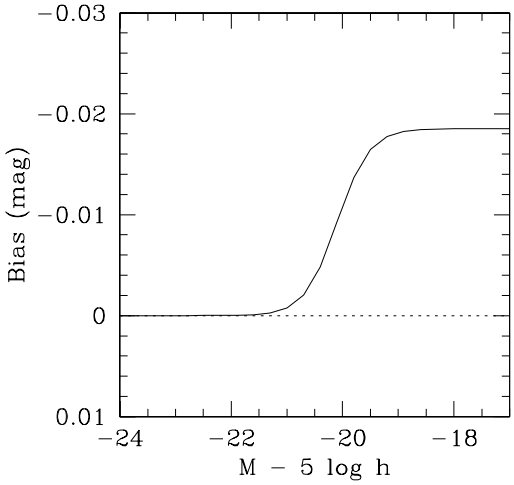



Figure 4.8: Cluster size - sample incompleteness for the Antlia cluster. This bias is due to preferentially seeing fainter galaxies on the near side of the cluster which means that their magnitudes are most likely to be overestimated if they are assumed to be at the cluster mean distance.

where c(M) is the completeness function in Eqn 4.10. The bias is simply

$$\beta_{\rm inc} = \overline{M} - M_0. \tag{4.16}$$

This correction is very small for most of the galaxies in our samples. The correction for galaxies in the Antlia cluster is shown in Fig. 4.8.

#### Homogeneous Malmquist Bias

Following G97b we argue that this correction is small for the clusters in our sample and therefore we neglect it.

### 4.3.3 Fitting the TF Relation

We fit "direct", "inverse", "bivariate" forms of the linear TF relation, as well as a quadratic function. The difference between the three linear fits is in which variable is considered to be independent and the treatment of the errors.

For the direct fit we consider

$$M(x) = a_{\rm dir} + b_{\rm dir} x, \tag{4.17}$$

the coefficients of which are found by minimizing

$$\chi^2 = \sum \frac{(M_i - M(x_i|a_{\rm dir}, b_{\rm dir}))^2}{(\sigma^2_{M,i} + \epsilon^2_{\rm int})} \tag{4.18}$$

Table 4.2: Incompleteness Function Co-efficients (see Equation 4.10) and cluster size bias

| Cluster Name | $y_F$ | $\eta$ | $\sigma_d/d$ | **in** $\beta_{\rm size}$ | **in+** $\beta_{\rm size}$ |
|---|---|---|---|---|---|
| N383 | -18.94 | 0.21 | 0.03 | -0.002 | -0.010 |
| N507 | -19.43 | 0.83 | 0.03 | -0.002 | -0.010 |
| A262 | -18.59 | 0.13 | 0.03 | -0.003 | -0.010 |
| A400 | -20.08 | 0.47 | 0.02 | -0.001 | -0.005 |
| Eridanus | -16.73 | 0.22 | 0.10 | -0.024 | -0.095 |
| Fornax | -17.08 | 0.42 | 0.11 | -0.032 | -0.129 |
| Cancer | -19.00 | 0.08 | 0.03 | -0.002 | -0.009 |
| Antlia | -20.01 | 0.45 | 0.05 | -0.006 | -0.023 |
| NGC 3557 | -19.71 | 0.37 | 0.05 | -0.005 | -0.020 |
| Hydra | -19.74 | 0.15 | 0.04 | -0.003 | -0.014 |
| A1367 | -20.51 | 0.51 | 0.02 | -0.001 | -0.005 |
| Ursa Major | -16.57 | 0.35 | 0.14 | -0.046 | -0.186 |
| Cen 30 | -18.61 | 0.21 | 0.05 | -0.005 | -0.020 |
| Coma | -20.03 | 0.31 | 0.02 | -0.001 | -0.004 |
| ESO 508 | -19.73 | 0.22 | 0.05 | -0.006 | -0.022 |
| A3574 | -19.58 | 0.19 | 0.03 | -0.002 | -0.010 |
| A2199/7 | -21.32 | 0.38 | 0.02 | -0.001 | -0.003 |
| Pavo 1 | -19.31 | 0.43 | 0.04 | -0.003 | -0.014 |
| Pavo 2 | -18.88 | 0.16 | 0.03 | -0.003 | -0.011 |
| MDL59 | -17.59 | 0.18 | 0.07 | -0.010 | -0.042 |
| Pegasus | -17.40 | 0.34 | 0.04 | -0.005 | -0.018 |
| A2634 | -20.95 | 1.05 | 0.02 | -0.001 | -0.003 |
| A194 | -17.76 | 0.30 | 0.03 | -0.002 | -0.009 |
| NOG 30109 | -19.32 | 0.33 | 0.03 | -0.003 | -0.010 |
| A779 | -19.53 | 0.69 | 0.02 | -0.001 | -0.004 |
| NOG 30603 | -17.39 | 0.54 | 0.07 | -0.013 | -0.054 |
| NOG 30617 | -17.72 | 0.03 | 0.06 | -0.009 | -0.037 |
| NOG 31108 | -18.97 | 0.06 | 0.03 | -0.003 | -0.010 |
| A496 | -19.36 | 0.44 | 0.02 | -0.001 | - |
| A397 | -20.07 | 0.69 | 0.02 | -0.001 | -0.002 |
| 30940 | -19.13 | 0.68 | 0.05 | -0.005 | -0.023 |
| A2806 | -20.677 | 1.009 | 0.02 | -0.001 | -0.004 |
| A2877 | -19.039 | 0.829 | 0.02 | -0.001 | -0.005 |
| A634 | -18.990 | 0.903 | 0.02 | -0.001 | -0.004 |
| A1314 | -19.102 | 0.034 | 0.02 | -0.001 | -0.002 |
| A569 | -18.21 | 0.04 | 0.02 | -0.001 | -0.006 |

where the error accounts for both measurement errors in the derived absolute magnitudes and the intrinsic error in the TF relation, again assumed here to be the value arrived at in G97b of $\epsilon_{\rm int} = 0.32 - 0.325x$ (recall $x = \log W - 2.5$).

The inverse fit assumes

$$x(M) = -a_{\rm inv}/b_{\rm inv} + (1/b_{\rm inv})M, \tag{4.19}$$

and the error used in the derivation of $\chi^2$ is $\epsilon_i^2 = \sigma_{x,i}^2 + (\epsilon_{\rm int}/b)^2$. The value of $b$ in the denominator of $\chi^2$ is here assumed to be constant at the UTF value.

The bivariate fit considers errors in both directions (ie. $\epsilon_i^2 = \sigma_{M,i}^2 + b_{\rm biv}^2\sigma_{x,i}^2 + \epsilon_{\rm int}^2$), and follows *Numerical Recipes* (Press *et al.* 2001) to minimize $\chi^2$ when the value of $b$ in the denominator can vary.

These three sets of linear co-efficients are calculated individually for each cluster, and also for the combined "global" sample. The average rms scatter is calculated using

$$\sigma^2 = \chi^2_{\rm min} / \sum(1/\epsilon_i^2) \tag{4.20}$$

and the absolute deviation, being the weighted mean of $|M_i - M(x_i)|$ is also calculated.

To the combined sample of all clusters, we also fit a quadratic TF relation,

$$M(x) = q_0 + q_1 x + q_2 x^2, \tag{4.21}$$

by minimizing $\chi^2$ as given in Eqn. 4.18.

### 4.3.4 Individual Cluster TF Relations

Figure 4.9 shows individual TF relations for all 36 clusters. Galaxies in the **in** and **in+** samples are plotted as solid and open circles respectively. The same line of slope -7.36 (from the bivariate fit to the combined **in** sample) is plotted over each cluster plot. The parameters of the fits to individual clusters samples are given in Table 4.3.

### 4.3.5 A TF Template Relation

Here we combine the data from all 36 clusters into a global TF template. This is done by shifting the points for each individual cluster by an amount $\Delta M_i$ taking into account the motion of each cluster in the CMB frame (*i.e.* its peculiar velocity). These offsets are found by assuming that all points fall on a linear TF relation with a global slope, and minimizing $\chi^2$ with respect the offsets. The global slope is assumed to be the bivariate fit to the combined sample and is found by iterating until the fit converges. Additionally an inertial reference frame is defined by requiring the that the net motion of a subset of the most distant clusters is zero, *i.e.*,

$$\sum_k N_k \Delta M_k / \sum_k N_k = 0 \tag{4.22}$$

Table 4.3: Tully-Fisher relation fits for individual cluster samples

| Sample | $N$ | $a_{dir}$ | $b_{dir}$ | $a_{inv}$ | $b_{inv}$ | $a_{bi}$ | $b_{bi}$ | $\epsilon_a$ | $\epsilon_b$ | $\sigma_{bi}$ | $\sigma_{abs}$ |
|---|---|---|---|---|---|---|---|---|---|---|---|
| N383 **in** | 11 | -20.818 | -6.585 | -20.771 | -7.361 | -20.810 | -6.960 | 0.117 | 0.893 | 0.295 | 0.274 |
| N383 **in+** | 29 | -20.797 | -6.058 | -20.828 | -8.595 | -20.808 | -6.929 | 0.069 | 0.543 | 0.537 | 0.422 |
| N507 **in** | 14 | -20.996 | -7.626 | -21.103 | -8.430 | -20.999 | -7.666 | 0.094 | 0.567 | 0.445 | 0.359 |
| N507 **in+** | 19 | -20.924 | -7.548 | -21.079 | -8.424 | -20.945 | -7.584 | 0.082 | 0.537 | 0.405 | 0.326 |
| A262 **in** | 27 | -20.754 | -6.274 | -20.622 | -7.182 | -20.700 | -6.560 | 0.073 | 0.423 | 0.457 | 0.362 |
| A262 **in+** | 51 | -20.790 | -6.459 | -20.744 | -8.143 | -20.755 | -6.767 | 0.053 | 0.336 | 0.518 | 0.400 |
| A400 **in** | 16 | -20.905 | -7.086 | -20.941 | -7.976 | -20.878 | -7.227 | 0.099 | 0.719 | 0.267 | 0.231 |
| A400 **in+** | 51 | -20.952 | -6.971 | -20.913 | -7.627 | -20.937 | -6.988 | 0.055 | 0.418 | 0.308 | 0.251 |
| Eridanus **in** | 22 | -20.586 | -8.346 | -19.851 | -5.483 | -20.448 | -8.047 | 0.117 | 0.613 | 0.552 | 0.431 |
| Eridanus **in+** | 36 | -20.445 | -7.606 | -20.109 | -7.441 | -20.377 | -7.582 | 0.088 | 0.443 | 0.512 | 0.408 |
| Fornax **in** | 23 | -20.619 | -7.480 | -20.707 | -8.622 | -20.641 | -8.122 | 0.103 | 0.483 | 0.498 | 0.368 |
| Fornax **in+** | 41 | -20.495 | -7.823 | -20.605 | -8.709 | -20.536 | -8.460 | 0.082 | 0.410 | 0.512 | 0.363 |
| Cancer **in** | 17 | -20.955 | -8.576 | -20.996 | -8.535 | -21.027 | -9.170 | 0.103 | 0.800 | 0.462 | 0.352 |
| Cancer **in+** | 50 | -20.839 | -7.345 | -20.804 | -9.189 | -20.828 | -7.597 | 0.053 | 0.430 | 0.493 | 0.379 |
| Antlia **in** | 17 | -21.104 | -8.011 | -21.182 | -8.486 | -21.061 | -8.253 | 0.109 | 1.000 | 0.300 | 0.242 |
| Antlia **in+** | 41 | -21.024 | -8.043 | -20.880 | -10.398 | -20.985 | -8.150 | 0.064 | 0.502 | 0.392 | 0.298 |
| N3557 **in** | 7 | -21.123 | -6.434 | -21.088 | -9.515 | -21.122 | -6.581 | 0.145 | 1.755 | 0.295 | 0.247 |
| N3557 **in+** | 14 | -21.043 | -5.226 | -21.043 | -5.460 | -21.052 | -5.240 | 0.101 | 0.610 | 0.433 | 0.379 |
| Hydra **in** | 21 | -20.703 | -6.171 | -20.777 | -10.101 | -20.724 | -6.667 | 0.084 | 0.843 | 0.333 | 0.296 |
| Hydra **in+** | 31 | -20.781 | -6.091 | -20.764 | -9.537 | -20.799 | -6.591 | 0.067 | 0.696 | 0.334 | 0.283 |
| A1367 **in** | 33 | -21.023 | -6.466 | -20.555 | -10.951 | -20.876 | -7.565 | 0.090 | 0.681 | 0.484 | 0.362 |
| A1367 **in+** | 34 | -21.010 | -6.499 | -20.600 | -10.701 | -20.866 | -7.590 | 0.088 | 0.678 | 0.478 | 0.354 |
| Ursa Major **in** | 31 | -20.258 | -8.770 | -20.464 | -8.779 | -20.278 | -8.800 | 0.073 | 0.464 | 0.388 | 0.308 |
| Ursa Major **in+** | 37 | -20.163 | -8.561 | -20.379 | -8.691 | -20.185 | -8.692 | 0.070 | 0.426 | 0.461 | 0.363 |

Table 4.3 (Continued)

| Sample | $N$ | $a_{dir}$ | $b_{dir}$ | $a_{inv}$ | $b_{inv}$ | $a_{bi}$ | $b_{bi}$ | $\epsilon_a$ | $\epsilon_b$ | $\sigma_{bi}$ | $\sigma_{abs}$ |
|---|---|---|---|---|---|---|---|---|---|---|---|
| Cen **in** | 25 | -21.086 | -7.445 | -21.090 | -11.168 | -21.104 | -7.924 | 0.094 | 0.675 | 0.424 | 0.353 |
| Cen **in+** | 38 | -21.144 | -7.611 | -20.923 | -9.297 | -21.153 | -7.950 | 0.068 | 0.518 | 0.405 | 0.332 |
| Coma **in** | 36 | -21.138 | -6.326 | -20.928 | -7.188 | -21.133 | -6.391 | 0.067 | 0.474 | 0.301 | 0.224 |
| Coma **in+** | 45 | -21.114 | -6.432 | -20.973 | -7.274 | -21.103 | -6.508 | 0.059 | 0.431 | 0.326 | 0.243 |
| ESO508 **in** | 10 | -21.133 | -6.905 | -21.362 | -7.369 | -21.146 | -6.801 | 0.145 | 1.277 | 0.265 | 0.235 |
| ESO508 **in+** | 18 | -21.051 | -6.911 | -21.134 | -8.015 | -21.067 | -7.098 | 0.099 | 1.055 | 0.281 | 0.228 |
| A3574 **in** | 13 | -20.958 | -6.025 | -19.984 | -13.795 | -20.949 | -6.090 | 0.108 | 0.812 | 0.312 | 0.214 |
| A3574 **in+** | 29 | -20.941 | -6.611 | -20.748 | -8.251 | -20.940 | -6.605 | 0.071 | 0.568 | 0.301 | 0.221 |
| A2199 **in** | 8 | -20.987 | -6.616 | -20.917 | -7.091 | -20.951 | -6.855 | 0.227 | 1.273 | 0.186 | 0.149 |
| A2199/7 **in+** | 22 | -21.211 | -5.298 | -20.949 | -7.737 | -21.054 | -6.559 | 0.130 | 0.980 | 0.340 | 0.261 |
| Pavo I **in** | 5 | -21.067 | -5.373 | -21.978 | -21.184 | -21.086 | -5.906 | 0.334 | 4.957 | 0.230 | 0.171 |
| Pavo I **in+** | 16 | -21.004 | -7.242 | -20.571 | -7.312 | -20.990 | -7.185 | 0.103 | 0.970 | 0.397 | 0.343 |
| Pavo II **in** | 8 | -21.101 | -7.521 | -21.233 | -6.967 | -21.100 | -7.538 | 0.142 | 0.825 | 0.244 | 0.176 |
| Pavo II **in+** | 25 | -20.965 | -6.690 | -20.934 | -6.254 | -20.965 | -6.737 | 0.077 | 0.465 | 0.361 | 0.293 |
| MDL59 **in** | 12 | -20.448 | -6.876 | -20.425 | -7.367 | -20.453 | -6.955 | 0.151 | 0.835 | 0.374 | 0.301 |
| MDL59 **in+** | 25 | -20.514 | -6.660 | -20.596 | -8.072 | -20.518 | -6.970 | 0.097 | 0.493 | 0.461 | 0.386 |
| Pegasus **in** | 20 | -20.689 | -6.956 | -21.124 | -8.998 | -20.710 | -7.110 | 0.119 | 0.682 | 0.360 | 0.285 |
| Pegasus **in+** | 33 | -20.554 | -6.851 | -21.293 | -12.219 | -20.587 | -7.149 | 0.088 | 0.553 | 0.498 | 0.376 |
| A2634 **in** | 20 | -21.039 | -6.760 | -20.937 | -7.118 | -20.976 | -7.040 | 0.086 | 0.537 | 0.338 | 0.257 |
| A2634 **in+** | 24 | -20.991 | -6.507 | -20.869 | -7.194 | -20.931 | -6.857 | 0.080 | 0.479 | 0.326 | 0.252 |
| A194 **in** | 24 | -20.888 | -6.819 | -21.091 | -10.609 | -20.846 | -7.484 | 0.092 | 0.642 | 0.568 | 0.460 |
| A194 **in+** | 32 | -20.775 | -6.701 | -20.931 | -8.765 | -20.722 | -7.005 | 0.074 | 0.403 | 0.554 | 0.437 |
| 30109 **in** | 5 | -21.009 | -4.711 | -20.612 | -6.743 | -20.960 | -5.130 | 0.181 | 1.853 | 0.374 | 0.349 |
| 30109 **in+** | 14 | -20.813 | -5.630 | -20.738 | -5.450 | -20.799 | -5.720 | 0.101 | 0.773 | 0.360 | 0.316 |

Table 4.3 (Continued)

| Sample | $N$ | $a_{dir}$ | $b_{dir}$ | $a_{inv}$ | $b_{inv}$ | $a_{bi}$ | $b_{bi}$ | $\epsilon_a$ | $\epsilon_b$ | $\sigma_{bi}$ | $\sigma_{abs}$ |
|---|---|---|---|---|---|---|---|---|---|---|---|
| A779 in | 14 | -20.664 | -7.798 | -20.594 | -8.085 | -20.647 | -7.801 | 0.107 | 0.830 | 0.280 | 0.199 |
| A779 **in+** | 18 | -20.656 | -7.714 | -20.557 | -8.330 | -20.637 | -7.790 | 0.097 | 0.699 | 0.268 | 0.187 |
| 30603 **in** | 7 | -21.145 | -8.165 | -21.220 | -8.526 | -21.190 | -8.170 | 0.239 | 0.982 | 0.317 | 0.235 |
| 30603 **in+** | 17 | -21.118 | -8.076 | -21.151 | -8.199 | -21.175 | -8.384 | 0.116 | 0.622 | 0.482 | 0.374 |
| 30617 **in** | 6 | -21.311 | -6.914 | -21.695 | -9.267 | -21.371 | -7.102 | 0.316 | 1.217 | 0.423 | 0.347 |
| 30617 **in+** | 15 | -21.154 | -6.819 | -21.688 | -9.380 | -21.408 | -7.789 | 0.202 | 0.860 | 0.676 | 0.489 |
| 31108 **in** | 8 | -20.678 | -4.504 | -20.618 | -5.674 | -20.675 | -4.626 | 0.132 | 1.222 | 0.311 | 0.260 |
| 31108 **in+** | 13 | -20.772 | -4.984 | -20.644 | -6.757 | -20.762 | -5.085 | 0.098 | 0.689 | 0.316 | 0.266 |
| A496 **in** | 9 | -21.073 | -9.578 | -21.016 | -11.960 | -21.063 | -10.372 | 0.154 | 2.165 | 0.247 | 0.204 |
| A397 **in** | 14 | -21.097 | -5.115 | -21.056 | -5.608 | -21.048 | -5.371 | 0.109 | 0.586 | 0.482 | 0.419 |
| A397 **in+** | 16 | -21.027 | -5.279 | -20.775 | -7.098 | -20.978 | -5.646 | 0.104 | 0.589 | 0.494 | 0.434 |
| 30940 **in** | 9 | -21.103 | -6.660 | -21.274 | -8.496 | -21.114 | -6.900 | 0.123 | 0.878 | 0.423 | 0.365 |
| 30940 **in+** | 16 | -20.937 | -6.843 | -21.120 | -8.953 | -20.944 | -7.053 | 0.091 | 0.632 | 0.388 | 0.315 |
| A2806 **in** | 10 | -21.155 | -7.025 | -20.997 | -8.334 | -21.101 | -7.420 | 0.134 | 1.106 | 0.268 | 0.236 |
| A2806 **in+** | 10 | -21.152 | -7.024 | -20.993 | -8.338 | -21.098 | -7.420 | 0.134 | 1.106 | 0.269 | 0.237 |
| A2877 **in** | 9 | -20.929 | -8.102 | -20.941 | -8.596 | -20.920 | -8.325 | 0.150 | 1.047 | 0.315 | 0.258 |
| A2877 **in+** | 9 | -20.925 | -8.099 | -20.937 | -8.594 | -20.915 | -8.322 | 0.150 | 1.047 | 0.315 | 0.258 |
| A634 **in** | 9 | -20.772 | -6.491 | -20.973 | -7.557 | -20.811 | -6.369 | 0.158 | 1.279 | 0.289 | 0.258 |
| A634 **in+** | 9 | -20.769 | -6.491 | -20.969 | -7.565 | -20.807 | -6.370 | 0.158 | 1.279 | 0.289 | 0.259 |
| A1314 **in** | 8 | -21.099 | -8.177 | -21.072 | -7.798 | -21.131 | -8.521 | 0.236 | 2.013 | 0.244 | 0.196 |
| A1314 **in+** | 8 | -21.098 | -8.177 | -21.070 | -7.800 | -21.129 | -8.522 | 0.236 | 2.013 | 0.245 | 0.196 |
| A569 **in** | 13 | -20.933 | -7.907 | -20.916 | -7.897 | -20.929 | -7.973 | 0.162 | 0.997 | 0.275 | 0.200 |
| A569 **in+** | 16 | -20.904 | -7.700 | -20.789 | -8.101 | -20.890 | -7.780 | 0.132 | 0.923 | 0.312 | 0.229 |

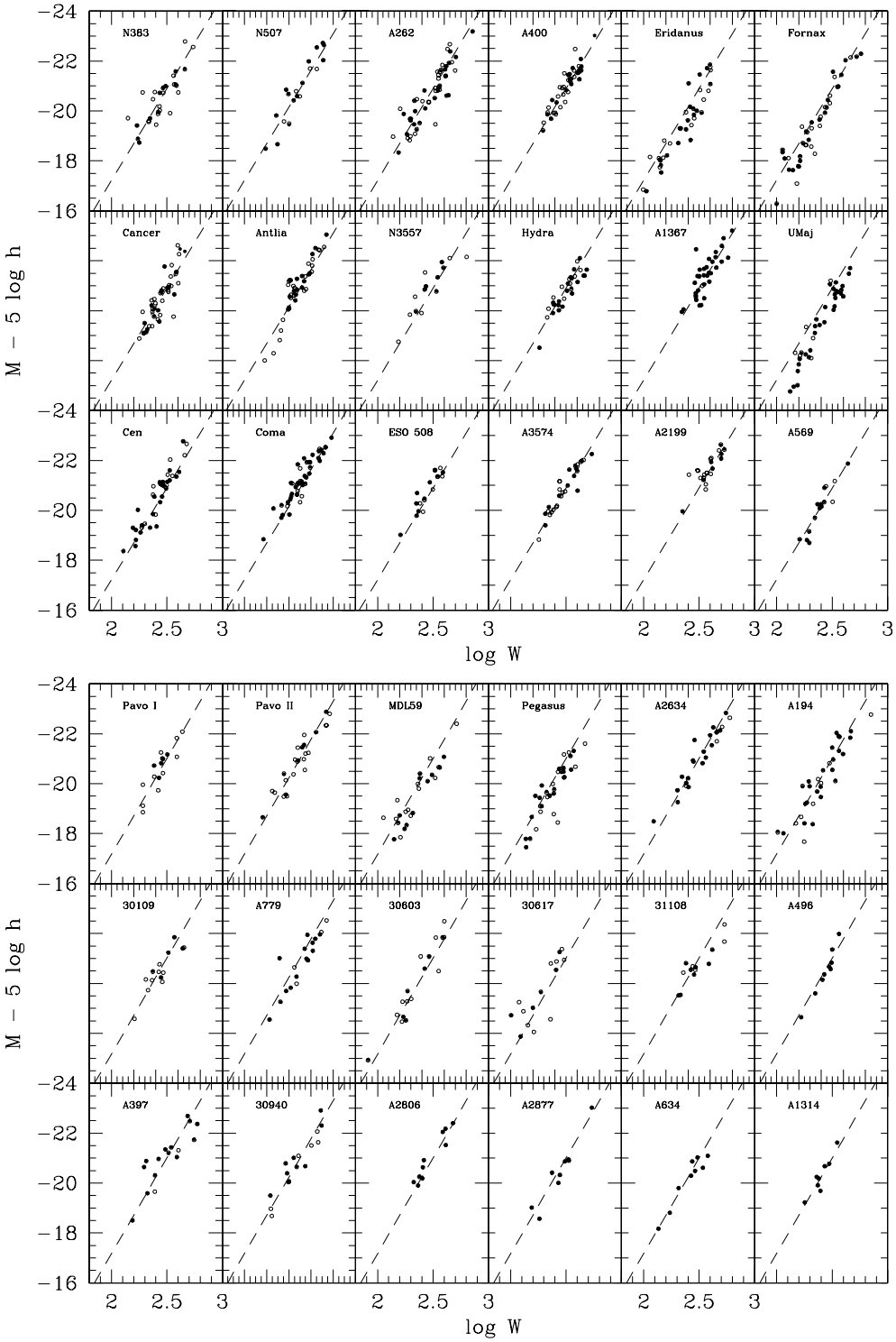



Figure 4.9: TF relations for individual clusters. Overlaid is the bivariate fit to the **in** sample from Section 4.3.5. Solid circles are **in** sample galaxies, open circles **in+**. These data have been corrected for the incompleteness bias and other biases discussed in Section 4.3.2.

(where this sum is weighted by the number of galaxies in the cluster).

The offsets for the **in** and **in+** samples are shown in Table 4.4. In that table, clusters used to define the velocity frame are marked with a * next to their CMB velocity. $\Delta M_0$ refers to offsets when no incompleteness bias corrections have applied. $\Delta M_1$ refers to the offsets when the incompleteness bias correction as discussed in Section 4.3.2 is applied. The error on these offsets is taken to be the scatter in the individual cluster TF relation divided by the square root of the number of galaxies in the cluster. Figure 4.10 shows the corresponding cluster peculiar velocity dispersion for the **in+** sample. The left panel shows all the clusters, the right panel only those clusters used to define the rest frame. The peculiar velocities of the clusters are represented as Gaussians of equal area $\propto 1/\sigma_{v,i} \exp[-(v_{\rm pec} - v_{{\rm pec},i0})^2/2\sigma_{v,i}^2]$, and their sum is shown as the heavy solid line. A Gaussian fitted with zero mean to the entire **in+** sample gives $\sigma = 404 \pm 25$ km s$^{-1}$ (for the **in** sample we get $\sigma = 463 \pm 35$ km s$^{-1}$). A simplistic correction for error broadening in the **in+** sample, using the mean peculiar velocity error gives $\sigma = 344 \pm 25$ km s$^{-1}$ ($396 \pm 35$ km s$^{-1}$ for **in**). We find a slightly larger cluster velocity dispersion than is commonly accepted. Giovanelli *et al.* (1998b) calculate values of $325 \pm 54$ km s$^{-1}$ and $375 \pm 63$ km s$^{-1}$ for their **in+** and **in** samples respectively, in agreement with other measures using the same data (Bahcall & Oh 1996; Watkins 1997), which all favor $\sigma_{1d} \sim 250$ km s$^{-1}$ once values have been corrected for error broadening. Watkins (1997) discuss a different sample, for which he measures a velocity dispersion higher than that found here, but argues that it is artificially inflated by the presence of clusters with suspect galaxy assignments. Using only clusters with $cz > 4000$ km s$^{-1}$(the Ref. clusters in Fig 4.10b), the velocity dispersion is reduced slightly to $\sim 380$ km s$^{-1}$ (or 315 km s$^{-1}$after correction for error broadening) in the **in+** sample. Even though we measure a value within $2\sigma$ of the Giovanelli *et al.* (1998b), this result (along with the larger scatter derived in Section 4.4 below) suggests that cluster assignments should be carefully reviewed.

Figures 4.11 shows the global TF relation for the **in** and **in+** samples. We also show the **in+** sample plotted with error bars. A summary of linear fits to various subsets of the full sample is shown in Table 4.5, while the quadratic fits are shown in Table 4.6.

### 4.3.6 Comparison with SCI TF Relation

As discussed above, the sample here is based on the cluster sample presented in Giovanelli *et al.* (1997a) to which a global TF relation is fit in G97b, but includes a significant amount of additional data, including 14 extra clusters (for which previously there was not sufficient numbers of galaxies with TF measurements to include). Additionally we have chosen not to include 2 of the clusters used by G97b (A2197 and A2666) because of the relatively small number of TF data points in each cluster (as compared to our richer sample). The methods we have used to correct for biases, and to fit the TF relation are also very similar to those discussed in G97b, so a direct comparison of the global TF relation should be made. The

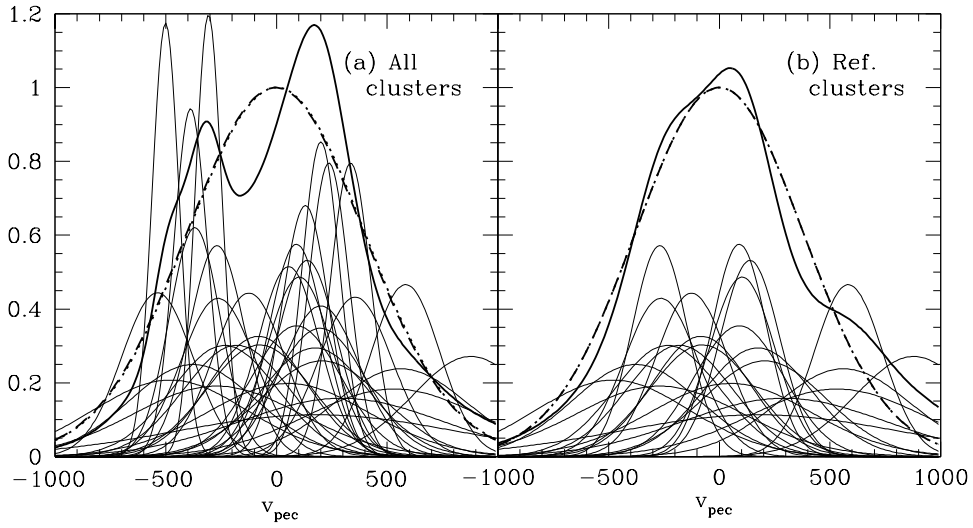



Figure 4.10: Line of sight peculiar velocities in the cluster reference frame for the **in+** samples of each cluster. On the left are shown all clusters, on the right only those clusters which were used to define the rest frame. The heavy solid line is an arbitrarily scaled sum of all the Gaussians. The dashed and dotted lines (which are almost exactly overlapping) are fits to the sum, the dotted line having the mean fixed to zero. When the mean is allowed to vary it is not significantly different from zero.

Table 4.4: Fit offsets for individual cluster samples

| Sample | $N$ | $v_{\rm CMB}$ | $\Delta M_0$ | $\Delta M_1$ |
|---|---|---|---|---|
| N383 **in** | 11 | 4865* | 0.08 | 0.07 |
| N383 **in+** | 29 | | 0.09 | 0.08 |
| N507 **in** | 14 | 4808* | -0.09 | -0.09 |
| N507 **in+** | 19 | | -0.04 | -0.04 |
| A262 **in** | 27 | 4665* | 0.21 | 0.19 |
| A262 **in+** | 51 | | 0.13 | 0.12 |
| A400 **in** | 16 | 6934* | 0.01 | 0.03 |
| A400 **in+** | 51 | | -0.06 | -0.04 |
| Eridanus **in** | 22 | 1536 | 0.48 | 0.42 |
| Eridanus **in+** | 36 | | 0.54 | 0.49 |
| Fornax **in** | 23 | 1321 | 0.35 | 0.31 |
| Fornax **in+** | 41 | | 0.50 | 0.45 |
| Cancer **in** | 17 | 4939* | 0.03 | 0.00 |
| Cancer **in+** | 50 | | 0.08 | 0.05 |
| Antlia **in** | 17 | 3120 | -0.21 | -0.21 |
| Antlia **in+** | 41 | | -0.16 | -0.14 |
| N3557 **in** | 7 | 3318 | -0.19 | -0.20 |
| N3557 **in+** | 14 | | -0.16 | -0.13 |
| Hydra **in** | 21 | 4075* | 0.24 | 0.25 |
| Hydra **in+** | 31 | | 0.13 | 0.14 |
| A1367 **in** | 33 | 6735* | -0.05 | -0.03 |
| A1367 **in+** | 34 | | -0.08 | -0.06 |
| Ursa Major **in** | 31 | 1101 | 0.76 | 0.72 |
| Ursa Major **in+** | 37 | | 0.86 | 0.81 |
| Cen **in** | 25 | 3322 | -0.15 | -0.16 |
| Cen **in+** | 38 | | -0.21 | -0.23 |
| Coma (A1656) **in** | 36 | 7185* | -0.20 | -0.17 |
| Coma **in+** | 45 | | -0.21 | -0.18 |
| ESO508 in | 10 | 3196 | -0.29 | -0.24 |
| ESO508 **in+** | 18 | | -0.19 | -0.17 |
| A3574 in | 13 | 4817* | 0.02 | 0.03 |
| A3574 **in+** | 29 | | -0.05 | -0.04 |
| A2199 in | 8 | 8996* | -0.02 | 0.03 |
| A2199 **in+** | 22 | | -0.20 | -0.14 |
| Pavo 2 in | 8 | 4444* | -0.20 | -0.19 |
| Pavo 2 **in+** | 25 | | -0.05 | -0.05 |

Table 4.4 (Continued)

| Sample | $N$ | $v_{\rm CMB}$ | $\Delta M_0$ | $\Delta M_1$ |
|---|---|---|---|---|
| Pavo in | 5 | 4055 | -0.22 | -0.25 |
| Pavo **in+** | 16 | | -0.10 | -0.11 |
| MDL59 in | 12 | 2317 | 0.47 | 0.42 |
| MDL59 **in+** | 25 | | 0.37 | 0.32 |
| Pegasus in | 20 | 3519 | 0.24 | 0.18 |
| Pegasus **in+** | 33 | | 0.36 | 0.31 |
| A2634 in | 20 | 8895* | -0.12 | -0.10 |
| A2434 **in+** | 24 | | -0.07 | -0.05 |
| A194 **in** | 24 | 5036* | 0.03 | 0.00 |
| A194 **in+** | 32 | | 0.13 | 0.10 |
| 30109 **in** | 5 | 4697* | 0.00 | -0.02 |
| 30109 **in+** | 14 | | 0.04 | 0.04 |
| A779 **in** | 14 | 7211* | 0.14 | 0.14 |
| A779 **in+** | 18 | | 0.14 | 0.14 |
| 30603 **in** | 7 | 2047 | -0.08 | -0.12 |
| 30603 **in+** | 17 | | -0.10 | -0.14 |
| 30617 **in** | 6 | 2473 | -0.54 | -0.50 |
| 30617 **in+** | 15 | | -0.33 | -0.34 |
| 31108 **in** | 8 | 4658* | 0.18 | 0.15 |
| 31108 **in+** | 13 | | 0.20 | 0.17 |
| 397 **in** | 14 | 9594* | -0.09 | -0.07 |
| 397 **in+** | 16 | | -0.06 | -0.04 |
| 496 **in** | 9 | 9809* | -0.04 | -0.05 |
| 496 **in+** | 9 | | -0.05 | -0.07 |
| 1314 **in** | 8 | 9970* | -0.08 | -0.11 |
| 1314 **in+** | 8 | | -0.09 | -0.12 |
| 2806 **in** | 10 | 7867* | -0.25 | -0.24 |
| 2806 **in+** | 10 | | -0.27 | -0.26 |
| 2877 **in** | 9 | 6974* | 0.02 | 0.00 |
| 2877 **in+** | 9 | | 0.00 | -0.02 |
| 634 **in** | 9 | 7922* | 0.10 | 0.08 |
| 634 **in+** | 9 | | 0.09 | 0.07 |
| 30940 **in** | 9 | 3162 | -0.17 | -0.18 |
| 30940 **in+** | 16 | | -0.03 | -0.04 |
| 569 **in** | 13 | 6011* | 0.10 | 0.04 |
| 569 **in+** | 16 | | 0.08 | 0.03 |

Table 4.5: Linear TF parameters for global samples.

| Sample | $N$ | $a_{dir}$ | $b_{dir}$ | $a_{inv}$ | $b_{inv}$ | $a_{bi}$ | $b_{bi}$ | $\epsilon_a$ | $\epsilon_b$ | $\sigma_{bi}$ | $\sigma_{abs}$ |
|---|---|---|---|---|---|---|---|---|---|---|---|
| No incompleteness correction | | | | | | | | | | | |
| **in** | 541 | -20.896 | -7.066 | -20.925 | -7.887 | -20.870 | -7.451 | 0.017 | 0.117 | 0.476 | 0.368 |
| **in+** | 911 | -20.872 | -7.052 | -20.906 | -7.985 | -20.850 | -7.421 | 0.013 | 0.087 | 0.504 | 0.385 |
| Incompleteness correction as described in Section 4.3.2 | | | | | | | | | | | |
| **in** | 541 | -20.915 | -7.114 | -20.918 | -7.949 | -20.896 | -7.355 | 0.017 | 0.115 | 0.389 | 0.302 |
| **in** $2.5\sigma$ clip | 496 | -20.908 | -7.303 | -20.919 | -7.741 | -20.899 | -7.392 | 0.018 | 0.121 | 0.314 | 0.258 |
| **in** $i > 45°$ | 495 | -20.910 | -7.225 | -20.917 | -7.973 | -20.892 | -7.399 | 0.017 | 0.116 | 0.382 | 0.297 |
| **in** $60° < i < 80°$ | 282 | -20.916 | -7.218 | -20.926 | -7.968 | -20.903 | -7.340 | 0.023 | 0.156 | 0.371 | 0.291 |
| **in** $W > 150$ km s$^{-1}$ | 502 | -20.932 | -6.867 | -20.919 | -7.882 | -20.910 | -7.133 | 0.017 | 0.126 | 0.373 | 0.293 |
| $M < -18.5$ mag | | | | | | | | | | | |
| **in** $W > 150$ km s$^{-1}$ | 515 | -20.920 | -7.036 | -20.913 | -7.990 | -20.899 | -7.287 | 0.017 | 0.122 | 0.382 | 0.298 |
| **in** earlier than Sb | 51 | -21.062 | -6.120 | -20.917 | -7.455 | -21.024 | -6.446 | 0.067 | 0.389 | 0.391 | 0.311 |
| **in** Sb | 117 | -20.925 | -6.784 | -20.854 | -7.821 | -20.894 | -7.055 | 0.038 | 0.267 | 0.352 | 0.284 |
| **in** later than Sb | 373 | -20.921 | -7.342 | -20.972 | -8.292 | -20.910 | -7.575 | 0.022 | 0.149 | 0.397 | 0.304 |
| **in** HI widths only | 370 | -20.914 | -7.086 | -20.912 | -7.943 | -20.896 | -7.308 | 0.020 | 0.132 | 0.401 | 0.314 |
| **in** ORC widths only | 171 | -20.919 | -7.192 | -20.937 | -7.998 | -20.901 | -7.541 | 0.034 | 0.243 | 0.353 | 0.269 |

Table 4.5 (Continued)

| Sample | $N$ | $a_{dir}$ | $b_{dir}$ | $a_{inv}$ | $b_{inv}$ | $a_{bi}$ | $b_{bi}$ | $\epsilon_a$ | $\epsilon_b$ | $\sigma_{bi}$ | $\sigma_{abs}$ |
|---|---|---|---|---|---|---|---|---|---|---|---|
| **in+** | 911 | -20.893 | -6.992 | -20.899 | -8.039 | -20.878 | -7.216 | 0.013 | 0.089 | 0.425 | 0.327 |
| **in+** $2.5\sigma$ clip | 825 | -20.886 | -7.132 | -20.897 | -7.667 | -20.878 | -7.206 | 0.013 | 0.092 | 0.329 | 0.271 |
| **in+** $i > 45°$ | 845 | -20.890 | -7.057 | -20.900 | -8.049 | -20.877 | -7.222 | 0.013 | 0.090 | 0.421 | 0.323 |
| **in+** $60°< i < 80°$ | 478 | -20.908 | -7.048 | -20.920 | -8.023 | -20.900 | -7.180 | 0.017 | 0.118 | 0.419 | 0.324 |
| **in+** $W > 150$ km s$^{-1}$ | 847 | -20.910 | -6.779 | -20.897 | -7.999 | -20.892 | -7.016 | 0.013 | 0.097 | 0.406 | 0.315 |
| $M < -18.5$ mag | | | | | | | | | | | |
| **in+** $W > 150$ km s$^{-1}$ | 872 | -20.893 | -6.998 | -20.888 | -8.159 | -20.877 | -7.229 | 0.013 | 0.095 | 0.419 | 0.323 |
| **in+**, earlier than Sb | 72 | -21.091 | -5.780 | -20.890 | -7.372 | -21.040 | -6.106 | 0.057 | 0.328 | 0.395 | 0.311 |
| **in+**, Sb | 181 | -20.954 | -6.575 | -20.857 | -7.883 | -20.919 | -6.888 | 0.031 | 0.211 | 0.379 | 0.302 |
| **in+**, later than Sb | 658 | -20.878 | -7.138 | -20.943 | -8.377 | -20.874 | -7.355 | 0.016 | 0.110 | 0.438 | 0.333 |
| **in+**, HI widths only | 662 | -20.901 | -6.943 | -20.897 | -8.036 | -20.886 | -7.145 | 0.015 | 0.100 | 0.436 | 0.335 |
| **in+**, ORC widths only | 249 | -20.875 | -7.101 | -20.907 | -8.070 | -20.858 | -7.488 | 0.028 | 0.203 | 0.380 | 0.296 |
| Only clusters used in G97b | | | | | | | | | | | |
| **in** | 419 | -20.906 | -7.032 | -20.861 | -8.090 | -20.885 | -7.368 | 0.019 | 0.128 | 0.421 | 0.308 |
| **in+** | 732 | -20.900 | -6.953 | -20.848 | -8.227 | -20.883 | -7.245 | 0.014 | 0.100 | 0.441 | 0.329 |

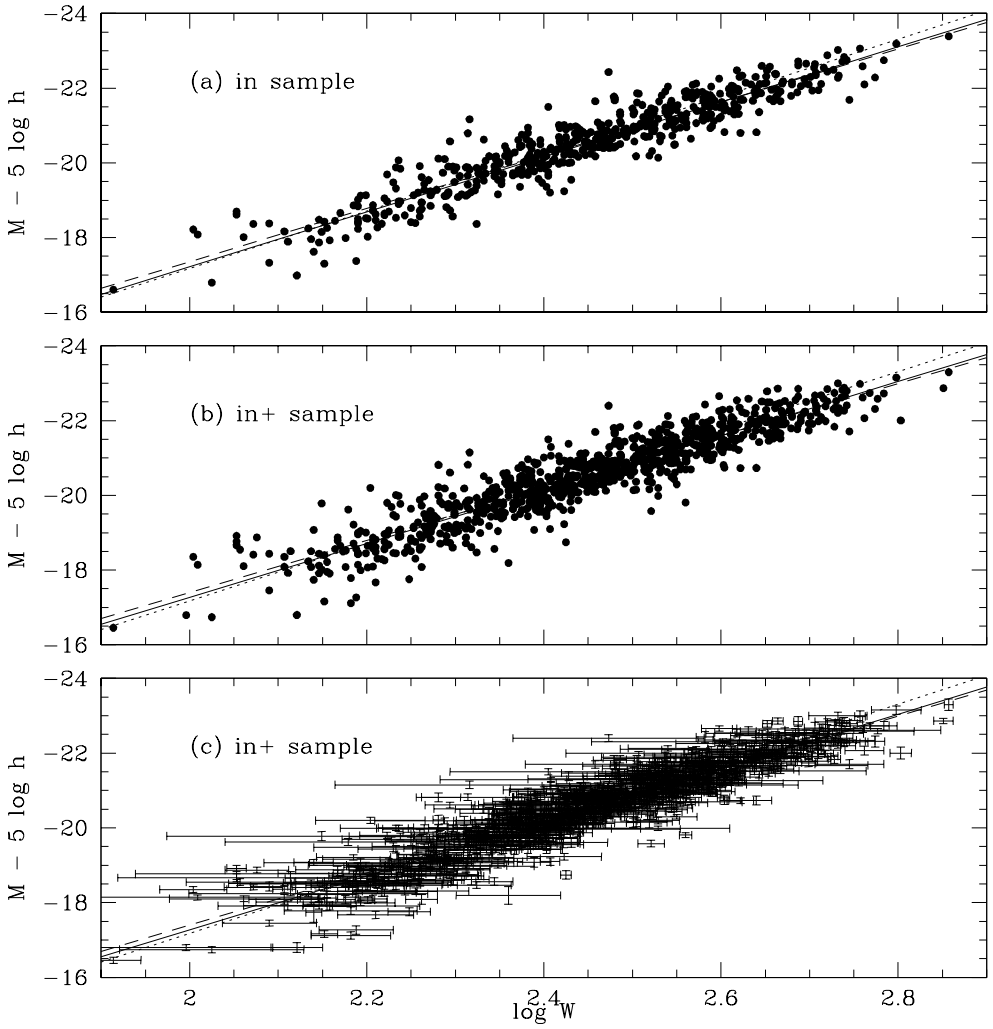



Figure 4.11: Global TF relation for (a) **in** sample, (b) **in+** sample, (c) **in+** sample plotted as errors. The direct and bivariate fits to the respective samples are overlaid as dashed and solid lines respectively, while the G97b bivariate fit to their **in+** sample is plotted as the dotted line.

Table 4.6: Quadratic TF parameters for global samples.

| Sample | $N$ | $q_0$ | $q_1$ | $q_2$ | $\sigma$ |
|---|---|---|---|---|---|
| No incompleteness correction | | | | | |
| **in** | 541 | -20.924 | -6.966 | 1.222 | 0.489 |
| **in+** | 911 | -20.907 | -6.948 | 1.510 | 0.512 |
| Incompleteness correction with $\alpha_{\rm LF} = 0.5$ | | | | | |
| **in** | 541 | -20.949 | -6.992 | 1.491 | 0.405 |
| **in** $2.5\sigma$ clip | 496 | -20.942 | -7.209 | 1.523 | 0.314 |
| **in+** | 911 | -20.925 | -6.893 | 1.433 | 0.434 |
| **in+** $2.5\sigma$ clip | 825 | -20.927 | -7.042 | 1.870 | 0.327 |

global slope we find is on average 0.3-0.4±0.15 mag$^{-1}$ shallower than found in G97b; considering only those clusters used in G97b (and reintroducing A2197 and 2166) this difference reduces to 0.2-0.3±0.15 mag$^{-1}$. A small difference in slope between the two samples is not too unexpected. As discussed earlier, the new width corrections applied to the HI widths (which make up about 60% of the velocity widths used) should alter the TF slope slightly. Also, where the SFI++ adds new galaxies to the SFI is at the smaller apparant diameters, so for galaxies in a cluster all at basically the same distance this will preferentially add galaxies at the low mass end of the TF relation, adding extra leverage to the measurement of the slope, and increasing the overall scatter. The distribution of absolute magnitudes of the two samples, illustrating this effect are shown in Figure 4.12.

## 4.4 The Scatter in the TF Relation

Figure 4.13 shows the total observed scatter in the TF relation fit to the **in+** sample, with the standard deviation

$$\sigma_{\rm SD} = \sqrt{\frac{\sum \frac{\delta M_i^2}{\epsilon_i^2}}{\sum 1/\epsilon_i^2}}, \tag{4.23}$$

shown as open squares and the average deviation,

$$\sigma_{\rm AD} = \frac{\sum \frac{|\delta M_i|}{\epsilon_i^2}}{\sum 1/\epsilon_i^2}, \tag{4.24}$$

as open circles. As discussed in Section 4.3.2, the observed scatter will be an underestimate due to the impact of incompleteness bias which preferentially removes galaxies scattered below the TF relation when they are near the magnitude limit of the sample. The bias corrected values (following G97b) are shown as filled squares and circles respectively. A linear fit to the bias corrected standard deviations gives

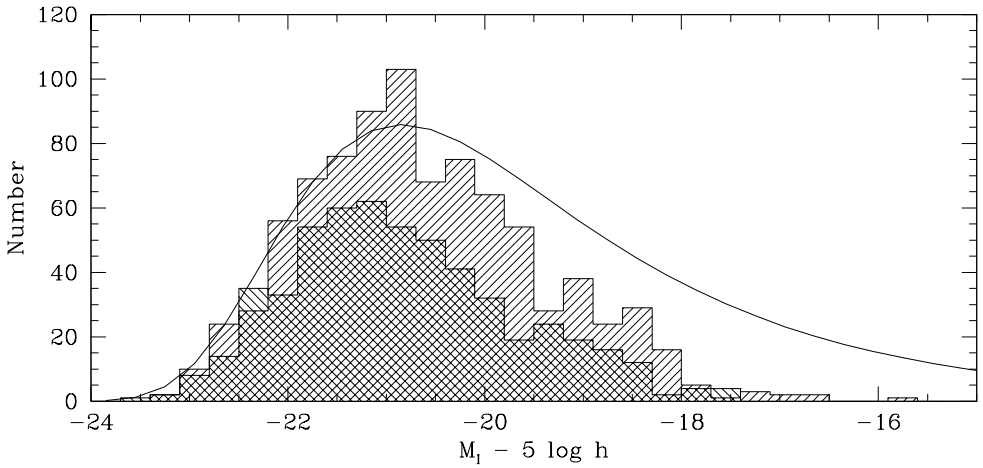



Figure 4.12: Distribution of absolute magnitudes for SFI++ cluster sample (single hatching), and similar (but smaller) SCI sample of G97b (cross hatching). The smooth line shows the luminosity function used in Section 4.3.2 to derive incompleteness bias corrections.

$\epsilon_{\rm obs} = 0.43 - 0.296(\log W - 2.5)$, a little larger than $\epsilon_{\rm obs} = 0.32 - 0.325(\log W - 2.5)$ found by G97b. The source of this additional scatter is currently unknown and should be investigated in future work. Like the slightly larger cluster velocity dispersion discussed in Section 4.3.5, this larger scatter may be related to suspect cluster membership assignments and suggests that a careful review of cluster assignments should be made.

## 4.5 Conclusions

In this Chapter we present the SFI++ sample of spiral galaxies. Galaxies in this sample have both I-band photometry and velocity widths (either from HI global profiles or optical rotation curves) suitable for use in the Tully-Fisher relation.

We introduce a subset of this sample which consists of 911 galaxies in the vicinity of 36 nearby clusters (within 10,000 km $s^{-1}$). This sample is divided into an **in** sample consisting of 541 *bona fide* cluster galaxies and an **in+** sample which also includes galaxies considered to be peripheral members of the cluster. Cluster membership assignments are discussed further in Springob (2005).

In Section 4.3.2, we discuss various biases which alter the observed TF relation from the intrinsic relation within a cluster sample. We derive corrections for these biases which include morphological type bias and incompleteness bias due to the implicit magnitude limit of the sample.

Individual TF relations are fit to all 36 clusters in the sample and presented in Section 4.3.4. These cluster samples are then combined in Section 4.3.5; in

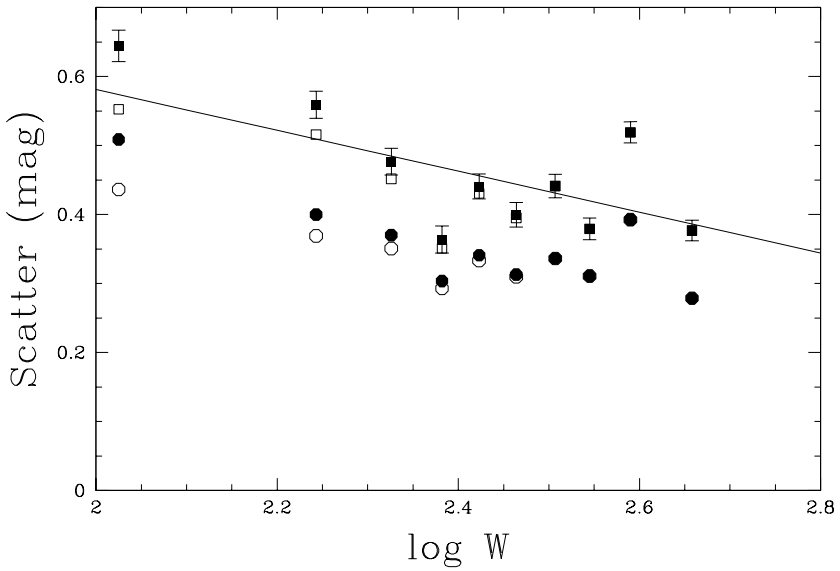



Figure 4.13: Total observed scatter in the TF relation fit to the **in+** sample. Open squares and circles show the observed standard deviation and average deviation respectively. The filled squares and circles have been corrected for incompleteness bias following G97b. The solid line shows a linear fit to filled squares (bias corrected standard deviation) of $\epsilon_{\rm obs} = 0.43 - 0.296(\log W - 2.5)$.

the process peculiar velocities are derived for the clusters and a cluster velocity dispersion of $\sim 400$ km s$^{-1}$ is measured.

Both linear and quadratic fits to the combined **in** and **in+** samples (and subsets of them) are presented. We favor the bivariate fit to the **in** sample, which gives a template TF relation of $M - 5\log h = -20.90 - 7.36(\log W - 2.5)$, or $L \propto v^{2.9}$. The error on the zeropoint is $\sim 0.02$ mag, while the error on the slope is $\sim 0.1$ mag$^{-1}$. This fit suggests a slightly shallower slope ($< 3\sigma$) than previously found by G97b. The scatter in the relation is found to be $\sim 0.4$ mags, and increases with decreasing velocity width.

The template TF relation derived here will be used in Chapter 6 to calibrate TF distances for a sample of field galaxies in the local universe. In Chapter 8 we use this sample to study the peculiar velocity in and around the Local Supercluster.

# Chapter 5

# Internal Extinction in Spirial Galaxies in the Near Infra-red *

## 5.1 Introduction

The determination of an accurate value for the internal extinction in galaxies is of relevance both in the understanding of their structure and in applications such as the determination of redshift independent distances. Edge-on spirals are used preferentially in studies that apply the luminosity-linewidth relation (Tully & Fisher 1977) and these are, of course, the galaxies in which extinction effects will be the largest. Inadequate corrections for extinction will produce systematic distance errors in our catalogs. Recent discussions of this issue can be found in Disney & Burstein (1995) and Calzetti (2001), while a comprehensive history of the study of internal extinction in galaxies can be found in the introduction of Huizinga (1994). Analyses similar to the ones carried out in this paper can be found in Giovanelli *et al.* (1994; hereafter G94, and 1995) and Tully *et al.* (1998).

Since there is intrinsic variability in the properties of galaxies, the determination of the amount of extinction is most readily obtained in a statistical way, in which case large samples are desirable. However, sample selection effects need to be well understood in order to avoid interpreting spurious effects as astrophysically significant. There will be further discussion of the effects of such biases on the results of this paper in Sections 5.3 and 6.2.

In this paper we report on statistical tests which search for the effects of extinction in spiral galaxies in the near infra-red (NIR) bands, I (0.81 $\mu$m), J (1.25 $\mu$m) , H (1.65 $\mu$m) and $K_s$ (2.17 $\mu$m). NIR bands are often used in cases where accurate total magnitudes of galaxies are needed, as they clearly minimize, if not eliminate, the need for extinction corrections. For this reason it is particularly interesting to search for the effects of extinction in these bands.

Samples and available data are described in Sections 7.2 and 7.3. In Section 7.4 we apply simple tests for reddening with inclination and in Sections 7.5 and 7.6 we discuss in more detail the effects of extinction on the isophotal radius and total magnitudes respectively. A simple photometric model for the extinction is discussed in Section 7.7 and in Section 7.8 luminosity dependences are discussed. A summary of the conclusions is given in Section 7.9.

*This Chapter is published in Masters, Giovanelli & Haynes (2003).

## 5.2 Description of the Samples

The Two Micron All-Sky Survey (2MASS) completed its coverage of the near infrared sky in February 2001. Data were taken in three NIR bands, J, H and $K_s$ using two identical 1.3m telescopes, one in Arizona, the other in Chile. With an extended source sensitivity of 14.8, 14.0 and 13.4 mag at J, H and $K_s$ (Jarrett *et al.* 2000) and an angular resolution of about 2-3 arcseconds, 2MASS has detected more than 1.65 million galaxies (Jarrett *et al.* 2003); the resultant data are available in the Extended Source Catalog (XSC)[†]

Two samples were extracted from the 2MASS All-Sky release XSC. For statistical studies the samples should be as large as possible, but it is also important for them to have well defined selection criteria. The first sample (and by far the largest) consists of all galaxies with well defined spiral morphology and known redshift taken from the Arecibo General Catalog (a private compilation by the authors known as the AGC). Nearby, peculiar motions contribute significantly to observed recessional velocities so we further limit the AGC to $cz > 3000$ km s$^{-1}$ in order to use the redshift as a reliable distance indicator. This large sample is referred to as the AGC$z$. The AGC is an all-sky compilation, but has varying completeness functions in different areas of the sky. A second, smaller sample consists of galaxies in the AGC$z$ for which I-band photometry is also available (as will be described below). This sample we call the SFI2 as it contains all of the SFI data (Giovanelli *et al.* 1997a; Haynes *et al.* 1999a,b) plus similar but newer and as yet unpublished additions to that. This sample is a homogeneous all-sky sample of mostly Sc galaxies. In summary:

**AGC$z$** Spiral galaxies of known redshift from the Arecibo General Catalog. The redshift was further confined to $cz > 3000$ km s$^{-1}$. This sample includes a total of 15244 galaxies.

**SFI2** Galaxies from AGC$z$ which also have I-band photometry available. This sample has a total of 3035 galaxies, which are mostly of types Sc and Sbc.

The detection fractions of these galaxies in the 2MASS XSC (within 12" of the previously cataloged position) are 80% for the AGC$z$ and 85% for the SFI2 sample. We expect that this is due in part to the detection limits of the 2MASS survey and in part to the accuracy of the currently tabulated positions of the galaxies in the AGC. In support of this assumption the detection fraction increases for the SFI2 galaxies that are expected to have more accurate positions in the AGC. For the Second Incremental release of 2MASS data, a discussion of completeness is included in the on-line Explanatory Supplement[‡]. When the search for a match is extended

[†]Available through the online catalog query service of the IR Science Archive: `http://irsa.ipac.caltech.edu/applications/Gator/`

[‡]The Explanatory Supplement to the 2MASS Second Incremental Release Curtri *et al.* (2000) is an on-line document:
`http://www.ipac.caltech.edu/2mass/releases/docs.html`

to a radius of 0.5' of known galaxies from the Zwicky Catalog, the detection rate is 95%. In the NIR, surface brightness decreases towards later type galaxies (Jarrett *et al.* 2003) making late type, gas rich galaxies (like the Sc galaxies which make up the bulk of the SFI2 sample) harder to detect than E/S0/Sa galaxies.

## 5.3 Description of data

For all of the galaxies in our samples various data are available. These included redshifts, coarse blue magnitudes and angular sizes from the AGC, photometry from 2MASS and I-band photometry for the SFI2 sample. In the computation of absolute magnitudes a value of $H_\circ = 100h$ km s$^{-1}$ Mpc$^{-1}$ is adopted.

### 5.3.1 I-band photometry

The I-band photometry for the SFI2 sample is described in Haynes *et al.* (1999a). Quantities of particular interest are:

$(a/b)_{\rm I}$ - I-band axial ratio derived from a fit of elliptical surface brightness contours to the I-band images. The average error in $\log(a/b)$ is 0.03.

$r_{23.5}$ - radius measured at the I-band isophote of 23.5 mag arcsec$^{-2}$.

$m_{\rm I}$ - total I-band magnitude. Calculated from an extrapolation of a fit to the disk to 8 scale lengths of the disk. Typical total errors are in the range 0.03-0.06 mag.

$r_d$ - scale length of the disk derived from a fit to the one-dimensional I-band photometric profile.

### 5.3.2 Photometric quantities from the 2MASS XSC

The photometric quantities in the XSC are derived by inspecting the 2MASS images with the extended source processor (GALWORKS), which was developed for this purpose (see Jarrett *et al.* 2000). By the time the 2MASS images get to GALWORKS a point source spread function has already been derived for each image. GALWORKS identifies extended sources (galaxies as well as other more nearby resolved sources) and measures a variety of parameters for each one as described in Jarrett *et al.* (2000) and in the 2MASS Explanatory Supplement (Curtri *et al.* 2000). Very large galaxies (greater than 5' in size at $\sim$ 20th mag arcsec$^{-2}$ in J-band) are first identified in in a separate large galaxy atlas[§] and then added to the XSC. The quantities from the XSC that we use are:

[§]See: `http://irsa.ipac.caltech.edu/applications/2MASS/LGA/`

$(a/b)_{\rm J}$ - J-band axial ratio fit to the $3\sigma$ isophote (which is close to the 20th mag arcsec$^{-2}$ isophote). The center of this ellipse fit is fixed to the peak intensity pixel and since only one isophote is fitted, it is an approximation to the ellipticity of the galaxy. If the $3\sigma$ isophote is too close to the center of the galaxy the bulge might interfere with the derived ellipticity, making the galaxy appear more face-on than it really is. Of the three 2MASS bands, the J axial ratio should suffer the least from this effect; we note that no systematic offset is seen between the J-band and I-band axial ratios, as can be seen Figure 5.4d. An estimate of the average error of 0.1 in $\log(a/b)$ is derived from the scatter in this plot; this is more than three times as large as the average error estimated for the equivalent I-band quantity.

$r_{21}^{\rm J}$, $r_{21}^{\rm H}$, $r_{21}^{\rm K}$ - semi-major axis of the isophotal elliptical aperture set to the 21st mag arcsec$^{-2}$ isophote individually in each band. An alternative to this would have been the semi-major axis of the ellipse fit to the 20th mag arcsec$^{-2}$ isophote, which is the preferred aperture in the XSC (Jarrett *et al.* 2003). In Section 5.1 it is shown that $r_{21}$ in J-band is at $\sim 2.5$ scale lengths of the disk ($r_d$), while in H and $K_s$ it is $\sim 3.3 r_d$. A similar analysis for $r_{20}$ shows that $r_{20}^{\rm J} \sim 1.6 r_d$, and $r_{21}^{\rm H,K} \sim 2.2 r_d$. We choose to use $r_{21}$ in order to trace the disks as far out as possible (which still is not far compared to $r_{23.5}^{I} \sim 3.5 r_d$). Since the typical 1 $\sigma$ background noise is 21.4, 20.6 and 20.0 mag in J, H and $K_s$ respectively (Jarrett *et al.* 2003), we must be careful in using the radii set to the 21st mag arcsec$^{-2}$ level, especially in H and $K_s$. In J-band $r_{21}$ should be reasonably well defined, and does indeed show good correlation with $r_{20}$ with a scatter of about 3 ". The same analysis for H and $K_s$ shows a similar correlation with a slightly larger scatter (3.5" and 4 " respectively). When $r$ is smaller than 7" or greater than 120" (for either isophote and in all bands) it does not follow the correlation well. These radii are not used.

$\mathbf{J}_{\rm 21f}$, $\mathbf{H}_{\rm 21f}$, $\mathbf{K}_{\rm 21f}$ - magnitudes within the 21st mag arcsec$^{-2}$ elliptical isophote set in J-band (referred to as "J fiducial" are used to construct colors because of the necessity of having a consistent aperture. The uncertainty on these magnitudes listed in the XSC is that associated with Poisson noise and background subtraction and does not include other errors such as the zero point calibration and the uncertainty in the elliptical isophotal aperture (see Jarrett et al. 2000 for more details). This formal uncertainty is small (with the largest quoted at only 0.2 mag) and the real uncertainty is likely to be larger. The "Level One Science Requirements" of 2MASS (which can be found in the on-line Explanatory Supplement) require that the extended source photometry be accurate and uniform to within 10%, and we assume this is a closer estimate of the error in the magnitudes.

$\mathbf{J}_{\rm 21f}$, $\mathbf{H}_{\rm 21f}$, $\mathbf{K}_{\rm 21f}$ - magnitudes measured within the 21st mag arcsec$^{-2}$ level set in J-band are used to construct colors.

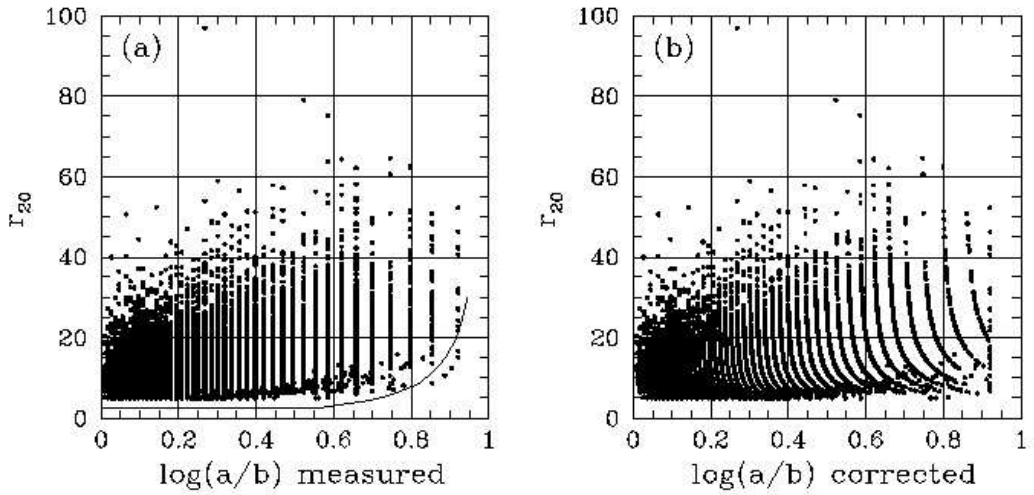



Figure 5.1: Isophotal angular semi-major axis (in arcsec) at the 20th mag arcsec$^{-2}$ level plotted against the log of the axial ratio (which is measured at about the 20th mag arcsec$^{-2}$ level). (a) As observed; the line shows the theoretical limit from our simulations. (b) Corrected for seeing with FWHM= 2.5" as described in text. The obvious banding is due to the accuracy of tabulated values in the XSC.

**$J_{ext}$, $H_{ext}$, $K_{ext}$** - XSC "extrapolated" magnitudes designed to represent the total magnitude of the galaxy. These magnitudes are derived from an extrapolation of the radial surface brightness profile from the 20th mag arcsec$^{-2}$ elliptical isophote down to $r_{tot}$ which is set to 5 times the scale length from the J-band fit. See Jarrett *et al.* (2003) for more details.

### 5.3.3 Corrections

In order to use the photometry from the 2MASS XSC to its best potential for our purposes, various corrections for seeing, galactic extinction and cosmological redshift need to be applied. These corrections have already been applied to the I-band quantities in a similar manner as that described below (for details, see Haynes *et al.* 1999a).

#### Seeing correction

Figure 5.1a shows a plot of $\log(a/b)_J$ vs. the 20th mag arcsec$^{-2}$ isophotal radius (the approximate isophotal radius at which $a/b$ is reported). We see that there is a lack of galaxies with both high axial ratio and small size. This is due mainly to the resolution of the images set by the seeing and the pixel size.

In the XSC, seeing is characterized using a modified exponential of the form

$$f(r) = f(0) \exp\left[-\left(\frac{r}{\alpha}\right)^{1/\beta}\right] \tag{5.1}$$

fit to many stars in each frame, where $f(0)$ is the central surface brightness, $r$ is the radius in arcseconds and $\alpha$ and $\beta$ are free parameters. The "radial shape" (sh $= \alpha \times \beta$) is reported, and an approximate relation is given in the 2MASS Seeing and Image Statistics ¶ to recover the full width at half maximum of the point spread function;

$$\text{FWHM(arcseconds)} = 3.13 \text{ sh} - 0.46. \tag{5.2}$$

The mean value of this FWHM is about 2.5" for the galaxies in our samples (the 2MASS raw images have a pixel size of 2" which sets the lower limit on the resolution), and the spread is small. We derive a correction by numerically convolving exponential disks of varying inclination and angular sizes with a Gaussian of FWHM = 2.5". Axial ratios are measured at a radial distance from the galaxy center of $1.7r_d$ (where $r_d$ refers to the scale length of the exponential disk), corresponding to $r_{20}$ in J-band (the ratio $r_d/r_{20}$ is obtained in the same way as $r_d/r_{21}$ in Section 5.1). The derived correction is parameterized as

$$(a/b)_{\rm corr} = (a/b)_{\rm obs}(1 - 0.02x + 0.21x^2 - 0.01x^3) \tag{5.3}$$

with

$$x = \text{FWHM}\left(\frac{a/b}{r_{20}}\right)_{\rm measured} \tag{5.4}$$

(where FWHM = 2.5" is used in all cases and $r_{20}$ is measured in arcseconds in the J-band image). Hereafter, when we refer to the J-band axial ratio, we refer to the quantity corrected by the above equation. The result of the correction can be seen in Figure 5.1b. In a few cases where the galaxy is very small and highly inclined the correction is large so to avoid over-correcting a maximum value of $a/b = 1/0.12$ is imposed and these galaxies are assumed to have an inclination of 90°. From Figure 1b it appears that the correction removes much but perhaps not all of the bias, so very small galaxies may appear less inclined than they really are. It should also be noted that the derived correction assumes light profiles are exponential, which may not be an ideal approximation within the $r_{20} \sim 1.7r_d$ radius in J-band where the contribution from a bulge may be significant.

### Galactic Extinction and K-corrections

Magnitudes are corrected for galactic (*i.e.* originating within the Milky Way) extinction using the DIRBE galactic extinction maps (Schlegel, Finkbeiner &

¶2MASS Seeing and Image Statistics (Cutrie 1998) is an on-line document found at: `http://spider.ipac.caltech.edu/staff/roc/2mass/`

Davis 1998). The column densities listed in the map are converted to extinction in the relevant bands by $A_J = 0.902E(B-V)$, $A_H = 0.576E(B-V)$ and $A_K = 0.367E(B-V)$. A small cosmological k-correction is also included using a simple linear fit to the low redshift end of the models of Poggianti (1997) which is $k_J = -0.68z$, $k_H = -0.40z$, and $k_K = -1.52z$.

The magnitude in band X corrected for galactic extinction and cosmological k-correction is then

$$m_{\rm X} = m_{\rm X}^{\rm obs} - A_{\rm X} + k_{\rm X}. \tag{5.5}$$

The isophotal radii also need to be corrected for galactic extinction. If we assume the disk photometric profiles are exponential with scale length $r_d$ in band X, then

$$r_{\rm X}^{\rm iso} = r_{\rm X}^{\rm obs} - r_d \frac{A_{\rm X}}{1.086} \tag{5.6}$$

(since the surface brightness at radius $r$ in an exponential disk is given by $\mu(r) = \mu(0) + 1.086\ r/r_d$). We also correct sizes for a cosmological stretch factor $(1+z)^2$.

## 5.4 Reddening

In this section we use the samples defined above in Section 2 to investigate the effects of internal extinction in the disks by investigating color gradients with inclination. This test has the advantage of suffering little from selection effects. For the SFI2 sample, we use the I-band axial ratios as the measure of inclination since these have errors almost three times smaller than the equivalent J-band measure from the XSC. The result is shown in Figure 5.2 in which colors (measured within an elliptical aperture with a semi-major axis of $r_{21}$ in J-band) are plotted vs. axial ratio. It is clear that reddening is present in all colors, which sets a lower limit to the extinction in the J and H bands by assuming that the extinction in $K_s$ is negligible. Following G94 and others, we parameterize the internal extinction as

$$\Delta M = \gamma \log(a/b). \tag{5.7}$$

The lower limit on $\gamma$ is then 0.3 mag in J and 0.1 mag in H. The formal error in fitting this slope to the data is 0.01 mag in both cases, while the scatter in the relationship is 0.1 mag. If there is extinction present in $K_s$-band (*i.e.* $\gamma_{\rm K} \neq 0$), the actual values of $\gamma$ in J and H will be $0.3 + \gamma_{\rm K}$ and $0.1 + \gamma_{\rm K}$ respectively. An indication that the linear law of Eqn 7 may not be appropriate for the highest inclinations is apparent in panels (a) and (c) of Figure 2, an issue we'll revisit below and in Section 6.

For the SFI2 sample, I-band magnitudes are also available. These magnitudes can be used to construct I-J, I-H and I-$K_s$ colors, with the understanding that the apertures are not consistent between I and the other bands. This mismatch should not, in the first order, affect the slope of the reddening, just the absolute color. The results of this are shown in Figure 5.3. Under the assumption that the

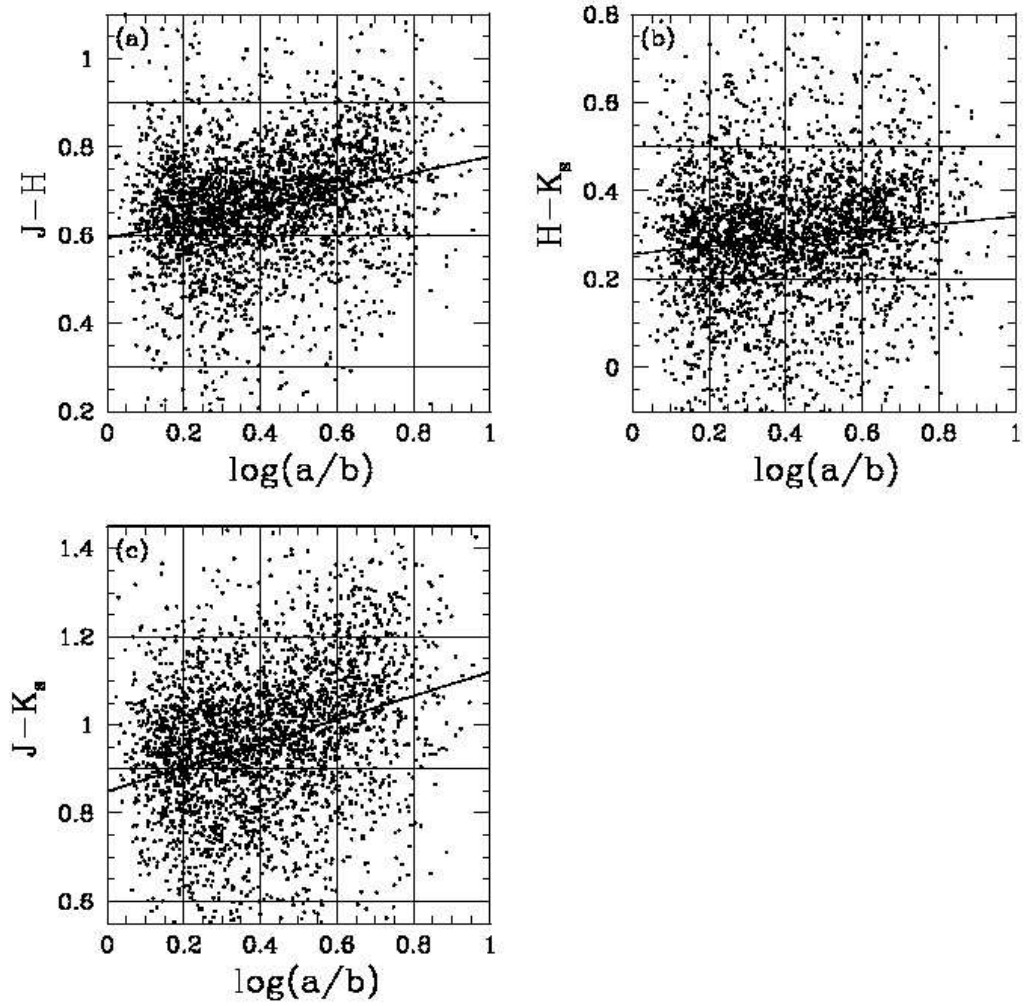



Figure 5.2: NIR color plotted against the log of the axial ratio (measured from I-band images) for 3035 galaxies for which I-band photometry is available (SFI2 sample). The slopes of the linear fits are 0.2 in J-H (a), 0.1 in H-$K_s$ (b), and 0.3 in J-$K_s$ (c). The formal error in determining the slope is 0.01 mag in all cases, while the scatter in the relationship is roughly 0.1 mag. Assuming there is no extinction in $K_s$-band (which will be tested below) this gives a lower limit to the value of $\gamma$ (where $\Delta M = \gamma \log(a/b)$) in J and H bands of 0.3 and 0.1 mag respectively. Note the indication of non-linearity in this relationship (especially in J-$K_s$ (c)) which is much more evident in Figure 5.4 and is discussed in Sections 4, 6.3 and 7.

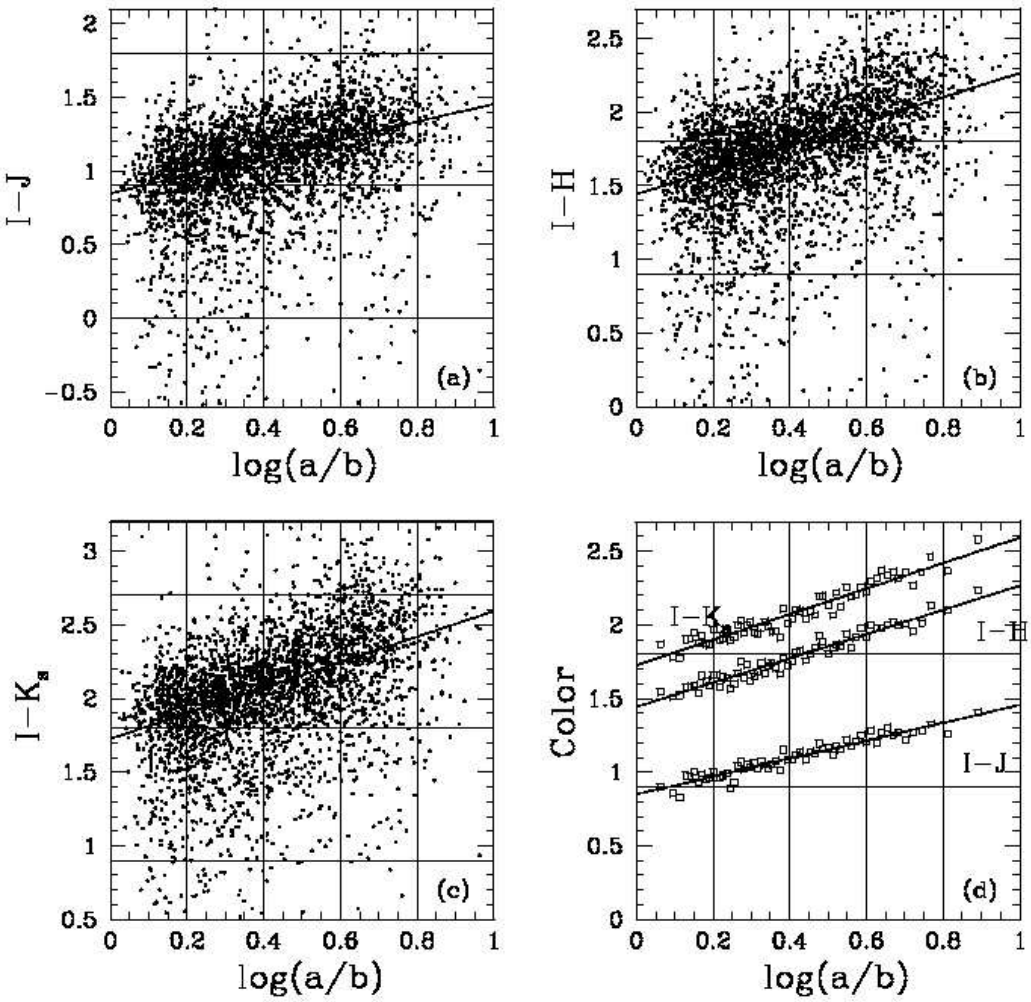



Figure 5.3: NIR color plotted against the log of the axial ratio (measured from the I-band images) for 3035 galaxies for which I-band photometry is available (SFI2 sample). Note that the aperture in which the I-band magnitude is measured is not the same as the J, H and $K_s$ apertures, but this should not affect the slope only the offset. The lines shown are fits to the median in bins of $\log(a/b)$ which is also shown in plot (d). The slope, $\gamma$ is 0.73 in I-J (a), 0.82 in I-H (b) and 0.94 in I-$K_s$ (c). The scatter is 0.4 mag in all cases, and the error on determining the slope from the medians is 0.03 mag. Assuming no extinction in $K_s$-band this then gives a lower limit to the extinction in I of 0.9 magnitudes, consistent with the value of $\gamma = 1.05 \pm 0.08$ derived in G94 and $\gamma \simeq 1.0$ in Tully *et al.* (1998). For comparison with Fig 5.2 the vertical scale is exactly three times larger.

extinction in $K_s$ is negligible, we derive a lower limit on the extinction in I-band of $\gamma = 0.94 \pm 0.03$ mag (where the error is the formal error in determining the slope). G94 find an extinction law of $\gamma_I = 1.05 \pm 0.08$, while Tully *et al.* (1998) derive $\gamma_I \simeq 1.0$, suggesting that if the extinction in $K_s$ is not equal to zero, it is likely to be small.

For the much larger AGC$z$ sample of galaxies (which does not have I-band photometry for all the galaxies), we can plot the J-H, J-$K_s$ and H-$K_s$ colors against the J-band axial ratios (Figure 5.4). Since the sample is large, we combine the points into averages in $\log(a/b)$ bins which makes the inadequacy of a simple linear law for the relationship (as noted in Figure 5.2) stand out. We fit two separate lines respectively for $\log(a/b)$ less than and greater than 0.5, and also include a quadratic fit for comparison. The parameterization of $\Delta M$ with a linear law in Eqn 7 is an expedient form, and internal extinction can well depart from such a linear law, depending on the details of the relative distribution of stars and dust (see, e.g. Evans 1992 and G94). In most simulations, in fact, $\Delta M$ steepens with increasing $\log(a/b)$ as will be shown for a simple photometric model in Section 5.7. Our adoption of bi-linear and quadratic fits reflects a least departure from simple expediency. The location of the break in the bi-linear law at $\log(a/b) = 0.5$ for all color trends is also practical but arbitrary. The slopes of the bi-linear relation are $0.10 \pm 0.02$ and $0.31 \pm 0.05$ for J-H, $0.05 \pm 0.02$ and $0.15 \pm 0.05$ for H-$K_s$, and $0.15 \pm 0.02$ and $0.46 \pm 0.05$ for J-$K_s$. The quadratic fit is 0.65(20) - 0.03(1)$\log(a/b)$ + 0.24(2)$[\log(a/b)]^2$ for J-H, 0.31(25) - 0.04(2)$\log(a/b)$ + 0.14(2)$[\log(a/b)]^2$ for H-$K_s$, and 0.97(28) - 0.07(2)$\log(a/b)$ + 0.39(3)$[\log(a/b)]^2$ for J-$K_s$.

## 5.5 Effect of inclination on isophotal radius

### 5.5.1 Formal corrections for inclination

If a galaxy is completely opaque within a given isophotal radius in the face-on perspective then no change in the measured radius is expected with inclination. If it is assumed that the face-on disk is transparent at that radius, then the isophotal radius should increase as the disk is tilted and we look through a longer path length. The expected change derived for the simple case of a pure exponential disk is

$$r_{iso} = r^{\circ}_{iso} + 2.302 r^{\circ}_{d} \log(a/b) \tag{5.8}$$

where $r^{\circ}_{iso}$ and $r^{\circ}_{d}$ are respectively the isophotal radius and the disk scale length in the face-on case. If we assume that the scale length changes with inclination like $r_{iso}$ (which is justified by the observation that the ratio $r_d/r_{21}$ does not change with inclination, as seen below) then we derive

$$\frac{r_{iso}}{r^{\circ}_{iso}} = 1 + 2.302 \frac{r_d}{r_{iso}} \log(a/b). \tag{5.9}$$

We have the scale lengths in I-band measured for the SFI2 sample and make the assumption that scale lengths do not change significantly between I, J, H and

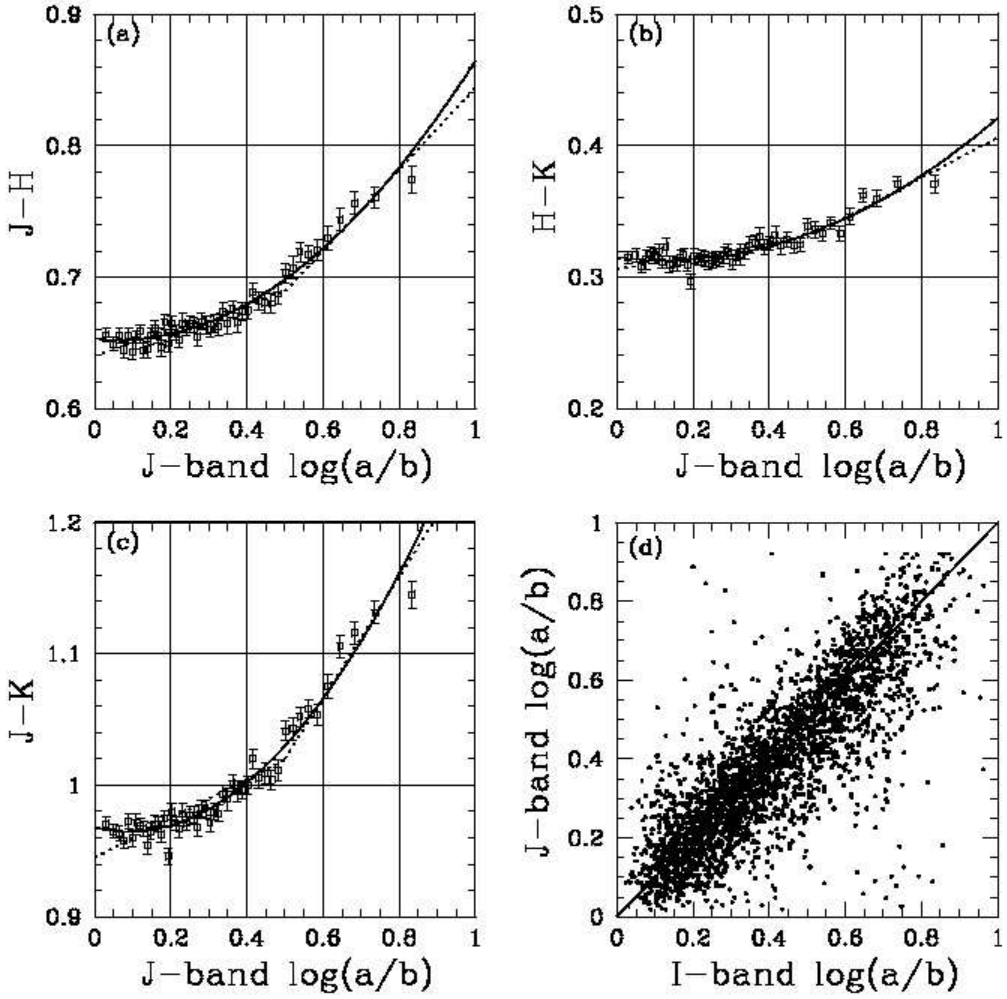



Figure 5.4: NIR color plotted against the log of the axial ratio (measured from the J-band images) for 15224 galaxies (AGC$z$ sample) binned in groups of 300 (error bars show the statistical error on determining the mean). The fit to the points is given as a quadratic (solid line) and as a bi-linear relation with a break at $\log(a/b) = 0.5$ (dotted line). Panel (d) shows $\log(a/b)$ in J vs. $\log(a/b)$ in I (both corrected for seeing) for the 3035 SF2 galaxies in the sample; the scatter is 0.1 in $\log(a/b)$ and there is no significant indication of bias in the J-band axial ratios. For comparison with Figure 5.2 the range in ordinate value in (a), (b) and (c) is exactly three times smaller.

$K_s$-band, as found by de Jong (1996) from a sample of 86 face-on spiral galaxies. In their sample, scale length is seen to decrease as the wavelength increases, but not significantly between I and K. A measure of the scale length is provided in the XSC for all of the galaxies in our sample, but given the notorious difficulties with fitting scale lengths, we choose not to use that automated measure here, and only use scale lengths from the SFI2 sample fit "by hand" (see Haynes *et al.* (1999a) for more details on the SFI2 scale lengths). Using these scale lengths we estimate $r_d/r_{21} = 0.4\pm0.1,\ 0.3\pm0.1$ and $0.3\pm0.1$ in J, H and $K_s$ for the SFI2 galaxies (where the error here is the scatter in the sample), and we assume that these ratios hold for all the galaxies in the AGC$z$ sample. The ratio $r_d/r_{21}$ in $K_s$ may be slightly smaller than in H, but this is within the errors. No significant dependence of the ratio on inclination is observed in any band. We note that the $r_d/r_{21}$ ratios imply that $r_{21}^J$ is at only $2.5 \pm 0.6$ scale lengths out in the disk, while in H and $K_s$, $r_{21}$ is still at only $3.3 \pm 1.1$ scale lengths. The commonly reported isophotal radius at I-band is $r_{23.5}$ at 3.5-4 scale lengths which is further out than $r_{21}^{\rm J}$.

If the face-on disks were transparent at $r_{21}$ we can rewrite Eqn 5.9 as

$$r_{21}/r_{21}^\circ = 1 + \delta \log(a/b) \tag{5.10}$$

where $\delta = 0.9 \pm 0.3, 0.7 \pm 0.2$ and $0.7 \pm 0.2$ in J, H and $K_s$ respectively, when we use the $r_d/r_{21}$ values given above. The isophotal radius does not change ($\delta = 0$) if the disk is opaque at $r_{21}$ so $\delta$ must decrease as the disk becomes less transparent. The main limitation on Eqn 5.9 is that it assumes that the photometric profile is exponential, while it is expected that the importance of the bulge light increases in these NIR bands.

### 5.5.2 Are disks transparent at $r_{21}$?

Here we test the often made assumption that the outer disks of galaxies are transparent, especially in the NIR. Suppose that stars and dust are exponentially distributed with scale lengths $r_d^{\rm dust} = r_d^\star = r_d$. The disk opacity at radius $r$ and inclination $i$ is then

$$\tau(r, i) = \frac{\tau^\circ(0) \exp(-r/r_d)}{\cos i} \tag{5.11}$$

where $\tau^\circ(0)$ is the opacity at $r = 0$ in the face-on perspective. There have been many attempts to derive $\tau^\circ(0)$ for spiral galaxies. G94 derive an upper limit in I-band of $\tau_I^\circ(0) < 5$ using statistical arguments with a sample of about 2000 Sc galaxies. A lower estimate of $\tau^\circ(0)$ was obtained by Xilouris *et al.* (1999): they claim that $\tau^\circ(0) < 1$ in 7 edge-on spiral galaxies they model in K, J, I, V and B-bands. Kuchinski *et al.* (1998) derive values of $\tau^\circ(0)$ using BVRIJHK photometry and radiative transfer models for 15 spiral galaxies. They adopt values in the ranges of 0.15-0.6, 0.1-0.4, and 0.05-0.2 for J, H and K respectively. Moriondo *et al.* (1998) find $\tau^\circ(0)$ =0.3-0.5 in H-band from a sample of 154 galaxies. Even if $\tau_I^\circ(0)$ were as high as 5 it is easy to see that at $r_{23.5,\rm I} \sim 3.5 r_d^\star$ the disk is close to

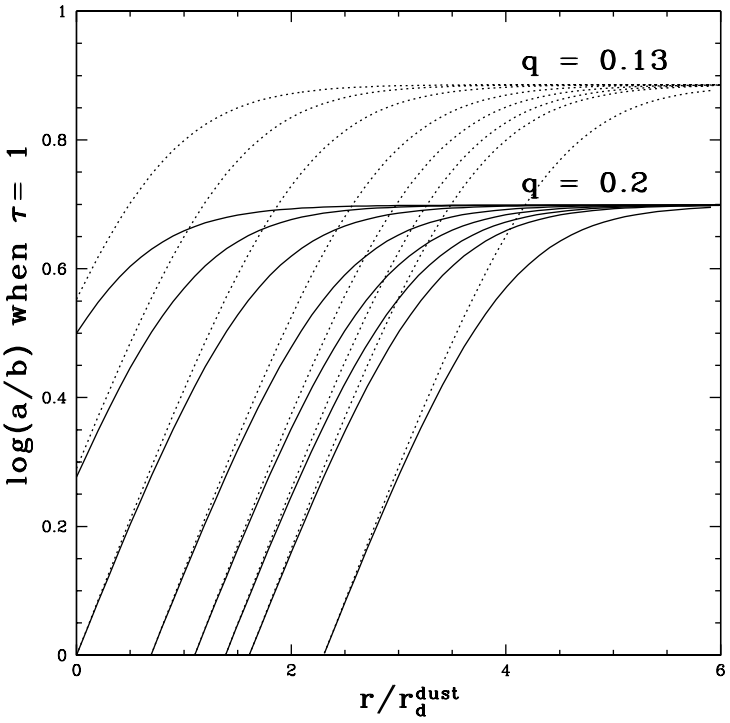



Figure 5.5: The observed axial ratio (assuming an intrinsic axial ratio, $q = 0.13$ for the dotted lines or 0.2 for the solid lines, where $\cos^2 i = ((b/a)^2 - q^2)/(1 - q^2)$) at which a galaxy with a pure exponential disk of dust (with $r_d^{\rm dust} = r_d^\star$) becomes opaque is shown as a function of galactic radius for various central optical depths (0.25, 0.5, 1, 2, 3, 4, 5, 10 from left to right). Far from the center, the disk is transparent at most inclinations, but further in the disk can become optically thick for fairly modest $\tau^\circ(0)$ at high enough inclinations.

transparent out to quite high inclinations. However it has been shown above that $r_{21}$ in J, H and $K_s$ is closer to the center of the disk than $r_{23.5,\rm I}$ so (in the above model) even for relatively low values of $\tau^\circ(0)$ the opacity could become significant in a highly inclined disk. Figure 5.5 shows the inclination at which the galaxy becomes optically thick ($\tau = 1$) plotted as a function of the radial distance for $\tau^\circ(0)$ varying between 0.25 and 10.

At $r_{21}$ in J-band, which is $2.5 \pm 0.6\ r_d$, the disk can become opaque before it is fully inclined for even the smaller $\tau^\circ(0)$. If we interpret the change of slope for high inclinations shown in Figures 5.4 and 5.8a as the onset of $\tau \geq 1$ at $r_{21}$, a "break" for J-band ($r_{21,\rm J} \sim 2.5 r_d$) and H and $K_s$ ($r_{21,\rm H/K} \sim 3.3 r_d$) near $\log(a/b) \sim 0.5$ would suggest that the disk opacity in the J, H and $K_s$ bands, while low, is non-negligible and that even at $r_{21}$ an important fraction of the light is extincted when disks are edge-on.

Recent studies suggest that the dust scale length is larger than that of the

Table 5.1: Samples for the study of $r_{\rm iso}$ and $m_{\rm ext}$ vs. $\log(a/b)$.

| Band | Limit | No. galaxies |
|---|---|---|
| J | $m_{\rm ext} < 11.5$ mag | 1774 |
| J | $r_{21} > 20$ " | 3120 |
| H | $m_{\rm ext} < 11$ mag | 2274 |
| H | $r_{21} > 25$ " | 3137 |
| $K_s$ | $m_{\rm ext} < 10.5$ mag | 1733 |
| $K_s$ | $r_{21} > 30$ " | 2377 |

stars, see for example Moriondo *et al.* (1998) who use $r_d^{\rm dust} = \xi r_d^\star$ with $\xi = 1.5$. In the above model this simply changes the position of $r_{21}$with respect to the dust scale length so that for example $r_{21,\rm J} \sim 2.5 r_d^\star \sim (2.5/\xi) r_d^{\rm dust}$. In that case a lower central face-on opacity is required to explain the behavior.

### 5.5.3 A statistical test for the inclination dependence of isophotal radius

It is possible to test the mean change in isophotal radius with inclination in a statistical way using large samples of galaxies. For the test described below, the biases introduced by the selection function of the sample can be quite severe. In order to keep track of these effects, we use only galaxies north of declination $= -3^\circ$ from the AGC$z$, since that region is known to be more homogeneously and completely sampled in the catalog. Most of the galaxies in the AGC were originally identified by eye from photographic plates on which small, dim galaxies are easier to pick out if they are edge-on. In an attempt to remove this bias we also restrict the sample to B $< 15.5$. The samples are then further reduced to be flux limited (using $m_{\rm ext}$ from the XSC) or angular size limited (using $r_{21}$) within each band. The final 6 subsamples are taken to represent complete flux or angular size limited samples, and are summarized in Table 5.1.

For either size or flux-limited samples, the mean value of $r_{\rm iso} = r_{21}$, expressed in kpc, will increase with distance. In order to remove this simple manifestation of the Malmquist bias, we divide our sample into five distance groups with the same number of galaxies in each. Within each group the mean of $r_{21}$ is then computed in bins of $\log(a/b)$. These bins all have an equal number of galaxies in them ($\sim$30-60 depending on the size of the subgroup). Since there are few galaxies at high inclinations this restricts analysis of subgroups to $\log(a/b) < 0.7$-0.8 in most cases. In each of the bins the values of $< r_{21} >_{\log(a/b)}$ are scaled by the mean of the value for the whole distance group ($< r_{21} >_{\rm dist}$). A relation $c_1 + c_2 \log(a/b)$ is fit to the points and the value of $\delta$ (see Eqn 10) is calculated as $c_2/c_1$. The results in $K_s$-band for both the size and flux-limited sub-samples are shown in Figure 5.6, and are summarized for each band in Table 5.2 along with the values of $\delta$ derived in Section 7.5.1 for the case of an exponential disk which is transparent at $r_{21}$.

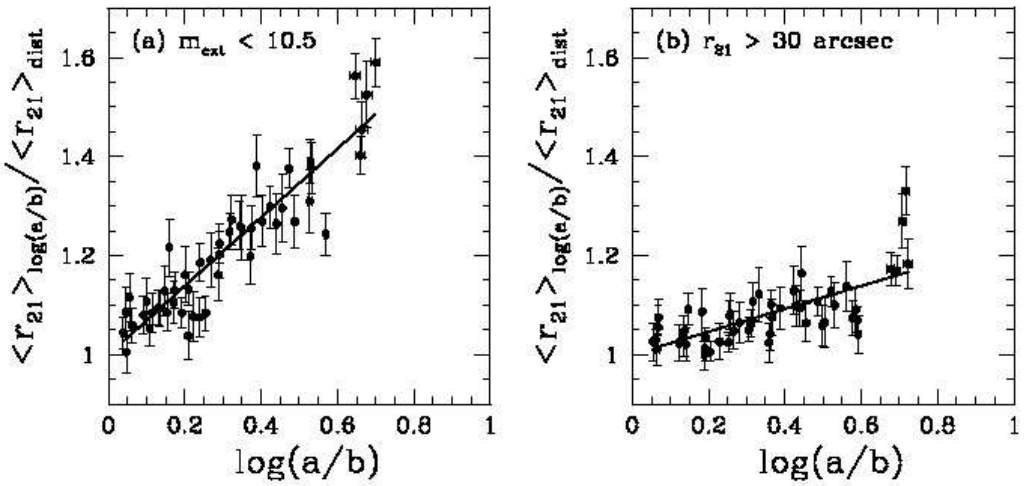



Figure 5.6: Averaged values of the isophotal radius, $r_{21}$ in $K_s$-band in bins of $\log(a/b)$ scaled by the value of all the galaxies in the same distance bin (as described in Section 5.5.3). Fit to this is a function $c_1 + c_2 \log(a/b)$, the plot shows the data and the fit divided by $c_1$. The slope, $\delta = c_2/c_1$ is 0.7 ± 0.1 in the magnitude limited sample (1733 galaxies) and 0.2 ± 0.1 in the radius limited sample (2377 galaxies), where the error is the formal error on determining the slope.

Table 5.2: Measured and estimated values of $\delta$.

| Band | Flux limited | Angular size limited | Transparent exponential disk |
|---|---|---|---|
| J | 1.2± 0.1 | 0.5 ± 0.1 | 0.9 ± 0.3 |
| H | 0.8± 0.1 | 0.3 ± 0.1 | 0.7 ± 0.2 |
| $K_s$ | 0.7± 0.1 | 0.2 ± 0.1 | 0.7 ± 0.2 |

A comparison of panels 6a and 6b, constructed from flux and angular size-limited samples respectively, well illustrates the amplitude of the bias introduced by the character of the sample. This is explained as follows; as disks become more inclined, on average $r_{21}$ moves out and the total magnitude dims (assuming that the galaxies are neither totally transparent throughout the whole disk or totally opaque at $r_{21}$). In a sample defined by a threshold angular size, $r_{\rm min}$, galaxies that in the face-on perspective would be smaller than $r_{\rm min}$ (and thus excluded from the sample) at high inclinations will appear to have a size greater than $r_{\rm min}$ and will be included in the sample. As a result, this sample will exhibit a shallow $r_{\rm iso}$ v. $\log(a/b)$ slope as shown by Figure 6b. Alternatively, in a magnitude limited sample, intrinsically larger galaxies fall below the threshold magnitude if they are edge-on due to the dimming caused by extinction. This will have the effect of steepening the slope, as seen in Figure 6a.

Note that if disks were opaque, $r_{21}$ would not change with inclination ($\delta = 0$),

and this result would be recovered by the analysis of an angular size-limited sample. On the other hand, if the disk dimming due to internal extinction is small or negligible, a flux-limited sample will return the correct value of $\delta$ through an analysis such as that represented in Figure 6a. The presumption of very low dimming at $K_s$-band, supported by the results discussed in Section 4, is further supported by the similarity of the value of $\delta$ in columns 1 and 3 of Table 3 for $K_s$-band. A final choice on the value of $\delta$ in each band needs to be made after an estimate of the amount of internal extinction so will be discussed in Section 6.3. It is probably safe to assume there is very little extinction in $K_s$ so we can conclude here that $\delta_K = 0.7 \pm 0.1$.

## 5.6 Effect of inclination on magnitude

### 5.6.1 Formal corrections for inclination

Note that if the disks of galaxies are completely transparent all the way to the center, then there should be no change in the total magnitude with inclination (*i.e.* $\gamma = 0$) , while the magnitude enclosed within a fixed isophote will brighten as the physical radius at which it is measured moves out. If the disks are completely opaque, then both the total and isophotal magnitudes will dim by an amount 2.5 $\log(a/b)$.

### 5.6.2 A statistical test for the inclination dependence of total magnitude

We test for the inclination dependence of the total magnitude (here taken to be $m_{\rm ext}$ as described in Section 5.3.3) using a method similar to that described in Section 5.5.3. We fit a relation $\Delta M = \gamma \log(a/b)$ to the mean values of the magnitude binned in $\log(a/b)$ within five separate distance groups. We use the flux and angular size limited samples described in Section 5.5.3, since (as for the test in Section 5.5.3) the interpretation must take into account bias introduced by the selection function of the sample. For an angular size limited sample with threshold $r_{\rm min}$, if the disk is not completely opaque all the way through, then $\gamma$ will be increased as intrinsically small and dim galaxies move above $r_{\rm min}$ at high inclinations. If the disks are completely opaque, this type of sample would recover the exact result of $\gamma = 2.5$ as the angular sizes are unaffected by inclination. For a flux limited sample, and if the galaxies are not completely transparent, internal extinction will dim galaxies at higher inclinations and force $\gamma$ to be smaller. If the disks are completely transparent, this sample would recover the exact result of no change of total magnitude with inclination. The change in $\gamma$ with sample selection is observed in all photometric bands explored here (as summarized in Table 5.3), providing further evidence that galaxies are neither completely opaque nor completely transparent in these bands. We note that under the assumption of

Table 5.3: Measured values of $\gamma$.

| Band | Flux limited | Angular size limited |
|---|---|---|
| J | 0.2± 0.1 | 1.2 ± 0.1 |
| H | 0.1± 0.1 | 0.8 ± 0.1 |
| $K_s$ | 0.2± 0.1 | 0.7 ± 0.1 |

little extinction in $K_s$, the flux-limited sample in that band should give a value of $\gamma$ very close to the real value. This implies $\gamma_K = 0.2 \pm 0.1$. In the other bands, J and H, we use this test to provide upper and lower limits to the actual extinction law as parameterized by $\gamma$.

### 5.6.3 The Modified Holmberg Test

Following G94 we use a modified version of the Holmberg test (Holmberg 1958, 1975). Define $\Sigma' = m_{\rm iso} + 5 \log r_{\rm iso}$ as the surface brightness within an elliptical aperture with semi-major axis $r_{\rm iso}$. The original Holmberg test consists of measuring the change of $\Sigma'$ with disk inclination. Unfortunately a similar trend can be found in both opaque and transparent galaxies. If the galaxy is totally opaque we expect that the radius at which a given isophote is measured will not shift with inclination and that the magnitude will dim by 2.5 $\log(a/b)$, so a slope of 2.5 is expected. In the fully transparent case, fixed brightness isophotes will move to larger radii as the galaxies are tilted which will also decrease $\Sigma'$. From Eqn. 8 this geometric dilution alone (*i.e.* not taking into account the change in the isophotal magnitude as the aperture changes) is given by

$$5 \log(r_{21,a}/r_{21,b}) = 5 \log \left[ \frac{1 + 2.302(r_d^\circ/r_{21}^\circ) \log(a/b)_a}{1 + 2.302(r_d^\circ/r_{21}^\circ) \log(a/b)_b} \right] \qquad (5.12)$$

between axial ratios $(a/b)_a$ and $(a/b)_b$. This would give a change in $\Sigma'$ between $\log(a/b) = 0$ and 1 of 1.1 ± 0.3 for the $r_d/r_{21}$ derived in Section 5.1 in H and $K_s$ and 1.4 ± 0.3 in J (where the errors indicate the scatter in $r_d/r_{21}$). These values provide an upper limit to the change since the isophotal magnitude will brighten slightly as the aperture increases.

Here, we do not use the isophotal magnitude, but rather a measure of the total magnitude (extrapolated magnitude from the XSC), to remove the effects of the physical size of the aperture changing with inclination. $r_{\rm iso}$ is respectively $r_{21,\rm J}$, $r_{21,\rm H}$ and $r_{21,\rm K}$ for the three 2MASS bands. In the following discussion we will refer to this radius as $r_{21}$, with the understanding that it is separately measured in each of the three bands. The slope fit to $\Sigma' = m_{\rm ext} + 5 \log r_{21}$ vs. $\log(a/b)$ for galaxies in the AGC$z$ sample with lower inclinations (below $\log(a/b) = 0.5$) is 2.0 ± 0.1 in J, 1.6 ± 0.1 in H and 1.3 ± 0.1 in $K_s$. Since this is higher than the values given above for the transparent case we take it to be indication that there is extinction present in the inner parts of these galaxies, while the outer parts are

largely transparent. This is supported by the radial variation of colors and surface brightness seen in large galaxies in the XSC (Jarrett *et al.* 2003). If the disk is transparent at the edges but not in the center, the change of $\Sigma' = m_{\rm ext} + 5\log r_{\rm iso}$ from face-on to edge-on will be larger than the values for geometric dilution alone and can in fact be larger than 2.5 as there will be some dimming of the magnitude which is dominated by light from the inner parts of the disk.

In order to remove the effect introduced by an inclination dependence of the isophotal radius, we adopt a modified version of the Holmberg test in which the isophotal radius in the face-on view is derived via Eqn 10. The value of $\delta$ which is used in Eqn 10 can significantly change the resulting slope. This is illustrated in Figure 5.7 which shows the standard Holmberg test (for galaxies observed in $K_s$-band) as well as the test with corrections using $\delta = 0.6$, 0.7 and 0.8 (spanning the error range for $\delta_{\rm K}$ discussed in Section 5).

We will discuss the obvious up turn of these relationships further in Section 5.7 but for now deal with the low inclination ($\log(a/b) < 0.5$) and high inclination ($\log(a/b) \geq 0.5$) regions separately. At the low inclinations in $K_s$-band, $\gamma$ changes from 0.31 (with $\delta = 0.6$) to 0.05 ($\delta = 0.8$); a significant difference within the plausible range of $\delta$. As a consequence of this interdependency, the best values of $\delta$ and $\gamma$ must be decided upon together. Considering all the available evidence (Sections 5.1, 5.3 and 6.2) we adopt $\delta = 0.7$ in $K_s$-band, $\delta = 0.7$ in H-band, and $\delta = 0.9$ in J-band. As a comparison, Moriondo *et al.* (1998) derive $\delta_{\rm H} = 0.85 \pm 0.16$ at the same isophotal level (from their sample of 154 galaxies). The results for just these values of $\delta$ in J and H can be seen in Figure 5.8, while the test with the chosen value of $\delta$ in $K_s$-band is shown in Figure 5.7c. We thus derive $\gamma_{\rm J} = 0.48 \pm 0.15$, $\gamma_{\rm H} = 0.39 \pm 0.15$, and $\gamma_{\rm K} = 0.26 \pm 0.15$ for $\log(a/b) < 0.5$ from this test (where the error indicates the variation in the value within the adopted value of $\delta \pm 0.1$. Similar values of $\gamma_H = 0.16 \pm 0.22$ Moriondo *et al.* (1998) and $\gamma_{\rm K} \simeq 0.22$ Tully *et al.* (1998) have been found before, although Graham (2001) and others suggest $\gamma_K \simeq 0$. While the variation of $\gamma$ with the wavelength band depends on the detailed form of the geometric mixing of stars and dust, it is interesting to note that, in the simple geometric case of a foreground absorbing screen model, the extinction curve of our galaxy would yield $\gamma_{\rm J} = 0.5$, $\gamma_{\rm H} = 0.3$, and $\gamma_{\rm K} = 0.2$, if $\gamma_{\rm I} = 1.0$ (see G94, Tully *et al.* 1998, Schlegel *et al.* 1998).

At the higher inclinations (above $\log(a/b) = 0.5$) the modified Holmberg test is not appropriate as the disk is probably not completely transparent at $r_{21}$. The values of $\delta$ used to correct to the face-on value of $r_{21}$ are therefore too large which artificially lowers the change in the average surface brightness and leads to an underestimate for $\gamma$. The standard Holmberg test (*i.e.* $\delta = 0$) does not work either. As discussed above, if there is significant extinction present in the inner parts of the disks where most of the light comes from, but the outer edges are still at least partly transparent, the slope of $\Sigma$ vs. $\log(a/b)$ can be larger than 2.5 and so is obviously an overestimate of $\gamma$. This is observed in J, H and $K_s$ (the slopes are $2.9 \pm 0.2$, $2.4 \pm 0.2$ and $2.4 \pm 0.2$ respectively), providing evidence that the most inclined galaxies are not totally opaque or transparent at $r_{21}$, and that there is significant extinction in

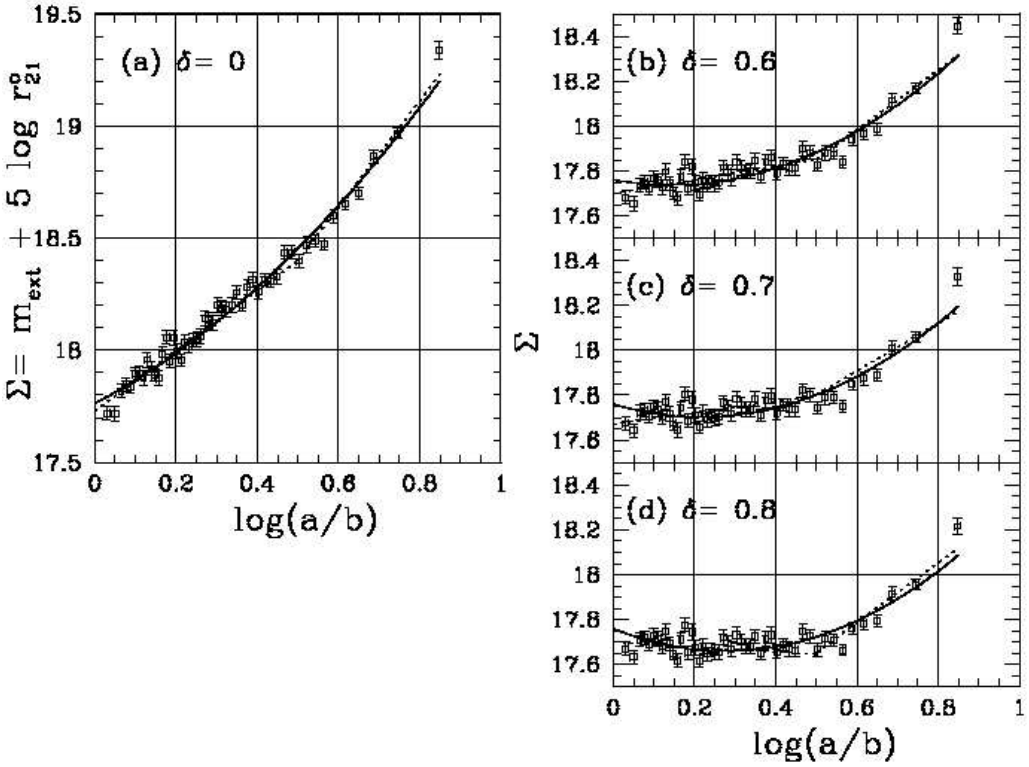



Figure 5.7: Holmberg test in $K_s$-band (see Section 5.6.3). The values of $\delta$ shown are that used to correct the isophotal radius to the face-one value using $r_{21}/r^{\circ}_{21} = 1+\delta \log(a/b)$. A bi-linear fit is shown (dotted line) with the break at $\log(a/b) = 0.5$. The fitted slopes are (a) 1.34 and 2.38, (b) 0.31 and 1.34, (c) 0.26 and 1.06, and (d) 0.05 and 1.07. The error on the slope is on the order of 0.1 for the low inclinations and 0.2 for the high inclinations. Also shown is a quadratic fit for comparison (solid line). This smooth function may be more desirable, but the unphysical upturn at low $\log(a/b)$ may make the bi-linear law more useful. Points are averages in bins of $\log(a/b)$ with roughly 300 galaxies per bin, where the error bars show the error in determining the mean in the bin.

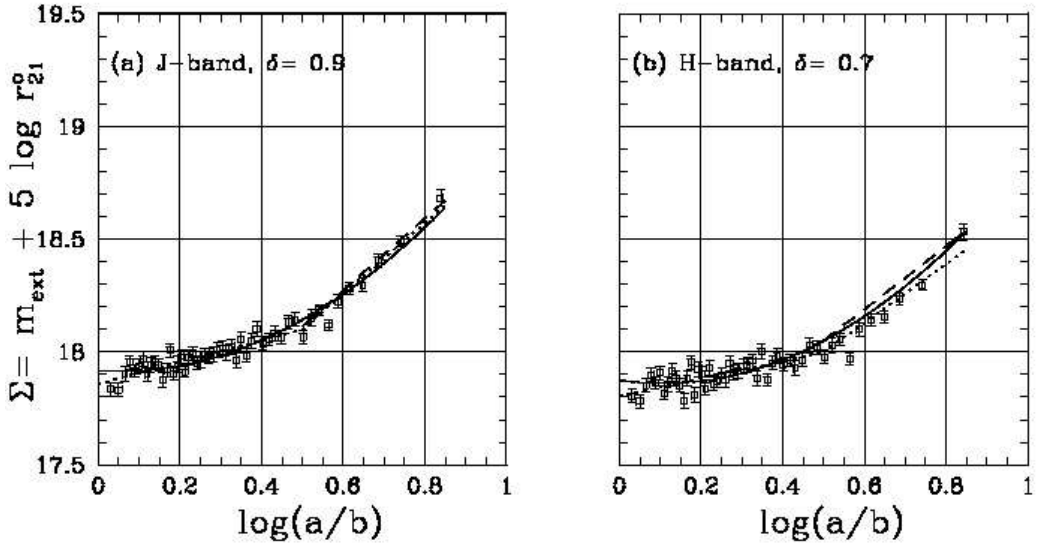



Figure 5.8: Modified Holmberg test in J and H-bands with the chosen value of $\delta$ (see Section 6.3). Shown is a bi-linear fit to both cases where the break is at $\log(a/b) = 0.5$ (dotted line). The slopes are 0.48 ± 0.1 and 1.57 ± 0.2 in J-band (a), and 0.39 ± 0.1 and 1.30 ± 0.2 in H-band (b). Also shown (long dashed line) is the adopted correction. The solid lines show a quadratic fit for comparison.

the central regions. Since the extinction is lowest in $K_s$ we expect that the disk is closest to transparent at $r_{21}$ in this band and therefore adopt the slope of the modified Holmberg test here to give a tentative value of $\gamma_K \simeq 1.1 \pm 0.2$ for the more inclined galaxies (up to $\log(a/b) \sim 0.85$). We then use the slopes of the reddening in J-$K_s$ and H-$K_s$ (above $\log(a/b) = 0.5$: $\gamma_J - \gamma_K = 0.46 \pm 0.05$ and $\gamma_H - \gamma_K = 0.31 \pm 0.05$ from Figure 4.) to suggest $\gamma_J \simeq 1.6 \pm 0.2$ and $\gamma_H \simeq 1.4 \pm 0.2$. The difference between the bi-linear and quadratic fit is quite small (as can be seen in Figure 5.8), so we also provide a smooth fit to the points giving $\gamma_J = -0.12(15) + 1.14(15)\log(a/b)$, $\gamma_H = -0.25(15) + 1.12(15)\log(a/b)$ and $\gamma_K = -0.53(15) + 1.23(15)\log(a/b)$. Below $\log(a/b) = 0.1, 0.2$, and 0.4 in J, H and $K_s$ respectively the value for the correction should be zero – the upturn in the quadratic fit at low inclination is obviously unphysical.

## 5.7 Photometric Model

Here we investigate a simple photometric model which can be used to explain the upturn in the $\Delta M$ vs. $\log(a/b)$ relation at high $\log(a/b)$ seen in all three bands. The model used is that described in Section 9 of G94 which is based on the "triple exponential" model of Disney *et al.* (1989). This model assumes that the dust is distributed in the disk with an exponential scale length equal to the stars and that

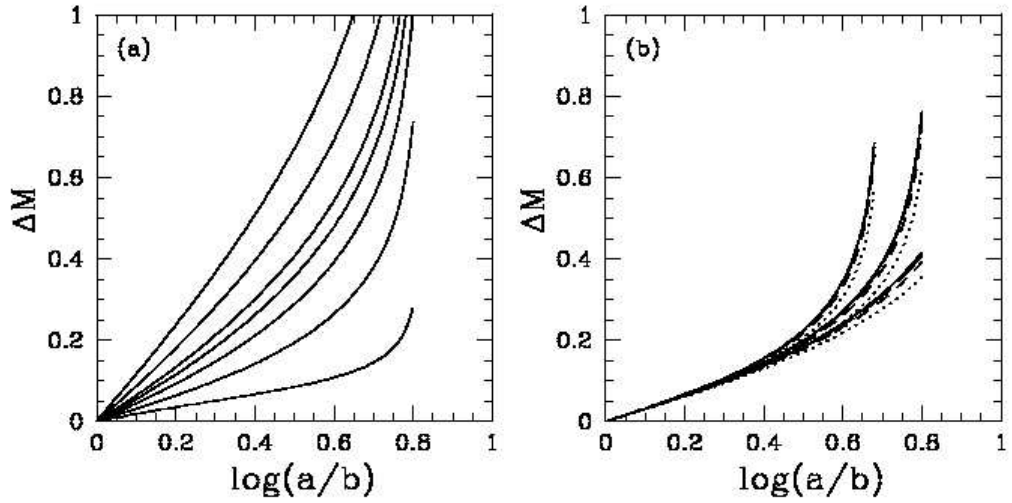



Figure 5.9: Difference between the "observed" magnitude and the face-on value from the "triple exponential" model of Disney *et al.* (1989) which assumes dust and stars are exponentially distributed with the same scale length. We vary the intrinsic axial ratio $q$, the ratio $\zeta$ between the scale heights of the dust and stars and the central face-on opacity, $\tau^{\circ}(0)$. (a) Results for $\zeta = 0.5$, $q = 0.15$ and $\tau^{\circ}(0) = 0.1, 0.5, 1.0, 1.5, 2, 4, 10$ (from right to left). (b) Results for $\tau^{\circ}(0) = 0.5$ and $q = 0.1, 0.15, 0.2$ (right to left). The small effect of varying $\zeta$ between 0.1 (dotted line), 0.4 (short dashed), 0.7 (long dashed) and 1.0 (solid line) is also shown.

the $z$ distributions are also exponential with a ratio $\zeta$ between the scale height of the dust and the stars. The face-on central surface brightness, $\tau^{\circ}(0)$ can be specified, as can the ratio, $q$, between the scale height and scale length of the stars. We use the "standard galaxy" of G94 which has 7% of the light in a central bulge.

Figure 5.9 shows the difference between the magnitude at a given axial ratio and the face-on magnitude calculated for various inputs to the model. In the model the upturn becomes more noticeable with increasing $q$ (*i.e.* as the disk becomes thicker) and as the central face-on opacity decreases. The ratio between the thickness of the disk in the dust and stars has a much smaller effect as shown in Figure 5.9b.

Figure 5.10 shows our "best fit" to the Holmberg test points (Section 5.6.3). Note that at high inclinations the points are artificially lowered (see discussion in Section 5.6.3). The simple photometric model described here can explain the observed behavior. While the dependence of the models on the dust-to-stars thickness ratio is weak, best fit models favor low values of $\zeta$. This is consistent with the expectation that stellar disks may appear somewhat thicker in NIR light, as they are dominated by an older stellar population. The models shown in Figure 5.10 were computed for $\zeta = 0.5$. The other parameters of the model are $\tau^{\circ}(0) = 1.1$, $q = 0.14$ in J-band, $\tau^{\circ}(0) = 0.7$, $q = 0.14$ in H-band and $\tau^{\circ}(0) = 0.3$, $q = 0.15$ in

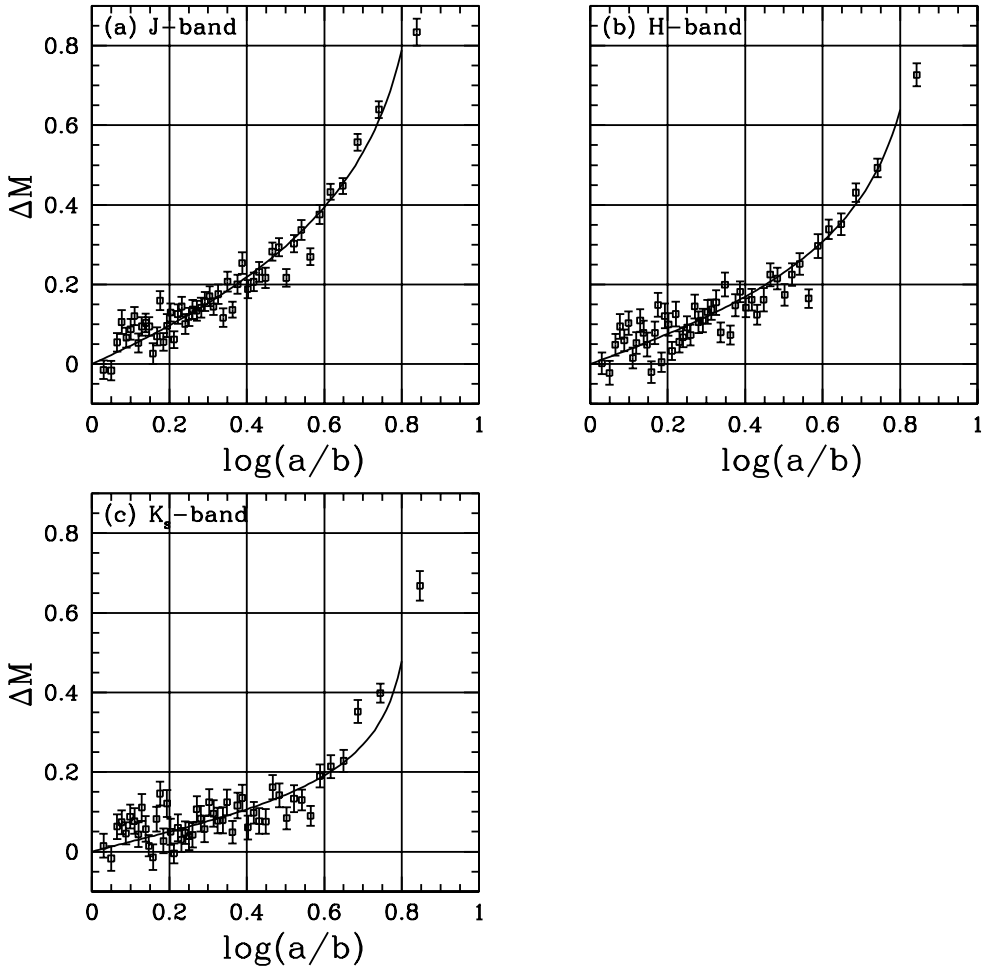



Figure 5.10: Shown here are the data points from the Holmberg test in J-band (from Figure 8a) in (a), H-band (from Fig 8b) in (b) and $K_s$-band (from Fig 7c) in (c), offset to zero at $\log(a/b) = 0$. The solid lines show the photometric model which best fits (by eye) the data. All models are for $\zeta = 0.5$. For the J-band data (a), $\tau^\circ(0) = 1.1$ and $q = 0.14$; for H-band (b), $\tau^\circ(0) = 0.7$ and $q = 0.14$ and for $K_s$-band (c), $\tau^\circ(0) = 0.3$ and $q = 0.15$.

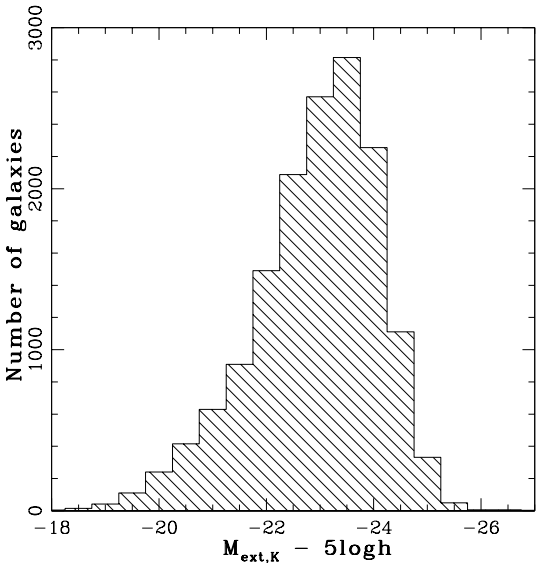



Figure 5.11: Distribution of total magnitude in $K_s$-band of galaxies in the AGC$z$ sample.

K-band. Reassuringly, the central face-on opacity of the best fit model decreases with increasing wavelength. Given the uncertainties in the Holmberg test (see Section 6.3) this model should be taken with caution, but does provide a plausible explanation for what is observed.

## 5.8 Luminosity dependence

Here we use the AGC$z$ sample of 15,244 galaxies to search for luminosity dependences of the extinction laws, as was done in both Giovanelli *et al.* (1995) and Tully *et al.* (1998). As a measure of the total luminosity of the galaxy we use $\mathrm{M_{ext,K}} - 5\log h$ in K-band since this is least affected by internal extinction. The luminosity distribution is shown in Figure 5.11. The peak of the distribution is at $\mathrm{M_{ext,K}} - 5\log h = -23$, which is near to $M_\star$ in K-band (Kochanek *et al.* 2001) and most of the galaxies in the sample are within one magnitude of this.

The expected dependence is that brighter galaxies will show more internal extinction at a given inclination than dimmer ones. This is due both to the increase in physical size (and thus optical path lengths) and to the increase in metallicity (and thus presumably dust content) in the more luminous galaxies.

### 5.8.1 Isophotal radius

Here we derive a parametric relation for the change of $\delta$ in $r_{21}/r^\circ_{21} = 1 + \delta\log(a/b)$ with total luminosity as measured by $\mathrm{M_{ext,K}} - 5\log h$. We discussed the expected value of $\delta$ for an exponential disk with scale length $r_d$ which is transparent at

$r_{21}$ in Section 5.1. This is given by $2.302 r_d/r_{21}$ and is shown by the points in Figure 5.12 for galaxies from the SFI2 sample in 9 bins of luminosity (each with an equal number of galaxies). There is a clear trend for the ratio $r_d/r_{21}$ (and thus $\delta$ if the disks are transparent at $r_{21}$) to decrease with luminosity, as was also found by Giovanelli *et al.* (1995) in I-band, who also discuss why this trend is to be expected. We fit a cubic to these points which we truncate at both the highest and lowest luminosities. These fits are shown by the solid lines in Figure 5.12 and the fit parameters are listed in Table 5.4.

### 5.8.2 Magnitude

Here we apply the "modified Holmberg test" discussed in Section 5.6.3 to the full AGC$z$ sample to investigate the dependence of internal extinction (as parameterized by $\gamma$ in Eqn 7.7) on galaxy luminosity. We divide the sample into 10 luminosity bins with $\sim 1500$ galaxies per bin. We correct the isophotal radius to the face-one view using the cubic fit to the points in Figure 5.12. We then fit a single linear law to $\Sigma$ vs. $\log(a/b)$ for each luminosity bin as the subdivision in luminosity bins restricts statistics, especially at high inclinations.

The extent of the luminosity dependence of $\gamma$ depends critically on the value $\delta$ used to correct radii to the face-on values. In the modified Holmberg test, an over-estimate of $\delta$ leads to an under-estimate of $\gamma$ (and vice-versa). Since $\delta$ clearly decreases with luminosity, using a constant value of $\delta$ for all galaxies thus leads to an over-estimate of $\gamma$ at low luminosities and an under-estimate at high luminosities and suppresses the expected luminosity dependence. The cubic fit in Figure 5.12 follows luminosity dependence of $\delta$ (under the assumption of transparency at $r_{21}$) and should be used here. The values of $\gamma$ derived by using this $\delta$ are shown in Figure 5.13 as a function of luminosity. We find that over much of the range of luminosities the value of $\gamma$ is roughly constant in each band. In support of this we observe that the slope of the reddening does not change much with luminosity. It is clear that at low luminosities the extinction in these bands does decrease significantly and (unlike as found for galaxies in I-band by Giovanelli *et al.* 1995) does fall off to zero for galaxies less luminous than $\mathrm{M_{ext,K}} - 5\log h = -20$, -20.7 and -20.9 in J, H and $\mathrm{K_s}$ respectively. The solid line in Figure 5.13 shows our adopted luminosity dependence for $\gamma$, which is broken into two regions. The relation is $\gamma_J = -0.26x + 0.77$, $\gamma_H = -0.26x + 0.58$, and $\gamma_K = -0.13x + 0.31$, for $x > 0.8$, and $\gamma_J = -0.04x + 0.60$, $\gamma_H = -0.01x + 0.38$, and $\gamma_K = 0.20$, for $x < 0.8$ (where $x = \mathrm{M_{ext,K}} - 5\log h + 23$). It should be noted that a straight line can fit within the errors on the points (dotted line in Figure 5.13), which are $\pm 0.15$ in $\gamma$.

If the assumption of transparency at $r_{21}$ is not valid then we are over-estimating $\delta$ and thus under-estimating $\gamma$. High luminosity galaxies have more extinction, but $r_{21}/r_d$ is also larger in these galaxies which could mean that they are more likely to be transparent at $r_{21}$ than low luminosity galaxies. What bias the assumption of transparency might introduce into this determinations of the luminosity dependence of $\gamma$ is not clear.

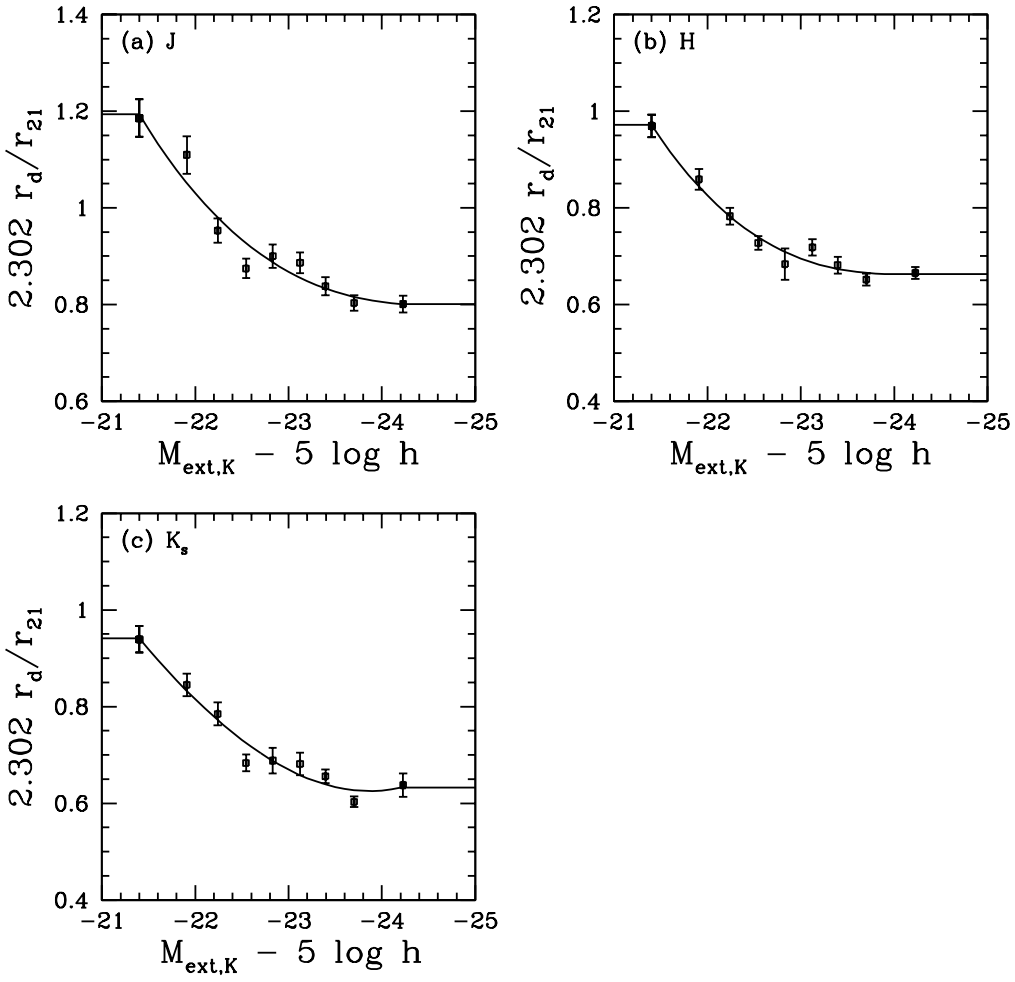



Figure 5.12: The change of $2.302 r_d/r_{21}$ with luminosity for galaxies in the SFI2 sample. This parameter approximates $\delta$ if disk are nearly transparent at $r_{21}$. Data points show the averages in 9 bins of luminosity (with equal numbers of galaxies), while the solid lines show a cubic fit to the points truncated for the highest and lowest luminosity galaxies to be the value of the fit at $\mathrm{M_{ext,K}} - 5\log h = -21.4$ and -24.2 respectively. The fits are respectively for $\mathrm{M_{ext,K}} - 5\log h > -21.4$, between -21.4 and -24.2 and brighter than -24: $\delta = 1.19$, $\delta = 0.87 + 0.11x + 0.05x^2 + 0.007x^3$, $\delta = 0.80$ for J-band (a); $\delta = 0.97$, $\delta = 0.70 + 0.07x + 0.05x^2 + 0.009x^3$, $\delta = 0.66$ for H-band (b); and $\delta = 0.94$, $\delta = 0.67 + 0.10x + 0.05x^2 - 0.004x^3$, $\delta = 0.63$ for $\mathrm{K_s}$-band (c). $x = \mathrm{M_{ext,K}} - 5\log h + 23$ in all cases.

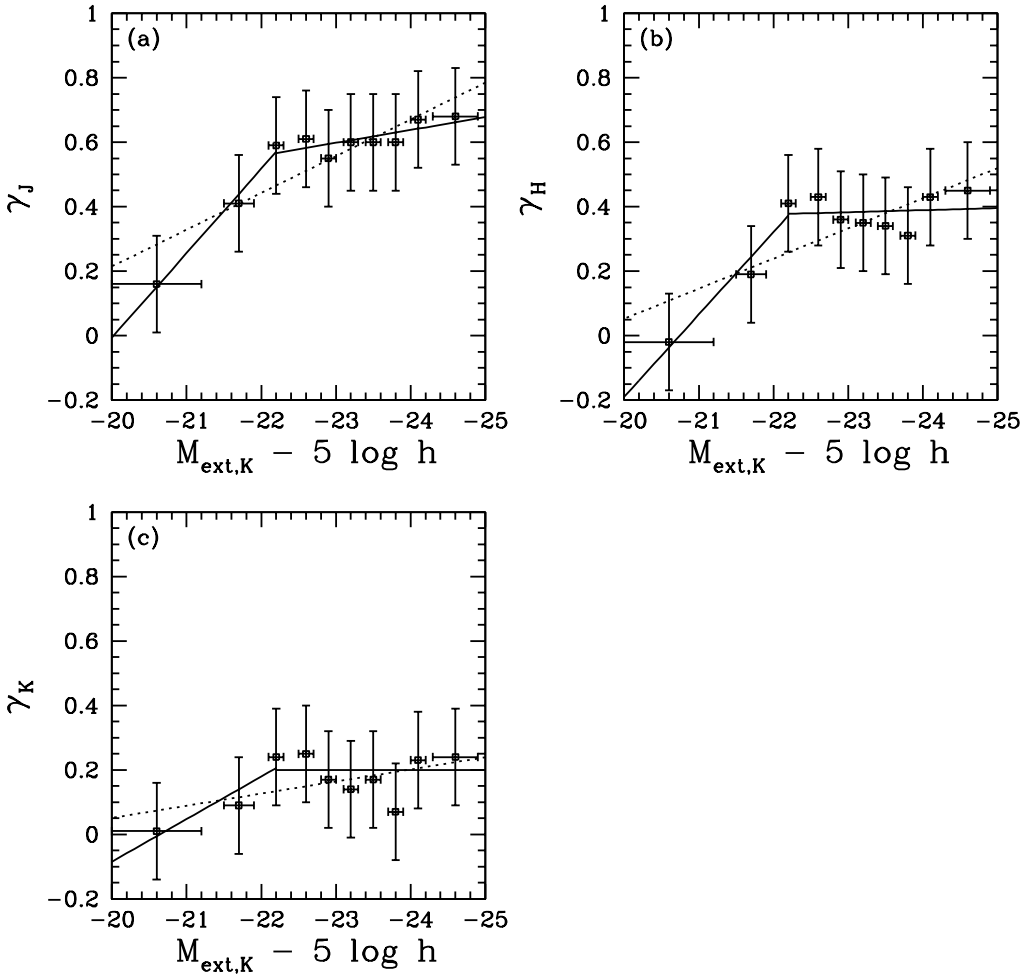



Figure 5.13: Values of $\gamma$ as a function of luminosity in (a) J-band, (b) H-band and (c) K-band derived using the modified Holmberg test with $\delta$ as given by the truncated cubic fit to the points in Figure 5.12. The dotted line shows a straight line fit to the points, the solid line our adopted luminosity dependence.

## 5.9 Conclusions

Two samples of spiral galaxies are constructed, both of which have photometry from 2MASS and redshifts from the AGC. For the smaller sample (which has over 3000 galaxies), I-band photometry is also available. We apply a variety of statistical tests to look for disk inclination dependences in these galaxies. The results of these tests can be highly sensitive to the selection function of the sample and some interdependencies exist, but taken together they provide reliable information on the average internal extinction in the galaxies. We parameterize internal extinction via Eqn 7 and change of the isophotal radius via Eqn 10; these results are summarized in Tables 5.4 and 5.5, where the numbers between brackets indicate the error on the last digit of the parameter value.

From the trends of NIR color with inclination in the SFI2 sample, we derive a firm lower limit to the total extinction in J and H-band of $\gamma_{\rm J} = 0.3 + \gamma_{\rm K}$ mag and $\gamma_{\rm H} = 0.1 + \gamma_{\rm K}$ mag respectively. The scatter in these trends is on the order of 0.1 mag, while the statistical error on determining the slope is 0.01 mag. Using the same argument, we derive a lower limit on the extinction in I-band of $0.9 + \gamma_{\rm K}$ mag, which when compared with those derived by G94 and Tully *et al.* (1998), is consistent with very low extinction in $K_s$-band. Using the much larger AGC$z$ sample, we note that the simple linear relation given by Eqn 7.7 does not adequately describe the variation of the 2MASS colors with inclination, but an upturn at high inclinations takes place instead which we fit with a bi-linear law.

The radius $r_{21}$ is seen to be closer to the center of the disk in J, H and $K_s$ ($\sim$ 2-3 scale lengths) than $r_{23.5}$ in I-band (at 3.5-4 scale lengths), and we work through a simple model to estimate at what inclination the disk might become opaque at that radius for a given central face-on opacity. Using samples defined according to different selection criteria, we explore the inclination dependence of $r_{21}$ and compare the data with the dependence that would be expected for pure exponential disks which are transparent at $r_{21}$ at all inclinations. *We find that complete transparency at $r_{21}$ is inconsistent with the data of very nearly edge-on galaxies.* Upper and lower limits are estimated for $\delta$ (as defined by Eqn 7.10), and we adopt as most probable values $\delta_{\rm J} \simeq 0.9 \pm 0.1$, $\delta_{\rm H} = 0.7 \pm 0.1$ and $\delta_{\rm K} = 0.7 \pm 0.1$.

Tracking the flux dependence on inclination and using a modified version of the Holmberg test we investigate the amount of internal extinction in disks in the three bands. This analysis confirms that a simple value of $\gamma$ (as defined by Eqn 7) is not adequate to describe extinction for all values of $\log(a/b)$. Because of this we fit a bi-linear law fitting separately high and low inclination systems as separated by $\log(a/b) = 0.5$. The value of $\gamma$ calculated from this test is sensitive to how the isophotal radii are corrected to the face-on value (*i.e.* the value of $\delta$ that is used in Eqn 10) and can change by a significant amount. Using the adopted values of $\delta$ we find $\gamma_{\rm J} = 0.48 \pm 0.15$, $\gamma_{\rm H} = 0.39 \pm 0.15$, and $\gamma_{\rm K} = 0.26 \pm 0.15$ for $\log(a/b) < 0.5$. If $\delta$ is increased, $\gamma$ decreases and vice-versa.

At the *higher inclinations* the modified Holmberg test is not appropriate as we expect a much smaller variation of $r_{21}$ with inclination than is corrected for.

Table 5.4: Summary of results for $\delta$ in $r_{21}/r_{21}^{\circ} = 1 + \delta \log(a/b)$.

| Method | J-band | H-band | $K_s$-band |
|---|---|---|---|
| For transparent exponential disks | 0.9(3) | 0.7(2) | 0.7(2) |
| | | | |
| Statistical test | | | |
| lower limit | 0.6(1) | 0.4(1) | 0.2(1) |
| upper limit | 1.2(1) | 0.8(1) | 0.7(1) |
| | | | |
| Adopted | 0.9(1) | 0.7(1) | 0.7(1) |
| | | | |
| Luminosity dependence | $0.87 + 0.11x$ | $0.70 + 0.07x$ | $0.67 + 0.10x$ |
| ($x = \mathrm{M_{ext,K}} - 5 \log h + 23$) | $+0.05x^2 + 0.007x^3$ | $+0.05x^2 + 0.009x^3$ | $+0.05x^2 - 0.004x^3$ |

Table 5.5: Summary of results for $\gamma$ in $\Delta M = \gamma \log(a/b)$

| Method | J-band | H-band | $K_s$-band |
|---|---|---|---|
| Reddening test | | | |
| All SFI2 | $0.3(1)+\gamma_K$ | $0.1(1)+\gamma_K$ | – |
| | $0.2(1)+\gamma_H$ | | |
| AGC$z$ | | | |
| low inclination[a] | $0.15(2)+\gamma_K$ | $0.05(2)+\gamma_K$ | – |
| | $0.10(2)+\gamma_H$ | – | – |
| high inclination[a] | $0.46(5)+ 0.08/\log(a/b)$ | $0.15(5) + 0.025/\log(a/b)$ | – |
| | $0.31(5) + 0.05/\log(a/b)$ | – | – |
| Statistical test | | | |
| lower limit | 0.2(1) | 0.1(1) | 0.2(1) |
| upper limit | 1.2(1) | 0.8(1) | 0.7(1) |
| Holmberg test[b] | | | |
| low inclination[a] | 0.48(15) | 0.39(15) | 0.26(15) |
| high inclination[a] | $\geq 1.6 + 0.24/\log(a/b)$ | $\geq 1.3 + 0.20/\log(a/b)$ | $\geq 1.1 + 0.13/\log(a/b)$ |
| Adopted | | | |
| low inclination[a] | 0.48(15) | 0.39(15) | 0.26(15) |
| high inclination[a] | $[1.6(2) + 0.24/\log(a/b)]$ | $[1.4(2)+0.20/\log(a/b)]$ | $[1.1(2) + 0.13/\log(a/b)]$ |
| Luminosity dependence | | | |
| $(x = M_{ext,K} - 5\log h + 23)$ | | | |
| $x > 0.8$ | $-0.26x + 0.77$ | $-0.26x + 0.58$ | $-0.13x + 0.31$ |
| $x < 0.8$ | $-0.04x + 0.60$ | $-0.01x + 0.38$ | 0.20 |

[a] Limit between low and high inclinations is $\log(a/b) = 0.50$.

[b] Assumes $\delta$ =0.9, 0.7 and 0.7 in J, H and $K_s$ respectively.

This implies that the measured slope is only a lower limit to the value of $\gamma$ in Eqn 7.7. We expect that the limit will be closest to the actual value of $\gamma$ in $K_s$ where the extinction is lowest and therefore adopt $\gamma_K = 1.1 \pm 0.2 + 0.13/\log(a/b)$. Using information on reddening we then derive $\gamma_J = 1.6 \pm 0.2 + 0.24/\log(a/b)$ and $\gamma_H = 1.4 \pm 0.2 + 0.20/\log(a/b)$.

We explore a simple photometric model for extinction due to dust in spiral galaxies. In the model the dust is distributed exponentially both radially and in the $z$-direction. The scale length of the dust is assumed to be the same as the stars, while a ratio $\zeta$ is assumed between the scale heights. The "best fit" models to the data (all with $\zeta = 0.5$) suggest a central face-on opacity, $\tau^\circ(0) = 1.1$ and intrinsic axial ratio, $q = 0.14$ for J-band, $\tau^\circ(0) = 0.7$ and $q = 0.14$ for H-band and $\tau^\circ(0) = 0.3$ and $q = 0.15$ for $K_s$-band. This model explains well the upturn in the extinction at high inclinations, which becomes more obvious for lower values of $\tau^\circ(0)$.

In Tables 7.4 and 7.5 we give estimates of our favored solutions for $\delta$ in Eqn 7.10 and $\gamma$ in Eqn 7.7 as compromises of derivations from different methods. They are listed in the row labelled "Adopted".

Finally, we explore the luminosity dependence of $\delta$ and $\gamma$. Under the assumption of transparency at $r_{21}$ the value of $\delta$ decreases with luminosity. We use the modified Holmberg test to explore the luminosity dependence of $\gamma$ and find that the extinction drops off to zero below a luminosity of $M_{ext,K} - 5\log h = -20$, -20.7 and -20.9 in J, H and $K_s$ respectively. and is roughly constant at $\gamma = 0.61$, 0.39 and 0.19 at the higher luminosities. There is marginal evidence of further increase at the very highest luminosities. The adopted luminosity dependences are also listed in Tables 7.4 and 7.5.

We have explored the commonly held view that there is little internal extinction in external galaxies at NIR wavelengths, especially $K_s$-band. We have shown that except for the least luminous galaxies, there is evidence for internal extinction (which increases with luminosity), and that in the most inclined galaxies the extinction becomes significant.

# Chapter 6

# A Local Field TF sample from the SFI++

## 6.1 Introduction

In this Chapter we select from the SFI++ Tully-Fisher (TF) sample a sample of galaxies suitable for the study of the local peculiar velocity field. The full SFI++ introduced in Chapter 4 contains 5653 spiral galaxies having both I-band photometry and either HI or ORC velocity widths, which can be used to measure a Tully-Fisher distance (or peculiar velocity). 911 of these galaxies which lie in the vicinity of 36 clusters have been used in that Chapter to derive a template TF relation. There is an introduction to the TF relation and a discussion of the observables needed to make a TF measurement in that Chapter which we will not repeat here.

## 6.2 Sample Selection

In order to study the local velocity field, we extract from the full SFI++ a sample of galaxies in the local universe. We make the volume cut at $H_0 d = 6000$ km s$^{-1}$ (or d = 86 Mpc/$h_{70}$) in TF distance. This is done to minimize the impact of the edge of catalog bias. If the cut were instead made in redshift, at large distances, galaxies with negative peculiar velocities would preferentially make it into the sample.

To minimize the impacts of non-linear virial motions on the sample, we require that none of the galaxies are included in the TF template discussed in Chapter 4, nor are they assigned to any nearby large clusters or groups (with more than about 15 members).

We include only galaxies with inclinations larger than 45°, and rotational widths larger than 178 km s$^{-1}$ ($\log W > 2.25$). Less inclined, or smaller width galaxies have too large errors to be useful for peculiar velocity studies.

Finally we remove any galaxies which have an offset from the Tully-Fisher template of more than $4\sigma$, where $\sigma = 0.43 - 0.296(\log W - 2.5)$, the total observed scatter in the template TF relation as found in Chapter 4; or which have implied peculiar velocities larger than 1500 km s$^{-1}$. This small fraction of galaxies (about 8% of the total) must have either significant intrinsic offsets from the TF template or erroneous data and therefore are not interesting for studying the mean velocity field. If the offsets are instrinsic they may however be very interesting for studies of galaxy evolution, because they must either be significantly dimmer or brighter than normal galaxies of the same mass.

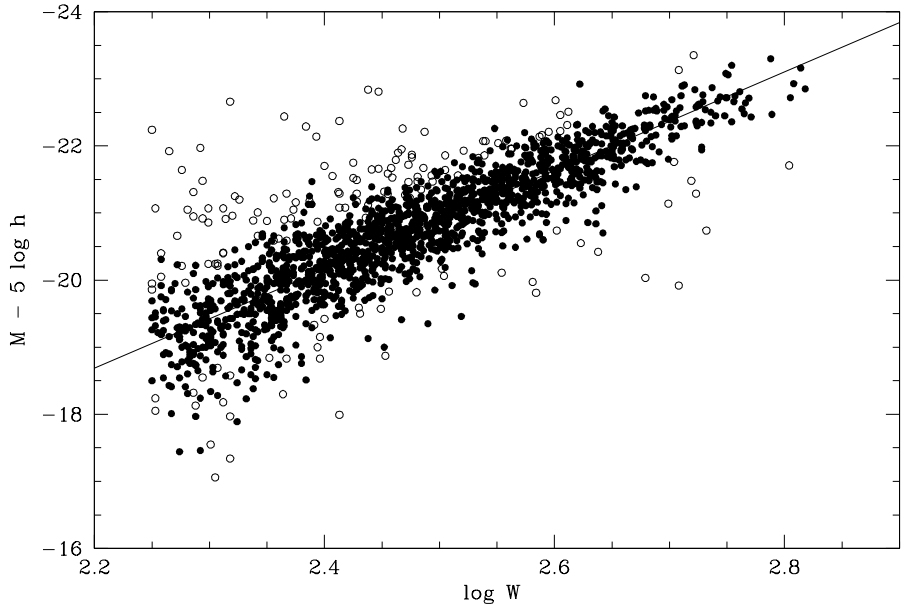



Figure 6.1: Tully-Fisher (TF) relation for field galaxies within 86 Mpc/$h_{70}$. Galaxies with inclinations less than 45° or widths, $\log W < 2.25$ have been removed. The open circles show galaxies more than $4\sigma$ away from the template relation, or which have implied peculiar velocities larger than 1500 km s$^{-1}$.

The final sample contains 1583 galaxies which are shown on the Tully-Fisher relation in Figure 6.1. That figure reveals a slight tendency for low mass galaxies to lie below the TF relation (meaning they are dimmer than expected), which has also been observed in previous TF samples (Giovanelli *et al.* 1997b), and may be hinting at an intrinsic non-linearity of the TF relation. Figure 6.2 shows the size and trends of the peculiar velocity and errors with observed CMB velocity. Here you can see that the low mass galaxies, seen preferentially nearby, create a region in which all peculiar velocities are negative. This spurious effect must be recalled when interpreting the peculiar velocity field from this sample. In both figures galaxies which made the cut are shown as filled circles, galaxies which have been removed are shown as open circles.

### 6.2.1 Grouping

The final step in compiling our data set of velocity field tracers in the local universe is to combine the peculiar velocities of galaxies in small groups. In the sample of 1583 galaxies, there are 138 small groups with 2, 3 or 4 galaxies with peculiar velocity measurements. Information on group assignments is provided in Springob (2005). The peculiar velocities of all galaxies in a group are combined into a weighted average, and the group CMB velocity, RA and DEC are used to give one velocity field tracer with error improved by $\sqrt{N}$. At this point we also add

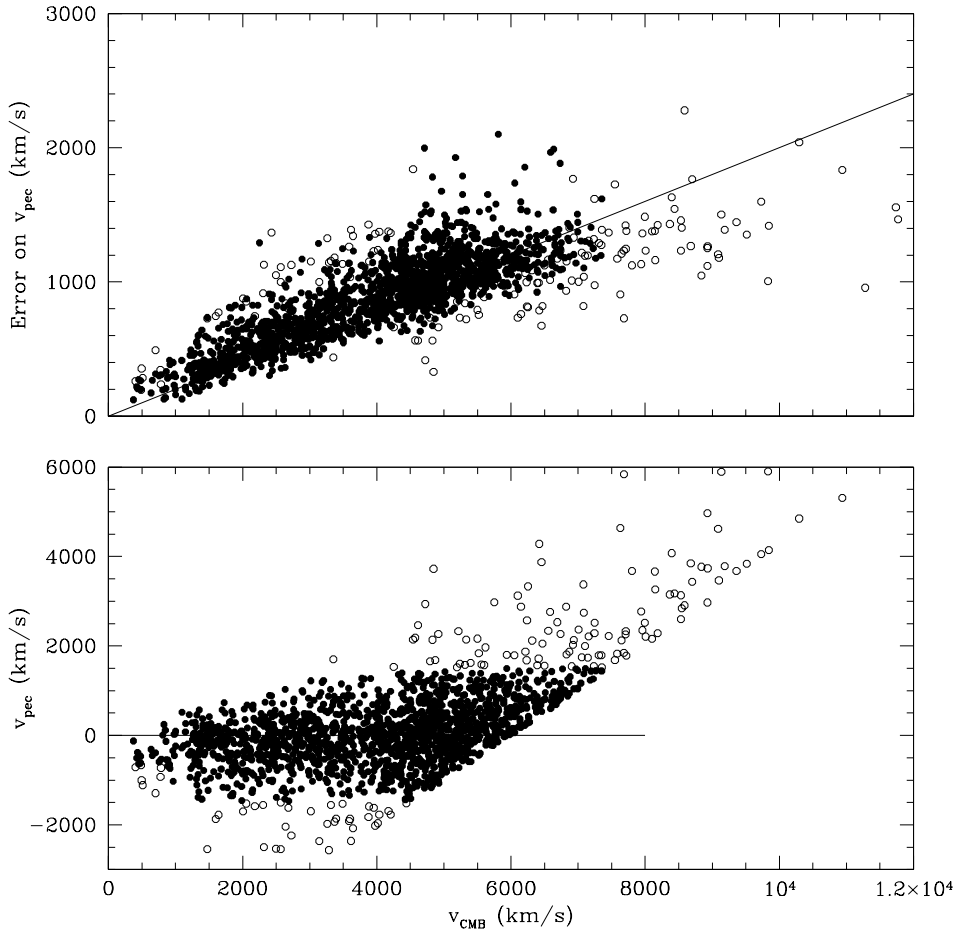



Figure 6.2: Peculiar velocity (lower panel) and errors (upper panel) as a function of velocity for field galaxies within a TF distance of 86 Mpc/$h_{70}$ (or 6000 km s$^{-1}$). The open circles show galaxies more than $4\sigma$ away from the template relation, or which have implied peculiar velocities larger than 1500 km s$^{-1}$. The solid line on the upper plot shows a line of 20% distance error.

in peculiar velocities found for the 23 clusters in the template sample (Chapter 4) which are within a distance of 6000 km s$^{-1}$ (or 86 Mpc/$h_{70}$).

The final step results in a velocity field tracer sample of 1425 objects, 1264 of which are individual galaxies, 23 are large clusters, and 138 are small groups.

## 6.3 Peculiar Velocities from Tully-Fisher

Figure 6.1 shows galaxies in the local SFI++ plotted on a Tully-Fisher relation. In this diagram, the magnitude has been calculated by assuming zero peculiar velocity for the galaxy, *i.e.*

$$M - 5\log h = m - 5\log v_{\rm obs} - 15 \tag{6.1}$$

where $M$ is the absolute magnitude, $h = H_0/100$ km s$^{-1}$ Mpc$^{-1}$, $m$ is the apparent magnitude and $v_{\rm obs}$ is the observed radial velocity in km s$^{-1}$. Under the assumption that each galaxy should lie on the template relation, the offsets, $\Delta M$ in Figure 6.1 are entirely due to the peculiar velocity of the galaxy ($v_{\rm pec} = v_{\rm obs} - H_0 d$), such that

$$\Delta M = 5\log\left(\frac{H_0 d}{v_{\rm obs}}\right), \tag{6.2}$$

or

$$v_{\rm pec} = v_{\rm obs}(1 - 10^{\frac{\Delta M}{5}}). \tag{6.3}$$

A positive offset in from the Tully-Fisher relation (meaning the galaxy is dimmer than expected, or below the line) therefore implies a negative peculiar velocity (*i.e.* the galaxy is moving towards us in the CMB reference frame and therefore its observed velocity places it at a smaller distance than it is really at so we underestimate its intrinsic brightness); conversely a negative offset implies a positive peculiar velocity.

The error on the peculiar velocity is calculated by combining measurement errors, both on the rotational width, and absolute magnitude with the total observed scatter in the TF relation, which we measure in Chapter 4 to be $\epsilon_{\rm obs} = 0.43 - 0.269(\log W - 2.5)$ mag. This amount will be an overestimate of the real error, because the total observed scatter contains some component due to observational errors which has not yet been corrected for. We calculate the peculiar velocity implied by $\Delta M$ plus and minus this error, and take as the peculiar velocity error the mean of the two.

## 6.4 The Local Peculiar Velocity Field from the SFI++

The resulting peculiar velocity field is shown in Figures 6.3 and 6.4, which show the peculiar velocities of galaxies within 15 Mpc of respectively the supergalactic plane (SGP), and its two orthogonal planes. Peculiar velocities are shown as arrows stretching from the real space location of the velocity field tracer to its

location in redshift space (projected onto the plane). If the peculiar velocity has a significant ($> 1\sigma$) positive or negative value it is shown with an open or closed circle respectively.

In Figure 6.3 and 6.4a the dominant pattern of motion is streaming towards $\sim$-SGX, or towards the Hydra-Centaurus supercluster (and Shapley in the background). In Figure 6.3, there is also a hint of infall onto Virgo, Pisces-Perseus, and perhaps Fornax (at SGX$\sim$ 20, SGY$\sim$ 20). Figure 6.4b, shows infall onto Virgo at +SGY, including the negative peculiar velocities of galaxies at -SGY.

## 6.5 Conclusions

In this Chapter we have constructed a sample of galaxies from the SFI++ which can be used to study the local peculiar velocity field. These galaxies are chosen to avoid large groups and clusters, and to provide good quality TF measurements. We combine the peculiar velocities of galaxies in small groups (using the group assignments described in Springob 2005), and also include the peculiar velocities of nearby clusters from Chapter 4.

We describe how peculiar velocities and their errors are derived from the TF relation, and graphically illustrate the resulting peculiar velocity field.

In Chapter 8 this sample will be combined with galaxies which have published primary distances to study the velocity field in and around the Local Supercluster.

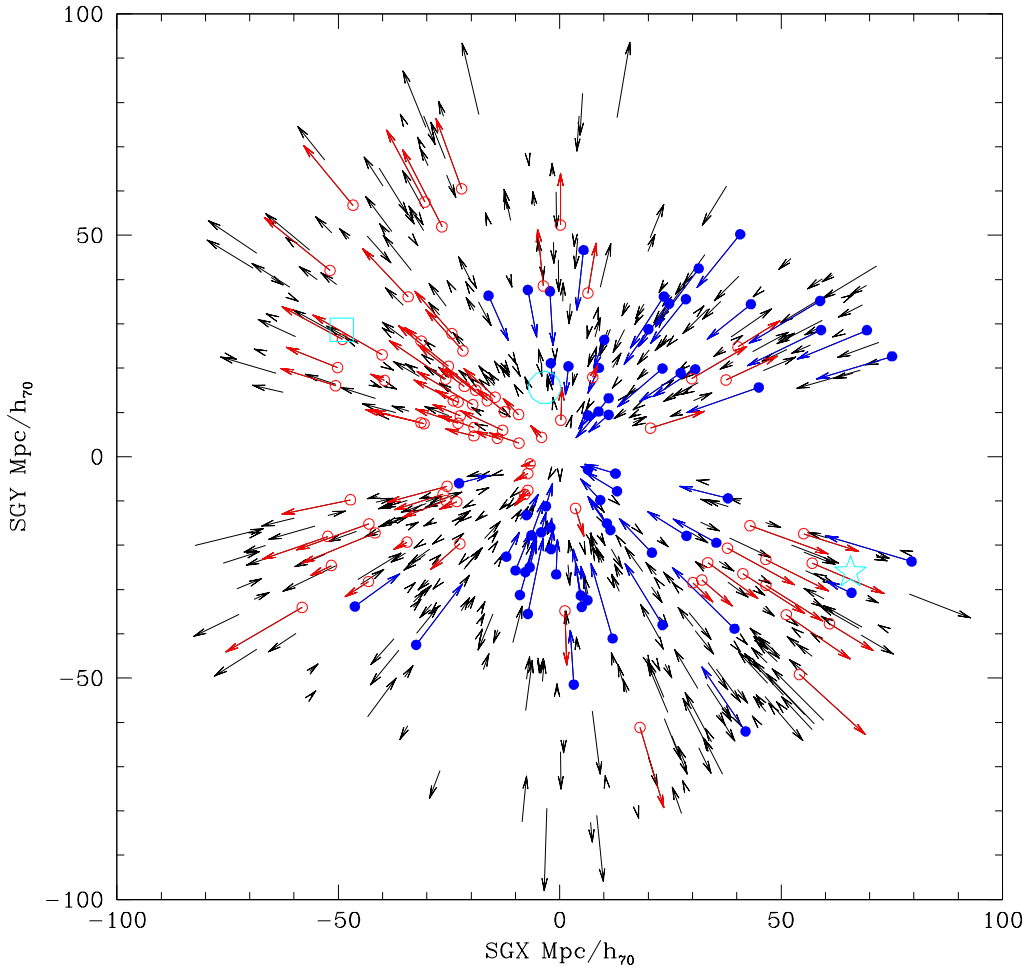



Figure 6.3: Peculiar velocities of velocity field tracers from the SFI++ within 15 Mpc of the SGP are shown projected onto the SGP. If the velocity has a significant ($> 1\sigma$) positive or negative value it is shown with a open or filled circle respectively. The large open circle indicates the location of the Virgo Cluster, the square shows the center of the Hydra-Centaurus supercluster and the star indicated Pisces-Perseus (positions as given in Einasto *et al.* 1997).

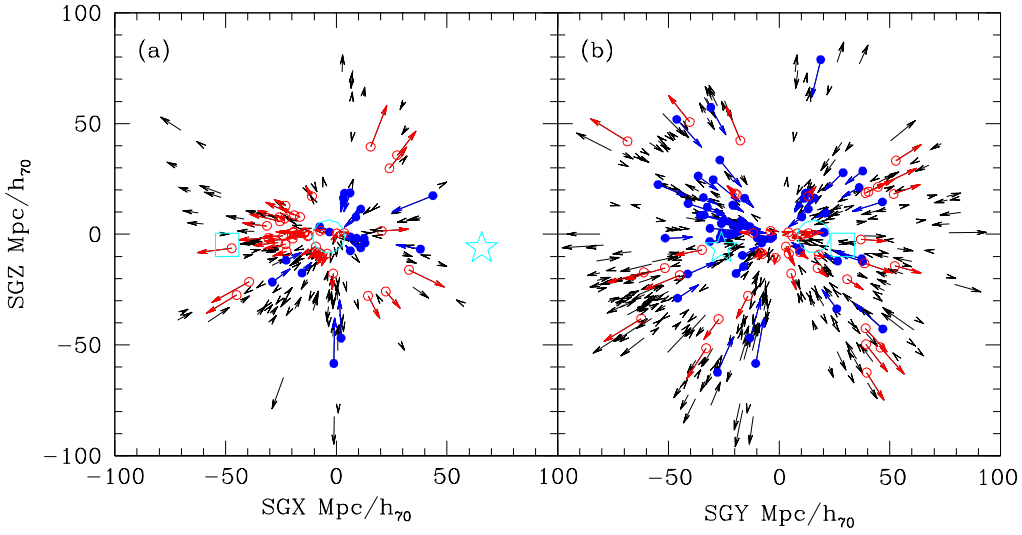



Figure 6.4: As in Figure 6.3, except for slices perpendicular to the Supergalactic plane. Panel (a) shows the SGX-SGZ plane, panel (b) shows the SGY-SGZ plane.

# Chapter 7

# Primary Distance Sample

## 7.1 Introduction

The Tully-Fisher relation is a secondary distance indicator, so called because its calibration builds on the use of other, primary distances to nearby galaxies. Secondary distances are practically easier to measure for an individual galaxy and thus can be derived for larger samples, but have correspondingly larger errors on individual measurements. In contrast primary distances generally take much more observational time, but have lower errors.

We have performed a search in the literature for galaxies with published primary distances, of which we find 588. This sample is heavily weighted towards distances which have been published in recent years, and at present includes no SNIa distances (of which there are only a small number in the nearby universe). The bulk of these galaxies ($\sim 300$) are elliptical galaxies with distances measured by the surface brightness fluctuation (SBF) method, not technically a "primary" distance method, but with similarly low errors. These data are presented in Tonry *et al.* (2001). For very nearby galaxies there are a large number of distance derived using the tip of the red giant branch (TRGB) method (see *e.g.* Karachentsev *et al.* 2004), which can be applied in any galaxy with an old stellar population. The Hubble Key Project (Freedman *et al.* 2001) present distances to several galaxies using Cepheid variable stars. Other distances come from the Planetary Nebular luminosity function (PNLF), or from the magnitude of the brightest stars. These methods will be described in more detail below.

A small fraction of the galaxies with primary distances (27/588) do not currently have published redshifts. This is typically because they are small, nearby and low surface brightness dwarf galaxies, for which redshifts are hard to measure, but distances can be obtained from their resolved stellar population. We are obviously not able to derive peculiar velocities for these galaxies, so they are not included in the final velocity field sample.

This primary distance sample provides an ideal compliment to the SFI++ Tully-Fisher sample described in Chapters 4, and 6. The two samples will be combined in Chapter 8 for a study of the local peculiar velocity field. Primary distances are generally only available for relatively nearby galaxies because of limitations on the techniques (as described below), while the SFI++ extends throughout a much larger volume. Primary distances however, can provide peculiar velocities for the very nearest galaxies to much higher precision than is possible using Tully-Fisher, and are available for elliptical and irregular galaxies to which the Tully-Fisher relation can not be applied. By combining these two complementary samples we are making use of the best available distances and constructing a sample sensitive to

Table 7.1: Typical errors and useful ranges of various redshift independent distance measures.

| Method | Typical error | Distance limit (Mpc) | Number gals | Galaxy type |
|---|---|---|---|---|
| Geometric | 4% | 7 | 2 | All |
| Cepheid | 5% | 30 | $\sim 30$ | Spirals |
| TRGB | 5% | 15 | $\sim 160$ | All |
| PNLF | 5% | 20-25 | $> 30$ | All |
| SBF | 10% | $> 100$ | $\sim 300$ | Ellipticals, bulges of spirals |
| TF | 15-18% | $> 100$ | 1000s | Spirals |
| $D_n - \sigma$ | 20% | $> 100$ | 1000s | Ellipticals |
| FP | 20% | $> 100$ | 1000s | Ellipticals |
| Stars | 20% | 30 | $> 75$ | Spirals |

the very nearby deviations from Hubble flow as well as being constrained on the larger scales. This sample is the best currently available for the study of the local peculiar velocity field.

## 7.2 Primary Distance Methods

Here we describe briefly various methods used to measure distances to nearby galaxies. We make no attempt to mention all possible distance measures, just those which are significant in the sample described here. A summary of various distance methods, along with their typical errors, distance range, an idea of the number of galaxies with published distances from that method and the type of galaxy they apply to is provided in Table 7.1. Many attempts have been made to graphically illustrate the distance ladder. The use of HST and emergence of the surface brightness fluctuations method in the last decade or so has significantly changed to picture, with the ranges of several methods being extended to more cosmologically useful distances. A recent illustration (if based on older versions) is found in Ciardullo (2003).

### 7.2.1 Cepheid Variable Stars

Perhaps the most famous and historically important method for measuring distances is the period-luminosity relation of Cepheid variable stars, discovered by Henrietta Leavitt in 1912; for a review of the early history see Fernie (1969). Cepheid distances can only be measured in galaxies close enough that their stars can be resolved. In the 1990s, the Hubble Space Telescope (HST) extended that distance limit by a factor of ten; using Cepheid variable stars as a calibration for other distance measurements to derive $H_0$ was one of the main science drivers for the telescope (Freedman *et al.* 2001). The modern Cepheid P-L relation has a

scatter of about 0.1 mag, resulting in 5% distance errors. The main systematic errors are due to uncertainties about extinction (Cepheid variable stars are young, and therefore commonly found in regions of galaxies with a lot of dust), the metallicity dependence of the relationship (see *e.g.* Shoko *et al.* 2004), and the risk of blending at large distances. Estimating distances from this method is relatively time consuming, because of the need to make several observations to monitor the periods of Cepheid stars in the galaxy. We find 29 galaxies with Cepheid distances in the literature.

### 7.2.2 Surface Brightness Fluctuations

The method of surface brightness fluctuations (SBF) relies on the statistics of photon counting in individual pixels to estimate distances to galaxies. Tonry & Schneider (1988) give an example illustrating the idea. Imagine a galaxy with a totally uniform distribution of stars at a distance where the average projected number of stars per pixel is 100. Pixel to pixel variations of the flux across this galaxy will be at the 10% level due to Poisson counting statistics of the stars. Now move the galaxy twice as far away. The area covered by each pixel (and therefore the number of stars per pixel) will increase by a factor of 4, while the observed flux per star drops by a factor of 4. The mean surface brightness of each pixel will therefore remain constant, but there will now be only 5% pixel to pixel variations due to stellar counting statistics.

SBF measurements in real galaxies are complicated by pixel to pixel fluctuations not due to stellar counting statistics. This means that the method is limited to intrinsically smooth stellar distributions, such as are found in ellipticals or the bulges of spirals, and the image processing required to make a measurement is quite intensive. Observational seeing smears out the image, causing adjacent pixels to be correlated, so SBF measurements also require an accurate PSF template. The absolute calibration of SBF distances has been an issue. Because Cepheid stars are young, and SBF measurements work only for smooth old stellar populations cross calibration of the two methods initially relied on using distances to groups with both ellipticals and spirals. For a full review of the method see Blakeslee, Ajhar & Tonry (1999).

The SBF method has emerged as an accurate and extremely useful distance indicator in recent years. The method was originally applicable only to elliptical galaxies within about 20 Mpc. Since the fluctuations are larger in the near infrared (NIR) than optical wavelengths, the installation of the NIR camera NICMOS on HST allowed the method to be extended out past 100 Mpc. We find 310 galaxies with SBF distances in the literature, the bulk of which come from Tonry *et al.* (2001).

### 7.2.3 Tip of the Red Giant Branch

The tip of the Red Giant branch (TRGB) on a Hertzsprung-Russell (HR) diagram has a remarkably constant absolute magnitude, to within $\sim 0.1$ mag in I-band. The stars at this location are old, low mass stars, just starting helium burning in their core. As a star evolves along the Red Giant branch, hydrogen burning in its outer shell causes the star to expand and increase in luminosity, moving upwards on the HR diagram. Meanwhile its core is contracting and getting hotter. Once the core is hot enough helium burning will start. In low mass stars this helium burning occurs in a runaway flash (or explosion), after which the core expands and cools, and the outer layers begin to contract again, moving the star quickly downwards in the HR diagram. The TRGB represents the luminosity of this core helium flash and is relatively insensitive to metallicity or age (Iben & Renzini 1983).

In galaxies which have a resolvable population of red giant stars it is therefore possible to estimate the distance to the galaxy from the apparent magnitude of the brightest red giant branch stars. There is a significant literature devoted to how to find the apparent magnitude of the tip (see *e.g.* McConnachie *et al.* 2004). Complications also arise because of the impact of blended stars, or background/foreground contamination. TRGB is yet another distance measure where the HST has played a key role. The resolution of HST allows the TRGB method to be extended fairly reliably to the distance of Virgo (Madore & Freedman 1995). We find 162 galaxies out to $d = 15$ Mpc with published TRGB distances.

### 7.2.4 Extragalactic Geometric Distances

The most direct way to measure a distance to an object is of course to use a geometric method. If it is possible find some known absolute length scale in the distant object the distance can be found directly from the angular scale. This method has been applied to the galaxy NGC 4258 using water masers in the accretion disk around its central black hole (Hernnstein *et al.* 1999). By modeling the disk as a set of Keplerian orbits the distance was measured using VLBI to track the motion of the masers in the plane of the sky, while simultaneously measuring the Doppler shift of the receding and approaching arms. A geometric distance has also been estimated for M33 by tracking the motion of HII regions on opposite sides of the galaxy (Brunthaler *et al.* 2005). These methods in theory can have extremely low errors, the errors being dominated by uncertainties in knowing the absolute scale being measured, and the extremely small angles which must be measured. Each distance requires several years of systematic, high precision tracking of the motions of objects in the galaxy, and at present is only possible with VLBI.

### 7.2.5 Brightest Stars

The brightest blue stars (BS) in a galaxy were among the first measures used to estimate distances to galaxies, and remain in use today, despite the dubious

physical origin and relatively large errors. Typically what is done is to compare the mean magnitude of the 3 brightest stars with the difference between this magnitude and the total integrated magnitude of the galaxy (a distance independent quantity which has been shown to have a rough correlation). This results in a nominal scatter of 0.45 mag, or 20% distance errors (Karachentsev & Tikhonov 1994), however the error has been found to be significantly larger in several galaxies with other distance measures. We only use this method where a galaxy does not have a more reliable primary distance.

### 7.2.6 Planetary Nebulae

The Planetary Nebulae Luminosity Function (PNLF) method, is in some ways similar to the method of brightest stars, in that it relies on the idea that the brightest planetary nebulae in a galaxy have the same absolute magnitude. Modern methods involve constructing the luminosity function of a complete sample of PNe in a galaxy and measuring its cut-off. The reason why the brightest PNe should have a constant absolute magnitude is not immediately apparent. The luminosity of a PNe should increase with the mass of the progenitor star. This effect however is mediated by a corresponding increase in the amount of extinction in the nebula. PNe which would otherwise be brighter than the cut-off are therefore dimmed by self extinction. For a review of PNLF as a distance indicator see Ciardullo (2003).

Like the TRGB, using PNLF as a distance measure has the advantage that it can be applied to any type of galaxy, as long as PNe can be identified. Observationally it is easier to identify PNe in old stellar populations (elliptical galaxies), as in late type galaxies they are sometimes difficult to distinguish from HII regions or supernova remnants. The method is limited to $\sim 25$ Mpc, beyond which individual PNe become too dim to be observed in a reasonable exposure time.

The primary distance sample presented here includes only 21 galaxies with PNLF distances, the bulk of which were presented with Cepheid calibration in Ferrarese *et al.* (2000). More PNLF distances exist in the literature, but at present have not been included in the sample.

### 7.2.7 Other methods

**RR Lyrae Variables:** RR Lyrae variable stars have a roughly constant average absolute magnitude meaning they can be used as a standard candle. They are quite dim however, so this method can only be used for galaxies in the Local Group. This method has traditionally had an important role on the distance ladder.

**GCLF:** the globular cluster luminosity function (GCLF) has a roughly Gaussian shape. Its peak appears to have a roughly constant magnitude and has therefore been used as a distance indicator.

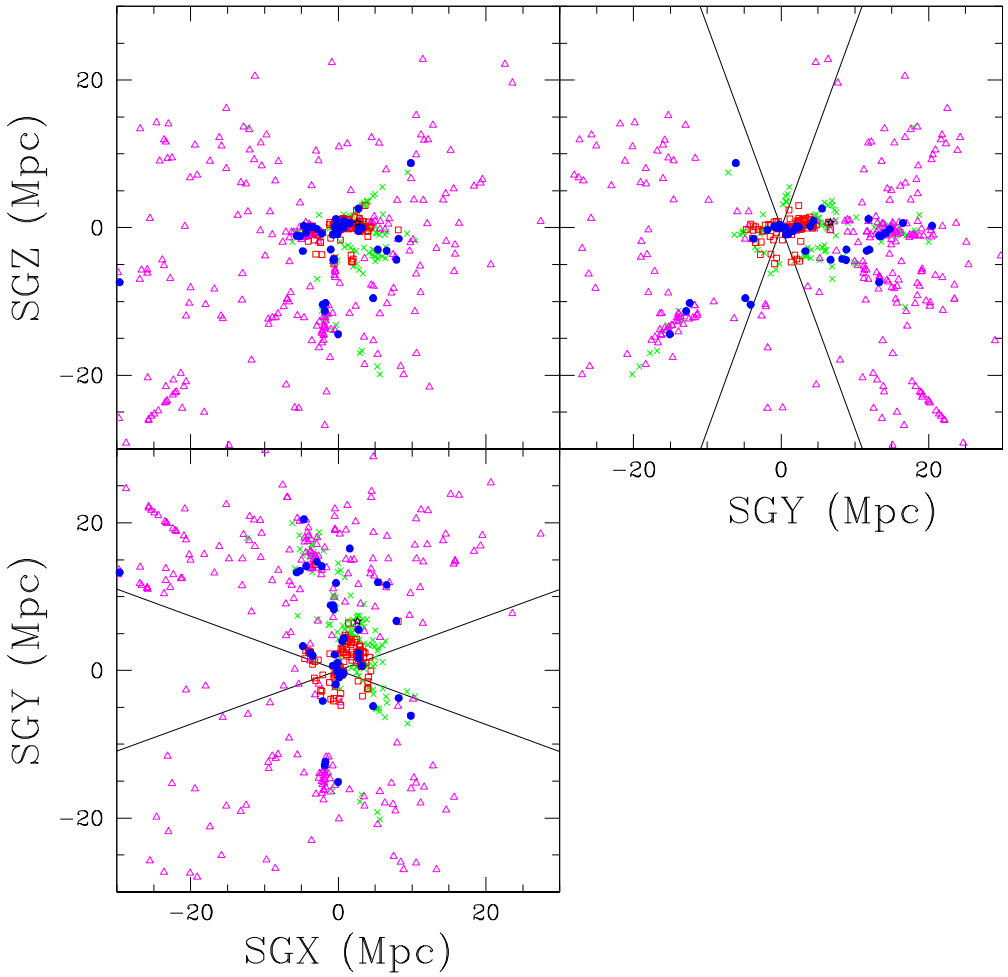



Figure 7.1: Shown is the distribution of galaxies with published primary distance (in supergalactic Cartesian co-ordinates). Symbols indicate the method used; triangles – SBF distances; filled circles – Cepheid distances; squares – TRGB; crosses – any other method. One star indicates the geometric distance to NGC 4258. The lines show the location of the zone of avoidance.

## 7.3 Data Presentation

Figure 7.1 shows the distribution in supergalactic Cartesian co-ordinates of all galaxies we have found with published primary distances. Galaxies are shown projected onto three orthogonal planes. As is obvious from this Figure, the distribution of galaxies with published primary distances is extremely uneven over the local volume, in particular, galaxies in several nearby clusters and groups are overrepresented, including 60 galaxies in the Virgo cluster at (SGX, SGY, SGZ) = (-3, 16, -1) Mpc, 24 galaxies in Fornax at (SGX, SGY, SGZ) = (-2, -15, -13) Mpc and several galaxies in Eridanus (4, -19, -16), Ursa Major (8, 17, 1), Sculptor (-0.4, -2, 0), M81 (2.9, 2.5, 0), Can Ven (0.5, 3.7, 0.3) and the Hydra cluster (-20, 20, -20). There are a significant number of Local Group galaxies with measured primary distances (about 35 in total), which will not be used in this study. This patchy volume coverage is natural for primary distance techniques which are costly in observing time.

Without grouping, the virial motions of galaxies in groups and clusters would dominate the local velocity field as traced by this sample. Normal grouping algorithms (such as those discussed in Springob 2005) don't work well in the very local universe, because they group on proximity in redshift space which is significantly distorted here. Fortunately, for the very local universe there have been numerous studies on grouping. We also use the distances and positions collected in this catalog (particularly the papers on TRGB distances from various studies of Karachentsev *et al.*.) and assign 290 (or 52% of the galaxies with primary distances outside the Local Group) to 39 groups and subgroups.

### 7.3.1 Galaxies with multiple distances

About 100 of the galaxies in the primary distance sample have distances measured from more than one method (or source). We make a judgment on the best distance to use, resulting in a catalog which contains 42 Cepheid distances, 131 TRGB distances, 285 SBF distances, 2 RRLy distance, 1 PNLF distance, 1 geometric distance (NGC 4258) and 74 distances from the method of brightest stars. The remainder of distances are mostly averages of various methods, calibrated by Cepheids (Ferrarese *et al.* 2000).

Figure 7.2 shows galaxies which have (a) Cepheid distances and distances from another source, and (b) TRGB distances and distances from another source. There is a good agreement, the largest scatter being when distances measured using the method of brightest stars are compared with the other methods. The scatter when 26 Cepheid distances are compared with other methods (except stars) is 0.21 mag (or 10%), while for the 38 TRGB distances we get 0.26 mag (12 %). The larger scatter when the method of brightest stars is used is illustrated in Figure 7.3 which shows all galaxies with distances measured using this method and with any other method. The distances are clearly correlated, the mean value of the residuals in distance modulus being -0.07±0.9 mag, but the scatter is large, at 0.58 mag (27%).

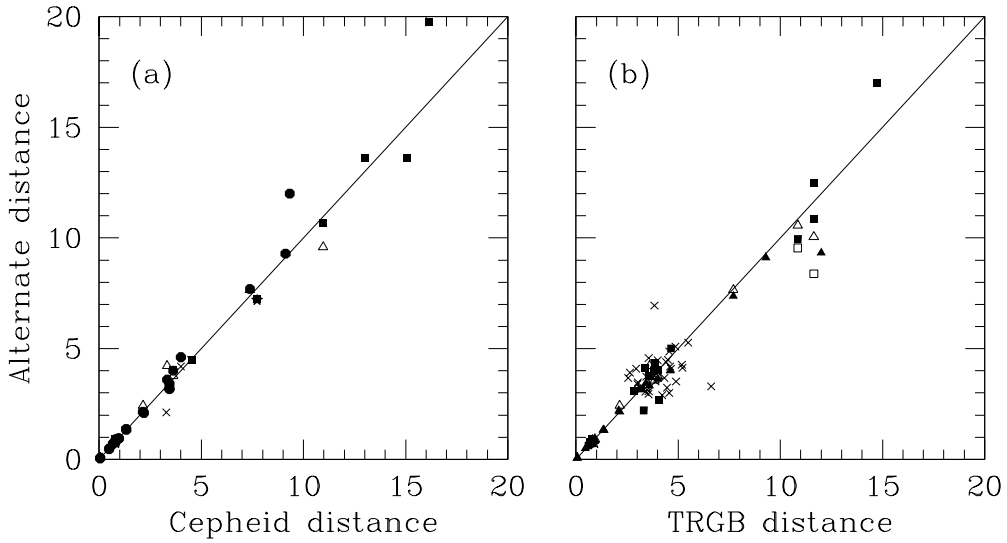



Figure 7.2: Shown are all galaxies with (a) Cepheid distances and distances from another method; (b) TRGB distances and distances from another method. Solid triangles indicate Cepheid distance, solid circle TRGB, solid square SBF, open triangle PNLF, open square GCLF, cross method of brightest stars. Error bars have been left off for clarity.

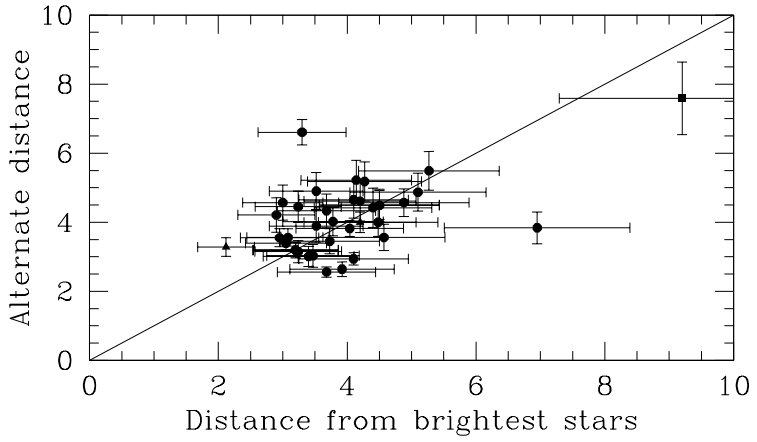



Figure 7.3: All galaxies with distances measured using the method of brightest stars and some other method. Symbol types as in Figure 7.2. Error bars for BS distances show assumed error of 0.45 mag (21%). The scatter in the diagram is 27% on distance.

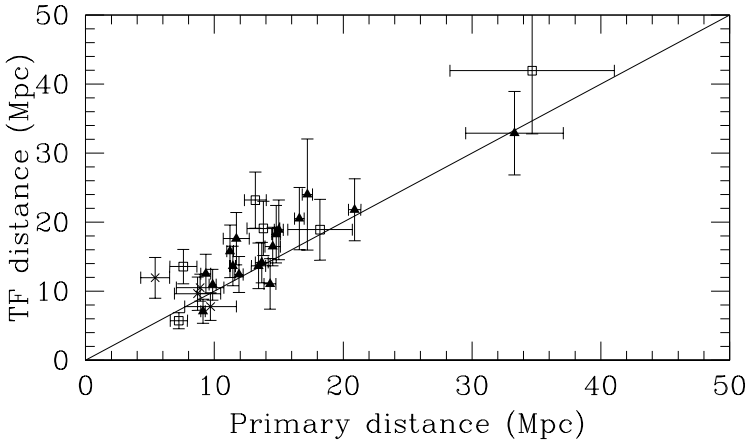



Figure 7.4: Galaxies with both TF distances and distances from a primary indicator. Solid triangles show galaxies with Cepheid distances; solid squares, SBF distances; and crosses, "stars".

### 7.3.2 Galaxies with Tully-Fisher distances

A small number (27) of the galaxies with published primary distances are also found in the SFI++ Tully-Fisher (TF) sample presented in Chapter 4. Most (17) of these spiral galaxies have Cepheid distances, a further 6 have SBF distances and 4 have distances estimated from the method of brightest stars. In Section 7.2 we discussed the application of different distance methods; Table 7.1 summarizes which methods can be used for spiral galaxies. The TRGB method can only be used very nearby, where large spirals suitable for TF work are rare so we do not find any TRGB distances for galaxies in our TF sample.

Figure 7.4 shows the primary distances of these galaxies against their TF distance. We have fairly small number statistics here, but there appears to be a slight tendency for the TF distances to be larger than the primary distances. The scatter for the 17 Cepheid distances is 0.41 mag (19%); for the 6 SBF distance it is 0.69 mag (32%), and for 4 distances from stars the scatter is 0.92 mag (42%). This appears consistent with the estimate of $\sim$ 18% errors on the TF distances suggested in Chapter 4, and also illustrates the fact that SBF distances for the bulges of spirals are less reliable than the average 10% error which applies to SBF distances in general.

We can use this information as a sanity check on the calibration of the TF relation presented in Chapter 4, which fit for the calibration of the TF relation and the motions of a set of clusters simultaneously. Figure 7.5 shows galaxies from SFI++ with Cepheid variable star distances on the Tully-Fisher relation. The solid line shows the bivariate fit to the **in** sample of Chapter 4, adjusted for $h = 0.7$, which shows good agreement with the Cepheid calibrated galaxies, again with a scatter of 0.4 mag (18% distance errors for TF). The dotted line is a simple linear fit

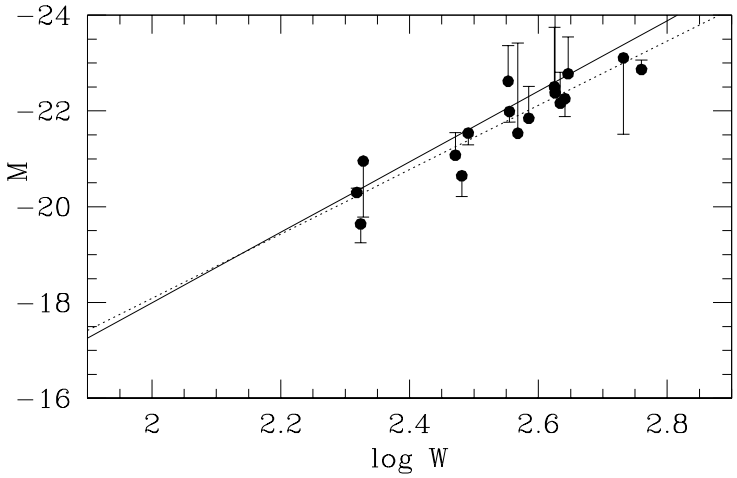



Figure 7.5: Shown is the TF relation for galaxies in the SFI++ which also have distances from Cepheid variable stars. The filled circles show the absolute magnitude using the Cepheid distance, while the error-bars show the galaxy's location using its CMB velocity to give a distance. The solid line is the bivariate fit to the **in** sample of Chapter 4. Note that the ordinate here is absolute magnitude $M$, while in Chapter 4, we use $M - 5 \log h$. The TF relation here has been adjusted using $h = 0.7$. The dotted line is a simple direct fit to the points.

to the points, giving a relation $M = -21.44 - 6.7\,(\log W - 2.5)$. Since these points do not represent a complete sample the slope is likely to be underestimated, but this data can be used to provide an independent estimate of the Hubble's constant similar to work done as part of the Hubble Key Project by Sakai *et al.* (2000) who presented a Cepheid calibration of the TF relation using distances to 21 galaxies and the 23 Giovanelli *et al.* (1997b) clusters. Using the slope of the bivariate fit to the **in** sample and simply fitting for the offset we estimate $H_0 = 77 \pm 4$ km s$^{-1}$ Mpc$^{-1}$ from these 17 galaxies, a value well within $2\sigma$ of the WMAP measurement of $71 \pm 4$ km s$^{-1}$ Mpc$^{-1}$ (Bennett *et al.* 2003).

## 7.4 The Peculiar Velocity Field

Figures 7.6 and 7.7 show the velocity field of 235 galaxies, and 39 groups with distances discussed in this Chapter. Peculiar velocities are shown as arrows stretching from the real space to redshift space position of the galaxy. The velocity field is shown in three orthogonal planes. Galaxies within 10 Mpc of the supergalactic plane are shown in Fig. 7.6, while two planes perpendicular to the SGP are shown in Fig. 7.7. Galaxies with positive or negative peculiar velocities larger than $3\sigma$ are shown as open and filled circles respectively.

Particularly evident in these figures is the motion of galaxies towards the Hydra-Centaurus region at +SGY, -SGX, but also noticeable is the infall motion onto Virgo along SGY, and perhaps Fornax at (SGY$\sim -15$, SGZ$\sim -15$ Mpc). These

figures can be compared with the equivalent for the SFI++ TF sample, and for the combined sample in Chapters 6 and 8 respectively, but note that the scale here is reduced, and the velocities are now highlighted if larger than $3\sigma$ since the errors are smaller.

## 7.5 Conclusions

We have searched the literature for galaxies with primary distances, and find a sample of $N = 588$. The distances are measured using various different methods, as described in Section 7.2. Almost 50% of the distances are from the SBF method, 22% from TRGB and 7% from Cepheids, while 13% of the galaxies have distances from the method of brightest stars (BS).

A subset of the galaxies have distances measured from multiple methods. We use this sample to briefly investigate consistency and errors in the methods. We find a scatter of 10% between Cepheid distances and all other methods (except BS), and 12% for TRGB distances. Distances from the BS method have a scatter of 27% with other distances.

A small number of galaxies in this sample are also found in the SFI++ TF sample introduced in Chapter 4. The scatter between these distances and TF appears consistent with 18% errors on TF distances used in this thesis. We show the TF relation of 17 galaxies with Cepheid distances, which is completely consistent with the template relation derived in Chapter 4, and use them to estimate a value for the Hubble's constant of $77 \pm 4$ km s$^{-1}$ Mpc$^{-1}$.

An initial look at the peculiar velocity field shown by these galaxies reveals bulk motion towards Hydra-Centaurus as well as hints of infall motions onto the Virgo cluster, and possibly Fornax. In Chapter 8 this data will be combined with the SFI++ sample of TF velocity field tracers (Chapter 6) to study the local peculiar velocity field in more detail. There we will fit multiattractor models to the velocity field, both as seen by the primary distance sample alone, and in combination with the SFI++.

The compilation of published primary distances described here has the potential to be exploited for many applications and would be a useful resource for Astronomers as a one stop location to find distances to galaxies. We intend to make the compilation available on-line in the near future, using National Virtual Observatory (NVO) standards.

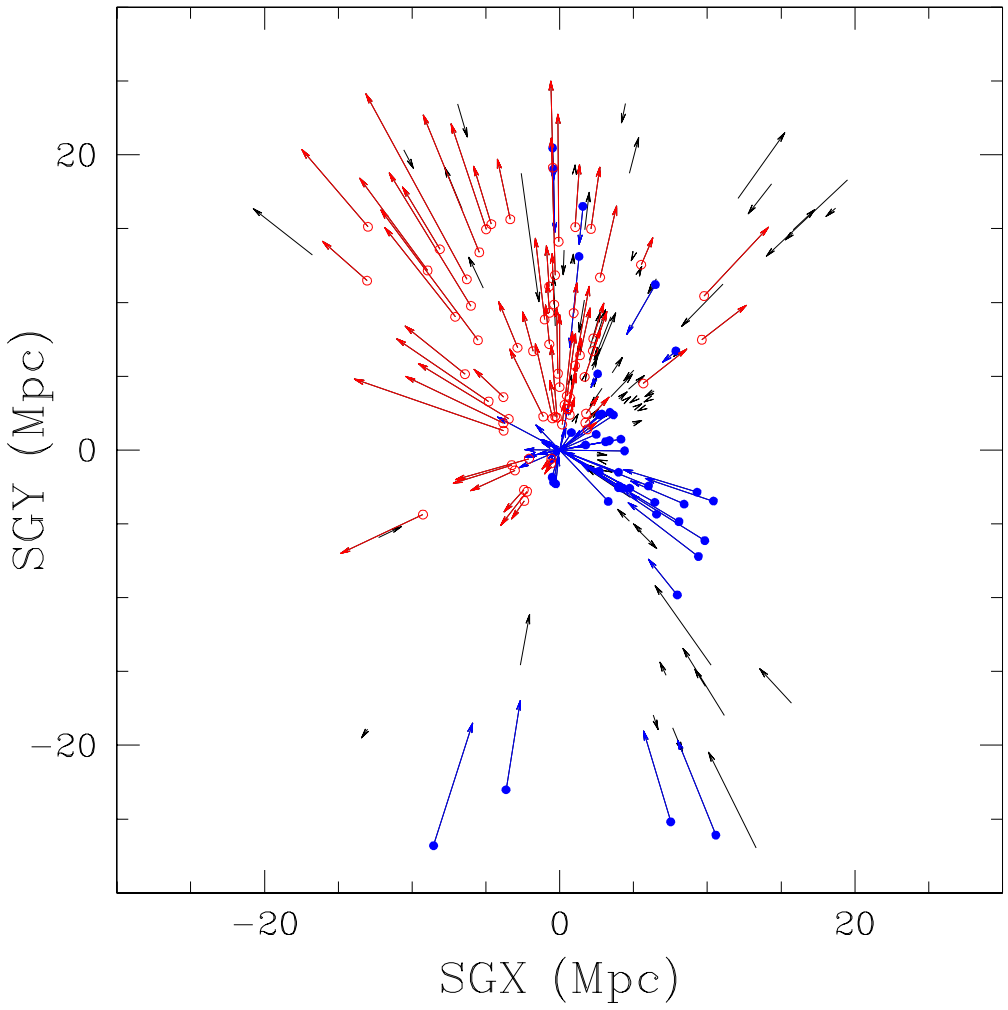



Figure 7.6: Peculiar velocities of galaxies and groups with primary distances within 10 Mpc of the SGP are shown projected onto the SGP. Galaxies with positive or negative peculiar velocities larger than $3\sigma$ are shown as open and filled circles respectively.

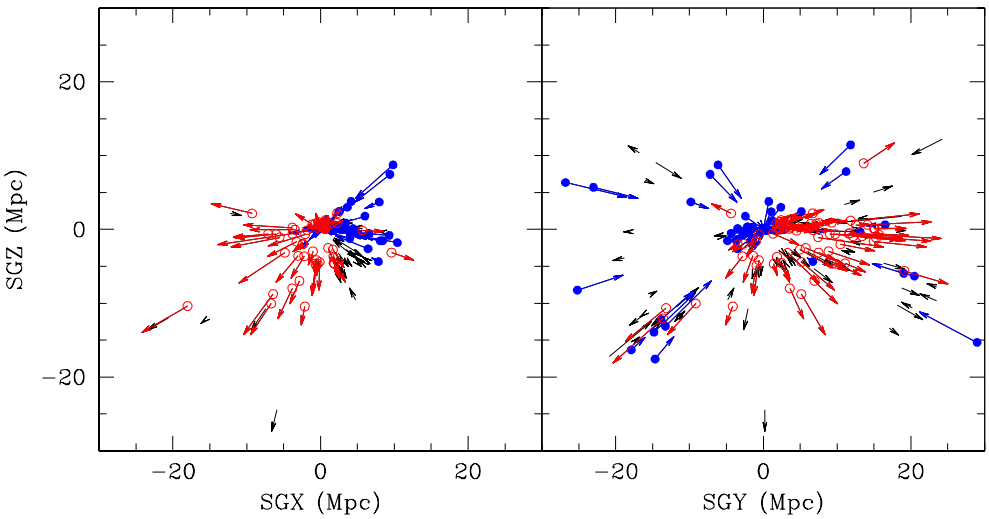



Figure 7.7: As Figure 7.6 except for planes perpendicular to the SGP.

# Chapter 8

# The Velocity Field in the Local Supercluster

## 8.1 Introduction

In this Chapter we tie together work presented in the rest of this thesis. Here we fit the velocity field model introduced in Chapters 2 and 3, to peculiar velocity data from a combination of galaxies with distances from the Tully-Fisher (TF) relation (as calibrated in Chapter 4; the peculiar velocity sample is described in Chapter 6), and published primary distances (Chapter 7). We provide an introduction and background to studies of the local velocity field in the Introduction (Chapter 1) and will not repeat that here. The two samples combined for this study are complementary, the SFI++ TF sample (Chapter 6) containing a much larger number of velocity field tracers extending over a larger volume, but with greater distance uncertainty than the primary distance sample (Chapter 7). By combining them we are better able to study the local velocity field than when using either alone, and for comparison we also discuss the results when either sample is considered separately. The full sample is almost an order of magnitude larger than those used in earlier modeling of the velocity field (*e.g.* Tonry *et al.*2000), and also has the advantage of covering a larger volume (albeit with large peculiar velocity errors at the edge). The SFI++ peculiar velocities have a relatively uniform sky distribution, important in peculiar velocity samples so that one region of the local universe will not dominate the fit, while the primary distances provide a higher density of more accurate peculiar velocities in the very nearby universe.

The SFI++ TF sample (Chapter 6) contains 1425 velocity field tracers, 1264 of which are individual galaxies; 138 small groups, and the remaining 23 are the nearest clusters in the template sample discussed in Chapter 4. There are published primary distances available for 588 galaxies (Chapter 7) which results in 274 velocity field tracers (235 galaxies and 39 groups/clusters). Here we combine the velocity field tracers from the two subsets. There are 7 groups and 8 individual galaxies which appear in both samples, we simply take weighted averages of the distances in these cases. The final sample consists of 1684 velocity field tracers, 1491 of which are individual galaxies (1256 with TF distances, 227 with primary distances and 8 with both); and 193 are groups or clusters, (154 of which have only TF distances).

As mentioned above, the models discussed here have exactly the same form as those introduced in Chapter 3. We also use the same measures for the goodness of fit and information criteria (AIC and BIC) described in that Chapter, and refer the

reader back to there for a detailed introduction to the model and fitting methods. As discussed in that Chapter, simple $\chi^2$ minimization is not appropriate for the fitting of peculiar velocity field models, because the errors are not necessarily Gaussian in the fitted parameter (the peculiar velocity). Also, because of the relatively large errors on the SFI++ peculiar velocities, we expect the Malmquist bias (the tendency for true distances to differ systematically from those measured due to the $r^2$ increase in volume along the line of sight, or intrinsic variability in the density of galaxies) to have a significant effect in that sample, and therefore use the likelihood which account for this effect, minimizing $\mathcal{L} = -2\Sigma \ln P_{\rm VELMOD}$ where $P_{\rm VELMOD}$ is the conditional probability of finding a galaxy at its observed distance $d$, given its observed radial velocity $v_{\rm obs}$ and the velocity field model (see Eqn. 3.13; this is based in the method described in Willick & Batra 2001),

$$P_{\rm VELMOD}(d|v_{\rm obs}) = \frac{\int P(r)P(d|r)P(v_{\rm obs}|r)dr}{\int P(r)P(v_{\rm obs}|r)dr}. \tag{8.1}$$

This goodness of fit measure could account for both homogeneous and inhomogeneous Malmquist bias, however in practice we assume that the probability of finding a galaxy at a "real" distance $r$, $P(r) \propto r^2$ (*i.e.* we assume a constant density), and therefore are only accounting for the homogeneous Malmquist bias in these fits. The primary distance sample should be much less affected by Malmquist bias, because of the lower distance errors. We test this assumption by also considering the $P_\mu$ goodness of fit estimator (Eqn 3.10), which takes into account the non-Gaussian errors, but not the Malmquist bias. This goodness of fit is similar to that used in Tonry *et al.* (2000), in their parametric modeling of the velocity field from $\sim 300$ SBF distances, which again should have a relatively small Malmquist bias.

The velocity field of the full sample is shown in Figure 8.1. In this figure galaxies with positive or negative peculiar velocities larger than $1\sigma$ are shown as open or filled circles respectively. The most obvious pattern in this figure is a significant streaming motion towards the upper left quadrant, the direction towards the Hydra-Centaurus and Shapley superclusters (and the "Great Attractor" of early velocity field models).

## 8.2 Dipole Only Model

The best fit dipole to the entire sample of velocity field tracers is 388±58 km s$^{-1}$ towards $(\alpha, \delta)$ = (10.9±0.5h, -28.2±5°), with a likelihood of 648.19 for 3 model parameters and $N = 1684$. If we fit a dipole to the SFI++ galaxies alone, we find 244±75 km s$^{-1}$ in the direction $(\alpha, \delta)$ = (13.2±1.5h, -46.4±10°), with a likelihood of $\mathcal{L} = 570.28$. The primary distance sample alone has a somewhat larger best fit dipole of magnitude 473±69 km s$^{-1}$ towards $(\alpha, \delta)$ = (10.6±0.5h, -24.5±5°), ($\mathcal{L} = 57.44$). Unsurprisingly, the combined sample gives a result which is between the values of the two individual sample fits. Although it is much closer in direction

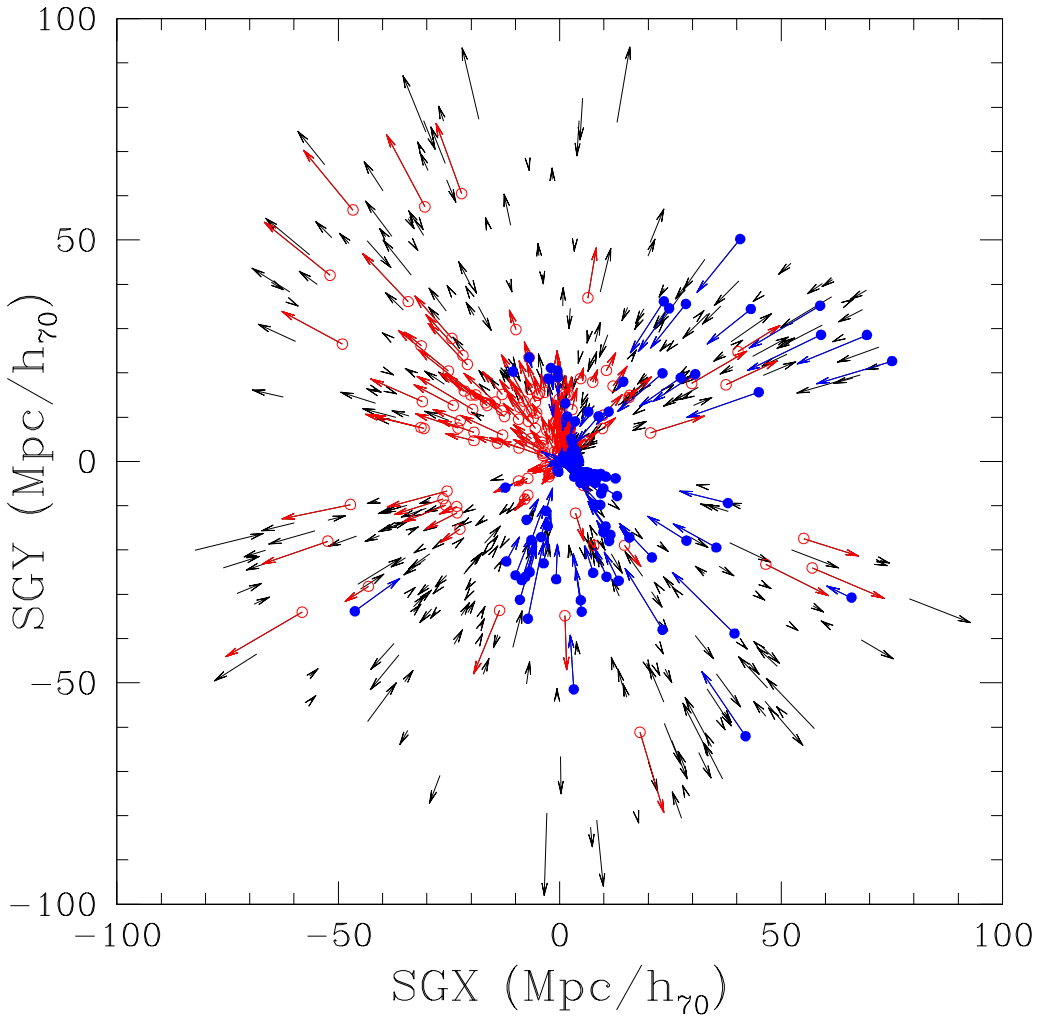



Figure 8.1: Peculiar velocities in the CMB frame of velocity field tracers (both from the SFI++ sample and from primary distances) within 10 Mpc of the supergalactic plane projected onto the supergalactic plane. Galaxies with positive or negative peculiar velocities larger than $1\sigma$ are shown as open and filled circles respectively. The most significant pattern is a bulk motion towards the upper left quadrant (mostly open circles to the upper left and filled circles to the lower right) or the direction of the Hydra-Centaurus and Shapley superclusters.

to the dipole fit to the primary distances alone, it is within the $2\sigma$ error contour of the result from SFI++ (which has much larger error contours because of the larger errors on individual peculiar velocities). The goodness of fit and information criteria for these models are summarized in Table 8.2, along with the results for all other velocity field models considered in this Chapter. The direction of the dipole is graphically illustrated in Figure 8.2. It is within a few $\sigma$ of the direction towards Hydra-Centaurus and the Shapley supercluster in the background, and also close to the direction of the dipole fit in the dipole only model of Tonry *et al.* (2000); not surprising as the bulk of the primary distances come from that sample.

For the primary distance sample we also consider fitting by minimizing $P_\mu$ (Eqn 3.10). This results in a dipole fit quite similar to that found by minimizing $P_{\rm VELMOD}$, with a magnitude 487±51 km s$^{-1}$ towards $(\alpha, \delta) = (11.7\text{h}, -37.6^\circ)$ backing up the hypothesis that the Malmquist bias in this sample has only a small impact. For ease of comparison with the other fits discussed in this Chapter, we will however continue to use $P_{\rm VELMOD}$ as the goodness of fit indicator for this sample.

If we plot the velocity field of the combined sample with this dipole removed, (Figure 8.3) the signature of infall onto the Virgo cluster is now noticeable at (SGX, SGY) $\sim$ (-4, 16). We also note a significant area at +SGX, -SGY where all peculiar velocities are positive. This is likely an indication that a larger than realistic dipole has been fit to take into account some of the infall motions towards +SGX, +SGY. If this were the case, then in the direction antipodal to the attractor, the velocity which is subtracted will be larger than needed, resulting in this area of positive peculiar velocities.

## 8.3 Infall onto a Single Attractor

The next most simple velocity field model after a pure dipole is a model which includes infall onto one attractor. We will start by using information on the location of nearby large concentrations of mass, therefore adding in only one extra parameter - the mass of the attractor, to the fits. A list of such concentrations in order of their estimated impact on the velocity of the Local Group is shown in Table 8.1. This table also includes the location and mass of the "Great Attractor", a concentration of mass lying behind the plane of the Galaxy which was first proposed by Lynden-Bell *et al.* (1988) in a study of the velocity field of 300 elliptical galaxies using the $D_n - \sigma$ relation. In fixing the position of these attractors in velocity space we are implicitly assuming $H_0 = 70$ km s$^{-1}$ Mpc$^{-1}$, this value is also implicit in the quoted masses (which are in units of $M_\odot/h_{70}$). Table 8.1 makes it immediately clear that a single attractor cannot account for all of the local peculiar velocity field, so obviously a single attractor infall model is an over-simplification of the actual velocity field. It should also be noted that not all of the listings in the table are independent (for example the Hydra and Centaurus clusters form the bulk of the Hydra-Centaurus supercluster).

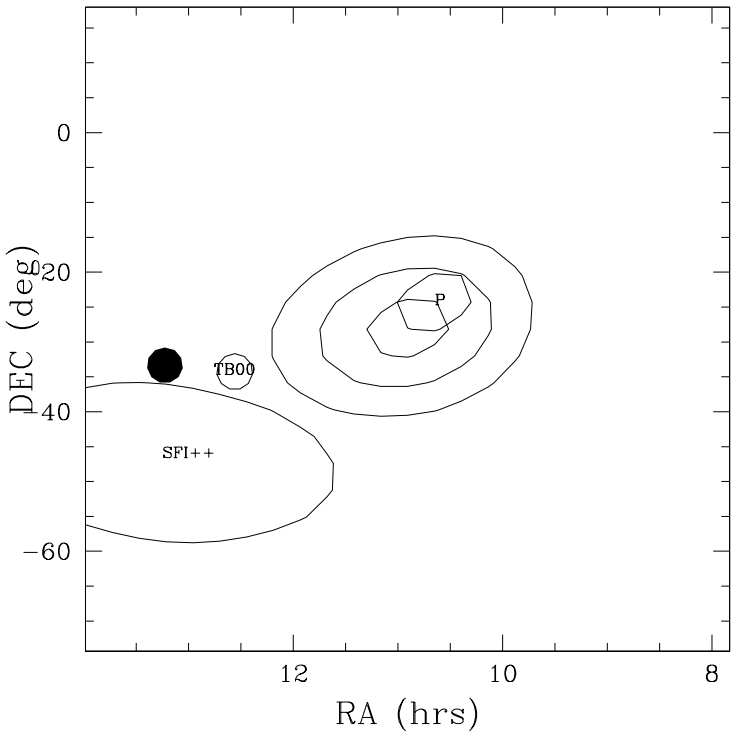



Figure 8.2: Contours of 1,2 and 3 $\sigma$ for the direction of the dipole in the dipole only model. Also shown are the directions and $1\sigma$ contours for the dipole fit to the SFI++ alone or the primary distance (P) sample alone. The direction towards Hydra-Centaurus and Shapley in the background is marked with the filled circle. The circle marked TB00 indicates the direction of the dipole fit to the SBF sample in Tonry *et al.* (2000).

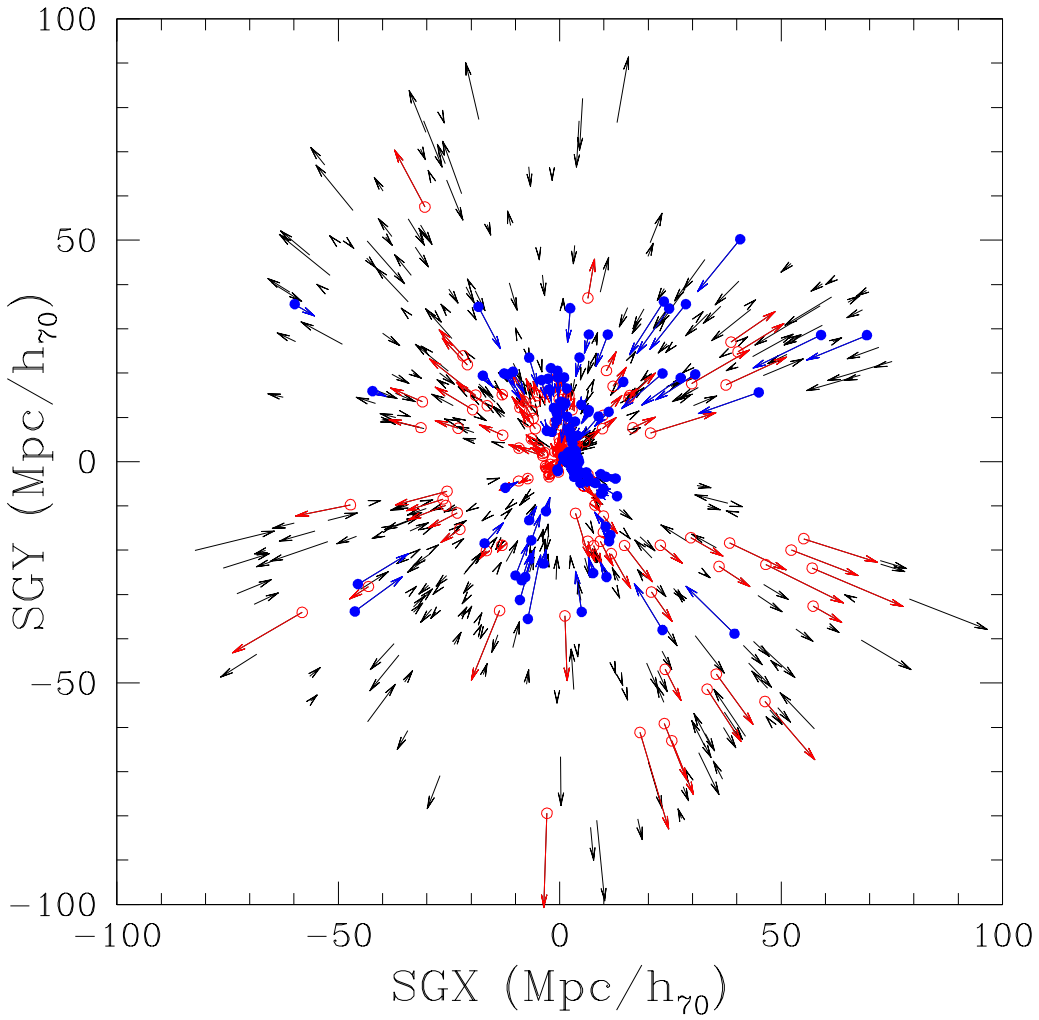



Figure 8.3: Peculiar velocities in the best fit dipole frame of velocity field tracers (both from the SFI++ sample and from primary distances) within 10 Mpc of the supergalactic plane, projected onto the supergalactic plane. Galaxies with positive or negative peculiar velocities larger than $1\sigma$ are shown as open and filled circles respectively. Note the signature of infall onto Virgo at SGX $\sim$ 4 Mpc, SGY $\sim$ 16 Mpc.

Table 8.1: Nearby Concentrations of Mass

| Name | RA, DEC (J2000)[a] | Distance (Mpc/$h_{70}$) | (SGX, SGY, SGZ) | Mass ($10^{15}$ $M_\odot$) | Infall velocity (km s$^{-1}$)[b] |
|---|---|---|---|---|---|
| Virgo | 12h26.5m, +12d43m | 16 [c] | (-3.4, 15.6, -0.9) | 0.2-1.2 (1) | 55-230 |
| Hydra-Centaurus | 13h13.5m, -33d22m | 45 (2) (55(3)) | (-38.8, 22.5, -3.8) | 1-10 | 30-300 |
| Pisces-Perseus | 02h13m +38d06m | 71(4) | (65.7, -26.1, -6.2) | $(8.5 \pm 1.5)$ (4) | 131±20 |
| Shapley | 13h06, -33d04m | $\sim 200$ (3) | (-171, 102, -22) | 20 (5) | 49 |
| Hydra | 10h37m, -27d32m | 40 (2) | (-24.1, 20.7, -24.4) | 0.3 (2) | 17 |
| Fornax | 03h38.5, -35d27m | 20.0±0.7(6) | (-1.9, -14.7, -13.4) | $(0.07 \pm 0.02)$ (7) | 15 |
| Norma Cluster | 16h15m33s, -60d54.5m | 67.2[d] | (-66.1, -9.5, 8.3) | 0.7 (11) | 14 |
| Centaurus | 12h49m, -41d18m | 45 [2] | (-40.4, 17.6, -8.9) | 0.3 (2) | 14 |
| Ursa Major | 11h57m, +49d17m | 18.6±3.4(8) | (7.7, 16.9, 0.9) | $\sim 0.6$ (9) | 14 |
| Coma | 12h60m, +27d59m | 98.8[d] | (0.7, 97.9, 14.3) | 1.3 (10) | 14 |
| Eridanus | 03h28m, 20d45m | 25 | (4.1, -18.5 -16.3) | $\sim 0.1$ | 14 |
| Horologium-Reticulum | 03h19m, -50d02m | ∼285(3) | (-96,-213,-163) | 1-10 | 2-14 |
| Sculptor | 00h24m, -38d00m | 2 | (-0.4,-2.0,-0.1) | $\sim 10^{-5}$ | 0.2 |
| Can Ven | 12h28m, +33d57m | 3.7 | (0.5, 3.7, 0.3) | $\sim 2 \times 10^{-5}$ | 0.2 |
| M81 Group | 09h37m, +68d19m | 3.8 | (2.9, 2.5, -0.1) | $\sim 10^{-5}$ | 0.1 |
| Great Attractor (12) | 13h18.5m, -53d39m | 62 | (-60.2, 10.9, -9.9) | $\sim 50$ | 686 |

[a] From NED; [b] At LG position assuming NFW profile; [c] Assumed, based on multiple estimates; [d] From NED redshift
References: 1. Fouqué *et al.* (2001), 2. Mieske *et al.* (2005), 3. Einasto *et al.* (1997), 4. Hanski *et al.* (2001), 5. Bardelli *et al.* (2000), 6. Jarrett *et al.* (2003), 7. Drinkwater *et al.* (2001), 8. Tully & Pierce (2000), 9. Tully (1987), 10. Colless & Dunn (1996), 11. From X-rays, Reiprich & Böhringer (2002), 12. Original "great attractor" (GA) of Lynden-Bell *et al.* (1988).

The best fit single attractor to the sample (and both subsets) is the Virgo cluster. Constraining the location of the Virgo cluster to be at (-3.4, 15.6, -0.9) Mpc, the best fit mass varies from $M_{200} = 0.4^{+0.2}_{-0.1} \times 10^{15} M_{\odot}$ in the primary distance subset, to $1.6^{+0.9}_{-0.7} \times 10^{15}\ M_{\odot}$ in the SFI++ subset. The full sample gives a best fit mass of $0.5 \pm 0.2 \times 10^{14}\ M_{\odot}$. It is interesting that the impact of Virgo seems to be larger in the larger volume SFI++ sample (although all values are consistent within the errors). The published mass of the Virgo cluster varies from about $0.2 \times 10^{15} M_{\odot}$ from measurements of the X-ray flux, to $1.2 \times 10^{15}\ M_{\odot}$ from dynamical considerations (see discussion in Fouqué *et al.* 2001), so the mass we fit from just this single attractor model is consistent with other estimates.

Ever since Lynden-Bell *et al.* (1988) suggested that there might be a source of gravitational attraction hidden behind the plane of the Milky Way which accounts for a significant fraction of the motion of the Local Group against the CMB, there has been much debate as to the true nature of this "great attractor" (GA). The situation is obviously complicated by the fact that spherical infall models are a huge over simplification of the true distribution of mass in the universe, and the location of an attractor in such a model should only be considered the center of mass of a complicated mass distribution in its vicinity. As a single attractor the original GA, the Hydra-Centaurus supercluster, and the Shapley supercluster all do roughly equally well at fitting the velocity field of our sample, (with Shapley marginally preferred in all samples). None do nearly as well as Virgo.

Despite being a relatively nearby large supercluster, Pisces-Perseus (PP) has never been found to have a large impact on the velocity field of the local universe, contrary to what is suggested in Table 8.1. We find that the best fit model with a single attractor at the location of the PP core is one in which there is no attractor (*i.e.* the mass is negligible), and the dipole obviously remains the same as in the pure dipole model. There is no signature of infall onto PP in this subset of the SFI++ sample or in published primary distances. For more details on the velocity field in this region see Springob (2005).

Allowing the location of the best fit single attractor to vary, we find that in the SFI++ sample alone, the goodness of fit estimator is extremely flat over much of the nearby volume (*i.e.* the location of the best fit attractor is not well constrained). Here we see a definite benefit to adding in the primary distances to our sample, which results in the fitting routine finding a best fit single attractor very close to the location of the Virgo cluster, at (-4.6±0.9, 15.6±0.7, 0.1±1.1) Mpc/$h_{70}$ in supergalactic Cartesian co-ordinates, or $D = 16.3 \pm 1.1$ Mpc/$h_{70}$, $\alpha = 12.75$, $\delta = 9.67$ ($\pm 4^{\circ}$). Moving the Virgo cluster to this location improves the goodness of fit and the AIC, although not the BIC (which is tougher on the addition of new parameters).

The dipole in our single attractor models in general changes relatively little from the model with a dipole alone, shifting to 379± 61 km s$^{-1}$ towards $(\alpha, \delta) =$ (10.5h, -29.3°) ±12° in the model with infall onto Virgo fit to the entire sample, which is within the $2\sigma$ error contour of the fit for the dipole alone. The biggest change in the dipole comes when the Shapley supercluster is considered as the single

attractor. In that case there is an obvious covariance between the magnitude of the dipole and the mass of the attractor, which is far enough outside of the sample volume that the signature of infall is not much different from a bulk motion in that direction (assuming the mass and distance to Shapley in Table 8.1, there is a gradient of only 100 km $s^{-1}$ across the entire sample). This serves to illustrate the difficulties faced when trying to fit infall onto an attractor at the edge (or past the edge) of your velocity field tracer sample, and the vagaries of multi-component model fitting. We believe that the dipole fit to the sample is partly accounting for infall onto the Shapley supercluster (see discussion later).

## 8.4 Infall onto Virgo and a Second Attractor

Here we investigate the impact of adding a second attractor (in addition to the Virgo cluster which is our best fit single attractor) to the velocity field model. Again we start by using the location of the large nearby concentrations of mass. We find only a small improvement of the likelihood in all samples when a second attractor is placed at either the location of Hydra-Centaurus, Shapley or the traditional GA. For all samples the best fit second fixed attractor is (very marginally) Shapley. The GA is found to be the worst fit for all samples.

Allowing the location of the second attractor to vary freely, we again find that using only SFI++ peculiar velocities the location is not well constrained. Several minima are found, including ones close to the Shapley, and Hydra-Centaurus cluster, but there is no evidence for a significantly better fitting attractor at a location different from known concentrations of mass. The likelihood is very flat, and both Shapley and Hydra-Centaurus are within the $3\sigma$ errors for the best fit (with an obvious covariance between the mass and distance to the second attractor). The best overall likelihood is found for a model with an attractor close to the origin. This is likely an artifact of the fact that low mass galaxies (which tend to be seen only nearby) are preferentially below the TF relation found in Chapter 4, so preferentially have negative peculiar velocities.

In the primary distance sample, and in the combination of the SFI++ and primary distances we find a best fit second attractor at a location close to that of the Hydra cluster, but a slightly behind it ($\alpha = 10.61$h, $\delta = -27.76°$, $D = 46.6$ Mpc in the primary distance sample; $\alpha = 10.60$h, $\delta = -27.69°$, $D = 50.5$ Mpc in the combined sample; Hydra is at $\alpha = 10.61$h, $\delta = -27.53°$, $D \sim 40$ Mpc). This model is preferred over those with a fixed second attractor by the AIC (although not by the BIC which is tougher on the introduction of new parameters), and may simply indicate that the angular location we are assuming (Einasto *et al.* 1997) for the center of mass of the Hydra-Centaurus supercluster is not quite right, but should be moved more towards the Hydra cluster (perhaps because of extra mass in that region currently hidden behind the plane of our Galaxy). The mass of this second attractor is $0.8^{+1.1}_{-0.4} \times 10^{15} M_{\odot}$ in the combined sample (slightly larger if just the tracers with primary distances are used); the mass of Virgo remains very

Table 8.2: Likelihoods and information criteria for multiattractor model fits.

| Sample | | SFI++ (N=1425) | | | Primary distance (N=274) | | | Combination (N=1684) | | |
|---|---|---|---|---|---|---|---|---|---|---|
| Model | No. parm | $\mathcal{L}$ | AIC | BIC | $\mathcal{L}$ | AIC | BIC | $\mathcal{L}$ | AIC | BIC |
| Dipole only | 3 | 570.28 | 576.28 | **592.07** | 57.44 | 63.44 | 74.28 | 648.19 | 654.19 | 670.48 |
| Single attractor, position fixed | | | | | | | | | | |
| Virgo | 4 | 560.40 | 568.40 | **589.45** | 48.20 | 56.20 | **70.65** | 630.02 | 638.02 | 659.74 |
| Hydra-Cen | 4 | 568.01 | 576.01 | 597.06 | 57.44 | 63.44 | 79.89 | 646.72 | 654.72 | 676.44 |
| Shapley | 4 | 567.22 | 575.22 | 596.27 | 57.19 | 63.19 | 79.64 | 646.25 | 654.25 | 675.97 |
| "GA" | 4 | 567.85 | 575.85 | 596.90 | 57.44 | 63.44 | 79.89 | 647.80 | 655.80 | 677.52 |
| Free | 7 | 552.48 | 566.48 | 603.31 | 45.79 | 59.79 | 85.05 | 627.71 | 638.71 | 679.71 |
| Two attractors | | | | | | | | | | |
| Virgo + Shapley | 5 | 557.38 | 567.38 | **593.69** | 48.12 | 58.12 | 76.19 | 628.18 | 638.18 | 665.32 |
| Virgo + Hydra-Cen | 5 | 558.10 | 568.10 | **594.41** | 48.20 | 58.20 | 76.27 | 628.94 | 638.94 | 666.08 |
| Virgo + GA | 5 | 559.06 | 569.06 | **595.37** | 48.20 | 58.20 | 76.27 | 629.97 | 639.97 | 667.11 |
| Virgo + "free" | 8 | 552.48 | 568.48 | 610.57 | 38.74 | 54.74 | 83.65 | 623.52 | 639.52 | 682.95 |
| 2 free attractors | 11 | - | - | - | 36.25 | 58.25 | 97.99 | 621.10 | 643.10 | 702.82 |
| Two attractors + quadrupole | | | | | | | | | | |
| Virgo + Hydra | 10 | **544.85** | **564.85** | 617.57 | **24.72** | **44.72** | 80.85 | **606.58** | **626.58** | 680.87 |
| Dipole + quadrupole only | 8 | 555.82 | 571.82 | 613.91 | 55.91 | 71.91 | 100.82 | 645.20 | 661.20 | 704.63 |
| Three attractors | | | | | | | | | | |
| Virgo + Hydra + Shapley | 6 | 554.19 | 566.19 | 597.76 | 38.10 | 50.10 | **71.78** | 620.48 | 632.48 | 665.05 |
| X-ray clusters | 5 | 560.05 | 570.05 | 596.35 | 35.36 | 45.36 | **63.43** | 616.53 | **626.53** | **653.67** |

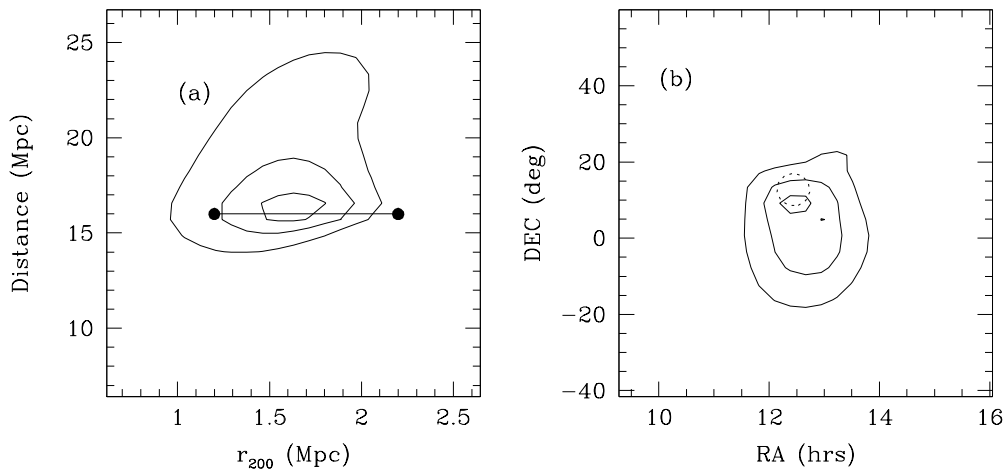



Figure 8.4: Contours of 1, 2 and 3 $\sigma$ errors for the angular direction (b) and mass-distance (a) of the Virgo attractor in a model in which the locations and sizes of two attractors are allowed to vary. The location of the Virgo cluster is marked with the dotted circle in Panel (b). The assumed distance with the horizontal line, which stretches from between two estimates of the mass of Virgo.

similar to that fit in the single attractor models above, consistent with (although on the small side of) other estimates of the mass of Virgo.

In the primary distance and combined samples, we also fit a model in which we allow the location of both attractors to vary. The best fit locations in fact vary very little from the location of the Virgo cluster, and the best fit second attractor above for a small improvement in the goodness of fit. Figures 8.4 and 8.5 show the errors contours for the direction, distance and mass of these two attractors. The first attractor is clearly associated with the Virgo Cluster. The second attractor is inconsistent with the mass of the traditional GA (Lynden-Bell *et al.* 1988), or the GA fit by Tonry *et al.* (2000) at the several sigma level. The $3\sigma$ contour for this attractor includes both the Hydra-Centaurus and Shapley superclusters (see Fig 8.5), but it seems most likely that this attractor is associated with the center of mass of the Hydra-Centaurus supercluster, which must lie roughly in the direction of the Hydra cluster, presumably shifted in that direction from the center presented in Einasto *et al.* (1997) due to mass in that region hidden to optical surveys by the plane of our Galaxy. This idea that the center of mass of the GA region is in fact associated with Hydra-Centaurus but shifted towards the zone of avoidance because of mass hidden from optical surveys it is not a new one (see *e.g.* Woudt & Kraan-Korteweg 2001 for a discussion of how the zone of avoidance impacts the GA region).

The dipole in the best fit two attractor model to the combined sample still has a relatively large magnitude of 343±61 km s$^{-1}$, pointing towards $\alpha = 10.51$h, $\delta = -29.4^\circ \pm 13^\circ$, still roughly in the direction of Hydra-Centaurus and Shapley.

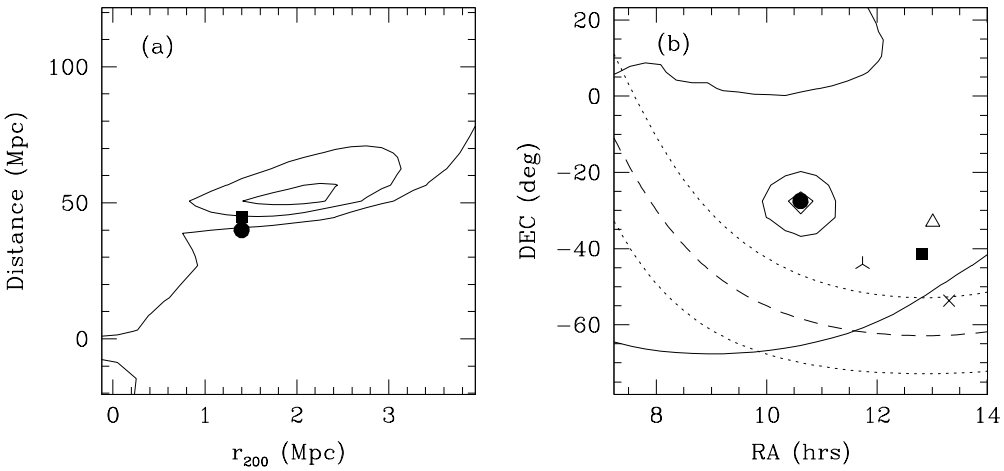



Figure 8.5: Contours of 1, 2 and 3 $\sigma$ errors for the location (b) and mass (a) of the second attractor in a model in which the locations and sizes of two attractors are allowed to vary. The location, mass and distance of major clusters in the region are marked: filled circle - Hydra cluster; filled square - Centaurus cluster; open triangle - Shapley supercluster; cross - GA of Lynden-Bell *et al.* (1988); 3 pronged cross - GA of Tonry *et al.* (2000). The Shapley supercluster and Lynden-Bell *et al.* (1988)'s GA have $r_{200} \sim 7.5$; Tonry *et al.* (2000)'s GA has $r_{200} \sim 4.3$. Lynden-Bell *et al.* (1988)'s GA is at $D \sim 60$ Mpc; Tonry *et al.* (2000)'s GA at $D \sim 50$ Mpc; Shapley at $D \sim 200$ Mpc. In Panel (b) the Galactic plane and $b \pm 20^\circ$ are also indicated.

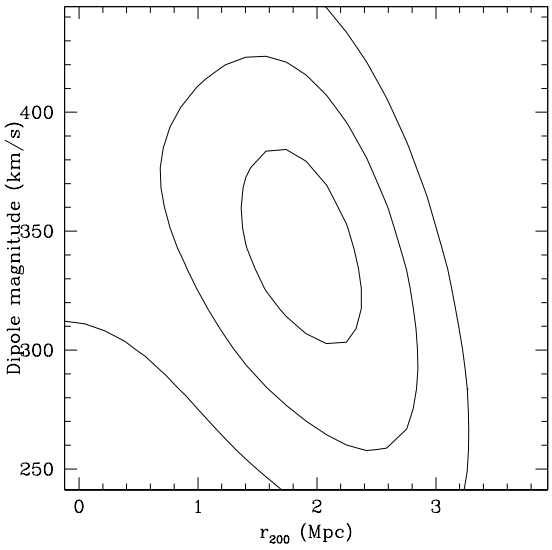



Figure 8.6: Contours of 1, 2 and 3 $\sigma$ errors for the magnitude of the dipole and size of the second attractor in a two attractor model.

If Shapley is considered the second attractor the dipole reduces, and shifts around to $\alpha = 8.68$h, $\delta = -19.46°$. This again suggests that the dipole is accounting for infall onto the Shapley supercluster (which is outside of the sample volume). In fact there is a covariance between the magnitude of the dipole and the mass of any second attractor we tried. This is illustrated for the best fit second attractor in Figure 8.6 – as the mass of the attractor increases the magnitude of the dipole decreases. This same covariance for at attractor at the position of Shapley added in addition to Virgo and an attractor in the Hydra-Centaurus region is shown in Figure 8.8. Clearly the dipole is adjusting itself to account for some of the infall motions in the Hydra-Centaurus/Shapley direction.

## 8.5 Two Attractors and a Quadrupole

As suggested by Tonry *et al.* (2000), a quadrupole component can be added to the velocity field, to account for either asphericity of the attractors (which is certainly expected) or a tidal component due to the influence of masses outside the volume in which velocity field tracers are present.

We experiment with adding a quadrupole centered on the origin to the velocity field, fixing attractors at the positions of Virgo and the best fit second attractor from the previous model. The addition of a quadrupole improves the goodness significantly. The quadrupole which is added, consists of a small expansion almost exactly along the SGZ axis, and corresponding contractions along SGX and SGY (note that we fit a traceless quadrupole so that the net expansion is carried by the Hubble's constant, see Chapter 3 for a full introduction of the model).

Using Hydra-Centaurus, or Shapley as the second attractor, the result is similar, but the goodness of fit is slightly worse. Obviously also, with Shapley the mass of the attractor is significantly larger (because of the larger distances), although the quadrupole interestingly remains quite similar. This is interesting because the Shapley supercluster is already outside the volume in which we have velocity field tracers, and therefore you might expect its influence on the velocity field to already look somewhat like a quadrupolar tide. The addition of a quadrupole in fact does reduce the mass of the best fit Shapley attractor.

The biggest difference in the quadrupole which is fit actually comes from whether or not the SFI++ peculiar velocities are included. In all cases the expansion is roughly along the SGZ axis, Just using the primary distances alone, the best fit quadrupole has a somewhat larger expansion of $\sim 14$ km s$^{-1}$ along this direction, with contractions of $\sim 13$ and 1 km s$^{-1}$ Mpc$^{-1}/h_{70}$ respectively along SGX and SGY. When the SFI++ is added the expansion drops a little to $\sim 9.2$ km s$^{-1}$ Mpc$^{-1}/h_{70}$ along SGZ and a contraction of $\sim 9.0$ km s$^{-1}$ Mpc$^{-1}/h_{70}$ along SGX. The SGY component is negligible in this fit. There is a significant covariance between the $xx$ and $zz$ components of the quadrupole which is illustrated in Figure 8.7, showing the 1,2 and 3 $\sigma$ error contours for the two parameters. This covariance acts to keep $Q_{zz} \gtrsim -Q_{xx}$, and since $Q_{yy} = -Q_{xx} - Q_{zz}$ this results in there being basically no quadrupole component along the SGY axis ($Q_{yy} \sim 0$). The full best fit quadrupole in Supergalactic Cartesian co-ordinates (with units km s$^{-1}$ Mpc$^{-1}/h_{70}$) is

$$Q = \begin{pmatrix} 8.5 \pm 1.9 & 0.5 \pm 1.7 & -2.7 \pm 2.4 \\ 0.5 \pm 1.7 & 0.3 \pm 2.8 & 0.4 \pm 1.8 \\ -2.7 \pm 2.4 & 0.4 \pm 1.8 & -8.8 \pm 2.1 \end{pmatrix} \tag{8.2}$$

As you can see, all off axis components are zero within the errors. The magnitude of the expansion/contraction in SGZ/SGX is constrained at the $3\sigma$ level to $\sim$5-12 km s$^{-1}$ Mpc$^{-1}/h_{70}$.

The dipole in this model has a value 368$\pm$60 km s$^{-1}$ towards $\alpha = 10.0$h, $\delta = -28.9° \pm 14°$.

## 8.6 Just dipole and quadrupole model

The big improvement seen in the goodness of fit when a quadrupole component is added suggests that the dipole and quadrupole alone might provide a reasonable fit to the velocity field. The quadrupole that is fit, now shows its expansion again in the supergalactic plane but in a direction roughly perpendicular to the direction towards Hydra-Centaurus. In the case of the SFI++ subset, which is relatively sparse around Virgo as previously discussed, this dipole plus quadrupole model actually has a better goodness of fit than a model including infall onto Virgo. When the primary distances are added, this is no longer the case, but it still does better than any single attractor other than Virgo.

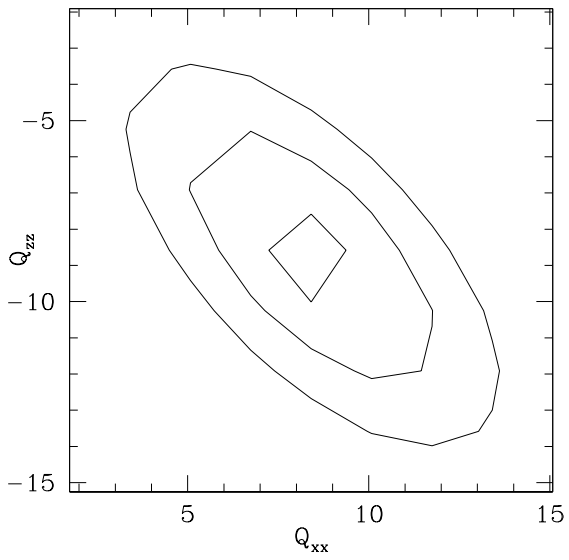



Figure 8.7: Contours of 1, 2 and 3 $\sigma$ errors illustrating the covariance between $Q_{xx}$ and $Q_{zz}$ (units km s$^{-1}$ Mpc$^{-1}/h_{70}$)

This model is very similar to the one fit in Karachentsev & Makarov (2001) to a sample of 145 galaxies within 8 Mpc, although obviously our sample traces a much larger volume, with the SFI++ extending out an order of magnitude further to 86 Mpc/$h_{70}$. In that paper a quadrupolar Hubble's constant with major axis of magnitude 81±3 km s$^{-1}$ Mpc$^{-1}$ pointing towards (-0.7, 0.8, 0.0) is found. In our full sample, we find a quadrupole with extra expansion of 29.2 km s$^{-1}$ Mpc$^{-1}/h_{70}$ pointing towards (0.9, 0.4, 0.1) (recall this is in addition to the 70 km s$^{-1}$ Mpc$^{-1}$ Hubble's constant which we set to carry the mean expansion), and contractions of 27.4 km s$^{-1}$ Mpc$^{-1}/h_{70}$ towards (-0.4, 0.9, 0.1) and 1.8 km s$^{-1}$ Mpc$^{-1}/h_{70}$ towards (0.0, 0.1, -1.0). The dipole we find in this model also points in a very different direction to the Karachentsev & Makarov (2001) dipole. The difference in volume between the two samples makes it hard to directly compare the models. However we note that using the primary distances alone (which cover a smaller volume than the full sample) the quadrupole is still much larger than, but points in roughly the same direction as the Karachentsev & Makarov (2001) result.

## 8.7 Three Attractors

Here we include attractors at the locations of the best fit two attractors to the combined sample, and also add in an attractor at the position of the Shapley supercluster. This model does reasonably at describing the velocity field, although the model which includes a quadrupolar component to the velocity field still does better. If we try these three attractors and a quadrupole component, we find essen-

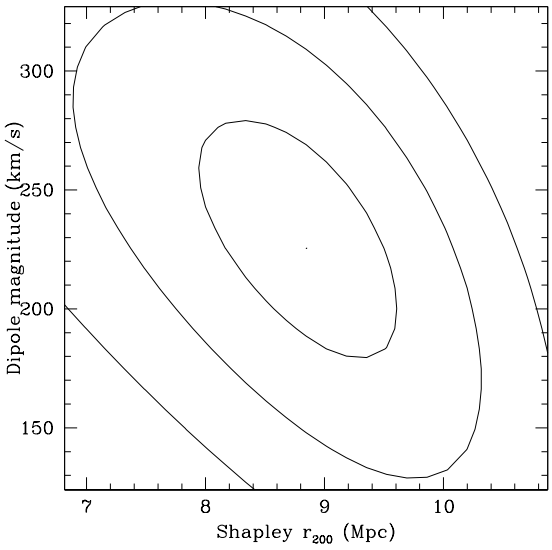



Figure 8.8: Covariance between the mass of the Shapley supercluster attractor and the magnitude of the dipole in the best fit three attractor model.

tially no improvement in the goodness of fit over the model with just 2 attractors and a quadrupole, and the likelihood is very flat over a wide range of masses for the attractor at the location of Shapley. Figure 8.8 illustrates the covariance between the magnitude of the dipole in the three attractor model (which points towards $\alpha, \delta = 8.7$h, -19.3°) and the best fit mass for the Shapley supercluster, which varies between 5-10 $\times 10^{16}$ $M_{\odot}/h_{70}$ in the $1\sigma$ error contour. The dipole is obviously able in increase to compensate for infall onto the Shapley supercluster. As discussed above, since Shapley is well outside our sample volume ($\sim 114$ Mpc$/h_{70}$ from the nearest edge) infall onto the supercluster is not much different to a bulk motion of the entire sample in that direction (assuming the mass and distance to Shapley in Table 8.1, infall would only result in a velocity gradient of 100 km s$^{-1}$ across the sample volume).

## 8.8 Multiple Attractors from Cluster Catalog

Here we use the X-ray selected cluster catalog (HIFLUGCS) presented in Reiprich & Böhringer (2002) as an input list of attractors, all of which are assumed to have an NFW density profile, and are placed at distances of $d = cz/H_0$, (which of course is incorrect for the nearest clusters). We use all 63 clusters which make it into the flux limited HIFLUGCS catalog, and in addition include the 11 clusters which make the flux limit but not the Galactic latitude limit. The mean distance to these clusters is 206±140 Mpc$/h_{70}$, the distribution in Supergalactic Cartesian co-ordinates in shown in Figure 8.9. As shown in that Figure, several of the clusters are outside our peculiar velocity sample volume. For attractor masses we use $r_{200}$

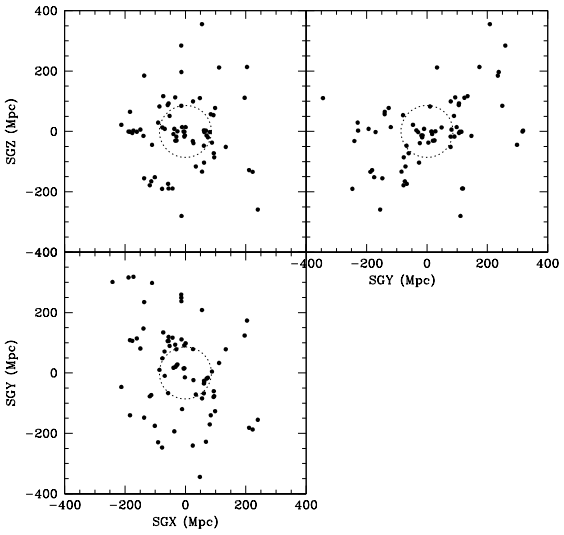



Figure 8.9: Distribution in supergalactic Cartesian co-ordinates of clusters from the X-ray sample HIFLUGCS which are used as attractors in a fit to the peculiar velocity data. The volume covered by the peculiar velocity data is marked with the dotted circle.

for these clusters as presented in Table 4 of Reiprich & Böhringer (2002), but allow for an arbitrary scaling in the fit, thus only using the X-ray data to provide relative masses. In addition we include an attractor at the location of Virgo (from Table 8.1, whose mass we allow to be a free parameter (the area of the Virgo cluster is excluded from HIFLUGCS along with low Galactic latitudes and the Magellanic Clouds), and like all other models considered here we also fit for an arbitrary dipole of the entire sample.

Using SFI++ peculiar velocities alone this model does only marginally better than a simple Virgo infall model, however when the primary distances are added the model has almost as low a goodness of fit as our preferred model (which has infall onto Virgo, Hydra-Centaurus and a quadrupolar component to the velocity field), and because we treat the masses of all 74 additional clusters as only one free parameter (a scaled version of the mass presented in Reiprich & Böhringer 2002), this model is assumed to have five less free parameters and therefore better BIC than the two attractor plus quadrupole model in both the primary distance and combined samples. The best fit mass of the Virgo cluster is found to be $M_{200} = 0.4 \pm 0.1 \times 10^{15} M_{\odot}$, similar to the mass found in simpler models. The best fit scaling for the values of $r_{200}$ presented in Table 4 of Reiprich & Böhringer (2002) ($r_{200}$ is radius within which the density is 200 times the background as calculated assuming the hot gas is isothermal) is 0.65±0.15. The residual dipole has a magnitude 353±60 km s$^{-1}$ and points towards $(\alpha, \delta)$ = (10.35h, -29.42°) ±13°, still roughly in the direction of the Shapley supercluster.

Contours of constant velocity in the CMB frame are shown for this model in

Figure 8.10. Panel (a) shows contours in the supergalactic plane (SGP) where the influence of the Virgo cluster at (SGX, SGY) $\sim$ (4,16) Mpc can be seen. The attractor at (SGX, SGY) $\sim$ (-27, 28) Mpc is cluster NGC 5044, which has a mass of $3.5\times10^{13}$ $M_\odot$. Panel (b) shows contours in a plane parallel to, but 10 Mpc above the SGP. In this you can see the influence of the Coma cluster at (SGX, SGY) $\sim$ (1, 98), which has a mass of $1.0\times10^{15}$ $M_\odot$, and Abell 3627 (the Norma cluster) at (SGX, SGY) $\sim$ (-67, -10) with a mass of $4.9\times10^{14}$ $M_\odot$. Panel (d) shows the contours 30 Mpc below the SGP, showing the region in which we find our best fit second attractor in the two attractor model. Here there are several attractors in that region, including Hydra at (SGX, SGY) $\sim$ (-30, 25) ($2.0\times10^{14}$ $M_\odot$) and the cluster Abel S636 near the Galactic plane at (SGX, SGY) $\sim$ (-34, 19) ($6.2\times10^{13}$ $M_\odot$). Also having an impact in that rough direction (although only 9 Mpc below the SGP so not showing up in Figure 8.10c) is the Centaurus cluster fitted with a mass of $2.0\times10^{14}$ $M_\odot$. In this panel the impact of the dipole is shown clearly, as even at large distances the contours differ from Hubble flow (shown with the dashed concentric circles). Panel (d) shows the contours in a plane perpendicular to the SGP, where again the influence of Virgo at SGY $\sim$ 16 and Coma at SGY $\sim$ 98 can most clearly be seen. Also in this panel you can see the Fornax cluster at (SGY, SGZ) $\sim$ (-14, -13).

This technique of using the positions of known concentrations of mass in the nearby universe to constrain peculiar velocity models clearly has the potential to provide more realistic velocity field models than simple 2 attractor models, and in theory with a velocity field tracer sample of $N = 1685$ we have enough information to constrain all 75 cluster masses individually. However for the present we will proceed with the simpler 2 attractor plus quadrupole model, which does not require as an input assumption the location and relative masses of 75 attractors.

## 8.9 Velocity Dispersion

In fitting all the above models we use the velocity dispersion found by Tonry *et al.* (2000) of 187 km s$^{-1}$, and also add extra velocity dispersion at the locations of the best fit attractors with a magnitude which is a Gaussian centered on the attractors, and of width 650 km s$^{-1}$ for the Virgo cluster, and 500 km s$^{-1}$ for all other attractors (this is again following Tonry *et al.* 2000). Calculating the velocity dispersion from the best fit model (with two attractors and a quadrupole component) as

$$\sigma_v = \frac{\Sigma(cz - v_{\rm model}(d))^2/H_0^2\sigma_d^2}{\Sigma 1/H_0^2\sigma_d^2} \tag{8.3}$$

we find values of 163±21 km s$^{-1}$ for the combined sample, 160±10 km s$^{-1}$ for the primary distance sample and a larger value of 406±24 km s$^{-1}$ for the SFI++. These values obviously contain a component from measurement errors, which has a larger mean value in the SFI++ sample alone, but there does also appear to be an intrinsically large scatter of the SFI++ spiral galaxies from the flow model

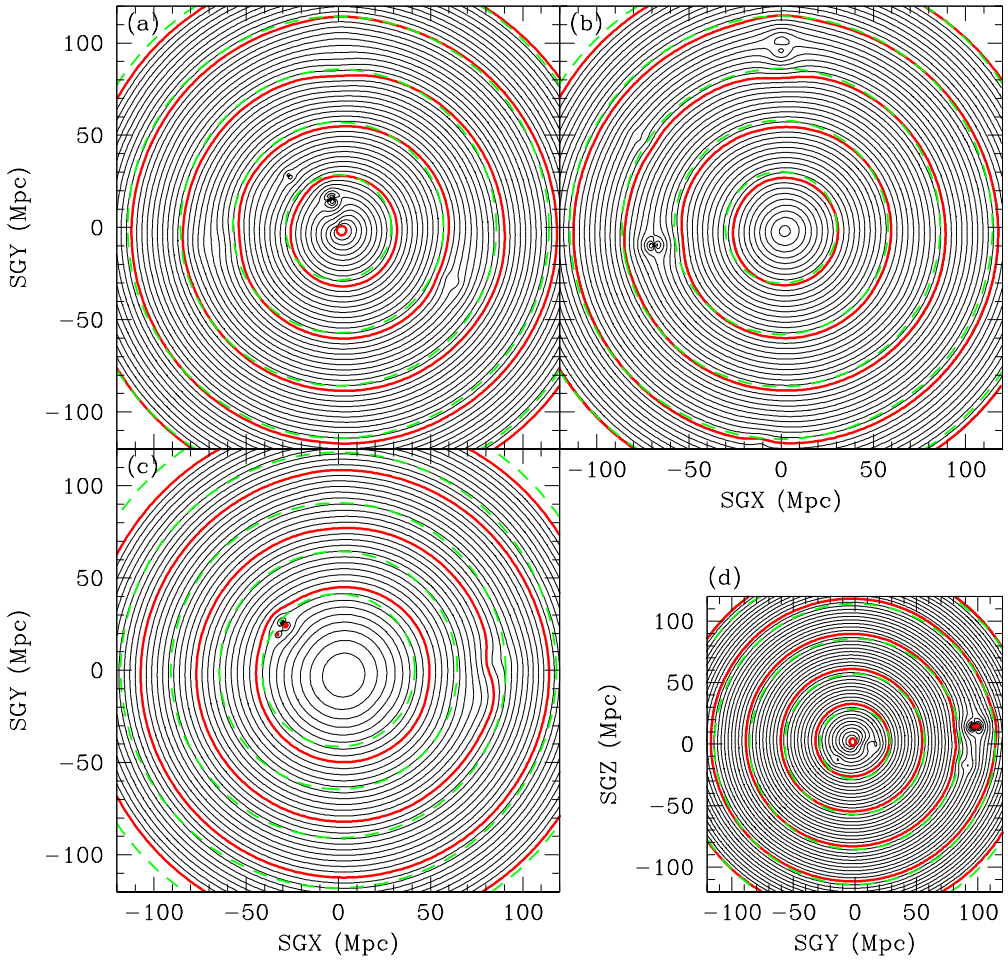



Figure 8.10: Shown are contours of constant velocity in the CMB frame for the multiattractor model fit to the full sample when X-ray selected clusters (from HIFLUGCS) are used as attractors. Also included is an attractor at the location of the Virgo cluster in Table 8.1. Panel (a) shows contours in the supergalactic plane, while Panels (b) and (c) show contours in a plane 10 Mpc above and 30 Mpc below the SGP respectively. Panel (d) shows contours in a plane perpendicular to the SGP. Heavy contours are spaced at intervals of 2000 km $s^{-1}$, light contours at 200 km $s^{-1}$. The dashed lines show what would be expected for pure Hubble flow.

than seen in the primary distance sample. The residual velocities from the best fit model are shown in Figure 8.11, where residuals larger than $1\sigma$ (where $\sigma = \sqrt{(H_0 d)^2 + \sigma^2_{\rm flow}}$ includes both measurement errors and an allowance for velocity in the model) are shown as filled circles if they are approaching or open circles if they are receding. As can be seen in that Figure, there is a small tendency for galaxies in the foreground of Hydra-Centaurus to have underestimated peculiar velocities in the model (at the less than $3\sigma$ level) and galaxies in the foreground and vicinity of Virgo to have over estimated peculiar velocities. However, at the $3\sigma$ level, there are only two significant residual velocities, so we conclude that this model does a reasonable job at describing the local velocity field within $\sim 86$ Mpc/$h_{70}$.

## 8.10 Summary of Velocity Field Models

### 8.10.1 Model fit to SFI++ data alone

The best goodness of fit (and AIC) is found for a model with infall onto Virgo and and attractor in the Hydra-Centaurus region, and also a quadrupolar component in the velocity field. This model is only marginally preferred over one in which the second attractor is the more distant (and correspondingly larger) Shapley supercluster, and the locations of the attractors are as found in the in a fit to the full sample below. In the SFI++, the errors on individual peculiar velocities are sufficiently large that it is not possible to improve on the locations of the attractors over known locations. The BIC is minimized for a simple Virgo infall model.

### 8.10.2 Model fit to primary distances alone

Fitting velocity field models to the primary distance sample alone, we find a much large dipole than for the SFI++ sample, most likely because of the smaller volume covered by the tracers. There are sufficiently deep minima in the goodness of fit estimator now to find the locations of the best fit attractors, and the best goodness of fit is found for a model in which there is infall onto Virgo (at almost exactly the same location as suggested in Table 8.1), a second attractor somewhat offset from nominal center of the Hydra-Centaurus cluster, but in that rough direction and the same distance,and a quadrupole component to the velocity field. Now we find the lowest BIC for the model discussed in Section 8.7 which fits for infall onto Virgo and clusters with relative masses and locations taken from HIFLUGCS (Reiprich & Böhringer 2002), however we still prefer the two attractor plus quadrupole model which has fewer input assumptions, and the lowest AIC.

### 8.10.3 Model fit to the Full Sample

In the combined sample, the best fit model again is one which includes infall onto Virgo, and attractor in the general region of the Hydra-Centaurus supercluster, and

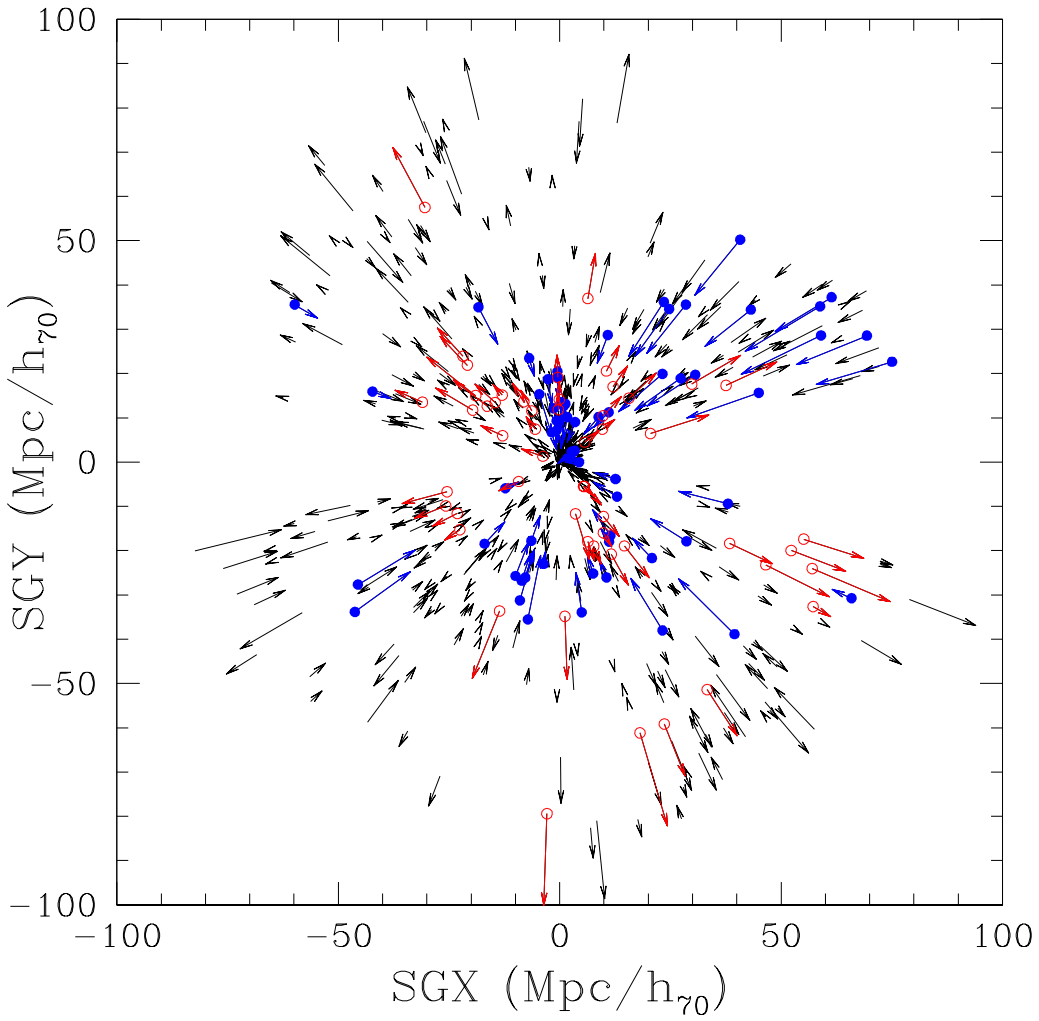



Figure 8.11: Shown are the residual velocities of all velocity field tracers within 10 Mpc of the supergalactic plane, after the best fit model with infall onto the Virgo cluster, Hydra-Centaurus and a dipole and quadrupole component have been subtracted. Velocities larger than $1\sigma$ (where $\sigma = \sqrt{(H_0 d)^2 + \sigma^2_{\rm flow}}$ includes both measurement errors and an allowance for velocity dispersion in the model) are marked with filled circles if they are approaching, open circles if they are receding.

a small quadrupolar component with extra expansion roughly along the SGZ axis. There is no significant improvement in the goodness of fit when an attractor at the location of the Shapley supercluster is added to this model. However (as when using the primary distances alone) the model with the best information criteria (although only marginally for the AIC) is one in which the locations and relative masses of HIFLUGCS clusters (Reiprich & Böhringer 2002) are used as an input. Because of the large number of input assumptions in this model (the locations and relative masses of 75 clusters) we still prefer the two attractor plus quadrupole field.

The value of combining the samples is seen, especially in the determination of the location of the best fit attractors (which is not possible using the SFI++ sample alone), and the magnitude of the quadrupole and dipole (which is reduced when the SFI++ sample is added to the primary distance sample). Obviously the lower errors in the primary distance sample mean that it dominates the fit in the nearby regions, while the benefit of adding in the SFI++ sample is seen in its larger and more uniform volume coverage.

## 8.11 Discussion

The best fit (and our preferred) model to the full velocity field tracers sample is one in which there is infall onto the Virgo cluster (found at (-4.7±0.7, 15.9±0.9, -0.3±1.0) Mpc/$h_{70}$ in supergalactic Cartesian co-ordinates), and an attractor roughly 10 Mpc behind the Hydra cluster (in the Hydra-Centaurus region, but offset from the nominal center of the supercluster as found by Einasto *et al.* (1997)). The addition of a quadrupolar component, describing extra expansion out of the plane of the local supercluster improves the goodness of fit significantly. The residual dipole in this model has a value 368±60 km s$^{-1}$ towards $\alpha = 10.0$h, $\delta = -28.9° \pm 14°$. The model parameters are shown in Table 8.3, and contours of constant CMB frame velocity are shown for this model in Figure 8.12. The residuals of the observed peculiar velocities are shown in Figure 8.11. In Section 8.8 above we calculated a mean velocity dispersion from this model of 163±21 km s$^{-1}$.

### 8.11.1 Infall onto Virgo

We find a mass for the Virgo cluster of $0.6 \pm 0.2 \times 10^{15} M_{\odot}$, consistent with (if on the small side of) previous determinations of its mass, both from X-rays and dynamical constraints. The best fit distance for Virgo is 16.6±1.5 Mpc. Virgo therefore creates an infall velocity at the location of the Local Group (LG) of $127^{+54}_{-46}$ km s$^{-1}$. Infall onto our second attractor in Hydra-Centaurus creates a Virgo-LG motion of $\sim 3$ km s$^{-1}$ however the quadrupole field creates a small compression -9 km s$^{-1}$ between Virgo and the LG giving a net Virgo-LG motion in the expanding frame of about 131 km s$^{-1}$, on the small side of what has previously been found. This differs from the Tonry *et al.* (2000) model in which the quadrupole produces

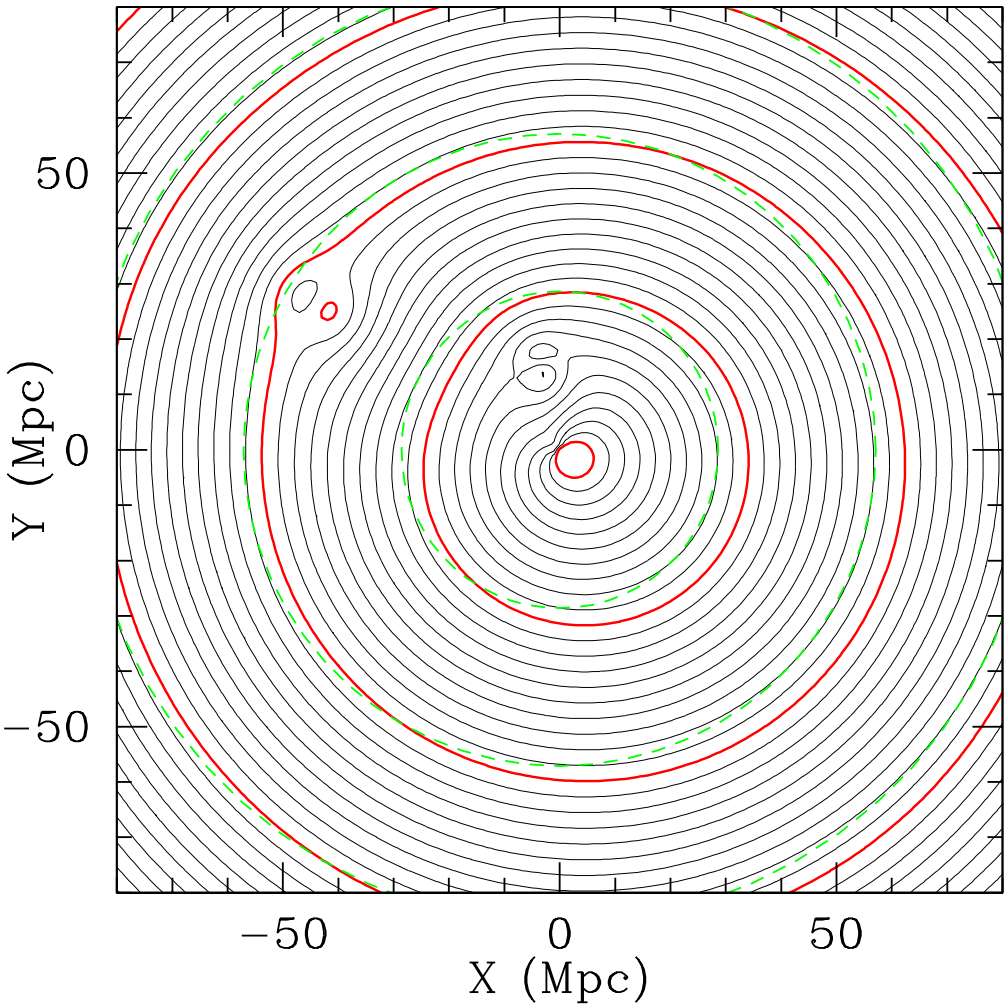



Figure 8.12: Contours of constant CMB velocity for the best fit multiattractor model to the combined SFI++ and primary distance sample. Contours are shown in a plane which goes through both Virgo, and the second attractor at SGB∼-40°. Heavy contours are spaced at intervals of 2000 km $s^{-1}$, light contours at 200 km $s^{-1}$. The dashed lines show what would be expected for pure Hubble flow.

Table 8.3: Parameters of the best fit multiattractor model.

| | |
|---|---|
| **Attractors:** | |
| **Virgo** | |
| Position (Mpc) | (-4.7±0.7, 15.9±0.9, -0.3±1.0) |
| Mass ($10^{15}$ $M_\odot$) | 0.6±0.2 |
| Enclosed overdensity | $0.8^{+0.5}_{-0.4}$ |
| **Hydra-Centaurus** | |
| Position (Mpc) | (-30.5±3.0, 26.2±3.4, -30.8±3.2) |
| Mass ($10^{15}$ $M_\odot$) | $1.2^{1.2}_{-}0.6$ |
| Enclosed overdensity | $0.07^{+0.1}_{-0.04}$ |
| **Dipole** (km s$^{-1}$) | (-204±34, 160±27, -261±41) |
| **Quadrupole:** | |
| Magnitude ($h_{70}$km s$^{-1}$ Mpc$^{-1}$) | Direction |
| 9.2±2.0 | (-0.2, 0.0, -1.0) ±0.2 |
| 9.0±2.0 | ( 1.0, 0.1, -0.2) ±0.2 |
| 0.3±2.0 | ( 0.0, -1.0, -0.1) ±0.2 |

a net expansion of 174 km s$^{-1}$ between Virgo and the Local Group, which when added to their pure Virgo infall of 139 km s$^{-1}$ gives a LG-Virgo motion in their model of 140-400 km s$^{-1}$.

The best fit location for Virgo is within 2 Mpc of that shown in Table 8.1 at (-4.7±0.7, 15.9±0.9, -0.3±1.0) Mpc. This is the location in a model with two free attractors fit to our full sample. Error contours for both the location and mass of Virgo are shown in Figure 8.4.

### 8.11.2 The "Great Attractor"

The best fit second attractor to the full sample is at a location in supergalactic Cartesian co-ordinates of (-30.5±3.0, 26.2±3.4, -30.8±3.2) Mpc, or a distance of 50.6±5.5 Mpc in the direction $\alpha = 10.6$h, $\delta = -27.5°$ ($l = 270°$, $b = 27°$) ±8°. This is in a direction very close to the Hydra cluster (one of the major clusters in the Hydra-Centaurus supercluster), but $\sim 10$ Mpc behind it (see Figure 8.5). We note that the "great attractor" of Lynden-Bell *et al.* (1988), is only 17±10° away from this direction, and is also within 10 Mpc of its distance. The "great attractor" of Tonry *et al.* (2000) was found at (-41.1, 16.4, -19.2) Mpc or $D = 48.2$ Mpc at $\alpha = 11.7$h, $\delta = -44.1°$, which is slightly behind the Cen 30 and Cen 45 clusters (note that we have adjusted the values for $H_0 = 70$ km s$^{-1}$ Mpc$^{-1}$). We use a very similar model to Tonry *et al.* (2000), the main differences being that we do not fit for the Hubble's constant and that the functional form of the attractor profile is different: we use NFW, while they use a power law with an exponential cut-off (which actually give a very similar shape to the infall profile, except at very small radii). The bulk of the primary distances in our sample also come from the same

data presented in Tonry *et al.* (2001). The GA in their model has significantly more impact on the velocity of the Local Group than we find because it is more massive ($\sim 9 \times 10^{15} M_{\odot}$, compared to our $1.2 \pm 0.6 \times 10^{15} M_{\odot}$), and is about 10 Mpc closer than our attractor, however we note the covariance that Tonry *et al.* (2000) show between the GA infall velocity and Hubble's constant. Their best fit value for the Hubble's constant is 77 km s$^{-1}$ Mpc$^{-1}$, while we use a standard value of 70 km s$^{-1}$ Mpc$^{-1}$ based on the 71±4 km s$^{-1}$ Mpc$^{-1}$ found from the WMAP result (Bennett *et al.* 2003). Using this value in their models would significantly decrease the GA infall velocity, more in line with what we find.

Mieske, Hilker & Infante (2005) discuss this Hydra-Centaurus region in more detail, and present SBF distances to 16 galaxies in the Hydra cluster (along with 15 SBF distances in the Centaurus cluster in Mieske & Hilker 2003). They argue for an attractor of $9 \times 10^{15}$ $M_{\odot}$, at a distance of about 45 Mpc, and shifted $\sim 15^{\circ}$ towards the position of Hydra from the location of the Tonry *et al.* (2000) attractor, but say they do not have enough data to independently fit for the location. They find a very small peculiar velocity for the Cen 30 component of Centaurus along with a large value for Hydra and therefore suggest that the attractor must be behind Hydra, with Centaurus mostly falling onto it in the tangential direction. We have included the distances they present in our primary distance sample (see Chapter 7), however when combined with all the other available data for Centaurus we still find a peculiar velocity for Centaurus consistent with it moving with Hydra in the direction towards Shapley in the background; and conclude that the dipole of our final model (with infall onto two attractors and a quadrupole) may be taking into account some of that motion towards Shapley. Using just the TF distances for Hydra and Centaurus (both of which are clusters used in the template sample of Chapter 4) we find a much smaller peculiar velocity for Centaurus, and the Hydra cluster is actually found to have a negative peculiar velocity (because it is put at a larger distance).

Considering this evidence it seems likely that the "great attractor" of our model is the center of mass of the Hydra-Centaurus supercluster, which is shifted towards Hydra from the cataloged position in Einasto *et al.* (1997), presumably because of clusters in the region hidden to optical catalogs by the plane of our Galaxy as has also been suggested by previous work (*e.g.* Woudt & Kraan-Korteweg 2001). We hypothesis that the residual dipole in the model in that direction takes into account some infall onto more distance concentrations of mass like Shapley which Hydra-Centaurus is also taking part in. The "great attractor" in our model is almost two orders of magnitude smaller than the one found by Lynden-Bell *et al.* (1988) and still almost an order of magnitude than the "great attractor" in Tonry *et al.* (2000), both of which are excluded at the several sigma level (as shown in Fig 8.5) . We suggest that the debate between the closer and more distant "great attractors" can be resolved by there being infall onto both Hydra-Centaurus and Shapley and that previous models which neglected infall onto Shapley (either by fixing the velocity frame of because they did not cover sufficient volume) found an artificially inflated nearby "great attractor" to compensate. Direct evidence

for infall onto Shapley will not be possible without more accurate distances which can provide useful peculiar velocities at the $D \sim 200$ Mpc ($cz \sim 14000$ km s$^{-1}$) distance of the Shapley supercluster.

### 8.11.3 The Dipole

Our best fit dipole is 368±60 km s$^{-1}$ towards $(\alpha, \delta)$=(10.0h,-28.9°), or $(l, b) = (264°, 21°)$ ±14°. This is the dipole in the model which also has infall onto Virgo, an attractor near the Hydra-Centaurus supercluster, and a quadrupolar component. If we fit just a dipole to the sample, the goodness of fit is significantly worse, but the resulting dipole is very similar at 388±58 km s$^{-1}$ towards $(\alpha, \delta)$=(10.9h,-28.2°). Both of these dipoles directions are within the error identical to the direction of motion of the LG in the CMB frame, though the magnitude is smaller, because some of the LG motion is accounted for within the volume. Other recent measurements of the dipole include $153 \pm 126$ km s$^{-1}$ towards $(l, b) = (294°, 67°) \pm 43°$ from a sample of 300 galaxies with SBF distances (Tonry *et al.* 2000); 200±65 km s$^{-1}$ towards $(l, b) = (295°, 25°) \pm 20°$ from the earlier field TF sample of Giovanelli *et al.* (1998a) (on which the SFI++ sample builds); 534±90 km s$^{-1}$ towards (268°, 19°) ± 16° from the cluster TF sample of Giovanelli *et al.* (1998b); and $372 \pm 127$ km s$^{-1}$ towards $(l, b) = (273°, 6°) \pm 16°$ from the SMAC cluster sample with the PSC$z$ velocity field subtracted (Hudson *et al.* 2004). These results are summarized in Table 8.4 which also shows the motion of the LG in the CMB. These results are all consistent with each other at the few sigma level, and inconsistent with the much larger streaming motions which have previously been suggested (*e.g.* Lauer & Postman 1994). Note that all these dipoles are calculated for nearby samples which have not yet reached the convergence depth of $cz \sim 10000$ km s$^{-1}$.

We argue that the residual dipole motion in the best fit model is partly due to infall onto the Shapley supercluster region which being significantly outside our sample volume has little other impact on the velocity field. If the entire motion were due to infall onto an attractor at $D \sim 200$ Mpc, it would have a mass $M \sim 10^{17}\ M_\odot$, but would create a significant gradient in infall velocity across the sample volume, which is not seen. If Shapley has a mass of $M \sim 2 \times 10^{16}\ M_\odot$ as suggested in Table 8.1, it could account for $\sim 50$ km s$^{-1}$ of the dipole, and would create only a small velocity gradient ($\sim 100$ km s$^{-1}$) across the sample, a hint of which is seen in the residuals from the model seen in Figure 8.11.

### 8.11.4 The Quadrupole

The best fit quadrupolar component shows extra expansion of size $\sim 9.2$ km s$^{-1}$ Mpc$^{-1}/h_{70}$ roughly along SGZ, and contraction of $\sim 9$ km s$^{-1}$ Mpc$^{-1}/h_{70}$ along SGX. The SGY component of the quadrupole is negligible. This quadrupole appears physically plausible. The low density of galaxies at ±SGZ might be expected to result in a slightly increased expansion in those directions. The SGY component is probably hard to disentangle from infall onto Virgo, so the fact that it

Table 8.4: Measurements of the dipole.

| Sample | Magnitude (km s$^{-1}$) | Direction $(l, b)$ |
|---|---|---|
| Ours (SFI++ and primary) | | |
| .. just dipole | 388±58 | (273°, 28°) ± 10° |
| .. full model | 368±59 | (264°, 21°) ± 14° |
| Giovanelli *et al.* (1998a) (field TF sample) | 200±65 | (295°, 25°) ± 20° |
| Giovanelli *et al.* (1998b) (cluster TF sample) | 534±90 | (268°, 19°) ± 16° |
| Tonry *et al.* (2000) (SBF sample) | 153±126 | (294°, 67°) ± 43° |
| Hudson *et al.* (2004) (SMAC sample) | 372±127 | (273°, 6°) ± 16° |
| LG-CMB motion | 621±24 | (272°, 28°) ± 2° |

is small presumably means all infall onto Virgo is accounted for by the attractor component of the model. Since the quadrupole is forced to have zero trace there cannot be expansion along SGZ without a corresponding contraction along SGX. This covariance between $Q_{xx}$ and $Q_{zz}$ is illustrated by Figure 8.7.

### 8.11.5 Net Motion of the Local Group

The Local Group (LG) has a net motion of 621±24 km s$^{-1}$ in the direction $(l, b) =$ (272°±3°, 28±1°), or breaking it down into supergalactic Cartesian co-ordinates, (-385±38, 337±3, -352±5) km s$^{-1}$. This information is not used in the velocity field modeling discussed above, but rather can provide an independent check of the model. We now ask what fraction of this motion is accounted for by the velocity model we fit in this Chapter. Subtracting the dipole component of 368±60 km s$^{-1}$ towards $\alpha = 10.0$h, $\delta = -28.1° \pm 14°$, or (-204±34, 160±27, -261±41) km s$^{-1}$, we are left with a residual motion of (-181±51, 177±27, -91±41) km s$^{-1}$. Infall onto Virgo in our best fit model, is 127 ± 50 km s$^{-1}$, or in supergalactic Cartesian co-ordinates, (-36±14, 121±48, 2±1) km s$^{-1}$, leaving a LG motion of (-145±53, 56±47, -89±41) km s$^{-1}$. Infall of $40 \pm 36$km s$^{-1}$ onto our second attractor in the direction of Hydra-Centaurus accounts for (-24±21, 21±19, -24±22) km s$^{-1}$, leaving a final local group residual velocity of (-121±57, 35±51, -65±47) km s$^{-1}$ (the quadrupole component is centered on the LG, therefore has no impact on its velocity). This velocity is zero within $2\sigma$ and certainly within the cosmic velocity dispersion of $\sim 170$ km s$^{-1}$, therefore we claim that the LG motion can by fully explained by the simple velocity field model presented here. We find no evidence for the "Local Anomaly" (unexplained motion of the LG in the SGZ direction) in contrast to earlier multiattractor model studies. The SGZ motion of the LG in our model is accounted for by a somewhat larger SGZ component of the dipole than has previously been found. This may be a result of the larger volume covered by the SFI++ sample showing the benefit of including this data in the fit.

## 8.12 Conclusions

We fit various simple velocity field models to samples of velocity field tracers

- The SFI++ – galaxies, groups and clusters with distances measured from the TF relation (see Chapters 4 and 6)
- Galaxies and groups with published primary distances (see Chapter 7)
- The combination of SFI++ TF velocity field tracers and primary distance sample

There is an improvement in the fit from combining the larger volume SFI++ Tully-Fisher sample with the much smaller sample of more precise primary distances. In particular without the primary distance sample there are no sufficiently deep minima in the goodness of fit measure to localize the attractors, while with the larger volume SFI++ sample the dipole and quadrupole components are better constrained.

Our best fit model includes infall onto the Virgo cluster, an attractor in the Hydra-Centaurus region, dipole and quadrupolar components. The residual dipole points in the direction of Hydra-Centaurus and the Shapley supercluster in the background, and we hypothesize that it is accounting for the signature of infall towards the Shapley supercluster, which being outside our survey volume has no other significant trace in the velocity field. The best fit quadrupole has excess expansion roughly along the SGZ direction, and contraction along SGX (the SGY component is negligible), perhaps showing the influence of the over-dense region in the supergalactic plane, and under-dense regions in the ±SGZ directions.

We find no evidence for the so-called "Local Anomaly", or excess motion of the Local Group in the SGZ direction. The entire motion of the LG in the CMB is accounted for in our best fit model. Our dipole SGZ component has increased over previous velocity field models which argued for a Local Anomaly.

We argue that the debate over the distance to the "Great Attractor" can be resolved by the physically obvious solution that there is infall onto both the Hydra-Centaurus supercluster (perhaps partly hidden by the ZoA) and Shapley behind it. When infall onto Shapley is neglected (*i.e.* by fixing the velocity frame, or in samples which do not cover enough volume), the size of the Hydra-Centaurus region attractor is artificially inflated, but even accounting for bulk motion of the entire local volume towards the Shapley supercluster we find evidence for infall onto an attractor which presumably represents the center of mass of the Hydra-Centaurus supercluster. Direct evidence of infall onto the Shapley supercluster will require much larger volume high quality peculiar velocity samples which are not possible at present because the errors on distances cannot provide useful peculiar velocities at the $D \sim 200$ Mpc$/h_{70}$, or $cz \sim 14000$ km s$^{-1}$ distance of the Shapley supercluster.

We find much promise in a model which uses an X-ray selected sample of clusters (and their corresponding masses) as an input list of attractors. This has

the potential to provide a more realistic model of the local velocity field than accounting for all motions by infall onto only two attractors, and we plan to explore it more in future work.

The parametric velocity field presented in this Chapter is fit to a sample of velocity field tracers almost an order of magnitude larger than any that has been used before. Simple parametric models provide insight into the dominant sources of attraction in the volume, but as may be clear from the above discussion, the model parameters can be hard to disentangle, for example the imprint of outside attractors in particular is difficult to distinguish from bulk motion of the entire sample. This sample represents the biggest (and perhaps final) of its generation of peculiar velocity samples; future work is concentrating on much larger numbers of galaxies, but with correspondingly lower quality peculiar velocities (*e.g.* plans to measure $D_n - \sigma$ distances for 15000 galaxies in the southern sky with 6dF; Jones *et al.* 2004). The SFI++ sample should be exploited for more complex non-parametric models of the velocity field, where the larger numbers along with high quality peculiar velocities will provide higher resolution views of the smoothed density field than was possible with previous samples (and this is work we plan for the future). Meanwhile, the parametric modeling here provides a the best currently available correction for redshift distances in the local universe.

# Chapter 9

# Conclusions

## 9.1 Summary of Conclusions

In this thesis we have presented a new look at the velocity field in and around the Local Supercluster using a much larger sample of velocity field tracers than has been previously available.

In Chapters 2 and 3 we gave motivations for the need for a better understanding of the local peculiar velocity field. Chapter 2 used mock HI survey data to study the impact of neglecting peculiar velocities in surveys used to measure the local HI mass function (HIMF); similar arguments could be applied to measuring local luminosity functions. We showed that if peculiar velocities are ignored serious biases can be introduced into the derived HIMF, with the exact size and nature of the bias depending on the survey area and depth. In particular we showed that for a survey of the Southern sky mimicking the HIPASS BGC (Zwaan *et al.* 2003), the number of low mass HI object will be underestimated if Hubble flow is assumed, due to the general motion of galaxies in the Southern sky toward the Hydra-Centaurus and Shapley superclusters. A simulated survey in the anti-Virgo direction pointed to the limitations of the flow model we used, which having been fit to a much smaller sample of velocity field tracers than we consider here, is badly constrained in this low density region. This Chapter is published in Masters, Haynes & Giovanelli (2004).

In Chapter 3 we fit a multiattractor model to a mock sample of galaxies taken from a constrained simulation of the local universe. There we provide a practical guide for the best method to estimate distances to galaxies from their redshifts divided into 12 regions of the sky. We note that when deriving distances from redshifts (either using a flow model or simple Hubble's Law) the cosmic velocity dispersion should always be taken into account, which gives errors $\sim 3$ Mpc minimum. Distances from redshifts should not therefore be trusted within 5 Mpc. Care should also be taken in directions towards the attractors in the model, where the velocity dispersion is significantly increased. We note that in an ideal world, all galaxies within the region of space where peculiar velocities make up a significant fraction of the recessional velocity would have redshift-independent distances. In the absence of that, a velocity field model applied with care can remove the systematic biases which are introduced by the use of Hubble's Law.

In Chapter 3 we also discuss the methods used to fit multiattractor models and how we choose the preferred model. An important point is that simple $\chi^2$ minimization is not appropriate because the errors on peculiar velocities are not distributed as a Gaussian. We note that using a $\chi^2$ minimization procedure, similar to that used by Lynden-Bell *et al.* (1988) to find the original GA, we find a similar

best fit attractor in the mock catalog. When a goodness of fit which accounts for the non-Gaussian errors is applied, the best fit single attractor is Virgo.

Information criteria as described in Liddle (2004) are used to select the preferred model out of a range of choices with different numbers of parameters. Our preferred model fit to the mock data includes infall onto Virgo, the Hydra-Centaurus superclusters and a quadrupole component.

In Chapter 4 we introduce the SFI++ sample of galaxies, which includes 5653 galaxies with measurements suitable for use in the Tully-Fisher relation. A subset of 911 of these galaxies, which lie in the vicinities of 36 nearby clusters are used to derive a template Tully-Fisher relation, $M - 5\log h = -20.90 - 7.36(\log W - 2.5)$, or $L \propto v^{2.9}$. The total scatter from this relationship is calculated to be $\epsilon_{\rm obs} = 0.43 - 0.296(\log W - 2.5)$, resulting in distance errors $\sim 18\%$.

The peculiar velocities of the 36 clusters are fit simultaneously with the template TF relation. We find a cluster peculiar velocity dispersion of $344 \pm 25$ km s$^{-1}$ after correction for error broadening, on the large side of previous measures. This result, along with the relatively large scatter from the template, suggests that clusters assignments should be carefully reviewed, and that it may be possible to improve the distance estimates by reducing the scatter slightly in this way.

In Chapter 5 we explore one of the largest sources of error in the Tully-Fisher relation: the correction of the observed magnitudes of galaxies for internal extinction. Two samples of galaxies are constructed both of which have photometry from 2MASS and redshifts; the smaller subset also having I-band photometry. We search for the impact of internal extinction in these galaxies by looking for disk inclination dependences of photometric quantities, and derive corrections for internal extinction in J, H and K-bands. We explore a simple photometric model for extinction which is able to qualitatively reproduce the observed trends. We also study variation in the amount of extinction with galaxy luminosity. This Chapter is published in Masters, Giovanelli & Haynes (2003).

In Chapters 6 we describe a local "field" spiral sample extracted from the SFI++. Galaxies are chosen to avoid large groups and clusters, and to have high quality TF data. We average the peculiar velocities of galaxies in small groups, and include the cluster peculiar velocities derived in Chapter 4.

Chapter 7 introduces various primary distance methods, and describes a sample of galaxies with primary distance measurements taken from the literature. We briefly investigate the consistency and errors of the methods using the subset of galaxies with multiple distance estimates. A small fraction of these galaxies are also found in the SFI++. The relationship between primary and TF distances for these galaxies is consistent with 18% error on TF. As a sanity check we look at the TF relation of galaxies with Cepheid distances, and find it consistent with the template derived in Chapter 4. These data can be used for a simple estimate of Hubble's constant which we measure to be $77 \pm 4$ km s$^{-1}$ Mpc$^{-1}$.

Chapter 8 ties together work presented in the rest of the thesis. In it, multi-attractor models as described in Chapter 3 are fit to the peculiar velocity samples from Chapters 6 and 7 (both individually after they are combined). The advantage

of combining the two samples is seen, in particular in the ability to locate attractors (which is not possible using the SFI++ alone), and in the magnitude and direction of the dipole and quadrupole components, which are better constrained in the larger volume SFI++ sample.

Our preferred model includes infall onto Virgo and the Hydra-Centaurus supercluster, a quadrupolar component describing extra expansion out of the supergalactic plane and compression along SGX and a residual dipole pointing towards the Hydra-Centaurus/Shapley superclusters. The motion of the Local Group can be completely explained by this model, leaving no evidence for a "Local Anomaly" (excess LG motion towards -SGZ) which has previously been suggested.

We argue that we see evidence for infall onto both the Hydra-Centaurus and Shapley superclusters. Infall onto Shapley, which is significantly outside our sample volume is best fit as a bulk flow and accounts for part of the residual dipole. We suggest that previous arguments about the nature of the "great attractor" are solved by this physically obvious result. In particular the mass of the nearby "great attractor" associated with Hydra-Centaurus is most likely inflated in models which do not also account for infall onto the Shapley supercluster and is therefore not as significant as suggested in previous "great attractor" models.

The parametric velocity field presented in Chapter 8 is fit to a sample of velocity field tracers almost an order of magnitude larger than any that has been used before. Simple parametric models provide insight into the dominant sources of attraction in the volume, but the model parameters can be hard to disentangle, for example the imprint of outside attractors is difficult to distinguish from bulk motion of the entire sample. This sample represents the biggest (and perhaps final) of its generation of peculiar velocity samples; future work is concentrating on much larger numbers of galaxies, but with correspondingly lower quality peculiar velocities (*e.g.* plans to measure $D_n-\sigma$ distances for 15000 galaxies in the southern sky with 6dF; Jones *et al.* 2004). The SFI++ sample should be exploited for more complex non-parametric models of the velocity field, where the larger numbers along with high quality peculiar velocities will provide higher resolution views of the smoothed density field than was possible with previous samples (and this is work we plan for the future). Meanwhile, the parametric modeling here provides the best currently available correction for redshift distances in the local universe.

## 9.2 Suggestions for Future Work

The samples presented in this thesis can be used for a variety of scientific applications going beyond what has been studied here. The SFI++ Tully-Fisher sample in particular represents a significant increase in the number of galaxies available for such studies. In this Section, we'll concentrate suggestions for future work in two main areas:

1. Further study of the Tully-Fisher relation and its scatter, with a view to investigate its implications on galaxy formation and evolution, and to improve

the measurement of galaxy distances.

2. More detailed and less model dependent studies of the local peculiar velocity field.

### 9.2.1 The Tully-Fisher Relation

#### The Extent of the TF Relation

The extension of the Tully-Fisher relation to low mass galaxies has been a matter of discussion ever since the relation was first identified. If the TF relation is a fundamental result of galaxy formation mechanisms, then all galaxies falling on the same relation presumably form in self similar ways. A systematic deviation of dwarf galaxies from the TF relation would suggest a different formation mechanism for these galaxies: *i.e.* that they are not just smaller versions of large spiral galaxies. Several studies have looked at this issue in optical pass bands, including Kannappan, Fabricant & Franx (2002) which describes a split in the dwarf extension of the TF relation in U, B and R-bands, confirming findings by Pierini (1999) in B-band. The large sample used to derive the template in Chapter 4, means that we have a larger extent to low mass galaxies than previous derivations of the I-band TF relation; the Giovanelli *et al.* (1997b) sample, SCI, had only 4 galaxies with $\log W < 2.1$, or $v_{\rm max} < 63$ km s$^{-1}$, while the SFI++ template sample has $\sim 15$. The cluster sample in Ursa Major illustrates a suggestion that low mass galaxies may lie preferentially below the TF relation (see Figure 9.1), which may also be evident in the local "field" sample constructed in Chapter 6 (see Figure 6.1). A study of the properties of low mass galaxies and their deviation from the template derived here would therefore be an interesting follow-up.

The SFI++ template sample also has more high mass galaxies (or fast rotators) than earlier samples, having about twice as many galaxies with $v_{\rm max} > 280$ km s$^{-1}$, than SCI (Giovanelli *et al.* 1997b). All but two of these galaxies lie below the TF relation presented in Chapter 4. It would be interesting to know if these offsets are intrinsic to the galaxies, or perhaps an impact of the larger extinction along the long path lengths in these physically big galaxies. At this high mass end of the TF relation the numbers of galaxies are also be limited by the steeply falling luminosity function, probably leading to an intrinsic incompleteness bias. An observational limit on the most massive, and fastest rotating disk galaxies has been set at $v_{\rm max} \sim 400$ km s$^{-1}$, physically this limit is likely due to disk stability criteria (Spekkens 2005). If such galaxies deviate from the TF relation the argument that they are otherwise normal spiral disks breaks down.

#### The Scatter in the TF Relation

The observed Tully-Fisher relation and its scatter provides constraints for theoretical models of galaxy formation. Recent work has focused on studies of the TF scatter, and trends with other galaxy parameters, both as a (so far unsuccessful)

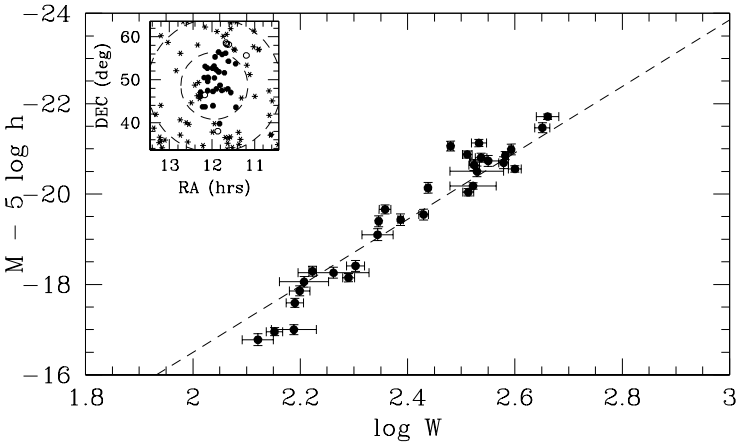



Figure 9.1: Tully-Fisher relation and sky distribution of galaxies in the Ursa Major cluster. *Bona fide* cluster galaxies are shown as filled circles and plotted on the TF relation. The dashed line shows the bivariate fit to the **in** sample of Chapter 4, adjusted for the calculated offset of the Ursa Major sample. Peripheral cluster members are shown as open circles, and other galaxies with TF data in the area, but not in the cluster are shown as asterisks.

search for a third parameter in the TF relation, and because the scatter in itself holds important clues for the understanding of galaxy formation (*e.g.* Kannappan *et al.* 2002). Intrinsic scatter from the TF relation can arise either because of variations in the total mass to light ratio (either from differences in the stellar mass to light ratio, or in the stellar mass fraction) or because the rotation velocity is not accurately representing the mass of the galaxy, for example because of distortions in the velocity field, or a lack of velocity tracers in the outskirts of the galaxy.

The high scatter in the relation presented in Chapter 4 of this thesis should be studied further. In particular a careful accounting of the sources of observational error should be made, to distinguish the intrinsic scatter from the total observed error. We should question if this larger scatter (as compared to Giovanelli *et al.* 1997b) is real, or if we can lower the scatter (and therefore provide more precise distances and peculiar velocities) by reviewing cluster membership assignments.

The larger numbers of galaxies in the SFI++ also means that a larger number of statistically unlikely outliers are seen. If these significant offsets from the TF are intrinsic, the outlier galaxies are very interesting to provide constraints on perhaps the least well understood pieces of the galaxy formation jigsaw – the physics of star formation, and the impact of feedback.

**A Near Infra-Red TF Relation**

The spectroscopic data presented here, combined with photometry from the all sky 2MASS survey could be used to derive TF relations in the J, H and K-bands. Deriving these templates in a way consistent with the I-band template would provide a unique four color near infra-red (NIR) TF relation. Such data would be extremely useful as a constraint for models of spiral galaxy formation, in particular in studies of the origin of the TF relation and its dependence on the details of star formation (van den Bosch 2000). NIR bands, in particular the K-band are most sensitive to the old stellar population in a galaxy, and therefore are more representative of the stellar mass of the galaxy, being less impacted by emission from young, recently formed stars. Previous studies of the TF relation in the NIR indicate that the slope steepens and the scatter decreases with increasing wavelength (*e.g.* the B,R,I,K study of galaxies in Ursa Major by Verheijn 2001).

The advantage of using the TF relation in the NIR has long been recognized. NIR bands suffer less from extinction due to dust (if not being completely free of it as shown in Masters, Giovanelli & Haynes 2003). This includes both dust internal to the galaxies themselves, and (as is especially important for studies of the local universe) dust in the plane of our own Galaxy. The SFI++ makes use of a subset of a large database of HI global profiles and H$\alpha$ optical rotation curves maintained at Cornell (see *e.g.* Springob (2005) and Catinella (2005) respectively), and is limited in numbers by the availability of I-band photometry. 2MASS photometry extends over the entire sky, so an accurately calibrated NIR TF relation would provide an even larger peculiar velocity sample than the SFI++, which would also extend further into the Zone of Avoidance.

### 9.2.2 The Velocity Field in the Local Universe

**Non-parametric reconstructions**

The SFI++ sample presented in this thesis should be exploited to study the velocity field in the local universe in as many ways as possible as it is the largest existing peculiar velocity sample from a single distance indicator. Parametric models like the one presented in this thesis, rely on the spherical infall approximation and are a logical first look study of the velocity field, providing useful analytic models for corrections to redshift models. Such models however are clearly an oversimplification of the real universe, and much more information on the local velocity field resides in the SFI++ sample which could be used to reconstruct the full three dimensional velocity and density fields in the the local universe.

In particular we plan to make a POTENT reconstruction of the density and velocity fields from SFI++. The POTENT method (Dekel *et al.* 1990) makes use of the result from gravitational instability theory, that the linear velocity field is directly proportional to the underlying gravitational potential field. The full three dimensional velocity and density fields can therefore be reconstructed from the observed radial velocity field. Application of this method requires the construction

of detailed mock catalogs to understand the unavoidable errors and biases in the peculiar velocity sample, as well as the impact of the uneven sky distribution. Such methods also require significant smoothing of the velocity field. The high density of SFI++ galaxies compared to earlier peculiar velocity samples means that the SFI++ POTENT reconstruction will be made at higher resolution (smaller smoothing lengths) than has previously been possible.

The SFI++ velocity field should also be compared to the velocity field derived from redshift surveys. A redshift survey complete to a known limit can be used to reconstruct the peculiar velocity field by assuming that the galaxies trace the distribution of mass and calculating the gravitational field and real space positions of the galaxies in an iterative manner. A comparison of SFI with the PSC$z$ velocity field is presented in Branchini *et al.* (2001); a similar study could be done with this significantly larger peculiar velocity sample. The velocity field of SFI++ could also be compared to the 2MASS redshift survey, which is using the all-sky 2MASS galaxy catalog as a source list for redshift targets and will provide a density and velocity field at significantly higher resolution than PSC$z$ on its completion.

### The Velocity Field on Smaller Scales

On smaller scales, the primary distance sample assembled for this thesis could also be used to study the very nearby peculiar velocity field in more detail. Two recent papers (Whiting 2003, 2005) have suggested that on scales intermediate between small groups and large scale structure either mass does not trace light or peculiar velocities are not caused by gravitational interactions. This result, if backed up by independent study would call into question the current paradigm for the growth of structure and contradicts the excellent agreement with theory found on larger scales. Those studies use a similar data set to the primary distance catalog assembled here.

A more detailed study of the dynamics of the Virgo cluster region would also be interesting. As shown in Chapter 3, distances to galaxies in this direction are extremely uncertain. A better understanding of the velocity field in the vicinity of the cluster would be desirable, both in terms of improving our understanding of cluster formation and in providing improved estimates to correct redshift distances in that direction. The primary distance sample presented here contains 60 galaxies in the vicinity of Virgo, while the SFI++ has $\sim 50$ galaxies in the cluster.

### Galaxy Alignments

Another potentially interesting application for the SFI++ is the study of galaxy alignments, both with local large scale structure, and perhaps with the direction of their own peculiar velocities. This field has generated a lot of interest in recent years partly because of the emergence of weak lensing as a cosmological tool. Intrinsic alignments of galaxies act as a source of noise in these measurements which must be understood. At a more fundamental level galaxy alignments are

also interesting for what they can reveal about the way galaxies are built up over time. Alignments could arise either from the initial conditions of galaxy formation, or as a result of gravitational interactions over the history of the universe. The angular momentum vectors of dark matter halos in numerical simulations have been studied (see *e.g.* Bailin & Steinmetz 2005) showing a preference for cluster and group sized objects to be aligned perpendicular to filaments because they are built up by a flow of matter along the filaments. Galaxy sized halos appear to be preferentially aligned parallel to the filaments, which in the local universe should mean that galaxy angular momenta preferentially lie in the supergalactic plane (as also suggested by Navarro, Abadi & Steinmetz 2004). Observationally there is still some disagreement over the detection of such alignments. The SFI++ provides an ideal sample for such a study. The I-band photometry provides carefully measured inclinations and position angles for almost 6000 galaxies within $cz \sim 10,000$ km s$^{-1}$, which also have distances and peculiar velocities.

This thesis, and the SFI++ Tully-Fisher sample presented in it come at the beginning of a new era in cosmology. Recently large redshift surveys have been used in combination with observations of the cosmic microwave background to provide such strong constraints on the cosmological parameters that many astronomers now consider cosmology 'solved' (see *e.g.* Tegmark *et al.* 2004), giving the concordance model of ΛCDM in which the universe consists of 4% baryons, 26% dark matter and 70% dark energy. Techniques, such as the study of the local peculiar velocity field which in the past depended too much on unknown cosmological parameters can now be reinvented to study the details of structures within the background of "solved" cosmology.

## BIBLIOGRAPHY


Aaronson, M., Huchra, J., Mould, J., Schechter, P. & Tully, R.B. 1982 ApJ 258, 64.

Allen S. W., Schmidt R. W., & Fabian A. C., 2001, MNRAS, 328, L37

Bahcall, N.A. & Oh, S.P. 1996, ApJ, 462, L49.

Bailin, J. & Steinmetz, M. 2005, ApJ, (in press; astro-ph/0408163).

Bardelli, S., Zucca, E., Zamorani, G., Moscardini, L. & Scaramella, R. 2000, MNRAS, 312, 540

Barnes, D.G., Staveley-Smith, L., de Blok, W.J.G., Oosterloo, T., Stewart, I.M. (and 34 co-authors), 2001, MNRAS, 322, 486

Begum, A., Chengalur, J.N., Karachentsev, I.D. & Sharina, M.E. 2005, MNRAS, 359, L53.

Bennett, C.L., Halpern, M., Hinshaw, G., Jarosik, N., Kogut, A., Limon, M., Meyer, S.S., Page, L., Spergel, D.N., Tucker, G.S., Wollack, E., Wright, E.L., Barnes, C., Greason, M.R., Hill, R.S., Komatsu, E., Nolta, M.R., Odegard, N., Peiris, H.V., Verde, L. & Weiland, J.L. 2003 ApJS, 148, 1.

Benson, B.A., Church, S.E., Ade, P.A.R., Bock, J.J., Ganga, K.M., Hinderks, J.R., Mauskopf, P.D., Philhour, B., Runyan, M.C. & Thompson, K.L. 2003, ApJ, 592, 674.

Binggeli, Sandage & Tammann 1988, ARA&A 26, 509

Blakeslee, J.P., Ajhar, E.A., & Tonry, J.L. 1999, in *Post-Hipparcos Cosmic Candles*, eds. A. Heck & F. Caputo (Boston: Kluwer), 181 (astro-ph/9807124)

Broeils, A.H. 1992. Ph.D. thesis, U. Groningen.

Branchini, E., Freudling, W., Da Costa, L.N., Frenk, C.S., Giovanelli, R., Haynes, M.P., Salzer, J.J., Wegner, G. & Zehavi, I. 2001 MNRAS 326, 1191.

Branchini, E., Teodoro, L., Frenk, C.S., Schmoldt, I., Efstathiou, G., White, S.D.M., Saunders, W., Sutherland, W., Rowan-Robinson, M., Keeble, O., Tadros, H., Maddox, S. & Oliver, S. 1999, MNRAS, 308, 1.

Brunthaler, A., Reid, M.J., Falcke, H., Greenhill, L.J. & Henkel, C. 2005, Science 307, 1440.

Buote, D. A., & Lewis, A. D. 2003, ApJ, 604, 116.

Burstein, D. & Heiles, C. 1978, ApJ, 225, 40.

Calzetti, D., 2001, PASP, 113, 1449

Catinella, B., Haynes, M.P. & Giovanelli, R. 2005, AJ, (in press; astro-ph/0506148)

Catinella, B. 2005, Ph.D. thesis, Cornell Univ.

Ciardullo, R. 2003. in *Stellar Candles for the Extragalactic Distance Scale*, ed. D. Alloin & W. Gieren, Lect. Notes Phys., 635, 243 (astro-ph/0301279).

Colless, M. & Dunn, A.M. 1996, ApJ, 548, 435.

Collister, A.A. & Lahav, O. 2005, MNRAS, (in press; astro-ph/0412516)

Courteau, S., Faber, S.M., Dressler, A. & Willick, J.A. 1993, ApJ, 412, L51.

Courteau, S. & van den Bergh, S. 1999, AJ, 118, 337.

Cutri, R. M., *et al.* 2000, Explanatory Supplement to the 2MASS Second Incremental Data Release (Pasadena: Caltech).

Dale, D.A. 1998, Ph.D. thesis, Cornell Univ.

David, L. P., Nulsen, P. E. J., McNamara, B. R., Forman, W., Jones, C., Ponman, T., Robertson, B., & Wise, M. 2001, ApJ, 557, 546.

Dekel, A., Bertschinger, E. & Faber, S.M. 1990, ApJ, 364, 349.

de Vaucouleurs, G. 1958, AJ, 63, 253.

Disney, J. I., Burstein, D. eds. 1995, *The Opacity of Spiral Disks* (Dordrecht: Kluwer)

Disney, M., Davis, J. & Phillips, S. 1989, MNRAS, 239, 939

Dressler, A. & Faber, S.M. 1990, ApJ, 354, L45.

Dressler, A., Lynden-Bell, D., Burstein, D., Davies, R.L., Faber, S.M., Terlevich, R. & Wegner, G. 1987, ApJ, 313, 42.

Drinkwater, M.J., Parker, Q.A., Proust, D., Slezak, E. & Quintana, H. 2004, PASP, 21, 89.

Drinkwater, M.J., Gregg, M.S. & Colless, M. 2001, ApJ, 548, L139.

Dolag, K., Hansen, F.K., Roncarelli, M. & Moscardini, L. 2005, MNRAS (submitted, astro-ph/0505258).

Einasto, M., Tago, E. Jaaniste, J., Einasto, J. & Andernach, H. 1996, A&A, 123, 119.

Evans, Rh. 1992, Ph.D. thesis, University of Cardiff

Fairall, A. & Lahav, O. 2004. astro-ph/0411436, conference summary; to appear in *Nearby Large Scale Structures and the Zone of Avoidance*, eds. A.P. Fairall and P.A. Woudt, ASP Conf. Series.

Federspiel, M., Tammann, G.A. & Sandage, A. 1998 AJ, 495, 115.

Fernie, J.D. 1969, PASP, 81, 707.

Ferrarese, L., Mould, J.R., Kennicutt, R.C.Jr., Huchra, J., Ford, H.C., Freedman, W.L., Stetson, P.B., Madore, B.F., Sakai, S., Gibson, B.K., Graham, J.A., Hughes, S.M., Illingworth, G.D., Kelson, D.D., Macri, L., Sebo, K. & Silbermann, N.A. 2000, ApJ, 529, 745.

Filippenko, A.V. & Ho, L.C. 2003 ApJ, 588, L13.

Fouqué, P., Solanes, J.M., Sanchis, T. & Balkowski, C. 2001, A&A, 375, 770.

Freedman, W.L., Madore, B.F., Gibson, B.K., Ferrarese, L., Kelson, D.D., Sakai, S., Mould, J.R., Kennicutt, R.C.Jr., Ford, H.C., Graham, J.A., Huchra, J.P., Hughes, S.M.G., Illingworth, G.D., Macri, L.M. & Stetson P.B. 2001, ApJ, 553, 47.

Giavalisco, M., Mancinelli, B., Mancinelli, P.J. & Yahil, A. 1993, ApJ, 411, 9.

Giovanelli, R., Haynes, M. P., Salzer, J. J., Wegner, G., da Costa, L.N., & Freudling, W. 1994, AJ, 107, 2036 (G94).

Giovanelli, R., Haynes, M. P., Salzer, J. J., Wegner, G., da Costa, L.N., & Freudling, W. 1995, AJ, 110, 1059.

Giovanelli, R., Haynes, M., Herter, T., Vogt, N.P., Wegner, G., Salzer, J. J., da Costa, L. N., & Freudling, W. 1997a, AJ, 113, 22.

Giovanelli, R., Haynes, M., Herter, T., Vogt, N.P., Wegner, G., Salzer, J. J., da Costa, L. N., & Freudling, W. 1997b, AJ, 113, 53 (G97b).

Giovanelli, R., Haynes, M.P., Freudling, W., da Costa, L.N., Salzer, J.J. & Wegner, G., 1998a, ApJ 505, L91.

Giovanelli, R., Haynes, M.P., Salzer, J.J., Wegner, G., da Costa, L.N. & Freudling, W. 1998b, AJ 116, 2632.

Giovanelli, R. & Haynes, M.P. 2002 ApJ, 571, L107.

Graham, A. W. 2001 MNRAS, 326, 543.

Han, M. & Mould, J. 1990 ApJ, 360, 448.

Han, M. 1992, ApJS, 81, 35

Hanski, M.O., Theureau, G., Ekholm, T. & Teerikorpi P. 2001, A&A, 378, 345.

Haynes, M. P., Giovanelli, R., Salzer, J. J., Wegner, G., Freudling, W., da Costa, L. N., Herter, T., & Vogt, N. P. 1999a, AJ, 117, 1668.

Haynes, M. P., Giovanelli, R., Chamaraux, P., da Costa, L. N., Freudling, W., Salzer, J. J., Wegner, G. 1999b, AJ, 117, 2039.

Henning, P.A., Staveley-Smith, L., Ekers, R.D., Green, A.J., Haynes, R.F., Juraszek, S., Kesteven, M.J., Koribalski, B., Kraan-Korteweg, R.C., Price, R.M., Sadler, E.M. & Schröder, A. 2000, AJ, 119, 2686.

Herrnstein, J.R., Moran, J.M., Greenhill, L.J., Diamond, P.J., Inoue, M., Nakai, N., Miyoshi, M., Henkel, C. & Riess, A. 1999, Nature, 400, 539 .

Holmberg, E. 1958, Medd. Lunds Astr Obs. Ser. 2, No. 136

Holmberg E. 1975, in *Stars and Stellars Systems, Vol. IX*, A. Sandage, M. Sandage, J. Kristian eds. (University of Chicago, Chicago).

Hudson, M.J., Smith, R.J., Lucey, J.R., Branchini, E. 2004 MNRAS, 352, 61.

Huizinga, J. E. 1994, Ph.D. thesis, University of Groningen

Iben, I.Jr., Renzini, A. 1983, ARA&A, 21, 271.

Izotov, Y.I., & Thuan, T.X. 2005, ApJ, 616, 768.

Jarrett, T. H., Chester, T., Cutri, R., Schneider, S., & Huchra, J. P., 2003, AJ, 125, 525.

Jarrett, T. H., Chester, T., Cutri, R., Schneider, S., Skrutskie, M., & Huchra, J.P. 2000, AJ, 119, 2498.

Jones, D.H., Saunders, W. , Colles, M., Read, M.A, Parker, Q.A. *et al.* 2004, MNRAS, 355, 747.

de Jong, R. S. 1996, A&AS, 118, 557.

Kannappan, S.J., Fabricant, D.G. & Franx, M. AJ, 123, 2358.

Karachentsev, I.D. & Makarov, D.I. 2001, Astrophysics (English translation of Astrofizika) 44, 1.

Karachentsev, I.D., Karachentseva, E.W., Huchtmeier, W.K. & Makarov, D.I. 2004, AJ 127, 2031.

Karachentsev, I.D. & Tikhonov, N.A. 1994, A&A, 286, 718.

Kauffmann, G., Colberg, J.M., Diaferio, A. & White, S.D.M. 1999, MNRAS, 307, 529.

Kochanek, C. S., Pahre, M. A., Falco, E. E., Huchra, J. P., Mader, J., Jarrett, T. H., Chester, T., Cutri, R., Schneider, S. E. 2001, ApJ, 560, 566.

Kolatt, T., Dekel, A., Ganon, G. & Willick, J. 1996, AJ, 458, 419.

Kron, R. G. 1980, ApJS, 43, 305.

Kuchinski, L. E., Terndrup, D. M., Gordon, K. D. & Witt, A. N. 1998, AJ, 115, 1438.

Lahav, O., Lilje, P., Primack, J.R. & Rees, M.J. 1991, MNRAS, 251, 128.

Lahav, O., Santiago, B.X., Webster, A.M., Strauss, M., Davis, M., Dressler, A. & Huchra, J.P. 2000, MNRAS, 312, 166.

Lauer, T.R. & Postman, M. 1994, ApJ, 425, 418.

Lewis, A.D., Buote, D.A. & Stocke, J.T. 2003, ApJ, 586, 133.

Liddle, A. 2004, MNRAS 351, L49.

Lineweaver, C.H., Tenorio, L., Smoot, G.F., Keegstra, P., Banday, A.J. & Lubin, P. 1996 ApJ, 470, 38.

Lu, N.Y., Salpeter, E.E. & Hoffman, G.L. 1994, ApJ, 426, 473.

Lynden-Bell, D., Faber, S.M., Burstein, D., Davies, R.L., Dressler, A., Terlevich, R.J, & Wegner, G. 1988, ApJ, 326, 19.

Madore, B.F. & Freedman, W.L. 1995, AJ, 109, 1645.

Masters, K.L., Haynes, M.P. & Giovanelli, R. 2004, ApJ, 607, L115.

Masters, K.L., Giovanelli, R. & Haynes, M.P. 2003, AJ, 126, 158.

Mathewson, D.S., Ford, V.L. & Buchhorn, M. 1992a ApJS, 81, 413.

Mathewson, D.S., Ford, V.L. & Buchhorn, M. 1992b ApJ, 389, L5.

Mathis, H., Lemson, G., Springel, V., Kauffmann, G., White, S.D.M., Eldar, A. & Dekel, A. 2002, MNRAS, 333, 739.

McConnachie, A.W., Irwin, M.J., Ferguson, A.M.N., Ibata, R.A., Lewis,G.F.& Tanvir, N. 2004 MNRAS, 350, 243.

Mieske, S. & Hilker, M. 2003, A&A, 410, 445.

Mieske, S., Hilker, M. & Infante, L. 2005, A&A, (in press; astro-ph/0503647).

Mo, H.J. & Mao, S. 2000 MNRAS, 318, 163.

Moriondo, G., Giovanelli, R., & Haynes, M. P. 1998, A&A, 338, 795.

Navarro, J.F., Abadi, M.G. & Steinmetz, M. 2004, ApJ, 613, L41.

Navarro, J.F., Frenk, C.S., & White, S.D.M. 1997, ApJ, 490, 493.

Navarro, J.F. & Steinmetz, M. 2000, ApJ, 538, 477.

Peebles, P.J.E. 1976, ApJ, 205, 318.

Pierini, D. 1999, A&A, 352, 49.

Poggianti, B. M. 1997, A&AS, 122, 399.

Pointecouteau, E., Arnaud, M., Kaastra, J. & de Plaa, J. 2004, A&A, 423, 33.

Press, W.H., Teukolsky, S.A., Vetterling, W.T. & Flannery, B.P. 2001. *Numerical Recipes in Fortran 77: The Art of Scientific Computing (Vol. 1 of Fortran Numerical Recipes)*, (2nd ed, reprinted with corrections; Cambridge Univ. Press.)

Press, W. & Schechter, P. 1974, ApJ, 187, 425.

Reiprich, T.H. & Böhringer, H. 2002, AJ, 567, 716.

Rosenberg, J.L. & Schneider, S.E. 2002, ApJ, 567, 247 (RS02).

Rubin, V.C. *et al.* 1976, AJ, 81, 687.

Sakai, S., Mould, J.R., Hughes, S.M.G., Huchra, J.P., Macri, L.M., Kennicutt, R.C.Jr., Gibson, B.K., Ferrarese, L., Freedman, W.L., Han, M., Ford, H.C., Graham, J.A., Illingworth, G.D., Kelson, D.D., Madore, B.F., Sebo, K., Silbermann, N.A. & Stetson, P.B. 2000, ApJ, 529, 698.

Scaramella, R., Baiesi-Pillastrini, G., Chincarini, G., Vettolani, G. & Zamorani, G. 1989, Nature 338, 562.

Schechter, P.L. 1980, AJ, 85, 801.

Schlegel, D. J., Finkbeiner, D. P., & Davis, M. 1998, AJ, 500, 525.

Shoko, S., Ferrarese, L., Kennicutt, R.C.Jr. & Saha, A. 2004, ApJ, 608, 42.

Silva, D.R., Massey, P., DiGioia-Eastwood, K. & Henning, P.A. 2005, ApJ623

Spekkens, K. 2005, Ph.D. thesis, Cornell Univ.

Springob, C.M. 2005, Ph.D. thesis, Cornell Univ.

Springob, C.M., Haynes, M.H., Giovanelli, R. & Kent, B. 2005, ApJS, (in press).

Strauss, M.A., Cen, R. & Ostriker, J.P. 1993, ApJ, 408, 389.

Sunyaev, R.A. & Zeldovich, Y.B. 1972, *Comm. Astrophys. Space Phys.*, 4, 173.

Tammann, G.A. & Sandage, A. 1985, ApJ, 294, 81.

Tegmark, M., Strauss, M.A., Blanton, M.R., Abazajian, K., Dodelson, S. (and 62 co-authors), 2004 PhRvD 69.

Thim, F., Hoessel J.G., Saha, A., Claver, J., Dolphin, A., Tammann, G.A. 2004 AJ, 127, 2322.

Tonry, J.L., Blakeslee, J.P., Ajhar, E.A. & Dressler, A. 2000, ApJ, 530, 625 (TB00).

Tonry, J.L., Dressler, A., Blakeslee, J.P., Ajhar, E.A., Fletcher, A.B., Luppino, G.A., Metzger, M.R. & Moore, C.B. 2001 ApJ, 546, 681.

Tonry, J.L. & Schneider, D.P. 1988, AJ, 96, 807.

Tully, R.B. & Pierce, M.J. 2000, ApJ, 533, 744.

Tully, R. B., Pierce, M. J., Huang, J-S., Saunders, W., Verheijen, M. A. W., Witchalls, P. L. 1998, AJ, 115, 2264.

Tully, R.B. 1987, ApJ 321, 280.

Tully, R.B. & Fisher, J.R. 1977, A&A, 54, 661.

van den Bosch, F.C. 2000, ApJ, 530, 177.

Verheijn, M.A.W. 2001, ApJ, 563, 694.

Verheijn, M.A.W. 1997, Ph.D. thesis, Univ. Groningen.

Vogt, N.P. 1995, Ph.D. thesis, Cornell Univ.

Watkins, R. 1997, MNRAS, 277, 1210.

Whiting, A.B. 2005, ApJ, 622, 217.

Whiting, A.B. 2003, ApJ, 587, 186.

Willick, J.A., Batra, P. 2001, ApJ, 548,564.

Willick, J.A., Strauss, M.A., Dekel, A & Kolatt, T. 1997, ApJ, 486, 629.

Woudt, P.A. & Kraan-Korteweg, R.C. 2001 A&A, 380, 44.

Xilouris, E. M., Byun, Y. I., Kyafis, N. D., Paleologou, E. V., & Papamastorakis, J. 1999, A&A, 344, 868.

Yahil, A. 1985, in *Workshop on the Virgo Cluster of Galaxies*, ed. O. G. Richter & B. Binggeli (Munich: ESO), 359.

Zwaan, M.A., Briggs, F.H., Sprayberry, D. & Sorar, E. 1997, ApJ, 490, 173 (Z97).

Zwaan, M.A., Staveley-Smith, L. Koribalski, B.S., Henning, P.A., Kilborn, V.A. (and 35 co-autors), 2003, AJ, 125, 2842 (Z03).